

ANALYSIS OF RADIATIVE DECAYS
OF CHARGED B MESONS TO
BARYONIC FINAL STATES

by
JAN STRUBE

A DISSERTATION
Presented to the Department of Physics
and the Graduate School of the University of Oregon
in partial fulfillment of the requirements
for the degree of
Doctor of Philosophy

September 2008

University of Oregon Graduate School

Confirmation of Approval and Acceptance of Dissertation prepared by:

Jan Strube

Title:

"ANALYSIS OF RADIATIVE DECAYS OF CHARGED B MESONS TO BARYONIC FINAL STATES"

This dissertation has been accepted and approved in partial fulfillment of the requirements for the Doctor of Philosophy degree in the Department of Physics by:

David Strom, Chairperson, Physics
James Brau, Advisor, Physics
John Toner, Member, Physics
Nilendra Deshpande, Member, Physics
Michael Kellman, Outside Member, Chemistry

and Richard Linton, Vice President for Research and Graduate Studies/Dean of the Graduate School for the University of Oregon.

September 6, 2008

Original approval signatures are on file with the Graduate School and the University of Oregon Libraries.

An Abstract of the Dissertation of

Jan Strube for the degree of Doctor of Philosophy
 in the Department of Physics to be taken September 2008

Title: ANALYSIS OF RADIATIVE DECAYS OF CHARGED B MESONS
 TO BARYONIC FINAL STATES

Approved: _____

Dr. James E. Brau

The abundance of B mesons at B factories opens the door to the search in rare decays for physics outside of the Standard Model. Flavor-changing neutral current transitions proceed only via higher order in the Standard Model, resulting in a $b \rightarrow s\gamma$ branching fraction of about 3×10^{-4} , but hypothesized particles could alter the rate significantly. Decays of B mesons that proceed via this electroweak penguin diagram are an interesting example of flavor-changing neutral currents, due to the large number of accessible final states with observables that are sensitive to new processes.

This dissertation describes the analyses of such decays $B^- \rightarrow \Lambda \bar{p} \gamma$, $B^- \rightarrow \Sigma^0 \bar{p} \gamma$, $B^- \rightarrow \Lambda \bar{p} \pi^0$ and $B^- \rightarrow \Sigma^0 \bar{p} \pi^0$ using about 350 million B meson pairs recorded by the *BABAR* detector in the years 2001 through 2006. In addition to the decay rate, the distribution of the invariant mass of the baryon pair is presented, using a method for statistical unfolding. The analysis is the first of these decays at the *BABAR* experiment and lays the groundwork for future analyses of the branching fractions and angular correlations of $b \rightarrow s$ decays containing Λ hyperons and other baryons at *BABAR* or higher luminosity B factories.

CURRICULUM VITAE

NAME OF AUTHOR: Jan Strube

PLACE OF BIRTH: Bremen, Germany

DATE OF BIRTH: January 22nd, 1978

GRADUATE AND UNDERGRADUATE SCHOOLS ATTENDED:

University of Oregon, Eugene, OR

Universität Ulm, Germany

DEGREES AWARDED:

Doctor of Philosophy in Physics, 2008, University of Oregon

ACADEMIC INTERESTS:

Cosmological Connections to Particle Physics

Simulation of Particle Detectors

Development and Implementation of Computational Algorithms

PROFESSIONAL EXPERIENCE:

Research Associate, Rutherford Appleton Laboratory, 2008-

Research Assistant, University of Oregon, 2002-2008

Teaching Assistant, Universität Ulm, 1999-2000

PUBLICATIONS:

J.E. Brau, C. Potter, J. Early, J. Strube, “Flavor Tagging and the Higgs branching ratio measurement at the Linear Collider”, Seogwipo 2002, Linear Colliders 487-490

B. Aubert *et al.* “Evidence for D0-anti-D0 Mixing”, Phys. Rev. Lett. 98 (2007) 211802

215 additional publications co-authored in refereed journals

ACKNOWLEDGMENTS

I came to the United States in an exchange program between the states of Baden-Württemberg and Oregon. Having had only a mediocre introduction to elementary particles at the Universität Ulm, I enthusiastically took the course *Elementary Particle Phenomenology* with Jim Brau, but I performed poorly on the final exam where one task was to fill out a table of particle properties. I was disappointed. Should this really be the essence of High Energy Physics? Learning properties of elementary particles like a phone book? That did not appeal to me very much. However, not to be put off by this, I decided to value the enthusiasm of the instructor over his choice of questions in that final exam, and took the second term of the course. This was the beginning of a very exciting journey which led me to many interesting places across the globe. The work that you are reading cannot be accomplished by a single person, and during the time it took to complete it, I was fortunate to make the acquaintance of several people who helped me along the course in various ways.

In that respect I would like to acknowledge my adviser Jim Brau, whose never-ending enthusiasm for particle physics kept my motivation high during the time of my studies. Although his commitments limited my access to his time, his guidance and encouragements were invaluable. I was able to benefit from his many connections, and I would especially like to mention Michael Peskin, who always has an open ear for students, and who seems to share the same never-ending enthusiasm for the field of high energy physics as Jim, and Norman Graf, who valiantly leads the effort to maintain the Simulation Group for the SiD project in times of harsh budget cuts. It was from him that I learned some of the intricacies of scientific collaborations and he generously let me look at a different side of what it means to carry out an analysis in

a group. His always diplomatic approach to controversies has been a valuable lesson to me.

I would like to thank all of the other students who came to the United States in the exchange program with me, especially my two roommates during the first year, Axel Fingerle, a truly brilliant mind whose deficiency from the academic field into patent law leaves a gaping hole, and Tobias Müller, whose various interests outside of physics kept life interesting and fun.

The students at the University of Oregon were a very diverse bunch, and I would like to thank Jim Gutierrez for being a good friend during my two years in Eugene. We spent countless hours at his house doing homework and studying for exams, but we were also able to enjoy a good couple games of basketball in the times between. The Oregon students that shared their time at SLAC with me, Nick Blount, Jeff Kolb, Rahmat Rahmat, were always up for discussions, lunches and breaks, and I would especially like to thank Jeff and his wife Ruthie for becoming witnesses at my wedding.

Last but not least, I have to mention my wife Yuki, whom I met in the first week after my arrival in Portland, and who has stuck with me since. Her patience, love, and wisdom made it worthwhile.

To Yuki, who makes everything better

TABLE OF CONTENTS

Chapter	Page
I INTRODUCTION	1
II THEORETICAL AND EXPERIMENTAL BACKGROUND	4
II.1 Particle Content	4
II.2 Electroweak Theory	7
II.2.1 The Masses of Gauge Bosons	7
II.2.2 Fermion Couplings and the CKM Matrix	8
II.3 $b \rightarrow s\gamma$	11
II.3.1 Baryonic Final States	12
II.3.2 Two Higgs Doublet Models	14
III THE <i>BABAR</i> EXPERIMENT	17
III.1 PEP-II	17
III.1.1 Backgrounds	19
III.2 The <i>BABAR</i> Detector	20
III.2.1 The Vertex Detector	22
III.2.2 The Drift Chamber	24
III.2.3 Track Reconstruction	26
III.2.4 The DIRC	28
III.2.5 The Electromagnetic Calorimeter	29

III.2.6	The Superconducting Magnet and the Instrumented Flux Return	32
III.3	Detector Simulation	35
IV	ANALYSIS OF BARYONIC B DECAYS	37
IV.1	Introduction	37
IV.2	Samples	38
IV.2.1	Data	38
IV.2.2	Simulation	39
IV.2.3	Lambda Antiproton Gamma	41
IV.2.4	Sigma Antiproton Gamma	42
IV.2.5	Lambda Antiproton Pi	44
IV.2.6	Sigma Antiproton Pi	46
IV.2.7	Backgrounds	46
IV.2.8	Summary of the Simulated Samples	47
IV.3	Event Preselection	47
IV.4	Candidate Reconstruction	49
IV.4.1	B Candidate Reconstruction	51
IV.4.2	Candidate Selection Cuts	51
IV.4.3	Best Candidate Selection	54
IV.5	Fit Strategy	64
IV.5.1	Overview	64
IV.5.2	Separation of the Samples	64
IV.5.3	Components	66
IV.5.4	Variables	66

Chapter	Page
IV.5.5 Summary of Fit Shapes	72
IV.5.6 Combined Fit Strategy to Extract Yields	77
IV.5.7 Toy Studies	86
IV.5.8 Errors	87
IV.6 Computation of the Branching Fraction	94
IV.6.1 Dependence on the Measurement Efficiency	95
IV.6.2 sPlots Validation	95
IV.7 Systematic Uncertainties	97
IV.7.1 Model Uncertainties	97
IV.7.2 B Counting	100
IV.7.3 Cuts	103
IV.7.4 Particle Identification	106
IV.7.5 Single Photon Efficiency	109
IV.7.6 Tracking	109
IV.7.7 Fitting	109
IV.7.8 Summary	110
V RESULTS	117
V.1 Visualization of the Four Fit Variables	117
V.2 Yields in the Data Samples	117
V.3 Reconstruction Efficiencies	131
V.4 Branching Fractions and Upper Limits	131
V.5 Discussion	135
V.5.1 Comparison with Expectation	135
V.5.2 Comparison with Other Experimental Results	135

Chapter	Page
V.5.3 Comparison with Theory	137
V.6 Conclusions	138
APPENDICES	139
A LIKELIHOOD FIT IN THE SIGNAL REGION OF $B^- \rightarrow \Lambda \bar{P} \gamma$	139
B PLOTS OF THE PHOTON ENERGY	146
C CORRELATION OF THE FIT VARIABLES	148
D ADDITIONAL PLOTS OF THE FIT VARIABLES	150
E ALTERNATIVE FIT SHAPES	154
F CUT VARIABLES	158
F.1 Cut Optimization	158
G CUT EFFICIENCIES	165
H CORRELATION OF FIT VARIABLES	170
H.1 Reconstruction as $B^- \rightarrow \Lambda \bar{p} \gamma$	170
H.2 Reconstruction as $B^- \rightarrow \Sigma^0 \bar{p} \gamma$	176
I ALTERNATIVE FIT VARIABLES	182

Chapter	Page
I.1	Correlation Coefficients 182
I.1.1	Reconstruction as $B^- \rightarrow \Lambda \bar{p} \gamma$ 185
I.1.2	Reconstruction as $B^- \rightarrow \Sigma^0 \bar{p} \gamma$ 185
I.2	Parametrization of the Samples 185
I.2.1	Pure Toys 185
I.2.2	Embedded Toys 185
J	VALIDATION OF SPLOTS 188
K	SPLOTS 191
K.1	inPlots 191
K.2	sPlots 192
K.3	Properties 192
L	VERTEX FITTING 194
L.1	A Brief Introduction to the Kalman Algorithm for Vertex Fitting . . . 194
REFERENCES 197

LIST OF TABLES

Table	Page
III.1	Cross sections for various processes at 10.58 GeV collision energy 18
IV.1	Integrated luminosity and number of $B\bar{B}$ pairs 38
IV.2	Branching fraction of the four modes under investigation. These numbers are used to combine the simulated samples in the right proportions. 47
IV.3	Number of events by <i>BABAR</i> run period for each simulated sample 48
IV.4	Relative skim efficiencies for the different samples 50
IV.5	Absolute selection rates of the two skims for the different modes, scaled to the luminosity of the data sample 50
IV.6	Summary of the cut variables 55
IV.7	Candidate Multiplicity after the skim 55
IV.8	Candidate Multiplicity after the cuts 56
IV.9	Fraction of truth-matched events that are correctly selected by the best candidate selection 58
IV.10	Absolute number of events that pass the set of cuts for each reconstruction mode 65
IV.11	Number of events that pass the set of cuts for each reconstruction mode, scaled to the integrated luminosity of the data sample 65
IV.12	Pdf parametrization for events containing only a $B^- \rightarrow \Lambda\bar{p}\gamma$ candidate 72
IV.13	Pdf parametrization for events with two candidates 77

Table	Page	
IV.14	Comparison of the spread of the yields from 1000 toy experiments with the error on the yield from the likelihood fit	93
IV.15	Correlation coefficient between the $B^- \rightarrow \Lambda \bar{p} \gamma$ and the $B^- \rightarrow \Sigma^0 \bar{p} \gamma$ reconstruction for each of the fit variables	93
IV.16	Comparison of the spread of the yields from 1000 toy experiments with the error on the yield from the likelihood fit. Candidates are fully correlated.	93
IV.17	Correlation coefficient with each of the four fit variables for the four signal samples and for data for $B^- \rightarrow \Lambda \bar{p} \gamma$ candidates	96
IV.18	Correlation coefficient with each of the four fit variables for the four signal samples and for data for $B^- \rightarrow \Lambda \bar{p} \gamma$ candidates in events that also contain a $B^- \rightarrow \Sigma^0 \bar{p} \gamma$	96
IV.19	Correlation coefficient with each of the four fit variables for the four signal samples and for data for $B^- \rightarrow \Sigma^0 \bar{p} \gamma$ candidates	96
IV.20	Summary of the systematic effect of changing the sample composition for one-candidate events (Figure IV.37)	113
IV.21	Summary of the systematic effect of changing the sample composition for simultaneous fits to two-candidate events (Figure IV.38)	113
IV.22	Systematic error on the yields for the different reconstruction modes . .	116
V.1	Yields, errors and significance in the sample of two-candidate events. Significances marked with * are computed by dividing the yield by the larger of the asymmetric errors.	124

Table	
V.2	Yields, errors and significance in the sample of one-candidate events. Significances marked with * are computed by dividing the yield by the larger of the asymmetric errors. 124
V.3	Yields of the likelihood fit to one-candidate events, where the yields of $B^- \rightarrow \Lambda \bar{p} \pi^0$ and $B^- \rightarrow \Sigma^0 \bar{p} \pi^0$ are fixed at 0 124
V.4	Yields of the likelihood fit to two-candidate events, where the yields of $B^- \rightarrow \Lambda \bar{p} \pi^0$ and $B^- \rightarrow \Sigma^0 \bar{p} \pi^0$ are fixed at 0 125
V.5	Branching fractions and upper limits of the signal modes in data samples accumulated in <i>BABAR</i> runs 1-5 133
V.6	Comparison of this analysis with current results 136
C.1	Correlation of fit variables in one-candidate events 148
C.2	Correlation of fit variables in $B^- \rightarrow \Lambda \bar{p} \gamma$ candidates in two-candidate events 149
C.3	Correlation of fit variables in $B^- \rightarrow \Sigma^0 \bar{p} \gamma$ candidates in two-candidate events 149
C.4	Correlation of the yields in the simultaneous fit 149
C.5	Correlation of the fit variables in the fit to the one-candidate sample . . 149
E.1	Parameterization of the four samples – $m_{\text{rec.}}$, $m_{\text{miss.}}$. Toy studies based on this parameterization show that it doesn't model the data sufficiently. 155
G.1	Cut efficiencies for reconstruction as $B^- \rightarrow \Lambda \bar{p} \gamma$ 166
G.2	Relative cut efficiencies for reconstruction as $B^- \rightarrow \Lambda \bar{p} \gamma$ 167
G.3	Cut efficiencies for reconstruction as $B^- \rightarrow \Sigma^0 \bar{p} \gamma$ 168

Table	Page
G.4	Relative cut efficiencies for reconstruction as $B^- \rightarrow \Sigma^0 \bar{p} \gamma$ 169
H.1	Correlations of the fit variables in correctly reconstructed $B^- \rightarrow \Lambda \bar{p} \gamma$ events. Parametrization of $m_{\text{rec.}}, m_{\text{miss.}}$ 170
H.2	Correlations of the fit variables in $B^- \rightarrow \Sigma^0 \bar{p} \gamma$ events that are incorrectly reconstructed as $B^- \rightarrow \Lambda \bar{p} \gamma$. Parametrization of $m_{\text{rec.}}, m_{\text{miss.}}$ 175
H.3	Correlations of the fit variables in $B^- \rightarrow \Lambda \bar{p} \pi^0$ events that are incorrectly reconstructed as $B^- \rightarrow \Lambda \bar{p} \gamma$. Parametrization of $m_{\text{rec.}}, m_{\text{miss.}}$ 175
H.4	Correlations of the fit variables in $B^- \rightarrow \Sigma^0 \bar{p} \pi^0$ events that are incorrectly reconstructed as $B^- \rightarrow \Lambda \bar{p} \gamma$. Parametrization of $m_{\text{rec.}}, m_{\text{miss.}}$ 175
H.5	Correlations of the fit variables in $B^- \rightarrow \Lambda \bar{p} \gamma$ events that are incorrectly reconstructed as $B^- \rightarrow \Sigma^0 \bar{p} \gamma$. Parametrization of $m_{\text{rec.}}, m_{\text{miss.}}$ 176
H.6	Correlations of the fit variables in correctly reconstructed $B^- \rightarrow \Sigma^0 \bar{p} \gamma$ events. Parametrization of $m_{\text{rec.}}, m_{\text{miss.}}$ 181
H.7	Correlations of the fit variables in $B^- \rightarrow \Lambda \bar{p} \pi^0$ events incorrectly reconstructed as $B^- \rightarrow \Sigma^0 \bar{p} \gamma$. Parametrization of $m_{\text{rec.}}, m_{\text{miss.}}$ 181
H.8	Correlations of the fit variables in $B^- \rightarrow \Sigma^0 \bar{p} \pi^0$ events incorrectly reconstructed as $B^- \rightarrow \Sigma^0 \bar{p} \gamma$. Parametrization of $m_{\text{rec.}}, m_{\text{miss.}}$ 181
I.1	Correlations of the fit variables in correctly reconstructed $B^- \rightarrow \Lambda \bar{p} \gamma$ events. Parametrization of $m_{\text{ES}}, \Delta E$ 182

Table

I.2	Correlations of the fit variables in $B^- \rightarrow \Sigma^0 \bar{p} \gamma$ events incorrectly reconstructed as $B^- \rightarrow \Lambda \bar{p} \gamma$. Parametrization of $m_{\text{ES}}, \Delta E$	183
I.3	Correlations of the fit variables in $B^- \rightarrow \Lambda \bar{p} \pi^0$ events incorrectly reconstructed as $B^- \rightarrow \Lambda \bar{p} \gamma$. Parametrization of $m_{\text{ES}}, \Delta E$	183
I.4	Correlations of the fit variables in $B^- \rightarrow \Sigma^0 \bar{p} \pi^0$ events incorrectly reconstructed as $B^- \rightarrow \Lambda \bar{p} \gamma$. Parametrization of $m_{\text{ES}}, \Delta E$	183
I.5	Correlations of the fit variables in $B^- \rightarrow \Lambda \bar{p} \gamma$ events incorrectly reconstructed as $B^- \rightarrow \Sigma^0 \bar{p} \gamma$. Parametrization of $m_{\text{ES}}, \Delta E$	183
I.6	Correlations of the fit variables in correctly reconstructed $B^- \rightarrow \Sigma^0 \bar{p} \gamma$ events. Parametrization of $m_{\text{ES}}, \Delta E$	184
I.7	Correlations of the fit variables in $B^- \rightarrow \Lambda \bar{p} \pi^0$ events incorrectly reconstructed as $B^- \rightarrow \Sigma^0 \bar{p} \gamma$. Parametrization of $m_{\text{ES}}, \Delta E$	184
I.8	Correlations of the fit variables in $B^- \rightarrow \Sigma^0 \bar{p} \pi^0$ events incorrectly reconstructed as $B^- \rightarrow \Sigma^0 \bar{p} \gamma$. Parametrization of $m_{\text{ES}}, \Delta E$	184
I.9	Parameterization of the four samples using $m_{\text{ES}}, \Delta E$	185

LIST OF FIGURES

Figure	Page
II.1	Fundamental fermion content of the Standard Model 5
II.2	Gauge boson content of the Standard Model 6
II.3	Forces, force carriers and fundamental particle content of the Standard Model 6
II.4	Feynman diagram of the flavor-changing neutral current $b \rightarrow s\gamma$ 12
II.5	$\mathcal{B}(\bar{B} \rightarrow X_s\gamma)$ as a function of the charged Higgs boson mass in the THDM II for $\tan\beta = 2$ (solid lines). The dashed and dotted lines show the SM result and experimental result, respectively. For numerical values, see text (Taken from (1), Fig. 3) 16
III.1	Schematic of the PEP-II storage rings 18
III.2	Technical drawing of the <i>BABAR</i> detector 21
III.3	Side view of the <i>BABAR</i> SVT and support structure 23
III.4	View of the SVT along the beam direction 24
III.5	dE/dx information vs. momentum from the SVT for various particle species 25
III.6	Schematic view of the arrangements of the wires in a layer with the drift isochrones shown 26
III.7	Side view and exploded view of the DIRC 29
III.8	Schematic of a crystal used in the EMC 31
III.9	Cross section of a RPC module 34

Figure	
III.10	Top view of an LST module. The protective sleeve has been partly retracted for a better view. 34
III.11	Dependence of the signal on the operating voltage for an exemplary LST 36
III.12	Comparison of the invariant mass distributions of the two baryons in the decay $B^- \rightarrow \Lambda \bar{p} \gamma$ for particles in vacuum (generator level) and perfectly reconstructed particles in the <i>BABAR</i> detector (detector level) 36
IV.1	Integrated luminosity versus time in <i>BABAR</i> runs 1 through 5 39
IV.2	Invariant mass of the $\Lambda - p$ system in the decay $B^- \rightarrow \Lambda \bar{p} \gamma$ according to the model by Cheng and Yang 40
IV.3	Distribution of the invariant mass of the baryon pair in the analysis of the decay $B^- \rightarrow \Lambda \bar{p} \gamma$ according to perturbative QCD 41
IV.4	Comparison of the distribution of the invariant mass of the baryon pair in the decays $B^- \rightarrow \Lambda \bar{p} \gamma$ and $B^- \rightarrow \Lambda \bar{p} \pi^0$. Two different models are underlying the generation of these decays. 42
IV.5	CMS Momentum distributions of the $B^- \rightarrow \Lambda \bar{p} \gamma$ final states at the generator level 43
IV.6	Comparison of the generator level CMS momentum distributions of the high energy photon in the decays $B^- \rightarrow \Lambda \bar{p} \gamma$ and $B \rightarrow X_s \gamma$ 44
IV.7	Comparison of the distribution of the invariant mass of the baryon pair in the decays $B^- \rightarrow \Lambda \bar{p} \gamma$ and $B^- \rightarrow \Sigma^0 \bar{p} \gamma$ 45

Figure		
IV.8	Comparison of the invariant mass of the two-baryon system in the decay $B^- \rightarrow \Lambda \bar{p} \pi^0$. The two samples were generated with the model by Chua et al.(2) and a generic phase space model, respectively.	45
IV.9	Daughter multiplicity in events with more than one B candidate – Reconstruction as $B^- \rightarrow \Lambda \bar{p} \gamma$	56
IV.10	Daughter multiplicity in events with more than one B candidate – Reconstruction as $B^- \rightarrow \Sigma^0 \bar{p} \gamma$	57
IV.11	Best candidate selection criteria for $B^- \rightarrow \Lambda \bar{p} \gamma$ candidates. The bits in order are the truth matching flags for Lambda, Proton from B, Gamma from B, B candidate	59
IV.12	Best candidate selection criteria for $B^- \rightarrow \Sigma^0 \bar{p} \gamma$ candidates. The bits in order are the truth matching flags for Sigma, Lambda from Sigma, Proton from B, Gamma from B, B candidate	61
IV.13	Generic B component in m_{rec} , scaled to the integrated luminosity of the data sample	67
IV.14	Lab energy of the photon to make the π^0 candidate	68
IV.15	Best π^0 mass for true π^0 candidates and for random combinations of photons	69
IV.16	Parametrization of the reconstructed mass for $B^- \rightarrow \Lambda \bar{p} \gamma$ candidates	73
IV.17	Parametrization of the missing mass for $B^- \rightarrow \Lambda \bar{p} \gamma$ candidates	74
IV.18	Parametrization of the ratio of the Legendre moments for $B^- \rightarrow \Lambda \bar{p} \gamma$ candidates	75
IV.19	Parametrization of the best π^0 mass for $B^- \rightarrow \Lambda \bar{p} \gamma$ candidates	76

Figure

IV.20	Parametrization of the reconstructed mass of different samples reconstructed as $B^- \rightarrow \Lambda \bar{p} \gamma$ in events also containing a $B^- \rightarrow \Sigma^0 \bar{p} \gamma$ candidate.	78
IV.21	Parametrization of the missing mass of different samples reconstructed as $B^- \rightarrow \Lambda \bar{p} \gamma$ in events also containing a $B^- \rightarrow \Sigma^0 \bar{p} \gamma$ candidate.	79
IV.22	Parametrization of the ratio of the Legendre moments L_2/L_0 of different samples reconstructed as $B^- \rightarrow \Lambda \bar{p} \gamma$ in events also containing a $B^- \rightarrow \Sigma^0 \bar{p} \gamma$ candidate.	80
IV.23	Parametrization of the best π^0 mass of different samples reconstructed as $B^- \rightarrow \Lambda \bar{p} \gamma$ in events also containing a $B^- \rightarrow \Sigma^0 \bar{p} \gamma$ candidate.	81
IV.24	Parametrization of the reconstructed mass of different samples reconstructed as $B^- \rightarrow \Sigma^0 \bar{p} \gamma$ in events also containing a $B^- \rightarrow \Lambda \bar{p} \gamma$ candidate.	82
IV.25	Parametrization of the missing mass of different samples reconstructed as $B^- \rightarrow \Sigma^0 \bar{p} \gamma$ in events also containing a $B^- \rightarrow \Lambda \bar{p} \gamma$ candidate.	83
IV.26	Parametrization of the ratio of the Legendre moments L_2/L_0 of different samples reconstructed as $B^- \rightarrow \Sigma^0 \bar{p} \gamma$ in events also containing a $B^- \rightarrow \Lambda \bar{p} \gamma$ candidate.	84
IV.27	Parametrization of the best π^0 mass of different samples reconstructed as $B^- \rightarrow \Sigma^0 \bar{p} \gamma$ in events also containing a $B^- \rightarrow \Lambda \bar{p} \gamma$ candidate.	85

Figure

IV.28	Pure and Embedded Toy Studies – using a mixture of parameterization and 2d hist pdfs. Simultaneous Fit to events containing both candidates	88
IV.29	Pure and Embedded Toy Studies – using a mixture of parameterization and 2d hist pdfs. Validation of the component to model $B^- \rightarrow \Lambda \bar{p} \gamma$	89
IV.30	Pure and Embedded Toy Studies – using a mixture of parameterization and 2d hist pdfs. Validation of the component to model $B^- \rightarrow \Sigma^0 \bar{p} \gamma$	90
IV.31	Pure and Embedded Toy Studies – using a mixture of parameterization and 2d hist pdfs for events containing only a $B^- \rightarrow \Lambda \bar{p} \gamma$	91
IV.32	Validation plots of the sPlots method used to extract the branching fraction in bins of the di-baryon invariant mass. Events containing a single $B^- \rightarrow \Lambda \bar{p} \gamma$ candidate	98
IV.33	Validation plots of the sPlots method used to extract the branching fraction in bins of the $\Sigma^0 - p$ invariant mass for Events containing both a $B^- \rightarrow \Lambda \bar{p} \gamma$ candidate and a $B^- \rightarrow \Sigma^0 \bar{p} \gamma$ candidate	101
IV.34	Validation plots of the sPlots method used to extract the branching fraction in bins of the $\Lambda - p$ invariant mass for Events containing both a $B^- \rightarrow \Lambda \bar{p} \gamma$ candidate and a $B^- \rightarrow \Sigma^0 \bar{p} \gamma$ candidate	104
IV.35	Cut efficiency for $B^- \rightarrow \Lambda \bar{p} \gamma$ and $B^- \rightarrow \Sigma^0 \bar{p} \gamma$ signal in bins of the di-baryon invariant mass	107

Figure

IV.36	Cut efficiency for $B^- \rightarrow \Lambda \bar{p} \gamma$ and $B^- \rightarrow \Sigma^0 \bar{p} \gamma$ signal in bins of the di-baryon invariant mass. The cut on the photon energy has been removed	108
IV.37	Effect on the fit when changing the composition of the sample of one-candidate events.	111
IV.38	Effect on the fit when changing the composition of the sample of two-candidate events.	114
V.1	Likelihood fit to the kinematic fit variables <i>reconstructed candidate mass</i> and <i>missing mass</i> in events containing only one candidate	118
V.2	Likelihood fit to the kinematic fit variables <i>ratio of the Legendre Moments</i> L_2/L_0 and <i>best</i> m_{π^0} in events containing only one candidate	119
V.3	Likelihood fit to the kinematic fit variables <i>reconstructed candidate mass</i> and <i>missing mass</i> for $B^- \rightarrow \Lambda \bar{p} \gamma$ candidates in events containing two candidates	120
V.4	Likelihood fit to the kinematic fit variables <i>ratio of the Legendre Moments</i> L_2/L_0 and <i>best</i> m_{π^0} for $B^- \rightarrow \Lambda \bar{p} \gamma$ candidates in events containing two candidates	121
V.5	Likelihood fit to the kinematic fit variables <i>reconstructed candidate mass</i> and <i>missing mass</i> for $B^- \rightarrow \Sigma^0 \bar{p} \gamma$ candidates in two-candidate events	122
V.6	Likelihood fit to the kinematic fit variables <i>ratio of the Legendre Moments</i> L_2/L_0 and <i>best</i> m_{π^0} for $B^- \rightarrow \Sigma^0 \bar{p} \gamma$ candidates in two-candidate events	123

Figure

V.7	Yield bins of the invariant mass of the baryon pair in the one-candidate sample	126
V.8	Yield bins of the invariant mass of the baryon pair in the two-candidate sample	128
V.9	Sum of the yields of the channels $B^- \rightarrow \Lambda \bar{p} \pi^0$ and $B^- \rightarrow \Sigma^0 \bar{p} \pi^0$ in the one- and two-candidate samples combined	130
V.10	Reconstruction efficiencies of the four signal channels. The efficiency is computed on simulated events as the ratio of events in the fit region to the total number of available events for each sample	132
V.11	Efficiency-corrected sPlots of the invariant mass of the baryon pair. The result of the fits to both data sets are combined	134
A.1	Likelihood fit to the kinematic fit variables <i>reconstructed candidate mass</i> and <i>missing mass</i> in events containing only one candidate	140
A.2	Likelihood fit to the kinematic fit variables <i>ratio of the Legendre Moments</i> L_2/L_0 and <i>best</i> m_{π^0} in events containing only one candidate	141
A.3	Likelihood fit to the kinematic fit variables <i>reconstructed candidate mass</i> and <i>missing mass</i> for $B^- \rightarrow \Lambda \bar{p} \gamma$ candidates in events containing two candidates	142
A.4	Likelihood fit to the kinematic fit variables <i>ratio of the Legendre Moments</i> L_2/L_0 and <i>best</i> m_{π^0} for $B^- \rightarrow \Lambda \bar{p} \gamma$ candidates in events containing two candidates	143
A.5	Likelihood fit to the kinematic fit variables <i>reconstructed candidate mass</i> and <i>missing mass</i> for $B^- \rightarrow \Sigma^0 \bar{p} \gamma$ candidates in two-candidate events	144

Figure

A.6	Likelihood fit to the kinematic fit variables <i>ratio of the Legendre Moments</i> L_2/L_0 and <i>best</i> m_{π^0} for $B^- \rightarrow \Sigma^0 \bar{p} \gamma$ candidates in two-candidate events	145
B.1	sPlots of the photon energy in $B^- \rightarrow \Lambda \bar{p} \gamma$ and $B^- \rightarrow \Sigma^0 \bar{p} \gamma$ events	147
D.1	Fit shape for the best π^0 mass of one-candidate $B^- \rightarrow \Lambda \bar{p} \gamma$ events	151
D.2	Fit shape for the best π^0 mass of $B^- \rightarrow \Lambda \bar{p} \gamma$ candidates in events that also contain a $B^- \rightarrow \Sigma^0 \bar{p} \gamma$ candidates	152
D.3	Fit shape for the best π^0 mass of $B^- \rightarrow \Sigma^0 \bar{p} \gamma$ candidates in events that also contain a $B^- \rightarrow \Lambda \bar{p} \gamma$ candidates	153
E.1	Parametrization of $m_{\text{rec.}}$ in $B^- \rightarrow \Lambda \bar{p} \gamma$ events with a “Crystal Ball” shape	154
E.2	Parametrization of misreconstructed $B^- \rightarrow \Sigma^0 \bar{p} \gamma$ events with a Cruijff function	155
E.3	Datasets and fit shapes of different samples reconstructed as $B^- \rightarrow \Lambda \bar{p} \gamma$. With this choice of fit shapes, the embedded toys show a poor performance of the fit.	156
E.4	Pull distributions of toy studies – pure and embedded for the pure parameterization	157
F.1	Distribution of the cut variables before the cuts – reconstruction as $B^- \rightarrow \Lambda \bar{p} \gamma$	159
F.2	Distribution of the cut variables before the cuts – reconstruction as $B^- \rightarrow \Sigma^0 \bar{p} \gamma$	160

Figure

F.3	Distribution of the cut variables before the cuts - log scale - reconstruction as $B^- \rightarrow \Lambda \bar{p} \gamma$	161
F.4	Distribution of the cut variables before the cuts - log scale - reconstruction as $B^- \rightarrow \Sigma^0 \bar{p} \gamma$	162
F.5	Optimization of signal significance for the different cuts - reconstruction as $B^- \rightarrow \Lambda \bar{p} \gamma$	163
F.6	Optimization of signal significance for the different cuts - reconstruction as $B^- \rightarrow \Sigma^0 \bar{p} \gamma$	164
H.1	Scatter plots of the four fit variables in $\Lambda \bar{p} \gamma$ MC	171
H.2	Scatter plots of the four fit variables in $\Sigma^0 \bar{p} \gamma$ MC	172
H.3	Scatter plots of the four fit variables in $\Lambda \bar{p} \pi^0$ MC	173
H.4	Scatter plots of the four fit variables in $\Sigma^0 \bar{p} \pi^0$ MC	174
H.5	Scatter plots of the four fit variables in $\Lambda \bar{p} \gamma$ MC	177
H.6	Scatter plots of the four fit variables in $\Sigma^0 \bar{p} \gamma$ MC	178
H.7	Scatter plots of the four fit variables in $\Lambda \bar{p} \pi^0$ MC	179
H.8	Scatter plots of the four fit variables in $\Sigma^0 \bar{p} \pi^0$ MC	180
I.1	Parameterization with m_{ES} and ΔE	186
I.2	Pure Toys of events reconstructed as $B^- \rightarrow \Lambda \bar{p} \gamma$	187
I.3	Embedded Toys of events reconstructed as $B^- \rightarrow \Sigma^0 \bar{p} \gamma$	187
J.1	Validation of the sPlots method for events with one candidate. The sample is fit in bins of the invariant mass	189
J.2	Validation of the sPlots method for events with two candidates. The sample is fit in bins of the invariant mass	190

CHAPTER I

INTRODUCTION

The classification of physics as a science can be related back to ancient Greek philosophers, who “studied” nature by means of contemplation. With the advancement of technology more objective means of scientific investigation became available, but they initially did not play a major role in developing theories of nature. It was not until Galileo Galilei that the role of physical experiments shifted from entertainment to the essential ingredient of scientific models that it is today. Today’s Standard Model of Particle Physics has been – and still is – subject to extensive testing on many fronts. This framework exhibits a fundamental symmetry, called CPT invariance. It means that physical laws in this theory remain invariant under simultaneous exchange of particles by their antiparticles (by conjugating their charge with the operator C and changing parity with the operator P) and time reversal (done by the T operator). Experimenters have found that the weak interaction – unlike the strong and the electromagnetic interactions – is not, however, symmetric under each of the C and P operations individually. Symmetry under the exchange of particles by their antiparticles, i.e. CP, or alternatively T symmetry, is conserved to a much larger extent, but is not perfect, either.

The list of tests that the Standard Model has passed is certainly impressive, but we also know of several shortcomings of the framework in key areas. The observed degree of the violation of CP symmetry is too low to explain our very existence. Gravity, probably the force that has been subject to human experimentation longer than any other force, still takes a special role in our theories and is not even part of the Standard Model. Furthermore, recent cosmological experiments have revealed

that our framework encompasses only about 4 % of the energy content of the *known* universe.

The level of precision of theoretical prediction is equal to that of experimental verification in many areas, and the values of many parameters computed by theorists agree with the experiment within errors. Although the precision of the parameters of the model is getting better and better, the “big questions” mentioned in the previous paragraph continue to evade our grasp. It is at this point obvious that the Standard Model in its current form is not able to accommodate the answers to these problems. Breakthroughs are expected from the next generation of colliders as particle physicists reach beyond their field and start bringing experiments of cosmological dimensions into the well-controlled environment of the laboratory. Answering these questions is going to require overcoming academic, economic as well as social challenges of a new magnitude.

On the theoretical side we reach out to new theories to accommodate the answers to our questions. Many of these new theories invoke new particles with properties that allow them to have evaded detection so far – such as not to disturb the excellent agreement between theory and experiment on many fronts – yet with interactions with the current theory that are large enough to explain at least some of the known discrepancies.

Direct searches for these new particles have so far remained unsuccessful, but we can also perform searches that are indirectly sensitive to contributions from outside the Standard Model. One class of these decays are *flavor-changing neutral currents*, of which the decays $b \rightarrow s\gamma$ are an example. The rate at which they occur could be altered by physics outside the Standard Model. This dissertation describes the observation of a new class of $b \rightarrow s\gamma$ decays, namely those containing baryons, that

have been underestimated by two orders of magnitude before(3). In addition to a measurement of their rate, which in itself is sensitive to contributions outside the Standard Model, an analysis of the differential branching fraction can give insights in the dynamics of this class of decays. Because their rate has been largely underestimated, other analyses in the $b \rightarrow s\gamma$ channel have so far ignored baryonic final states. This analysis therefore also affects studies that sum a large number of exclusive measurements in an attempt to reconstruct the inclusive branching fraction, which can be computed more precisely than that of exclusive decays.

In Chapter II, we describe in more detail the theoretical and experimental background against which this analysis is carried out. Throughout this dissertation we will imply that CP symmetry is conserved unless otherwise stated. Chapter III serves as an overview of the experimental apparatus, the *BABAR* detector and the PEP-II storage rings at the Stanford Linear Accelerator Center in Menlo Park, California. Details of the analysis of the decays $B^- \rightarrow \Lambda \bar{p} \gamma$, $B^- \rightarrow \Sigma^0 \bar{p} \gamma$, $B^- \rightarrow \Lambda \bar{p} \pi^0$ and $B^- \rightarrow \Sigma^0 \bar{p} \pi^0$ are presented in Chapter IV, while Chapter V discusses the results of the analysis and gives an outlook on future measurements.

CHAPTER II

THEORETICAL AND EXPERIMENTAL BACKGROUND

In this chapter we will give a brief introduction to the *Standard Model* (SM) of particle physics, as far as it is relevant for our purpose, and as such we will introduce it from an experimental viewpoint, starting with the particle content. We will then see how the particle content is embedded in the theoretical framework, leading to observables and predictions that make the theory falsifiable – the most important feature of a scientific theory. The last part of the chapter is dedicated to an area in which the model is particularly sensitive to tests, and we will show why and how we intend to test it.

II.1 Particle Content

Like every successful theoretical framework, the *Standard Model* has passed rigorous tests by experiments. As of this writing, all visible matter is composed of weakly interacting leptons and strongly interacting hadrons. The leptons are fundamental particles, and we have observed the electron, the muon and the tauon, each with their accompanying flavor of neutrino. The hadrons themselves are composed of quarks, fundamental particles that are not observed freely but only in combinations that form singlets of the strong charge, or *color singlets*. We have observed three generations of quarks to complement the three generations of leptons, and the list of these fundamental fermions is shown in Figure II.1. The two combinations of quarks that have been observed are a combination of a quark and an anti-quark of the same charge with opposite signs - called *mesons*, and a combination of three quarks

FERMIONS			matter constituents spin = 1/2, 3/2, 5/2, ...		
Leptons spin = 1/2			Quarks spin = 1/2		
Flavor	Mass GeV/c ²	Electric charge	Flavor	Approx. Mass GeV/c ²	Electric charge
ν_L lightest neutrino*	$(0-0.13)\times 10^{-9}$	0	u up	0.002	2/3
e electron	0.000511	-1	d down	0.005	-1/3
ν_M middle neutrino*	$(0.009-0.13)\times 10^{-9}$	0	c charm	1.3	2/3
μ muon	0.106	-1	s strange	0.1	-1/3
ν_H heaviest neutrino*	$(0.04-0.14)\times 10^{-9}$	0	t top	173	2/3
τ tau	1.777	-1	b bottom	4.2	-1/3

Fig. II.1: Fundamental fermion content of the Standard Model

with each of the three possible values of the strong charge - called *baryons*. Other, *exotic* states could exist, but no convincing evidence of these has been found so far. Leptons and quarks interact in various ways mediated by the force-carrying bosons in Figure II.2, each of which couples to a different quantum number, or charge. Photons mediate the electromagnetic force that acts on all electrically charged particles, Z and W bosons mediate the weak force and gluons are the carriers of the strong force that acts only on hadrons. Each of these particles has been found experimentally. As presented in the two figures, however, the SM is incomplete: The theoretical framework that incorporates the particles and forces predicts that all of the gauge bosons in Figure II.2 are massless - contrary to observation. A mechanism to correct this feature is known - the Higgs Mechanism - but it introduces an additional scalar field into the theory and predicts a yet unseen particle - the Higgs particle. Figure II.3 shows a summary of the fundamental fermions - quarks and leptons, the four gauge bosons and the Higgs boson.

Unified Electroweak spin = 1			Strong (color) spin = 1		
Name	Mass GeV/c ²	Electric charge	Name	Mass GeV/c ²	Electric charge
γ photon	0	0	g gluon	0	0
W^-	80.39	-1			
W^+ W bosons	80.39	+1			
Z^0 Z boson	91.188	0			

Fig. II.2: Gauge boson content of the Standard Model

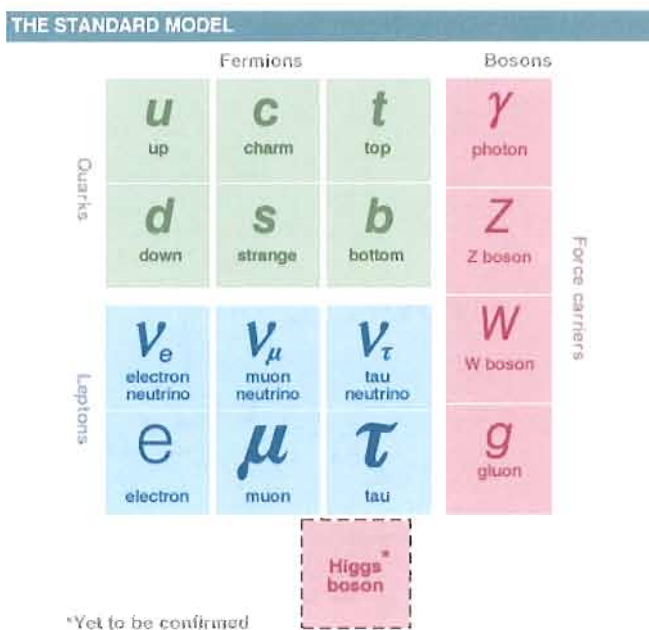


Fig. II.3: Forces, force carriers and fundamental particle content of the Standard Model

II.2 Electroweak Theory

II.2.1 The Masses of Gauge Bosons

We will now proceed to describe the theoretical framework that incorporates these particles (except for the gluon on the right side of Figure II.2). The model was developed by Glashow, Weinberg and Salam(4; 5; 6), and is hereafter referred to as the GWS theory. From the already observed particle content of the SM we know that we have to find a theory with one massless and three massive vector bosons. The GWS theory is a $SU(2) \times U(1)$ theory that is spontaneously broken by a scalar field ϕ that is represented by a doublet of the $SU(2)$ group. The covariant derivative of the scalar field in this theory is

$$\mathcal{D}\phi = \left(\partial_\mu - ig \underbrace{A_\mu^a}_{SU(2)} \tau^a - i\frac{1}{2}g' \underbrace{B_\mu}_{U(1)} \right) \phi \quad (\text{II.1})$$

The mass term of the gauge bosons comes from eq. II.1 squared, evaluated at the expectation value of the scalar field. The relevant term in the Lagrangian is

$$\Delta\mathcal{L} = \frac{1}{2} \frac{v^2}{4} \left(g^2 [(A_\mu^1)^2 + (A_\mu^2)^2] + [-gA_\mu^3 + g'B_\mu]^2 \right)$$

This expression now contains three massive and one massless vector bosons, as desired. Simplifying the expression by introducing the *weak mixing angle* θ_w , the rotation angle from the basis of the gauge fields (A^3, B) to the massive bosons (Z^0, A) , the terms for the bosons and their masses are

$$\begin{aligned}
W_\mu^\pm &= \frac{1}{\sqrt{2}}(A_\mu^1 \mp iA_\mu^2) && \text{with mass} && m_W = g\frac{v}{2} \\
Z_\mu^0 &= \cos\theta_w A_\mu^3 - \sin\theta_w B_\mu && \text{with mass} && m_Z = \frac{m_W}{\cos\theta_w} \\
A_\mu &= \sin\theta_w A_\mu^3 + \cos\theta_w B_\mu && \text{with mass} && m_A = 0
\end{aligned}$$

We identify the massless boson A_μ with the photon and note further that the coupling constant to the electromagnetic field $e = g \sin\theta_w$ with quantum number $Q = T^3 + Y$, and can now write the covariant derivative in terms of the gauge bosons and their couplings

$$\mathcal{D}_\mu = \partial_\mu - i\frac{g}{\sqrt{2}}(W_\mu^+ T^+ + W_\mu^- T^-) - i\frac{g}{\cos\theta_w} Z_\mu (T^3 - \sin^2\theta_w Q) - ieA_\mu Q \quad (\text{II.2})$$

For a more detailed treatment we refer to the excellent textbook by Peskin and Schroeder(7).

II.2.2 Fermion Couplings and the CKM Matrix

We now have to account for the fact that the W bosons only couple to particles of left-handed helicity. This can be achieved by assigning different representations to left-handed and right-handed fermions, making left-handed fermions doublets of the $SU(2)$ group, while right-handed fermions become singlets. This means that the fermions can be classified in three *generations*.

$$\begin{array}{ccc}
\begin{pmatrix} e \\ \nu_e \end{pmatrix}_L & \begin{pmatrix} \mu \\ \nu_\mu \end{pmatrix}_L & \begin{pmatrix} \tau \\ \nu_\tau \end{pmatrix}_L & \text{and} & \begin{pmatrix} u \\ d \end{pmatrix}_L & \begin{pmatrix} c \\ s \end{pmatrix}_L & \begin{pmatrix} t \\ b \end{pmatrix}_L \\
e_R & \mu_R & \tau_R & \text{and} & u_R & d_R & c_R & s_R & t_R & b_R
\end{array}$$

Ignoring the mass terms for the fermions, and omitting the interactions of the leptons, the relevant Lagrangian for the kinetic energy term for weak interactions of quarks is

$$\mathcal{L} = \bar{Q}_L^k(i\mathcal{D})Q_L^k + \bar{u}_R^k(i\mathcal{D})u_R^k + \bar{d}_R^k(i\mathcal{D})d_R^k$$

where Q_L^k is a left-handed quark doublet of generation k , and u_R^k and d_R^k are the right-handed singlets of the same generation. With the covariant derivative written in terms of the physical bosons, this becomes

$$\mathcal{L} = \bar{Q}_L^k(i\cancel{\partial})Q_L^k + \bar{u}_R^k(i\cancel{\partial})u_R^k + \bar{d}_R^k(i\cancel{\partial})d_R^k + g(W_\mu^+\mathfrak{J}_{W^+}^\mu + W_\mu^-\mathfrak{J}_{W^-}^\mu + Z_\mu^0\mathfrak{J}_{Z^0}^\mu) + eA_\mu\mathfrak{J}_{\text{EM}}^\mu$$

The electroweak currents can be written down looking at equation II.2.

$$\begin{aligned}\mathfrak{J}_{W^+}^\mu &= \frac{1}{\sqrt{2}}\bar{u}_L^k\gamma^\mu d_L^k \\ \mathfrak{J}_{W^-}^\mu &= \frac{1}{\sqrt{2}}\bar{d}_L^k\gamma^\mu u_L^k \\ \mathfrak{J}_Z^\mu &= \frac{1}{\cos\theta_w} \left[\bar{u}_L^k\gamma^\mu \left(\frac{1}{2} - \frac{2}{3}\sin^2\theta_w\right)u_L^k + \bar{u}_R^k\gamma^\mu \left(-\frac{2}{3}\sin^2\theta_w\right)u_R^k \right. \\ &\quad \left. + \bar{d}_L^k\gamma^\mu \left(-\frac{1}{2} + \frac{1}{3}\sin^2\theta_w\right)d_L^k + \bar{d}_R^k\gamma^\mu \left(-\frac{1}{3}\sin^2\theta_w\right)d_R^k \right]\end{aligned}\quad (\text{II.3})$$

$$\mathfrak{J}_{\text{EM}}^\mu = \bar{u}^k\gamma^\mu\frac{2}{3}u^k - \bar{d}^k\gamma^\mu\frac{1}{3}d^k \quad (\text{II.4})$$

But in this expression the quarks are massless. They acquire mass by coupling to the Higgs field. In the most general case, these couplings contain off-diagonal terms that mix the generations, i.e. there are terms that couple two different generations to the Higgs field. In physical experiments, we identify particles by their mass. We therefore choose to diagonalize the Higgs couplings in a unitary transformation, but this means changing the basis of the quark fields. In other words, by diagonalizing

the Higgs couplings, we have now mixed different generations of the “raw” theory to create what we call “a quark” in an experiment.

We can now write down the quark fields for up- and down-type quarks in terms of the physical quark fields, i.e. the fields that have diagonal couplings to the Higgs field. This diagonalization is a unitary transformation.

$$u_L^i = U_u^{ij} u_L^{\prime j} \quad d_L^i = U_d^{ij} d_L^{\prime j}$$

In these new fields the W boson current is written

$$\mathfrak{J}_{W^+}^\mu = \frac{1}{\sqrt{2}} \bar{u}^i \gamma^\mu (U_u^\dagger U_d)^{ij} d_L^{\prime j}$$

The matrix $V = U_u^\dagger U_d$ that incorporates mixing of the generations in the off-diagonal elements is called CKM matrix after Cabbibo(8), and Kobayashi and Maskawa(9). On the other hand, the neutral currents \mathfrak{J}_Z^μ and \mathfrak{J}_{EM}^μ contain terms of the form

$$\bar{u}^i \gamma^\mu (U_u^\dagger U_u)^{ij} u_L^{\prime j} \quad \text{and} \quad \bar{d}^i \gamma^\mu (U_d^\dagger U_d)^{ij} d_L^{\prime j},$$

but because the matrices U_u and U_d are unitary, the expressions for these two currents are the same in the quark fields and in the physical fields (eq. II.3 and eq. II.4). This means that while charged currents can change the flavor of quarks via couplings whose strength is given by the CKM matrix, for neutral currents the couplings of vertices involving off-diagonal elements in U_u or U_d vanish because of the unitarity of these matrices. This feature is usually referred to as the *absence of flavor-changing neutral currents (FCNC) at tree level* in the Standard Model.

II.3 $b \rightarrow s\gamma$

The absence of flavor-changing neutral currents at tree level in the SM opens the door to precision measurements: One way to mediate this type of decay in the SM is via a loop diagram, which reduces the branching fraction to about 10^{-5} . The exact value is sensitive to coupling constants and the propagators of the particles in the loop, so that a precise comparison between computation of the branching fraction of these decays within the framework of the Standard Model and measurement could reveal contributions from new sources.

An example of such a decay that proceeds via a FCNC is the decay $b \rightarrow s\gamma$, shown in Figure II.4. The decay cannot be observed as shown at the quark level, but rather in combination with a so-called *spectator quark* as the decay of neutral or charged B mesons. This fact complicates greatly the computation of the branching fraction and makes these *exclusive decays* less sensitive candidates in the search for contributions from outside the SM compared to the *inclusive decay*. In order to reconstruct the inclusive decay, experimentalists take one of two approaches: One way is to only use the fact that the energy transfer in the quark-level decay is large and reconstruct the decay mainly based on the properties of the photon, the other way is to reconstruct as many exclusive decays that contain the $b \rightarrow s\gamma$ diagram as possible and extrapolate the inclusive branching fraction from the sum of the measured decays. While the first approach is experimentally more challenging, the latter approach suffers from ignorance of the missing modes, i.e. the decays that are not reconstructed. In order to be able to confidently infer the total from the sum of measured modes it is therefore essential to increase the number of measured decays.

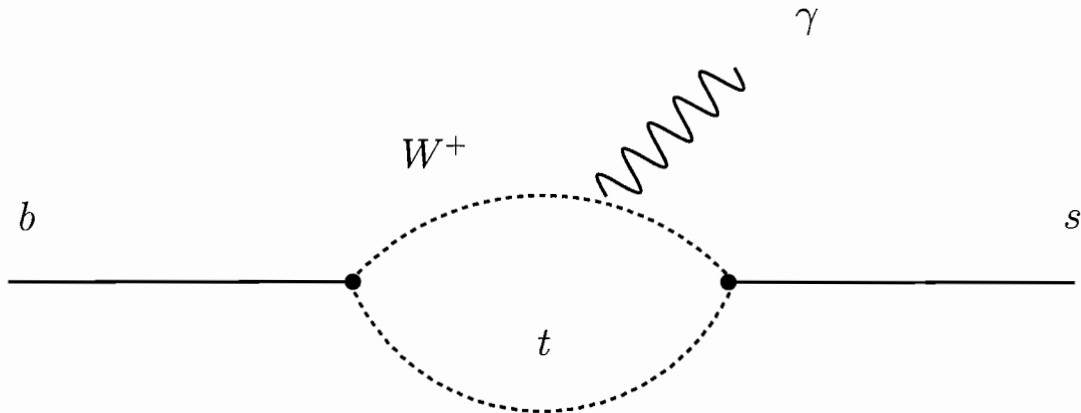


Fig. II.4: Feynman diagram of the flavor-changing neutral current $b \rightarrow s \gamma$

II.3.1 Baryonic Final States

The claim of the first observation of the transition $b \rightarrow u$ was made by the ARGUS collaboration in 1987 in the channels $B^- \rightarrow p\bar{p}\pi^-$ and $\bar{B}^0 \rightarrow p\bar{p}\pi^+\pi^-$ (10). This spurred interest in the decay, but the search by the CLEO collaboration found no signal(11), and it was ruled out at the observed rate in the Standard Model by a computation based on QCD counting rules(12). An updated measurement on a larger data sample by the ARGUS collaboration(13) later yielded no significant signal and the presented measurement was consistent with the CLEO measurement and with the Standard Model prediction.

Decays to final states with higher multiplicity were henceforth largely dismissed as being of low interest, because the additional vertices involved would lead to rates that are reduced compared to the two-body final states that still had not been found.

However, discoveries of three-body baryonic decays by the B factories *BABAR* and *Belle* starting with the observation of the decay $B^\pm \rightarrow p\bar{p}K^\pm$ (14) re-ignited interest in these modes. Two features of this observation are significant:

- Contrary to the decays of $b \rightarrow s$ to mesons, where the two-body final states contribute with a larger branching fraction than their three-body counterparts, in B decays to baryons the branching fraction seems to be generally enhanced for decays with a higher multiplicity in the final state. While the search for the decays $B^0 \rightarrow p\bar{p}, \Lambda\bar{\Lambda}$ and $B^+ \rightarrow p\bar{\Lambda}$ (15) has not yielded any results to this point, a few of their three-body counterparts have been observed(16; 17).
- The distribution of the invariant mass of the baryon pair peaks at threshold. This appears to be a feature common to B decays to baryons and explanations range from additional states near threshold to low-mass enhancements favored by the fragmentation process(18).

An explanation for the peaking behavior of the invariant mass of the baryon pair was conjectured for the first time by Hou and Soni(19), where the authors argue that the smaller momentum transfer of the three-body modes would be an explanation for the enhancement in branching fraction. Their arguments are based on earlier treatments of baryonic decays using a pole model(20; 21) that themselves were inspired by the ARGUS announcement of the observation in 1987, and the treatment has been expanded to cover several decays to a baryon pair and a meson(22).

The pole model argument appears to hold true as well for the decay $b \rightarrow s\gamma$ to baryonic final states. Naïvely, one would assume a suppression of order α_{em} relative to the two-body modes, however, since the observation of the decay $B^- \rightarrow \Lambda\bar{p}\gamma$ the pole model treatment as well as the computation based on QCD counting rules have been refined to be consistent both with the measured branching fraction of the decay and with the shape of the distribution of the invariant mass of the baryon pair(23; 3).

A Note on the Computation of the Decay Rates

The main contribution to the rate of decays of the type $B^- \rightarrow \Lambda \bar{p} \gamma$ comes from the amplitude $\langle \Lambda \bar{p} | H | B^- \rangle$, where $H = -\frac{G_F}{\sqrt{2}} V_{tb} V_{ts}^* c_7^{\text{eff}} O_7$ with the tensor operator $O_7 = \frac{e}{8\pi^2} m_b \bar{s} \sigma_{\mu\nu} F^{\mu\nu} (1 + \gamma_5) b$. The matrix element is very difficult to compute, because it contains an unknown 3-body matrix element. Two approaches have proven useful in solving this problem: The pole model with the assumption that the main contribution to the amplitude stems from low-lying baryon and meson intermediate states, and an approach based on QCD counting rules, which instead parametrizes the amplitude in terms of three unknown form factors(24).

While the two models are in agreement with current measurements, they differ significantly in the prediction of the rates of to date unobserved channels and feature different asymptotic behaviors of the distribution of the invariant mass of the baryon pair. The form factors are functions of $t = (p_A + p_p)^2$, which is just the invariant mass of the baryon pair squared. This means that the asymptotic behavior of the form factors ultimately determines the computed shape of the differential branching fraction. The QCD counting rules lead to a sharper peak due to a $1/t^3$ asymptotic behavior, while the pole model shows a $1/t^2$ behavior. A sufficiently precise measurement of the distribution of the invariant mass could therefore help distinguish between the models.

II.3.2 Two Higgs Doublet Models

As mentioned earlier, contributions from particles outside the SM could result in branching fractions that significantly deviate from SM predictions. A large class of these theories, such as MSSM theories, contain two Higgs doublets rather than one doublet like the SM.

Two complex Higgs doublets give rise to five Higgs bosons rather than one in the SM, the particles are called h, H, A, H^\pm . Only the A is a pseudoscalar, the others are scalar bosons. The neutral h boson is SM-like and has a heavy neutral partner in the H . Because the charged Higgs bosons H^+ and H^- couple to the same particles as the W^\pm bosons, albeit in different strength, they could take the place of the W^\pm in the diagram and contribute to the decay, altering the branching fraction from the SM prediction. Figure II.5 shows a comparison between current experimental value of $\mathcal{B}(\bar{B} \rightarrow X_s \gamma) = (3.55 \pm 0.24_{-0.10}^{+0.09} \pm 0.03) \times 10^{-4}$ and SM prediction of $\mathcal{B}(\bar{B} \rightarrow X_s \gamma) = (3.15 \pm 0.23) \times 10^{-4}$ for the decay $\bar{B} \rightarrow X_s \gamma$ and how the branching ratio of the decay depends on the mass of the charged Higgs boson. The primary decays of interest for this analysis are the decays $B^- \rightarrow \Lambda \bar{p} \gamma$ and $B^- \rightarrow \Sigma^0 \bar{p} \gamma$ because these channels can be fully reconstructed, allowing for a clean measurement. As a final state of $b \rightarrow s \gamma$ they are sensitive to contributions from outside the SM, while at the same time playing an important role for the measurement of the inclusive branching fraction. Because of the small predicted value of the branching fraction of the $b \rightarrow s \gamma$ transition to baryonic final states, they are usually ignored when scaling the combined branching fraction of the measured modes to obtain the inclusive value. The modes with pions substituted for the high-energy photons, $B^- \rightarrow \Lambda \bar{p} \pi^0$ and $B^- \rightarrow \Sigma^0 \bar{p} \pi^0$, have to be considered, because of the proximity in their kinematic properties. Additionally to the importance of a measurement of the branching fraction itself, a comparison of the branching fraction of these decays with their counterparts containing a charged pion instead of a neutral pion can serve as a validation of the factorization assumption that is used in the computation of the decay rate.

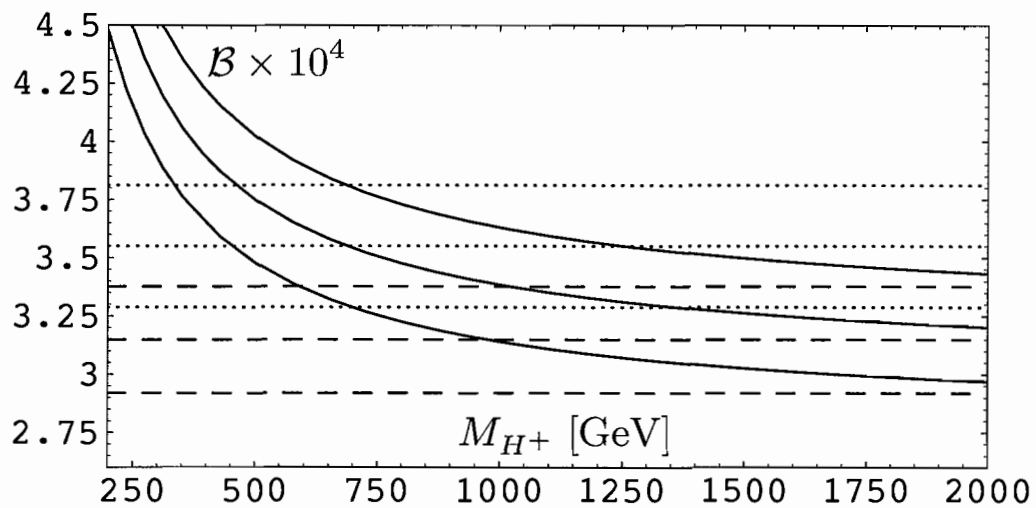


Fig. II.5: $\mathcal{B}(\bar{B} \rightarrow X_s \gamma)$ as a function of the charged Higgs boson mass in the THDM II for $\tan \beta = 2$ (solid lines). The dashed and dotted lines show the SM result and experimental result, respectively. For numerical values, see text (Taken from (1), Fig. 3)

CHAPTER III

THE *BABAR* EXPERIMENT

This chapter gives an overview over the instrumentation of the *BABAR* experiment, namely the accelerator and the detector(25). Conventionally, the coordinate system in this chapter is right-handed cylindrical such that the positive z axis is defined by the direction of the electron beam, the polar angle ϕ stretching from 0° to 360° , such that a vector with $\phi = 90^\circ$ points straight up. In some cases it is preferable to describe a problem in terms of an additional angle θ , which then extends from 0° to 180° .

III.1 PEP-II

The facilities that are used to produce the large number of B mesons that are necessary for the success of the *BABAR* experiment are the Positron Electron Project II (PEP-II) storage rings at SLAC. Electrons and positrons are accelerated in the linear accelerator and fed into the PEP-II storage rings (Figure III.1).

Operating at the $\Upsilon(4S)$ resonance, PEP-II has achieved a peak luminosity of $12 \times 10^{33} \text{cm}^{-2}\text{s}^{-1}$ which by far exceeds its design luminosity of $3 \times 10^{33} \text{cm}^{-2}\text{s}^{-1}$ (26). Taking advantage of the fact that $\Upsilon(4S)$ decays to B meson pairs with a branching ratio of $> 96\%$, the number of B mesons can be estimated from the relation for the number of $\Upsilon(4S)$ mesons $N = \sigma\mathcal{L}$, with the cross section for the production of $\bar{b}b$ $\sigma = 1.05 \text{ nb}$, $\mathcal{L} = f \frac{n_1 n_2}{4\pi\sigma_x\sigma_y}$. n_1 and n_2 are the number of positrons in the Low Energy Ring (LER) with an energy of $3.1 \pm 0.0023\text{GeV}$ and electrons in the High Energy Ring (HER) with an energy of $9.0 \pm 0.0055\text{GeV}$, respectively. During its time of operation at the $\Upsilon(4S)$ resonance PEP-II has recorded almost 500 / fb. In addition

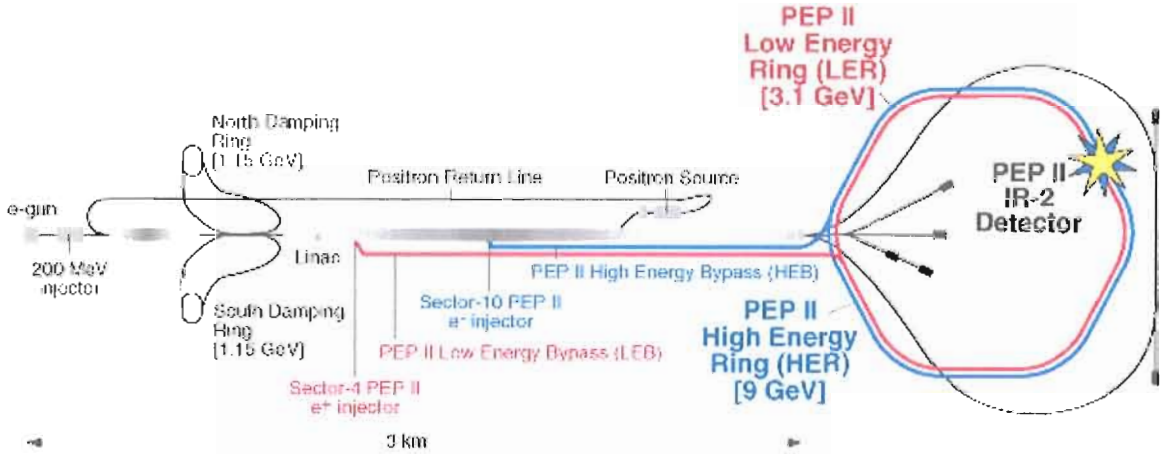


Fig. III.1: Schematic of the PEP-II storage rings

to B pairs, this data sample consists of a number of other particles, the cross sections for which are listed in Table III.1 (taken from(27)) The asymmetry in the two beam energies results in a boost of the $B\bar{B}$ system of $\beta\gamma = 0.56$, which allows the B decay vertex to be reconstructed in the *BABAR* detector, an essential requirement to measure time-dependent CP violation. The value of the center-of-momentum (cm) energy of the collisions is calculated from machine parameters (total magnetic bending strength and the average deviations of the accelerating frequencies from their central values), while monitoring the branching ratio in an enriched sample of $B\bar{B}$ events to lepton

$e^+e^- \rightarrow$	cross section (nb)
$b\bar{b}$	1.05
$c\bar{c}$	1.30
$s\bar{s}$	0.35
$u\bar{u}$	1.39
$d\bar{d}$	0.35
$\tau^+\tau^-$	0.94
$\mu^+\mu^-$	1.16
e^+e^-	≈ 40

Tab. III.1: Cross sections for various processes at 10.58 GeV collision energy

pairs online ensures that data is recorded close to the peak of the $\mathcal{T}(4S)$ resonance. A deviation from the resonance of 2 MeV in either direction results in a 2.5 % drop in the $B\bar{B}$ production rate. Additionally, the cm energy is computed from fully reconstructed B decays offline; a sample of 1 / fb can be used to determine the value to within 1.1 MeV.

III.1.1 Backgrounds

During normal operation, the the following are the main sources of backgrounds, in increasing order of importance: synchrotron radiation in the vicinity of the interaction region, interactions between the beam particles and the residual gas in the rings, and electromagnetic showers generated by beam-beam collisions.

Synchrotron Radiation

Synchrotron radiation is a potentially large source of background. It is caused by the various types of magnets in the interaction region, but the vacuum-pipe apertures and synchrotron radiation masks have been designed to channel most of these photons into a distant dump. The remainder is dominated by X-rays generated by beam tails and is forced to undergo multiple scatters before it can enter the *BABAR* detector. These measures have proven effective enough that synchrotron radiation is not presenting any significant problems for operations.

Beam-Gas Scattering

Bremsstrahlung due to beam-gas interactions and residual gas particles that are Coulomb-scattered can escape the acceptance of the ring. The rate of these processes is proportional to the product of the beam current and the residual gas pressure. The separation magnets bend the energy-degraded particles in the two beams in opposite directions, leading to larger occupancies in the horizontal plane.

Backgrounds from beam-gas scattering are the primary source of radiation damage in the SVT and are the dominant source of backgrounds in all detector systems except the DIRC.

Luminosity Background

The main source of background for the DIRC stems from radiative Bhabha processes that result in interactions between electrons or positrons and aperture limitations and cause electromagnetic showers. When these interactions occur in the proximity of the IP, the debris from the showers can reach the *BABAR* detector. The rate of these backgrounds is proportional to the instantaneous luminosity.

III.2 The *BABAR* Detector

The detector of the *BABAR* experiment (see Figure III.2) consists of the following main parts, listed from the inside out:

The Silicon Vertex Tracker (SVT) measures the trajectories of charged particles with high precision close to the point of the primary interaction(IP). This is essential for the reconstruction of decay vertices of the B mesons and other short-lived particles and used to measure the decay lifetime. The presented analysis takes advantage of these capabilities of the SVT to select Λ hyperons with high purity.

The Drift Chamber (DCH) is used to measure momenta of charged particles that leave a trace of ionization as they traverse the chamber. Additionally information about the energy loss aids in particle identification (PID).

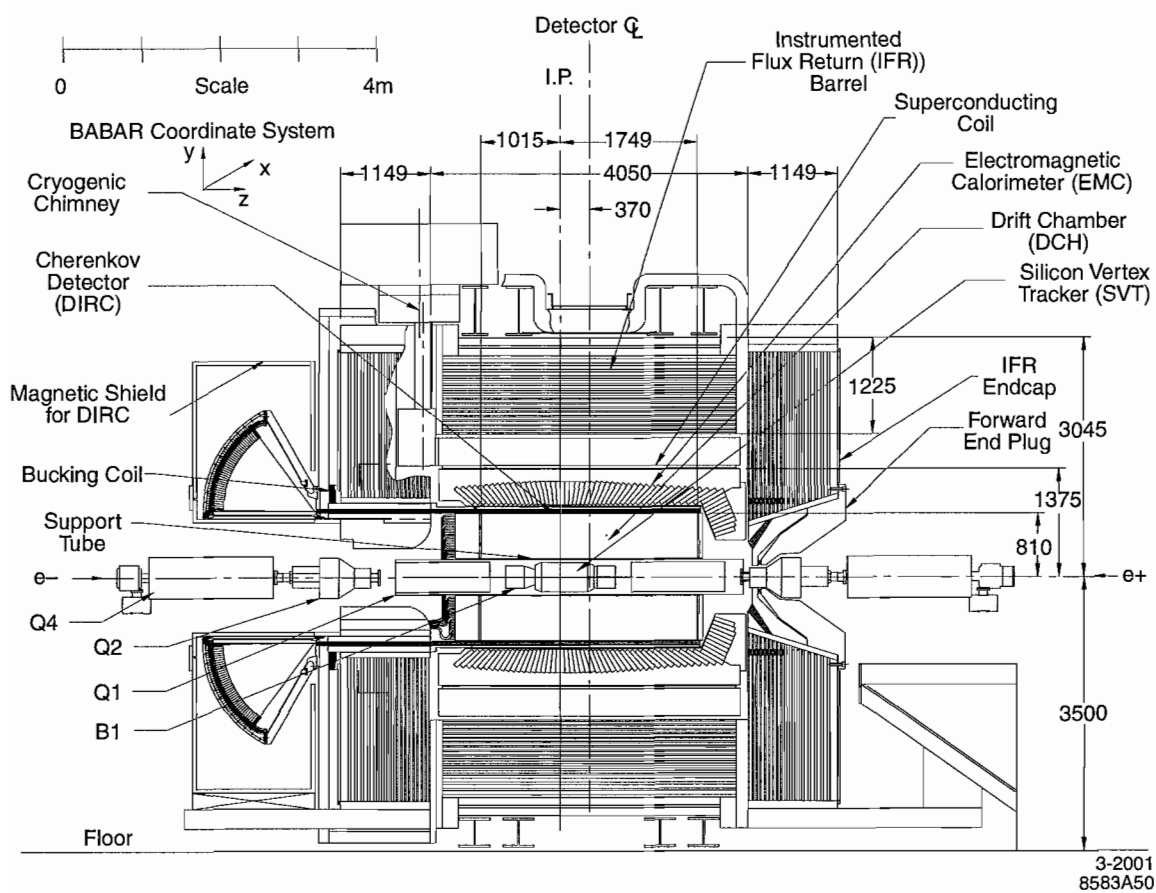


Fig. III.2: Technical drawing of the *BABAR* detector

The Detector of Internally Reflected Cerenkov radiation (DIRC) is mainly used for particle identification. It detects light that ionizing particles emit while they traverse bars of radiator material. This information is primarily used for separating charged kaons, protons and charged pions from each other. The presented analysis uses the particle identification capabilities of DCH and DIRC in selecting protons from A and B decays.

The Electromagnetic Calorimeter (EMC) is used to measure the energy of particles that produce showers in the material by the electromagnetic interaction. At the *BABAR* experiment those particles are mainly photons that are virtually invisible to other components of the detector, and electrons. The reconstruction of photons with a high resolution is an important aspect in the separation of photons from π^0 and η mesons.

The Instrumented Flux Return (IFR) can only be reached by particles that are able to pass the large amounts of material of the super-conducting coil. It is segmented into sextants and has been instrumented with Resistive Plate Chambers (RPC) and Limited Streamer Tubes (LST) to obtain additional information from those particles that reach beyond the magnet. The muon identification at *BABAR* relies primarily on information from the IFR.

III.2.1 The Vertex Detector

In order to measure the lifetimes of particles, it is essential to be able to reconstruct decay vertices with high precision. The purpose of the *BABAR* Silicon Vertex Tracker (SVT, Figures III.3 and III.4) is to provide precise reconstruction of charged particle trajectories near the interaction region in order to measure the decay length of B mesons. Additionally, the SVT must be able to provide standalone tracking for

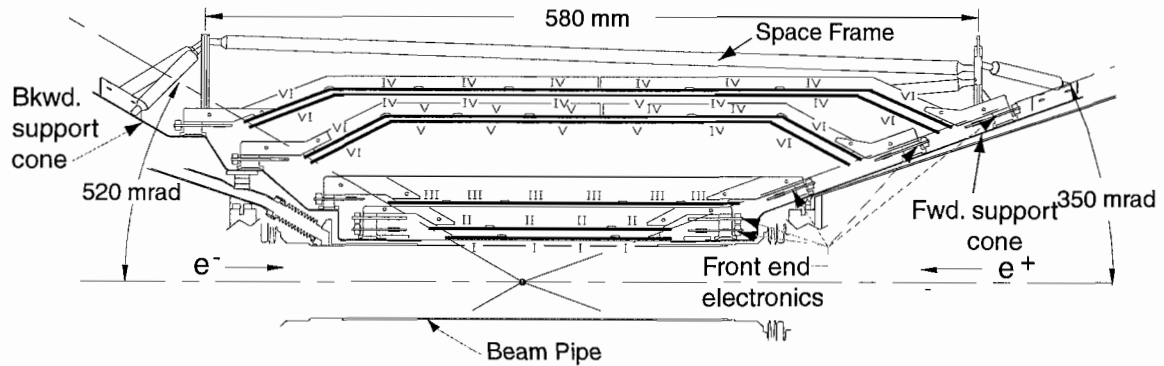


Fig. III.3: Side view of the *BABAR* SVT and support structure

tracks with a minimum transverse momentum of < 120 MeV, the minimum required for a track to be measured in the drift chamber. The SVT consists of five layers of silicon ladders around the PEP-II interaction point (IP). The inner three layers are situated close to the beam pipe, which has a radius of 27.8 mm, at radii between 32 mm and 54 mm. The outer two layers are at 127 mm and 144 mm, and they are arched to increase the angular coverage and to minimize the angle of incidence. Each of its modules is constructed with readout strips on the inside and on the outside, the ones on the inside are arranged perpendicular to the beam direction to measure the z information, and the ones on the outside run parallel to the beam and measure the angle ϕ . The single hit resolution in the SVT is 10-35 mm for both z and ϕ strips, depending on the incident angle and the momentum.

Reconstruction

In order to reconstruct the trajectories of charged particles from measured hits, in a first step the time information of the measurement is compared to the event time as determined by the DCH, and hits recorded more than 200 ns away from the event

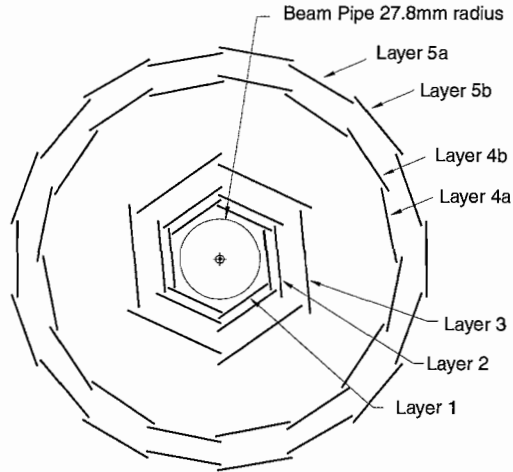


Fig. III.4: View of the SVT along the beam direction

time are discarded. Accounting for the fact that particles can produce more than one hit per layer, hits are then grouped to clusters by weighted averaging over adjacent strips before they are passed on to the pattern recognition algorithm.

Because the pulse height gives a measure of dE/dx , up to 10 measurements of this quantity are available for each particle from the SVT alone. This allows for the separation of 2σ for pions and kaons with momenta up to 500 MeV and of kaons and protons with momenta below 1 GeV (see Figure III.5). It should be noted that the coordinate system of the SVT does not coincide with the coordinate system of the rest of *BABAR*. Diurnal fluctuations in temperature cause deviations of ± 50 mm in the relative position of the two. After detector access, the coordinate systems have to be aligned again using $e^+e^- \rightarrow \mu^+\mu^-$ events and cosmic muons that pass through the detector close to the IP.

III.2.2 The Drift Chamber

The *BABAR* drift chamber for measurement of the momenta of charged particles is a cylindrical container of gas and extends from the inner radius of 236 mm to the

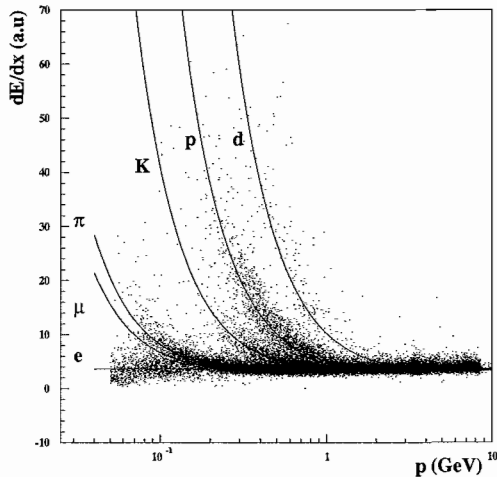


Fig. III.5: dE/dx information vs. momentum from the SVT for various particle species

outer radius of 809 mm. Its active region is 2764 mm long, and its center is offset by 370 mm in forward direction to account for the boost of the event. Particles traversing one or more of its 40 layers cause ionization of the helium - isobutane gas mix that fills the chamber. The electric field of the *field wires* (see Figure III.6) causes the charge to drift to the *sense wires*. The drift time-to-distance relationships are determined from Bhabha and $e^+e^- \rightarrow \mu^+\mu^-$ scattering for each layer individually. The gas gain is obtained from the total charge that is deposited in each drift cell. The measurements of dE/dx that can be obtained with this knowledge help in the particle identification at low momenta. For track reconstruction the 40 layers are grouped into 10 so-called *superlayers* of four. Sequential layers are staggered by half a cell, which allows for local track-segment finding and resolution of the left-right ambiguity in each superlayer, even if one signal is missing. In order to allow for measurements of longitudinal information, 24 of the 40 layers are arranged at a small angle with the z axis. The angle is the same in each superlayer, and the superlayers are arranged in the pattern AUVAUVAUVA, where A corresponds to wires parallel to z , U to an

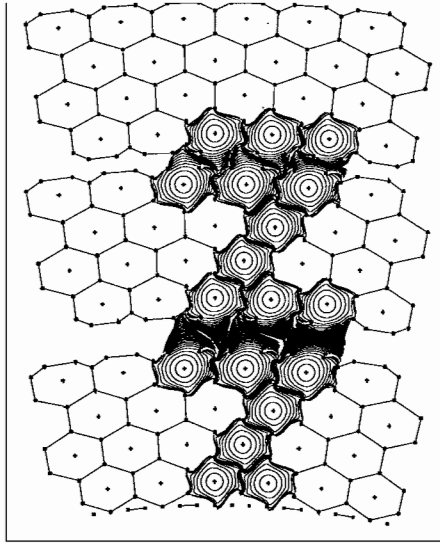


Fig. III.6: Schematic view of the arrangements of the wires in a layer with the drift isochrones shown

angle between 45 mrad and 69 mrad and V to an angle between -52 mrad and 76 mrad. This allows for the reconstruction of vertices outside the SVT, e.g. from the decay of a K_s^0 .

III.2.3 Track Reconstruction

When a charged particle traverses the detector, the magnetic field of the solenoid forces it on a helical path that can be described with five parameters: the distance of closest approach in the x-y plane d_0 , the inverse of the radius of the circle that is the projection of the trajectory to the x-y plane ω , the polar angle coordinate of the point of closest approach to the IP ϕ_0 , the dipping angle of the helix λ , and the coordinate along z of the point of closest approach z_0 . Multiple scattering in the detector material causes deviations from this trajectory. Trajectories of charged particles are reconstructed using a Kalman algorithm as follows: Track segments - groups of 4 hits that are found in the DCH by the L3 trigger - are taken as the

seed of the tracking. Hits that are not associated with a track after this procedure are then used in the search for tracks that do not originate from the IP or do not traverse the whole DCH. After this procedure, all tracks are refit with the Kalman approach. SVT track segments and hits are added if they are consistent within the expected error due to extrapolation taking into account material budget and field inhomogeneity. Ambiguities are resolved by considering the number of layers and size of the residuals.

The remaining hits in the SVT are then passed to two additional track finding algorithms. One is starting with triplets of hits (ϕ and z information) in layers 1, 3, 5 of the SVT and adding consistent hits, requiring at least four hits to make a good track. The other is starting out with circular trajectories, using only the ϕ information, adding z information to build the helical trajectory.

In a last step, an attempt is made to merge trajectories that consist of only hits in only one detector, in order to recover particles that scattered in the material of the support tube. The track parameter resolution at the point of closest approach is:

- $\sigma_{d_0} = 23\mu\text{m}$
- $\sigma_{\phi_0} = 0.43 \text{ mrad}$
- $\sigma_{z_0} = 29\mu\text{m}$
- $\sigma_{\tan\lambda} = 0.53 \times 10^{-3}$
- $\sigma_{p_t}/p_t = (1.3 \pm 0.1) \times 10^{-3} p_t + (4.5 \pm 0.3) \times 10^{-3}$

This results in a resolution of $70 \mu\text{m}$ for the position along z of the vertex of a fully reconstructed B meson.

III.2.4 The DIRC

Helping in the particle identification and supplying mainly the information for the separation of pions and kaons is the *BABAR* Detector of Internally Reflected Cerenkov light (DIRC), shown in Figure III.7. Particles moving faster than the speed of light in the medium emit Cerenkov radiation at an angle $\cos(\theta_C) = 1/n\beta$ ($\beta = v/c$), with $n = 1.473$ the mean index of refraction of fused silica, the main radiator material in the DIRC. In *BABAR* this material is arranged in 12 boxes containing 12 bars, 17 mm thick, 35 mm wide and 4.9 m long. Particles traversing this material usually emit many photons isotropically in ϕ creating rings of Cerenkov radiation. The photons are reflected internally, preserving the Cerenkov angle. In order to avoid having to instrument both sides of the detector – because of the boosted center-of-momentum frame most particles arrive at the forward end of the *BABAR* detector – the forward end is furnished with mirrors. On the backward end, incoming Cerenkov photons arrive at a water-filled *standoff box*, where they have to go through a silica wedge that reflects photons at large angles relative to the bar axis, thereby effectively reducing the detection area and recovering photons that would otherwise be lost to total reflection at the silica-water interface. At the end of the standoff box they are detected by an array of photo-multiplier tubes (PMT). The DIRC is by design a three-dimensional imaging device, using the position and arrival time of the PMT signals. The measured information about the photon propagation angles are augmented by information from the tracking system to determine θ_C and ϕ_C . Cerenkov photons from charged particles arrive within a window of 50 ns after the event, and they are accompanied by hundreds of background photons. Time resolution from the PMT is not competitive with the spatial resolution of the reconstruction of the Cerenkov angles, but time information from the PMT can be used to resolve forward-

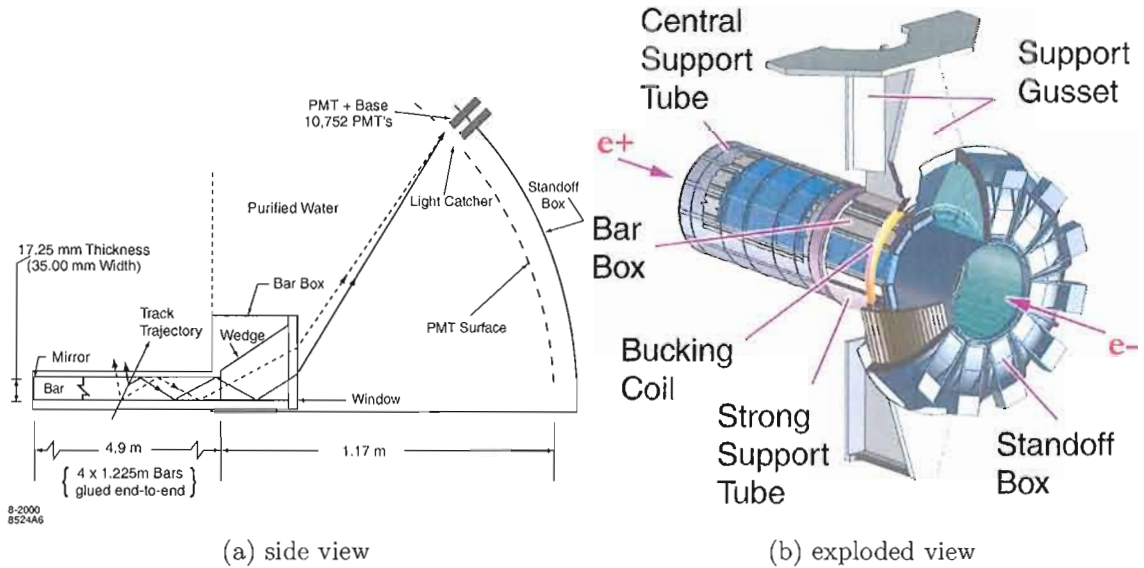


Fig. III.7: Side view and exploded view of the DIRC

backward ambiguities in the reconstruction and aid in associating the signal to the right track. The time difference Δt_γ between measured and expected photon arrival is an important observable to distinguish signal from background. It is calculated using the time-of-flight of the track (with a charged pion hypothesis) and the photon propagation time to the PMT. This procedure reduces the number of accelerator-induced background photons approximately by a factor of 40 and helps in the correct matching of photons with tracks. The measured time resolution of 1.7 ns is close to the intrinsic transit time spread of the PMT of 1.5 ns.

III.2.5 The Electromagnetic Calorimeter

The purpose of the electromagnetic calorimeter is to measure the energy of electromagnetic showers with high precision over the energy range from 20 MeV to 9 GeV in order to measure QED processes like $e^+e^- \rightarrow e^+e^-(\gamma)$ and $e^+e^- \rightarrow \gamma\gamma$ for calibration purposes. The ability to measure rare decays like $B \rightarrow \gamma\gamma$ sets stringent requirements

on the energy resolution as well as the angular resolution, as the mass resolution of reconstructed π^0 mesons is dominated by the energy resolution for energies below 2 GeV, and by the angular resolution for energies above it.

The EMC consists of a cylindrical barrel around the interaction region and within the superconducting field of 1.5 T. It has full coverage in the azimuth and together with its conical forward endcap its coverage extends in polar angle from 15.8° to 141.8° corresponding to a coverage of 90 % in the c.m. frame.

Reconstruction Algorithm

The Molière radius of CsI(Tl) being 3.8 cm, electromagnetic showers typically spread out over several adjacent crystals with a cross section of $4.7 \text{ cm} \times 4.7 \text{ cm}$ on the front face and $6.0 \text{ cm} \times 6.1 \text{ cm}$ on the back end, shown in Figure III.8. Pattern recognition algorithms have to efficiently identify these *clusters* and distinguish between those with a single energy maximum and merged clusters with several local maxima, or *bumps*. In a first step, clusters are divided into bumps, then each crystal in a cluster is assigned a weight

$$w_i = \frac{E_i \exp(-2.5r_i/r_M)}{\sum_j E_j \exp(-2.5r_j/r_M)},$$

where r_M is the Molière radius¹ and r_i is the distance of the crystal i from the centroid of the bump. The energy of a bump is then simply the sum of the energies of the crystals in a cluster times their weight.

$$E_{\text{bump}} = \sum_i w_i E_i,$$

¹The Molière radius is a material constant and specifies the scale of the transverse dimension of a fully contained electromagnetic shower. It can be related to the radiation length X_0 , i.e. the distance over which a high-energy electron loses all but 1/e of its energy, by the empirical formula $r_M = 0.0265X_0(Z + 1.2)$

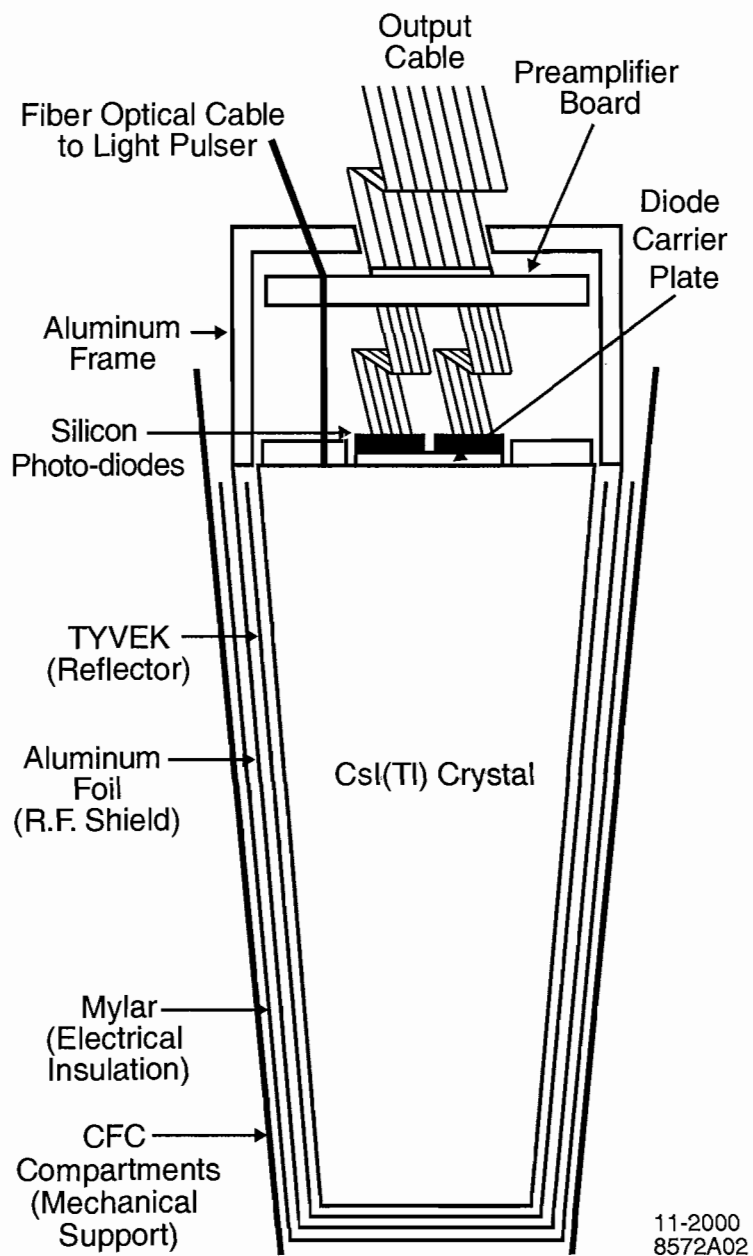


Fig. III.8: Schematic of a crystal used in the EMC

The position of a bump is computed with a center-of-gravity method with logarithmic weights $W_i = 4.0 + \ln(E_i/E_{\text{bump}})$ in order to emphasize lower-energy crystals. Only crystals with positive weights are considered, so that only crystals that make the core of the cluster enter the computation. The systematic bias in the computed polar angle that comes from the non-projectivity of the crystals is corrected for by a simple offset of -2.6 mrad for $\theta > 90^\circ$ and +2.6 mrad for $\theta < 90^\circ$. Bumps are then associated with tracks by projecting the track to the inner face of the calorimeter. If the distance between track impact point and the bump centroid is consistent with the angle and momentum of the track, the bump is associated with this track. Otherwise the bump is assumed to come from a neutral particle.

Resolution

The resolution of the EMC is measured directly with a neutron-irradiated fluorinert yielding $\sigma_E/E = 5.0 \pm 0.8\%$ at 6.13 MeV. For high energies, the resolution is derived from Bhabha scattering, where the energy of the shower depends on the polar angle of the electron or positron, $\sigma_E/E = 1.9 \pm 0.07\%$. Combining the calibrations at different energies yields

$$\frac{\sigma_E}{E} = \frac{(2.32 \pm 0.30)\%}{\sqrt[4]{E(\text{GeV})}} \oplus (1.85 \pm 0.12)\%$$

The angular resolution can be parametrized as

$$\sigma_\theta = \sigma_\phi = \left(\frac{3.87 \pm 0.07}{\sqrt{E(\text{GeV})}} + 0.00 \pm 0.04 \right) \text{ mrad}$$

III.2.6 The Superconducting Magnet and the Instrumented Flux Return

The preceding detector subsystems are surrounded by a superconducting magnet that generates a 1.5 T field. For identification of μ and K_L^0 particles, the steel of the

flux return has been segmented into 18 layers and instrumented with resistive plate chamber (RPC) detectors. In 2004, because of degradation of the performance, the RPCs in two sextants in the barrel were exchanged with limited streamer tube (LST) detectors; the other four sextants were exchanged in 2005.

RPC

Resistive plate chambers as installed in the *BABAR* detector (see Figure III.9) consist of two thin foils of copper on top of a bakelite plate that are separated by a gap of 5 cm filled with a gas mix of isobutane and fluorinert. The high resistivity carbon coating on the inside of the bakelite plates gives these plates their name. A high voltage is connected to the plates, and when a particle traverses the plates and ionizes the gas, it produces a localized shower cascade that is read out. Rather than a signal that is proportional to the applied voltage, the RPC are operated in so-called *streamer* mode, where the field is high enough that the ionized gas creates secondary avalanches by photoemission that cancel the external field. In this regime the signal is rather independent of the applied voltage.

LST

An open Limited Streamer Tube is shown in Figure III.10. Limited streamer tubes work in a way very similar to RPCs, but because of the more robust design, this technology was preferred for the upgrade of the IFR in 2004.

An LST consists of a plastic case with either 6 or 8 chambers of dimensions $15\text{ mm} \times 15\text{ mm} \times 3000\text{ mm}$, each coated on the inside with a high resistivity carbon coating and housing a copper wire. Strips of copper foil along the tube on the bottom are used to read out the x-y position of a particle and strips across the top read out the z position.

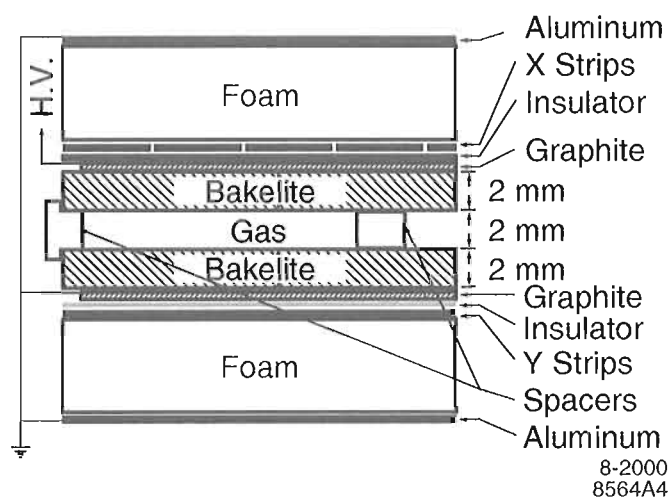


Fig. III.9: Cross section of a RPC module



Fig. III.10: Top view of an LST module. The protective sleeve has been partly retracted for a better view.

The tubes are filled with an admixture of gases similar to that in the RPCs. The *BABAR* LST can be operated both in a proportional mode, where the signal is proportional to the applied voltage, and in a streamer mode. Figure III.11 shows the dependence of the signal on the applied voltage for an exemplary module. During installation into the 18 layers of the barrel of the IFR, some layers were filled with brass instead of the LST detectors. This additional absorbing material increases the resolution of muon detection, but reduces the detection efficiency of K_0 mesons.

III.3 Detector Simulation

A full simulation of the *BABAR* detector is written in the GEANT4(28) framework for the simulation of the passage of particles through matter. Event records provided by event generators are transported through the material and the magnetic field of the detector and the response of the sensitive material is simulated and recorded in the same format as the actual measurements of data taking. Additionally, an algorithm attempts to match reconstructed objects with the simulated particles that caused the detector response. This procedure is known as truth matching and aids in the validation of several parts of the analysis and helps analysts to perform a “blind analysis” (29). Figure III.12 shows the effect of the detector simulation on the distribution of the invariant mass of the baryon pair in the decay $B^- \rightarrow \Lambda \bar{p} \gamma$. The distribution marked with “Generator level” corresponds to a decay in vacuum, with no final state radiation. The distribution marked with “Detector level” shows the effect of both the detector simulation as well as a possible confusion in the reconstruction of the parent particle due to final state radiation.

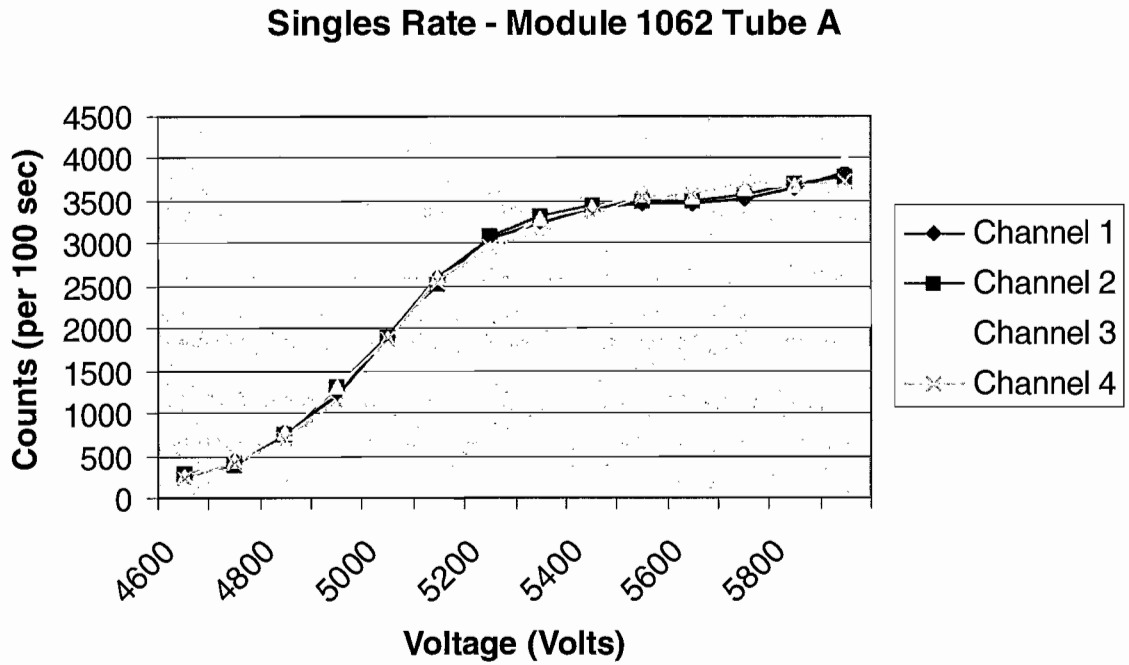


Fig. III.11: Dependence of the signal on the operating voltage for an exemplary LST

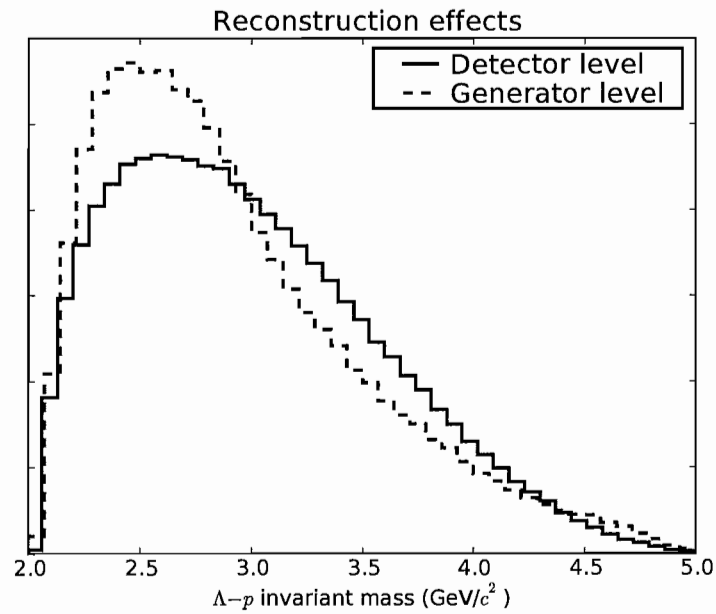


Fig. III.12: Comparison of the invariant mass distributions of the two baryons in the decay $B^- \rightarrow \Lambda \bar{p} \gamma$ for particles in vacuum (generator level) and perfectly reconstructed particles in the *BABAR* detector (detector level)

CHAPTER IV

ANALYSIS OF BARYONIC B DECAYS

IV.1 Introduction

This chapter documents the analysis in detail and intends to give the motivation for the decisions that were made, supporting them with graphical material wherever appropriate. Any material that is not immediately relevant to the discussion at hand but might give further insight or serve as background can be found in the Appendices.

It is important to note that the analysis is developed exclusively on simulated samples in order to comply with the rules of a *blind analysis*(29). Only after review of the strategy is the analysis actually carried out on data. This chapter has to be understood in this context. All steps of the analysis as described here apply to simulated samples as well as to data if not specified otherwise. We adopt the following conventions in the remainder of the text:

Data refers to events recorded by the *BABAR* detector, as opposed to simulated events.

Candidates are reconstructed objects in either data or simulation that are composed of tracks and clusters. Because this object is just a hypothesis of a particle, it is called a candidate for this particle type.

The text is sectioned as follows: Starting with an introduction of the samples of events, we describe in detail the models that are used to generate the samples of $B^- \rightarrow \Lambda \bar{p} \gamma$, $B^- \rightarrow \Sigma^0 \bar{p} \gamma$, $B^- \rightarrow \Lambda \bar{p} \pi^0$ and $B^- \rightarrow \Sigma^0 \bar{p} \pi^0$. The next step of the analysis deals with reducing the data sample based on loose cuts on variables that

are inexpensive to compute. This is the so-called *skimming* of events. It reduces the data sample so that computationally more expensive steps can be taken. This involves reconstruction of candidate B mesons with a vertex fit and a more sophisticated set of cuts, which is the subject of the following section. After these steps the selection of B candidates is complete, and we develop the strategy to compute the branching ratios of the relevant decays, as well as a way to reconstruct the (unknown) distribution of the invariant mass of the baryon pair. Before applying these steps to the *BABAR* data sample, we perform a set of validations and give an overview over the errors that are associated with the final result.

IV.2 Samples

IV.2.1 Data

This analysis uses the data sample collected in runs 1-5 at the $\Upsilon(4S)$ resonance, as well as the sample collected 40 MeV below the resonance in the same time period for background studies. The integrated luminosity and number of $B\bar{B}$ pairs in the different runs is shown in Table IV.1. Figure IV.1 shows the integrated luminosity for the data.

run	integrated luminosity (fb^{-1})	$N_{B\bar{B}}$ (10^6)
1	20	22
2	61	67
3	32	36
4	98	110
5	130	150
total	340	390

Tab. IV.1: Integrated luminosity and number of $B\bar{B}$ pairs

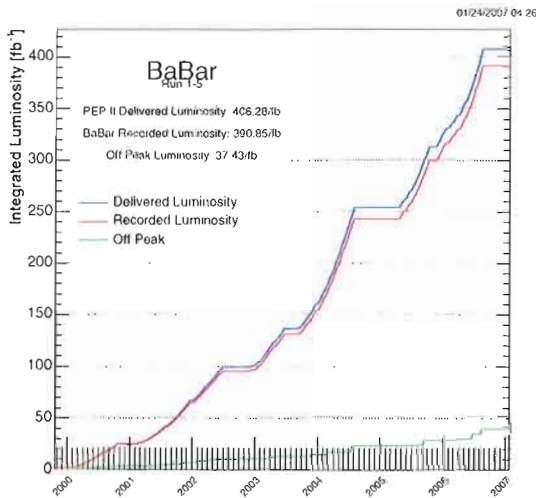


Fig. IV.1: Integrated luminosity versus time in *BABAR* runs 1 through 5

IV.2.2 Simulation

Simulation of decays at the *BABAR* experiment is mainly handled by the EvtGen(30) event generator. This program generates the correct angular correlations of B meson decays given a theoretical model. Decays for which no dedicated model has been implemented are treated generically by the JetSet(31) program, but in this case the angular correlations between decay products can be incorrect which can have quite significant effects on the analysis. (see Section IV.2.5)

A significant characteristic of baryonic B decays is that the distribution of the invariant mass of the baryon pair peaks close to threshold. In order to account for this feature, the samples of $B^- \rightarrow \Lambda \bar{p} \gamma$ and $B^- \rightarrow \Sigma^0 \bar{p} \gamma$ decays were generated based on a pole model treatment of $b \rightarrow s \gamma$ decays with baryons in the final state(32). This model features a shape of the invariant mass distribution that is compatible with the Belle measurement(16), and the more realistic distribution of events allows for a more accurate validation of the analysis. Therefore the model was coded for

the EvtGen event generator under the name B_TO_LAMBDA_PBAR_GAMMA. The events generated with the new model clearly show the threshold enhancement (Figure IV.2). Figure IV.3 shows the distribution in an alternative model based on QCD counting rules(3), which also shows a threshold enhancement, but was not used to simulate events for this analysis. The decays $B^- \rightarrow \Lambda \bar{p} \pi^0$ and $B^- \rightarrow \Sigma^0 \bar{p} \pi^0$ are a background

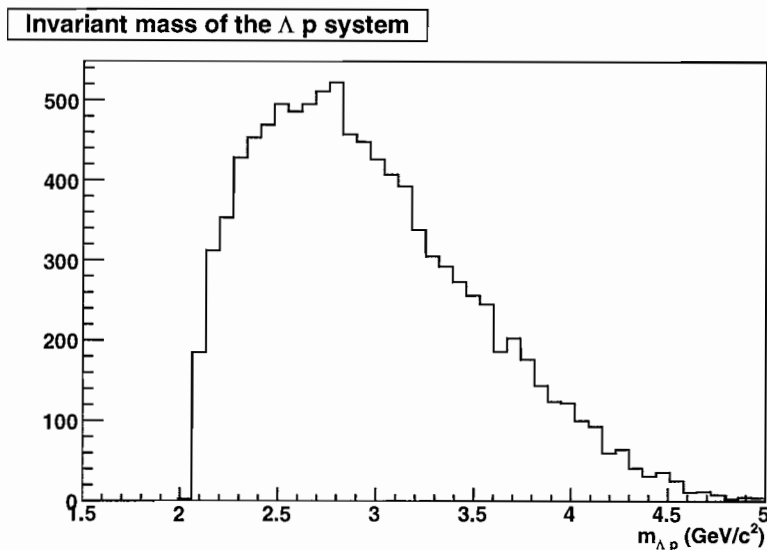


Fig. IV.2: Invariant mass of the $\Lambda - p$ system in the decay $B^- \rightarrow \Lambda \bar{p} \gamma$ according to the model by Cheng and Yang

to the analysis of $B^- \rightarrow \Lambda \bar{p} \gamma$ and $B^- \rightarrow \Sigma^0 \bar{p} \gamma$, because the B also decays to a baryon pair with the invariant mass peaking near threshold. Because of the π^0 in the final state decaying via $\pi^0 \rightarrow \gamma \gamma$, the final states of the four decays look very similar. However, because the decays $B^- \rightarrow \Lambda \bar{p} \pi^0$ and $B^- \rightarrow \Sigma^0 \bar{p} \pi^0$ are incompatible with the previously described generator model B_TO_LAMBDA_PBAR_GAMMA, a model of this decay(2) was turned into a new EvtGen model with the name B_TO_2BARYON_SCALAR. The model is based on a factorization assumption, which means the amplitudes for the $B - \pi$ transition is factored out from the amplitude for the $B - \Lambda p$ transition, and the

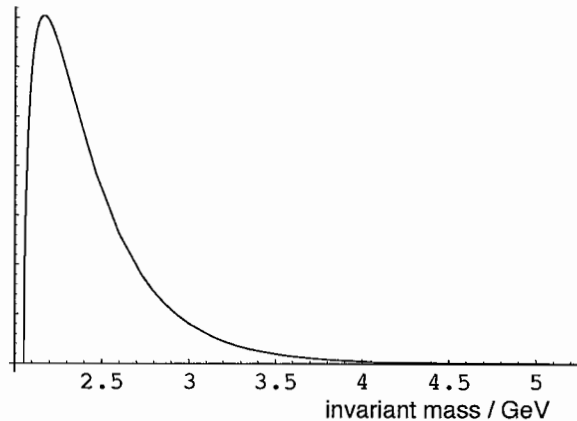


Fig. IV.3: Distribution of the invariant mass of the baryon pair in the analysis of the decay $B^- \rightarrow \Lambda \bar{p} \gamma$ according to perturbative QCD

branching ratio for the decays is expected to be $1/2$ that of the corresponding decays of neutral B mesons to a baryon pair and a charged pion due to isospin symmetry. Figure IV.4 shows a comparison of the distribution of the invariant mass of the baryon pair in the decay $B^- \rightarrow \Lambda \bar{p} \gamma$ from the `B_TO_LAMBDA_PBAR_GAMMA` generator, and the same variable in the decay $B^- \rightarrow \Lambda \bar{p} \pi^0$ from the `B_TO_2BARYON_SCALAR` generator.

IV.2.3 *Lambda Antiproton Gamma*

A sample of events was generated with the `B_TO_LAMBDA_PBAR_GAMMA` decay amplitude. The decay of the Λ hyperon was limited to $\Lambda^0 \rightarrow p^+ \pi^-$ in the sample. Plots of the momenta in the CMS at the generator level like those in Figure IV.5 can give an indication of reconstruction efficiencies and possible analysis strategies. At this level it is already fairly obvious that the standard skim of the Radiative Penguin AWG `BToXsGamma` cannot be used. The `BToXsGamma` skim exploits the fact that the photon in two-body $b \rightarrow s \gamma$ events has a high energy (see Figure IV.6). Baryonic final states however take up a large amount of phase space, so that the photon momentum is considerably lower than for decays to mesons.

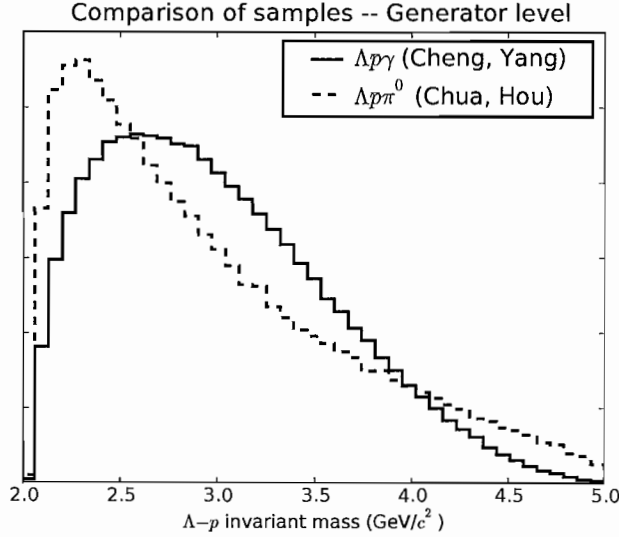


Fig. IV.4: Comparison of the distribution of the invariant mass of the baryon pair in the decays $B^- \rightarrow \Lambda \bar{p} \gamma$ and $B^- \rightarrow \Lambda \bar{p} \pi^0$. Two different models are underlying the generation of these decays.

Comparing Figure IV.5(c) with Figure IV.6 reveals the effect of the `Photos` package in the reconstruction code. This package simulates QED radiation of charged particles. The low-momentum peak in Figure IV.6 is due to photons generated by this package. Since the `Photos` package adds a (low energy) photon to the simulated decay, the most energetic photon was taken for the truth matching.

IV.2.4 *Sigma Antiproton Gamma*

Decays of the kind $B^- \rightarrow \Sigma^0 \bar{p} \gamma$ are a significant source of background in the reconstruction of $B^- \rightarrow \Lambda \bar{p} \gamma$ and vice versa, because the decay $\Sigma^0 \rightarrow \Lambda \gamma$ has a branching fraction of 100 % and because the small mass difference of the two baryons $m_{\Sigma^0} - m_{\Lambda} = 77 \text{ MeV}$. The large number of low-energy background photons makes it easy to find a candidate that combines with a Λ candidate to form a suitable Σ^0 candidate. As Figure IV.7 clearly shows, the momentum distributions for the two

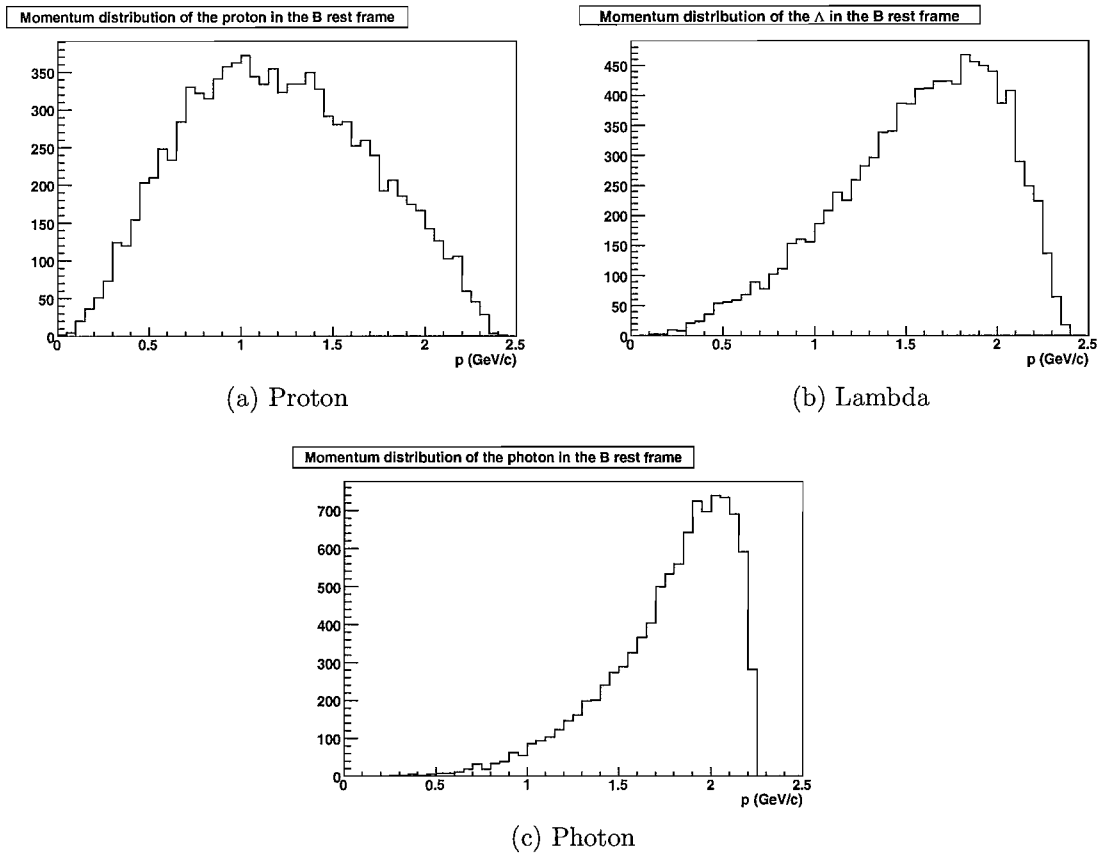


Fig. IV.5: CMS Momentum distributions of the $B^- \rightarrow \Lambda \bar{p} \gamma$ final states at the generator level

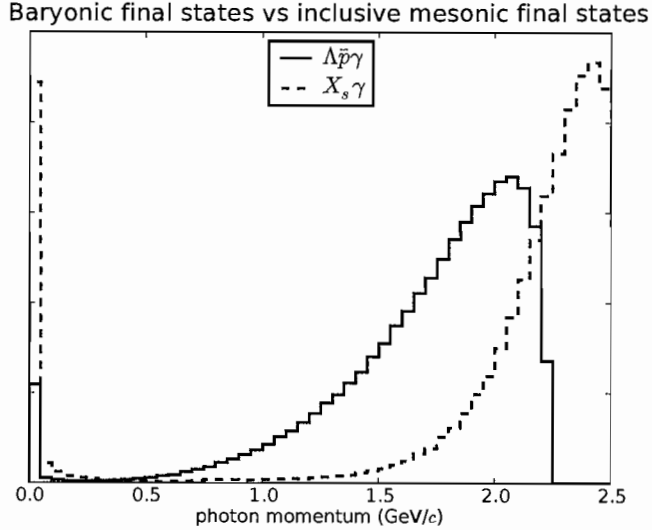


Fig. IV.6: Comparison of the generator level CMS momentum distributions of the high energy photon in the decays $B^- \rightarrow \Lambda \bar{p} \gamma$ and $B \rightarrow X_s \gamma$

modes are very similar, making it difficult to separate the two decays. A sample of events was generated with the `B_TO_LAMBDA_PBAR_GAMMA` amplitude. The decay of the Λ hyperon was limited to $\Lambda \rightarrow p \pi^-$.

IV.2.5 *Lambda Antiproton Pi*

A comparison of the invariant mass of the baryon system between events generated with a generic phase space model and those generated with the amplitude according to the `B_TO_2BARYON_SCALAR` model is shown in Figure IV.8. Applying the selection cuts (see section G) to both samples shows that 50% more events generated with the specific amplitude model pass the cuts than those generated with the phase space model. The Λ hyperon decay is limited to $\Lambda^0 \rightarrow p \pi^-$. The recent measurement by the BELLE collaboration(33) indicates that this mode has to be taken into account as a possible source of confusion when measuring $B^- \rightarrow \Lambda \bar{p} \gamma$ or $B^- \rightarrow \Sigma^0 \bar{p} \gamma$. Because the

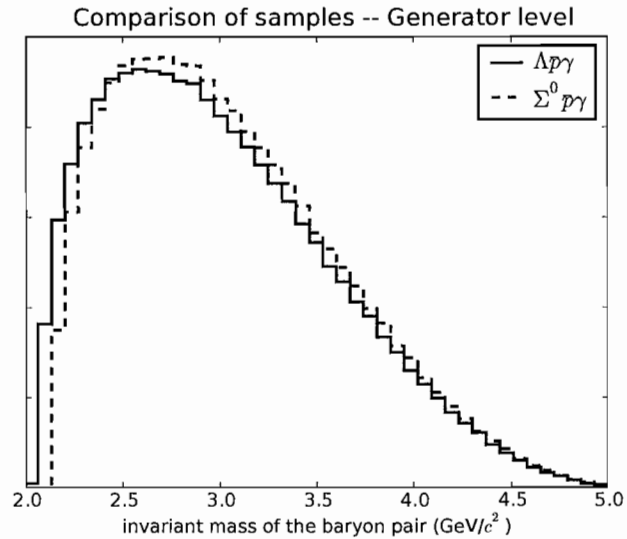


Fig. IV.7: Comparison of the distribution of the invariant mass of the baryon pair in the decays $B^- \rightarrow \Lambda \bar{p} \gamma$ and $B^- \rightarrow \Sigma^0 \bar{p} \gamma$

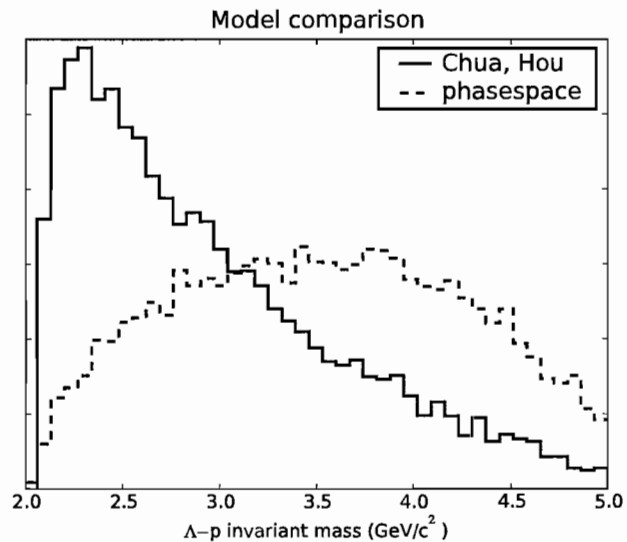


Fig. IV.8: Comparison of the invariant mass of the two-baryon system in the decay $B^- \rightarrow \Lambda \bar{p} \pi^0$. The two samples were generated with the model by Chua et al.(2) and a generic phase space model, respectively.

distributions of two of the discriminating variables¹ are close to those of $B^- \rightarrow \Lambda \bar{p} \gamma$, it has to be modeled separately and we are including this mode in the list of signal decays.

IV.2.6 Sigma Antiproton Pi

The proximity in the fit variables of this decay to $B^- \rightarrow \Lambda \bar{p} \pi^0$ warrants separate parametrization, we also include this mode in the list of signal decays and measure the branching fraction for this decay. The model used to generate the samples is also `B_TD_2BARYON_SCALAR`, with $\Sigma^0 \rightarrow \Lambda^0 \gamma$ and $\Lambda^0 \rightarrow p \pi^-$.

IV.2.7 Backgrounds

Decays that look sufficiently like the signal decays, such that they cannot be removed with simple rectangular cuts are

$$e^+ e^- \rightarrow u\bar{u}, d\bar{d}, s\bar{s}$$

$e^+ e^- \rightarrow c\bar{c}$ Events with lighter quarks can be a background (and are in fact the dominant background source), because of their large cross section.

generic charged B

generic neutral B These two samples encompass all decays in the list `DECAY.DEC` for the `EvtGen` generator. They contain events where the generic phase space algorithm in the generator produces a Λ or a Σ^0 , a proton and a photon in the final state. The branching fraction for these modes is largely overestimated in these samples, so $B^- \rightarrow \Lambda \bar{p} \gamma$ and $B^- \rightarrow \Sigma^0 \bar{p} \gamma$ events are explicitly excluded from these samples by vetoing events in which a photon and an X_s state are direct daughters of a B and the X_s decays into a proton and a Λ or Σ^0 .

¹namely $m_{\text{rec.}}$ and $m_{\text{miss.}}$, see equations IV.1 and IV.2

IV.2.8 Summary of the Simulated Samples

In the sample of generic B decays, for the components that have been previously analyzed the measurement of the branching fraction or average of existing measurements was taken. The decay $B^- \rightarrow \Sigma^0 \bar{p} \gamma$ has not been observed at this point and so the existing upper limit was taken as a cross section. For the decay $B^- \rightarrow \Lambda \bar{p} \pi^0$ Belle's measurement of the branching fraction was taken at face value. Similar to $B^- \rightarrow \Sigma^0 \bar{p} \gamma$, no measurement of $B^- \rightarrow \Sigma^0 \bar{p} \pi^0$ has been made to date. Because of isospin symmetry, the branching fraction is expected to half that of $B^0 \rightarrow p \bar{\Sigma}^0 \pi^-$ (17), and since no measurement exists half of the value for the upper limit for $B^0 \rightarrow p \bar{\Sigma}^0 \pi^-$ is assumed as the branching fraction to estimate the effect on this analysis. The numbers are listed in Table IV.2. The number of events available for the simulated

Mode:	branching fraction (10^{-6})
$B^- \rightarrow \Lambda \bar{p} \gamma$	2.16
$B^- \rightarrow \Sigma^0 \bar{p} \gamma$	< 4.60
$B^- \rightarrow \Lambda \bar{p} \pi^0$	3.00
$B^- \rightarrow \Sigma^0 \bar{p} \pi^0$	< 1.9

Tab. IV.2: Branching fraction of the four modes under investigation. These numbers are used to combine the simulated samples in the right proportions.

samples are listed in table IV.3. Cross-sections and branching fractions underlying these estimations are taken from tables III.1 and IV.2.

IV.3 Event Preselection

In order to reduce the BaBar data sample to a more manageable size, the following selection was applied to the samples before performing an actual reconstruction and analysis of the decay chain. Table IV.4 shows the fraction of events that pass this selection, while Table IV.5 shows the number of events that are still available after

Sample	Run 1 (10 ³)	Run 2 (10 ³)	Run 3 (10 ³)	Run 4 (10 ³)	Run 5 (10 ³)	total (10 ³)
light quark	83,168	122,700	66,894	209,150	213,908	695,820
charm quark	82,226	156,242	77,184	147,144	128,402	591,198
charged B generic	69,596	102,142	46,698	168,312	168,824	555,572
neutral B generic	69,238	103,164	50,556	163,084	166,372	552,414
$B^- \rightarrow \Lambda \bar{p} \gamma$	31	94	50	153	202	530
$B^- \rightarrow \Sigma^0 \bar{p} \gamma$	31	94	50	153	170	498
$B^- \rightarrow \Lambda \bar{p} \pi^0$	10	31	17	50	56	164
$B^- \rightarrow \Sigma^0 \bar{p} \pi^0$	31	94	50	153	89	417

Tab. IV.3: Number of events by *BABAR* run period for each simulated sample

the selection, scaled to the luminosity of the available data. The cross sections for the different samples are taken from table III.1.

- We require three charged tracks in the event and apply a cut on the event shape
- The photon in the B decay is required to be a single EMC bump that is not matched to a track, subject to $0.3 < E_{\text{cms}} < 3.5$, and for which the lateral moment is < 0.8 .
- Λ candidates are defined as:
 - The proton is a charged track, subject to the cuts
$$L_{\text{kaon}}/L_{\text{kaon}} + L_{\text{proton}} < 0.75 \text{ and } L_{\text{proton}}/L_{\text{proton}} + L_{\text{pion}} > 0.5^2$$
 - The pion is a charged track with no further requirements
 - The Λ is fit with the Cascade algorithm with a geometrical constraint
 - The Λ itself is subject to a cut on the mass within 10 MeV of the PDG value of 1115.683 ± 0.006 MeV

² $L_{\text{pion}}, L_{\text{kaon}}, L_{\text{proton}}$ denote the likelihood of a particular reconstructed candidate to be of the respective type. The likelihood is computed from inputs of SVT, DCH and DIRC. For details on the computation, see http://www.slac.stanford.edu/BFROOT/www/Physics/Tools/Pid/Hadrons/Description_of_the_LH_selectors.html

- The proton is a charged track with no further requirements
- Σ^0 candidates are composed of
 - Λ candidates that are subject to the same requirements as above with additional cuts on the vertex $\chi^2 > 0.001$ and the flight significance (flight length/error on flight length) > 3
 - which are combined with a photon vector required to be a single EMC bump that is not matched to a track, for which the lateral moment is < 0.8 with an additional cut of $\text{LabE} > 0.04 \text{ GeV}$.
 - The mass of the sum of the Lorentz vectors is required to be within 25 MeV of the PDG value of $1192.642 \pm 0.024 \text{ MeV}$ and the candidate is required to be consistent with the primary vertex.
- The reconstructed B was subject to cuts on the sum of the four-vectors
 - $|m_{\text{rec.}}^3 - \text{PDGvalue}| < 0.4 \text{ GeV}$
 - $5.0\text{GeV} < m_{\text{miss.}}^4 < 5.4 \text{ GeV}$

IV.4 Candidate Reconstruction

The following describes the selection criteria that go into composing B candidates from the reconstructed final states. Since the B candidates are not vertexed during skimming, the selection of candidates can differ slightly from the skim.

³see eq. IV.1

⁴see eq. IV.2

Sample	BtoLambdaPbarGamma	BtoSigmaPbarGamma
light quark	3.24E-03	1.06E-03
charm quark	2.41E-03	9.21E-04
charged B generic	1.76E-04	2.81E-05
neutral B generic	1.45E-04	2.79E-05
$B^- \rightarrow \Lambda \bar{p} \gamma$	3.89E-01	2.28E-01
$B^- \rightarrow \Sigma^0 \bar{p} \gamma$	2.40E-01	1.78E-01
$B^- \rightarrow \Lambda \bar{p} \pi^0$	1.91E-01	1.34E-01
$B^- \rightarrow \Sigma^0 \bar{p} \pi^0$	1.48E-01	1.53E-01
On-res data	8.01E-04	3.12E-04
Off-res data	7.78E-04	3.12E-04

Tab. IV.4: Relative skim efficiencies for the different samples

Sample	BtoLambdaPbarGamma	BtoSigmaPbarGamma
light quark	2,325,013.68	762,905.68
charm quark	1,075,666.34	411,229.31
charged B generic	31,745.79	5,033.70
neutral B generic	25,934.75	5,022.34
$B^- \rightarrow \Lambda \bar{p} \gamma$	302.08	177.17
$B^- \rightarrow \Sigma^0 \bar{p} \gamma$	376.97	280.08
$B^- \rightarrow \Lambda \bar{p} \pi^0$	137.15	96.72
$B^- \rightarrow \Sigma^0 \bar{p} \pi^0$	50.51	52.40
On-res data	4,202,970	1,625,870
Off-res data	384,889	154,197

Tab. IV.5: Absolute selection rates of the two skims for the different modes, scaled to the luminosity of the data sample

IV.4.1 *B Candidate Reconstruction*

B candidates are made from the previously described photon and Λ or Σ^0 candidates with an additional proton candidate from the `ChargedTracks` list. The three candidates are then fit to a common vertex using the `TreeFitter` algorithm and the cuts

- $5.1\text{GeV} < m_{\text{miss}} < 5.4\text{ GeV}$
- m_B within 400 MeV of the PDG value

are applied for the reconstruction of $B^- \rightarrow \Lambda \bar{p} \gamma$. The requirements for $B^- \rightarrow \Sigma^0 \bar{p} \gamma$ are a bit looser:

- $4.9\text{GeV} < m_{\text{miss}} < 5.5\text{ GeV}$
- m_B within 600 MeV of the PDG value

IV.4.2 *Candidate Selection Cuts*

In order to reduce the contribution from background sources, the following cuts are applied. Figures F.1 and F.2 show the variables that are being cut on. Each plot is made after all previous cuts are applied. For the order of the cuts and the exact cut limits, see Table IV.6. Tables G.1 and G.3 show the efficiencies for each cut for each sample of events.

Λ selection

Λ vertex significance Candidates with a value for the Λ vertex χ^2 probability of 0.001 or less are thrown away.

Λ decay length significance The `TreeFitter` vertex fitter that is used to combine charged tracks to a B candidate also calculates the decay length of the Λ candidate

as well as an error on this value. The ratio

$$\sigma_L = \frac{\text{decay length}}{\text{error on decay length}}$$

is a measure of how significantly the decay length of the Λ candidate differs from 0. Candidates with a value greater than 5 are retained.

Λ mass Since there is no mass constraint on the fit of the Λ candidate, the difference of this quantity with the PDG value was considered as an additional discriminating variable but it was found to have no discriminating power.

Σ^0 selection

The only variable under consideration is the difference between the fitted candidate mass and its nominal value.

Photon quality cuts

Energy The final state photons in the decays $B^- \rightarrow \Lambda \bar{p} \gamma$ and $B^- \rightarrow \Sigma^0 \bar{p} \gamma$ have an appreciably lower energy than other radiative decays with mesons in the final state. The cut of 1.5 GeV that is usually applied in analyses of these mesonic final states would lead to an unacceptable loss in signal efficiency here, resulting in a large systematic uncertainty due to the poorly known photon energy spectrum. The invariant mass of the final state baryons determines the upper value for this cut. Only events with a photon energy between 1 GeV and 2.3 GeV are kept.

Isolation The loose cut on the photon energy during skim selection is in no way enough to cut against background from π^0 decays and photons from bremsstrahlung processes. In order to reduce the number of events from these sources, the photon

is required to be isolated from other neutrals (to cut against $\pi^0 \rightarrow \gamma\gamma$ decays) and tracks (to cut against bremsstrahlung processes). The distance for each of those from the center of the photon cluster is required to be greater than 25 cm at the face of the EMC.

Mass Vetoes A dominant source of confusion when selecting a photon candidate comes from π^0 and η^0 decays. A cut on the invariant mass of two photon candidates is used to reduce these kinds of backgrounds. The invariant mass of the photon daughter of a given B candidate and any other photon candidate with a lab energy greater than 0.2 GeV in the event is calculated and the mass of the pair with a mass closest to the η^0 mass is retained. The veto cut is then performed on this quantity. The invariant mass of any pair that is closest to the nominal π^0 mass is not vetoed, but used to discriminate against background events as a component in the likelihood fit.

Legendre Moments

The ratio of the two so-called ‘‘Legendre Moments’’ L_2/L_0 is a powerful variable in the discrimination between signal and background. The L_i are defined as

$$L_i = \sum_{k \in \text{ROE}} |p_k| |\cos(\theta_k)|^i$$

where ‘‘ROE’’ stands for ‘‘Rest Of Event’’ and denotes the particles that are not associated with the reconstructed B . θ_k is the angle between the thrust axis and the momentum of particle k . Both p and θ are evaluated in the center-of-momentum frame.

Reconstructed Mass

The reconstructed candidate mass defined as

$$m_{\text{rec.}} := |q_{\text{rec}}| \quad (\text{IV.1})$$

where q_{rec} is the 4-momentum of the reconstructed candidate.

Missing Mass

The missing mass⁵ is defined as

$$m_{\text{miss.}} := |q_{e^+e^-} - q_{\text{rec}}|_{m_{\text{rec.}}=m_{\text{B}}^{\text{PDG}}} \quad (\text{IV.2})$$

The fact that a mass constraint is imposed on $m_{\text{miss.}}$ can improve the resolution of composite candidates in cases where the resolution of the composite is dominated by a single daughter particle. In the present case the imposed constraint cancels the contribution of the neutral daughter particle and the resolution is then given by the resolution of the charged tracks.

IV.4.3 Best Candidate Selection

For each event, one or more reconstructed candidates may pass all cuts. At most one of the two B mesons from the $\Upsilon(4S)$ decay is expected to decay into the signal mode. It may therefore be necessary to select the “best” of the candidates in the event. Tables IV.7 and IV.8 list the multiplicity daughter particles of B candidates $B^- \rightarrow \Lambda \bar{p} \gamma$ and $B^- \rightarrow \Sigma^0 \bar{p} \gamma$ after the skim and after the candidate selection cuts, respectively.

⁵The parametrization of the missing mass has a cut-off point that is given by the center-of-momentum energy, which varies slightly between events. This variation complicates the normalization of the parametrization. In order to simplify the treatment, we additionally shift the missing mass by the difference between the per-event center-of-momentum energy and a mean value of 5.3 GeV, i.e. in the following we use the term “missing mass” to denote $m_{\text{miss.}}^* = m_{\text{miss.}} - (E_{\text{cm}} - 5.3)$

Variable	$B^- \rightarrow \Lambda \bar{p} \gamma$	$B^- \rightarrow \Sigma^0 \bar{p} \gamma$
photon cms energy (GeV)	$1 < x < 2.3$	$1 < x < 2.3$
missing mass (GeV/c^2)	$5.2 < x$	$5.2 < x$
$\chi^2(\text{Vtx}_\Lambda)$	$0.001 < x$	$0.001 < x$
Λ decaylength significance	$5 < x$	$5 < x$
Δm_{Σ^0} (GeV/c^2)	-	$x < 0.02$
photon – track distance (cm)	$25 < x$	$25 < x$
photon – cluster distance (cm)	$25 < x$	$25 < x$
η mass veto (GeV/c^2)	$0.51 < x < 0.57$	$0.51 < x < 0.57$
ratio of legendre moments	$x < 0.55$	$x < 0.55$
ΔB mass (GeV/c^2)	$-0.4 < x < 0.15$	$-0.4 < x < 0.15$

Tab. IV.6: Summary of the cut variables

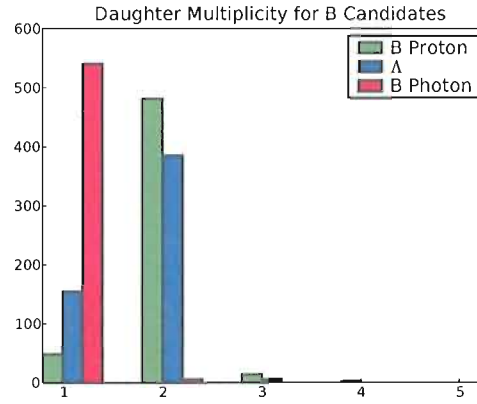
While there is mostly only one candidate per event in the $B^- \rightarrow \Lambda \bar{p} \gamma$ sample after all cuts, on average 1.56 B candidates survive the cuts in the sample of $B^- \rightarrow \Sigma^0 \bar{p} \gamma$ events. Figures IV.9 and IV.10 give a visual presentation of how many daughters of B candidates each event contains after all cuts. The different colors show which of the daughter particles of the B meson is responsible for the multiplicity. Basing the selection criteria on this daughter particle will then automatically reduce the number of B mesons in the event. These figures indicate that most events reconstructed as $B^- \rightarrow \Lambda \bar{p} \gamma$ only have one reconstructed B that passes all devised cuts. Selecting the so-called “best candidate” is therefore only of minor importance for this reconstruc-

Sample	Skim selection of $B^- \rightarrow \Lambda \bar{p} \gamma$	Skim selection of $B^- \rightarrow \Sigma^0 \bar{p} \gamma$
$B^- \rightarrow \Lambda \bar{p} \gamma$	1.65	3.19
$B^- \rightarrow \Sigma^0 \bar{p} \gamma$	1.48	3.56
$B^- \rightarrow \Lambda \bar{p} \pi^0$	1.46	2.75
$B^- \rightarrow \Sigma^0 \bar{p} \pi^0$	1.36	2.90
on peak data	1.50	2.77
off peak data	1.45	2.70

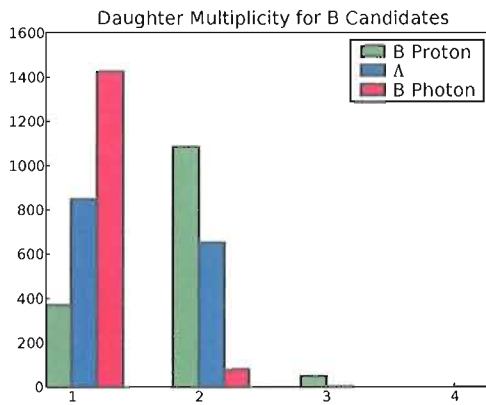
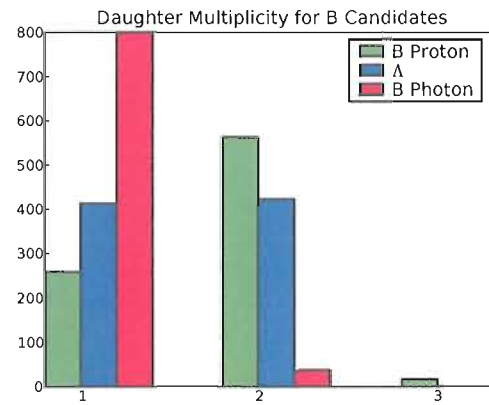
Tab. IV.7: Candidate Multiplicity after the skim

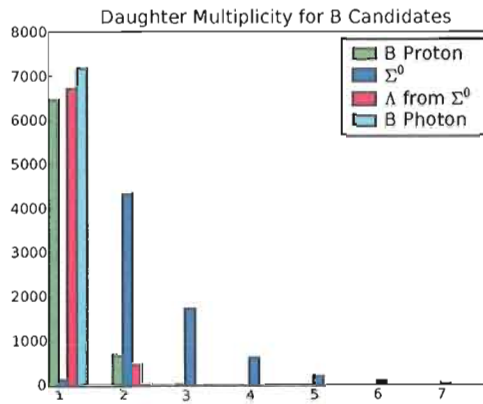
Sample	BtoLambdaPbarGamma cuts	BtoSigma0PbarGamma cuts
$B^- \rightarrow \Lambda \bar{p} \gamma$	1.01	1.65
$B^- \rightarrow \Sigma^0 \bar{p} \gamma$	1.01	2.02
$B^- \rightarrow \Lambda \bar{p} \pi^0$	1.01	1.73
$B^- \rightarrow \Sigma^0 \bar{p} \pi^0$	1.01	2.00
on peak data	1.03	1.56
off peak data	1.04	1.64

Tab. IV.8: Candidate Multiplicity after the cuts



(a) On Peak data

(b) $B^- \rightarrow \Lambda \bar{p} \gamma$ (c) $B^- \rightarrow \Sigma^0 \bar{p} \gamma$ Fig. IV.9: Daughter multiplicity in events with more than one B candidate – Reconstruction as $B^- \rightarrow \Lambda \bar{p} \gamma$



(a) On Peak data

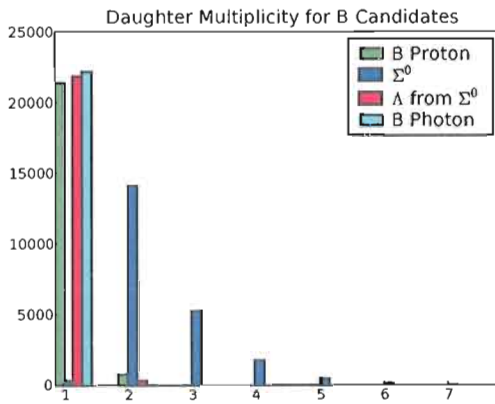
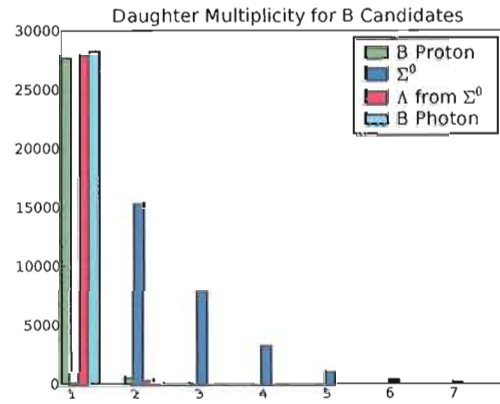
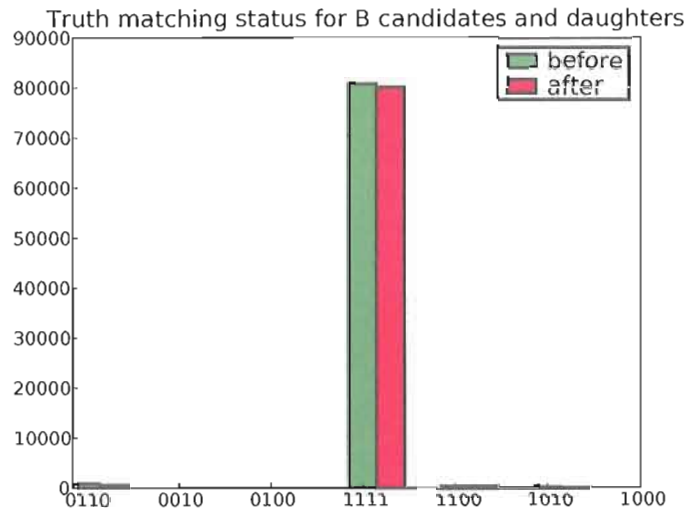
(b) $B^- \rightarrow \Lambda \bar{p} \gamma$ (c) $B^- \rightarrow \Sigma^0 \bar{p} \gamma$

Fig. IV.10: Daughter multiplicity in events with more than one B candidate – Reconstruction as $B^- \rightarrow \Sigma^0 \bar{p} \gamma$

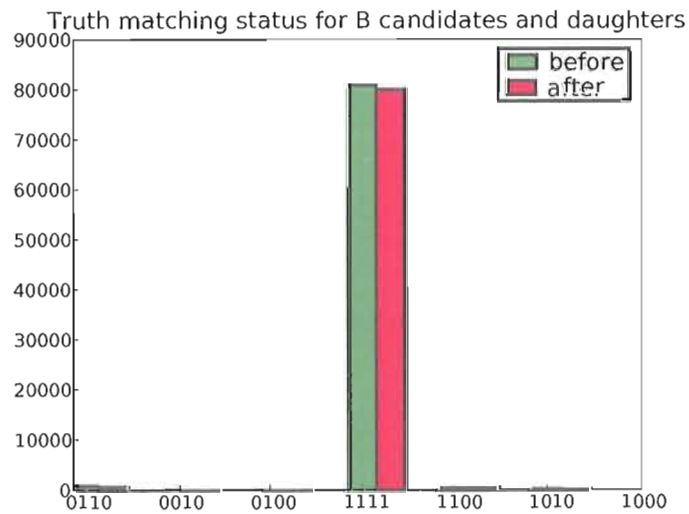
tion mode. The events reconstructed as $B^- \rightarrow \Sigma^0 \bar{p} \gamma$ show that candidate multiplicity is mainly due to a high multiplicity of Σ^0 candidates, mainly due to the low energy of the photon from the decay $\Sigma^0 \rightarrow \Lambda \gamma$. The following selection criteria were applied when there is more than one reconstructed B in the event: For $B^- \rightarrow \Lambda \bar{p} \gamma$ events the B candidate with the Λ daughter with the highest decay length significance is taken. For events reconstructed as $B^- \rightarrow \Sigma^0 \bar{p} \gamma$ the B candidate with the Σ^0 daughter with the mass closest to the PDG value is taken. This resolves the ambiguity in 100% of the cases for $B^- \rightarrow \Lambda \bar{p} \gamma$ and in 99.9% of the events for $B^- \rightarrow \Sigma^0 \bar{p} \gamma$. Any remaining ambiguity is resolved by selecting the B candidate with the highest lab energy of the photon. Using this method, 30204 out of the 46225 $B^- \rightarrow \Sigma^0 \bar{p} \gamma$ events after cuts contain a fully truth-matched B candidate. For the selection of $B^- \rightarrow \Lambda \bar{p} \gamma$, 80323 truth-matched candidates out of 81479 events are selected. Table IV.9 reviews the efficiencies of different selection criteria. Figures IV.11 and IV.12 show the efficiencies of different selection criteria on truth-matched candidates for $B^- \rightarrow \Lambda \bar{p} \gamma$ and $B^- \rightarrow \Sigma^0 \bar{p} \gamma$ events, respectively. The x-axis shows the different combinations of truth-matched candidates. The numbers are encodings of the different candidates, each position refers to a different candidate, 0 stands for a non-truth-matched candidate, 1 means the candidate has been truth-matched. The height of the bar graph shows how many candidates are truth-matched before and after the selection.

Variable	$B^- \rightarrow \Lambda \bar{p} \gamma$	$B^- \rightarrow \Sigma^0 \bar{p} \gamma$
highest photon CMS energy	0.991	0.525
highest photon lab energy	0.990	0.523
best composite baryon mass	0.992	0.653
highest Λ decay length significance	0.993	0.520

Tab. IV.9: Fraction of truth-matched events that are correctly selected by the best candidate selection



(a) highest photon CMS energy



(b) highest photon lab energy

Fig. IV.11: Best candidate selection criteria for $B^- \rightarrow \Lambda \bar{p} \gamma$ candidates. The bits in order are the truth matching flags for Lambda, Proton from B, Gamma from B, B candidate

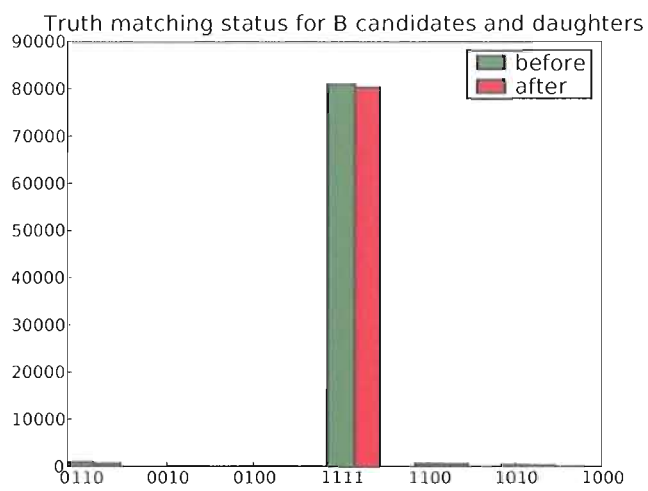
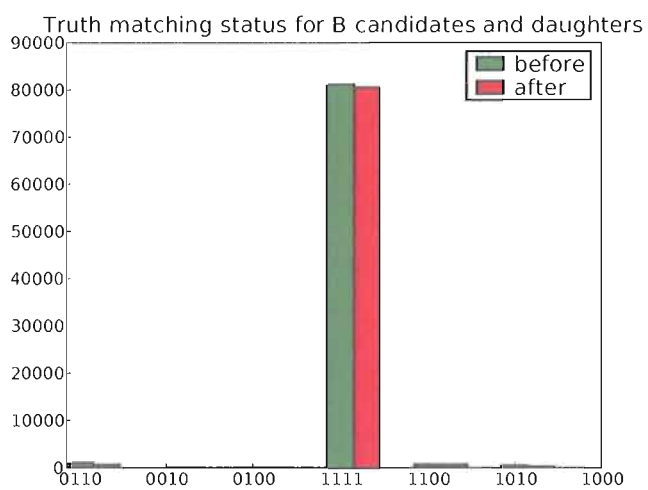
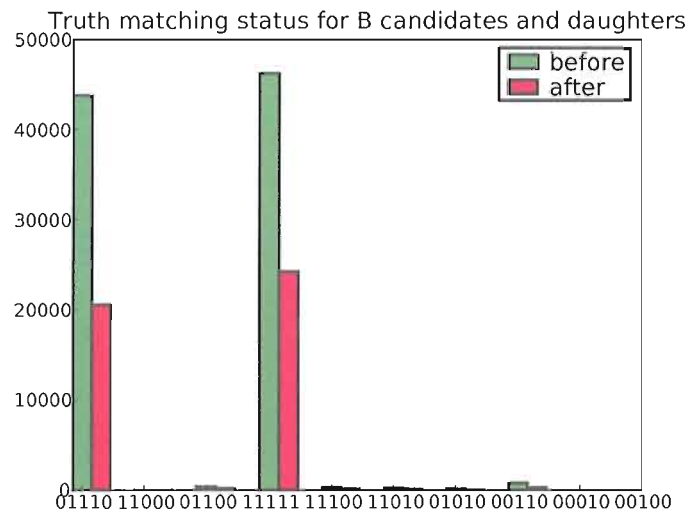
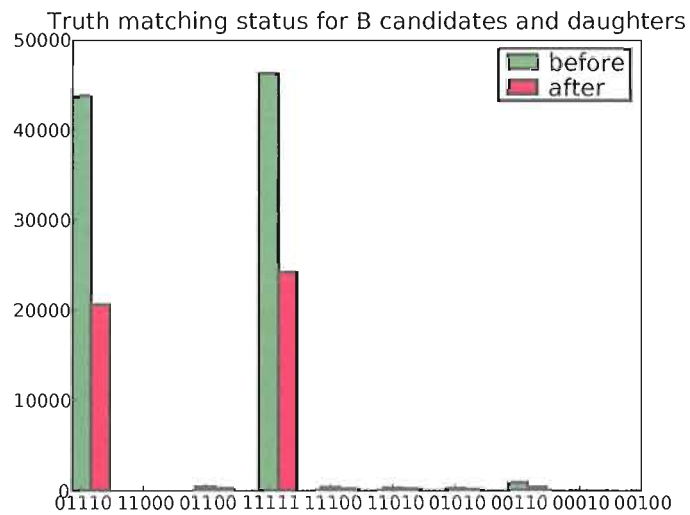
(c) best A mass(d) highest Λ decay significance

Fig. IV.11: continued

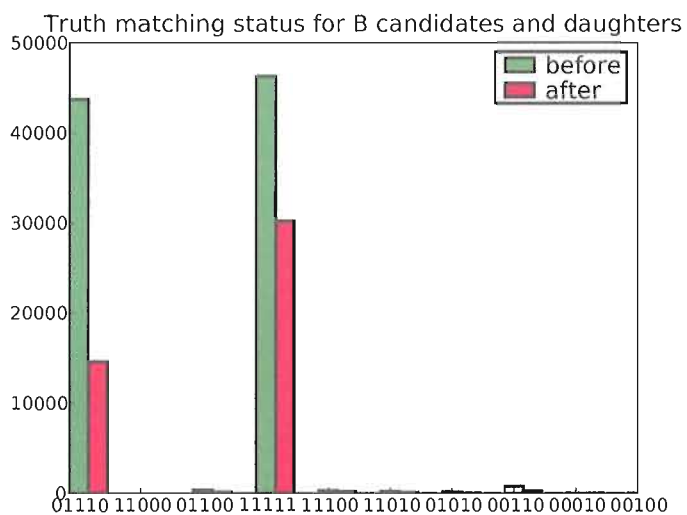
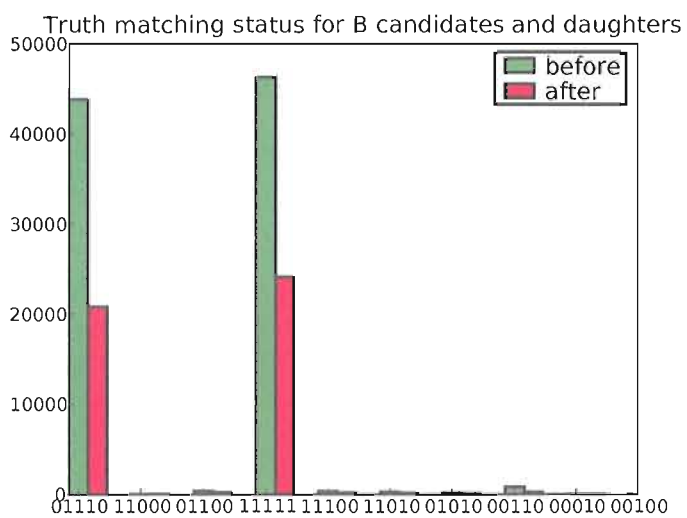


(a) highest photon CMS energy



(b) highest photon lab energy

Fig. IV.12: Best candidate selection criteria for $B^- \rightarrow \Sigma^0 \bar{p} \gamma$ candidates. The bits in order are the truth matching flags for Sigma, Lambda from Sigma, Proton from B, Gamma from B, B candidate

(c) best Σ^0 mass(d) Λ decay length significanceFig. IV.12: Best candidate selection criteria for $B^- \rightarrow \Sigma^0 \bar{p} \gamma$ candidates continued

Truth matching

In order to evaluate the best candidate selection, so-called truth matching has to be performed. This is the attempted matching of the simulated particle with a reconstructed particle candidate based on the sharing of underlying reconstructed hits and clusters. In order to be called a truth partner, this analysis requires final state particles to be matched with a simulated Object. For composite candidates, all reconstructed final states of the candidate are required to be matched. With this method, 15206 “true” $B^- \rightarrow \Sigma^0 \bar{p} \gamma$ candidates are found in 45471 simulated events that pass all cuts, and 78063 $B^- \rightarrow \Lambda \bar{p} \gamma$ simulated events out of 81479 are truth-matched.

IV.5 Fit Strategy

IV.5.1 Overview

The yields of the four different samples is obtained from a four-dimensional maximum likelihood fit. Events are split into two independent classes as described below, and the yields are computed for each class separately. One class of events contains only $B^- \rightarrow \Lambda \bar{p} \gamma$ candidates, the other class contains both a $B^- \rightarrow \Lambda \bar{p} \gamma$ and a $B^- \rightarrow \Sigma^0 \bar{p} \gamma$ candidate in each event. For each of the three sets of candidates, a separate parametrization of the four variables is chosen.

IV.5.2 Separation of the Samples

After the cut selection, the candidates can be split into the following categories, with a different parametrizations for each: single $B^- \rightarrow \Lambda \bar{p} \gamma$ candidates in the event, $B^- \rightarrow \Lambda \bar{p} \gamma$ candidates that appear in events together with a $B^- \rightarrow \Sigma^0 \bar{p} \gamma$ candidate, $B^- \rightarrow \Sigma^0 \bar{p} \gamma$ candidates that appear in events together with a $B^- \rightarrow \Lambda \bar{p} \gamma$ candidate. Because of the low signal to noise ratio, events that contain only a $B^- \rightarrow \Sigma^0 \bar{p} \gamma$ candidate are removed from the sample.

As a result of this classification, there are two classes of events: Those with only a $B^- \rightarrow \Lambda \bar{p} \gamma$ candidate and those with both a $B^- \rightarrow \Sigma^0 \bar{p} \gamma$ candidate as well as a $B^- \rightarrow \Lambda \bar{p} \gamma$ candidate. The yields for each class are obtained in separate fits. The events containing both candidates are handled in a simultaneous two-category fit and events containing only a $B^- \rightarrow \Lambda \bar{p} \gamma$ candidate are treated in a separate fit. The yields from the two classes of events are then combined to compute the branching fraction. The number of events in each class is shown in Table IV.10 and Table IV.11.

Sample	$B^- \rightarrow \Lambda \bar{p} \gamma$ only	$B^- \rightarrow \Sigma^0 \bar{p} \gamma$ only	both
light quarks	1071	872	1099
charm quarks	775	843	929
generic charged B	9	31	13
generic neutral B	13	37	19
$B^- \rightarrow \Lambda \bar{p} \gamma$ events	35191	2379	48424
$B^- \rightarrow \Sigma^0 \bar{p} \gamma$ events	6771	3428	43929
$B^- \rightarrow \Lambda \bar{p} \pi^0$ events	2855	688	4919
$B^- \rightarrow \Sigma^0 \bar{p} \pi^0$ events	1980	4659	13099

Tab. IV.10: Absolute number of events that pass the set of cuts for each reconstruction mode

Sample	$B^- \rightarrow \Lambda \bar{p} \gamma$ only	$B^- \rightarrow \Sigma^0 \bar{p} \gamma$ only	both
light quarks	1104	897	1134
charm quark	585	636	702
generic charged B	3	10	4
generic neutral B	3	12	6
$B^- \rightarrow \Lambda \bar{p} \gamma$ events	52	4	71
$B^- \rightarrow \Sigma^0 \bar{p} \gamma$ events	20	10	129
$B^- \rightarrow \Lambda \bar{p} \pi^0$ events	12	3	22
$B^- \rightarrow \Sigma^0 \bar{p} \pi^0$ events	2	4	11
on-peak data	2142	1915	2845

Tab. IV.11: Number of events that pass the set of cuts for each reconstruction mode, scaled to the integrated luminosity of the data sample

IV.5.3 Components

We attempt to model the data as follows: Four “peaking” components, $B^- \rightarrow \Lambda \bar{p} \gamma$, $B^- \rightarrow \Sigma^0 \bar{p} \gamma$, $B^- \rightarrow \Lambda \bar{p} \pi^0$ and $B^- \rightarrow \Sigma^0 \bar{p} \pi^0$ are added to a “continuum” of mixed background events: $u\bar{u}$, $d\bar{d}$, $s\bar{s}$, $c\bar{c}$ and generic B decays. This is possible, because as figure IV.13 shows, the generic B component does not peak strongly in the mass of the reconstructed B candidate.

IV.5.4 Variables

The following variables are used as ingredients in the fit because of their discriminative power.

$m_{\text{rec.}}$ the reconstructed candidate mass

$m_{\text{miss.}}$ the invariant mass of the event excluding the reconstructed candidate, with a mass constraint on the reconstructed candidate $m_{\text{rec.}} \equiv m_{\text{B}}^{\text{PDG}}$

L_2/L_0 the ratio of the Legendre Moments L_2/L_0

best m_{π^0} the photon of the $b \rightarrow s\gamma$ decay is combined with every other photon in the event that is not part of the reconstructed decay. The invariant mass of the photon-pair that is closest to the nominal value of the mass of a π^0 meson is retained. Because of the abundance of photons in any given event that make it too likely to find a good π^0 candidate, a cut of $E_{\text{lab}} > 70\text{MeV}$ is placed on the pion candidate. Plots of this variable for $B^- \rightarrow \Lambda \bar{p} \gamma$ and $B^- \rightarrow \Lambda \bar{p} \pi^0$ events are shown in Figure IV.14. Selection of the “best” candidate could introduce a potential bias in the selection of backgrounds. The fact that this is not the case is shown in Figure IV.15

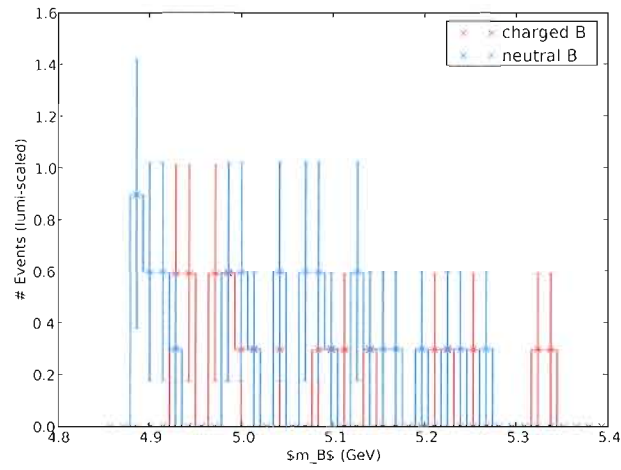
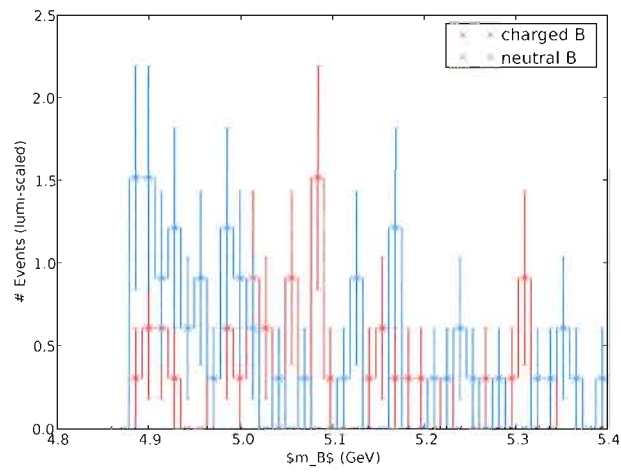
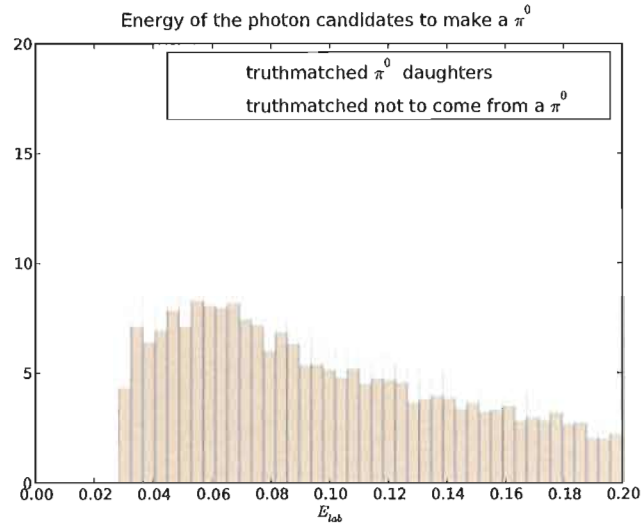
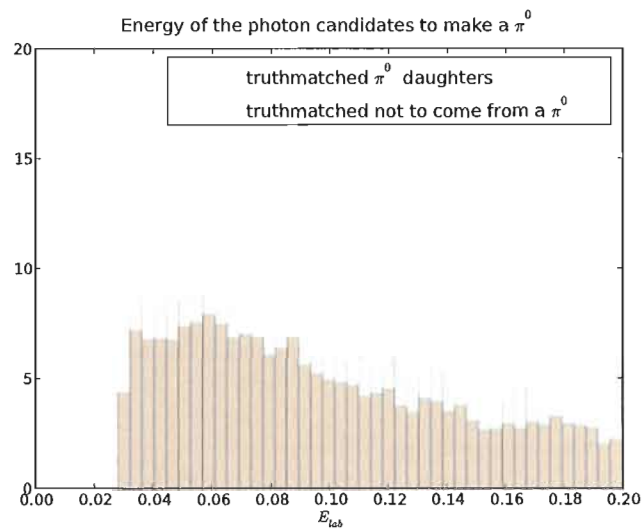
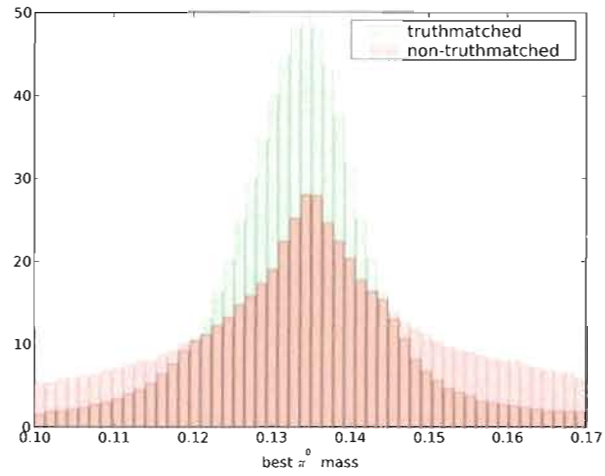
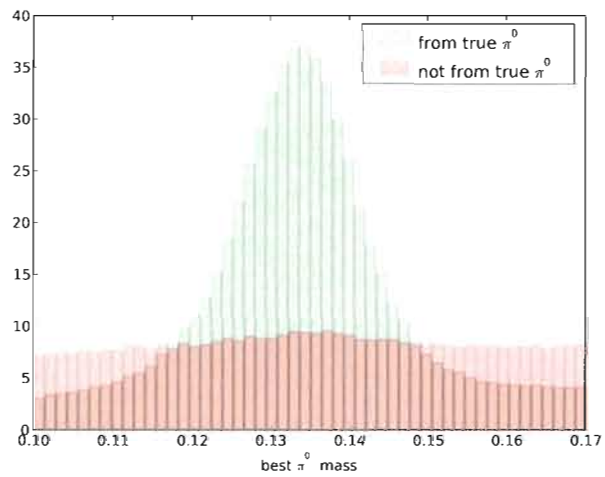
(a) $B^- \rightarrow \Lambda \bar{p} \gamma$ (b) $B^- \rightarrow \Sigma^0 \bar{p} \gamma$

Fig. IV.13: Generic B component in m_{rec} , scaled to the integrated luminosity of the data sample

(a) $B^- \rightarrow \Lambda \bar{p} \gamma$ (b) $B^- \rightarrow \Lambda \bar{p} \pi^0$ Fig. IV.14: Lab energy of the photon to make the π^0 candidate



(a) without minimum energy cut



(b) with minimum energy cut

Fig. IV.15: Best π^0 mass for true π^0 candidates and for random combinations of photons

Legendre Moments

For all samples containing B mesons this variable is modeled with a Cruijff shape, which is a bifurcated Gaussian with tail parameter for each side.

$$f_{\text{Cruijff}}(x) := \exp \left[-\frac{(x - m)^2}{2\sigma_{\pm}^2 + \alpha_{\pm}(x - m)^2} \right], \quad (\text{IV.3})$$

where $+$ ($-$) corresponds to $x - m > 0$ ($x - m < 0$). The background sample in each category is modeled with a fourth-order polynomial.

Best π^0 mass

The best π^0 mass in $B^- \rightarrow \Lambda \bar{p} \pi^0$, $B^- \rightarrow \Sigma^0 \bar{p} \pi^0$ and background events is modeled with a Gaussian peak, with an additional Cruijff shape component for combinatorial backgrounds. Unlike the other variables, the best π^0 mass for these three samples is modeled on a sample of data events that lies outside of the region that contains the signal events. The same shape is used consistently for these three samples.

For $B^- \rightarrow \Lambda \bar{p} \gamma$ and $B^- \rightarrow \Sigma^0 \bar{p} \gamma$ candidates, the shape of this variable is also parametrized with a Cruijff shape. However, there appears to be a turn-on effect, i.e., the efficiency for low values of this variable is steeper than closer to the peak, so that a single Gaussian-like shape cannot model the data over the whole range. The turn-on is modeled with a Fermi function.

$$f(x) := [1 - 1/(\exp((x - a)/b))]^2$$

Shapes with this turn-on are implemented as piecewise functions, with the point of switch a parameter of the fit.

$$f(x; a) := \begin{cases} \text{fermi}(x) & x < a \\ \text{Cruijff}(x) & x \geq a \end{cases}$$

A turn-off is modeled in analogous fashion.

Reconstructed Candidate Mass

Since embedded toy studies show that an attempt to parametrize the shape as a product of one-dimensional functions resembles the data poorly (see Appendix fig. E.3), the variables $m_{\text{rec.}}$ and $m_{\text{miss.}}$ for the samples $B^- \rightarrow \Lambda \bar{p} \gamma$ and $B^- \rightarrow \Sigma^0 \bar{p} \gamma$ are better modeled with a two-dimensional pdf whose shape is taken from the binned Monte Carlo samples (2D HistPdf). This shape is chosen for events for both candidates in each event in these samples.

For the $B^- \rightarrow \Lambda \bar{p} \pi^0$ and $B^- \rightarrow \Sigma^0 \bar{p} \pi^0$ samples, the shape of choice is the Cruijff function. The background of continuum events is modeled with a polynomial of 2nd order, because those events do not contain B mesons, for which this variable would peak.

Missing Mass

For light quark (u,d,s,c) events $m_{\text{miss.}}$ is modeled with the ‘‘ARGUS’’ shape(34)

$$f_{\text{ARGUS}}(x) := x \sqrt{1 - \left(\frac{x}{c}\right)^2} \exp\left(-\chi \left(1 - \left(\frac{x}{c}\right)^2\right)\right),$$

where c is a cutoff parameter and χ describes the curvature. For the two species containing a π^0 , this variable is modeled with the Cruijff function.

IV.5.5 Summary of Fit Shapes

In each event, a $B^- \rightarrow \Lambda \bar{p} \gamma$ candidate and a $B^- \rightarrow \Sigma^0 \bar{p} \gamma$ candidate is being reconstructed. For some events, only one of the candidates survives the cuts, other events still contain both candidates. (Events in which both candidates fail one cut are dropped from consideration for obvious reasons).

Events Containing Only $B^- \rightarrow \Lambda \bar{p} \gamma$ Candidates

The four variables of $B^- \rightarrow \Lambda \bar{p} \gamma$ candidates in events where the $B^- \rightarrow \Sigma^0 \bar{p} \gamma$ candidate fails the cuts are parametrized with the shapes summarized in Table IV.12. Figures IV.16, IV.17, IV.18 and IV.19 visualize the maximum-likelihood fit of these parameterizations to the simulated samples and the they were fit to. In other words the points represent the simulated samples and the continuous line is the maximum likelihood fit to that sample. Since the four-dimensional fit is composed of a product of four one-dimensional samples, the figures can be interpreted as one-dimensional. In the variables $m_{\text{rec.}}$ and $m_{\text{miss.}}$, the figures, however, are projections of the two-dimensional shape to the respective variable.

$B^- \rightarrow \Lambda \bar{p} \gamma$ Candidates in Events That Also Contain a $B^- \rightarrow \Sigma^0 \bar{p} \gamma$ Candidate

The sample of events containing only $B^- \rightarrow \Lambda \bar{p} \gamma$ candidates apparently looks different from events containing also a $B^- \rightarrow \Sigma^0 \bar{p} \gamma$ candidate. Therefore these events are

Sample	$m_{\text{rec.}}$	$m_{\text{miss.}}$	m_{π^0}	L_2/L_0
$B^- \rightarrow \Lambda \bar{p} \gamma$	40×40	40×40	Cruijff	Cruijff
$B^- \rightarrow \Sigma^0 \bar{p} \gamma$	2d hist	2d hist	w/ Fermi	
$B^- \rightarrow \Lambda \bar{p} \pi^0$	Cruijff		Gauss+Cruijff	
$B^- \rightarrow \Sigma^0 \bar{p} \pi^0$	Cruijff			
background	Chebychev	Argus	Gauss+Cruijff	

Tab. IV.12: Pdf parametrization for events containing only a $B^- \rightarrow \Lambda \bar{p} \gamma$ candidate

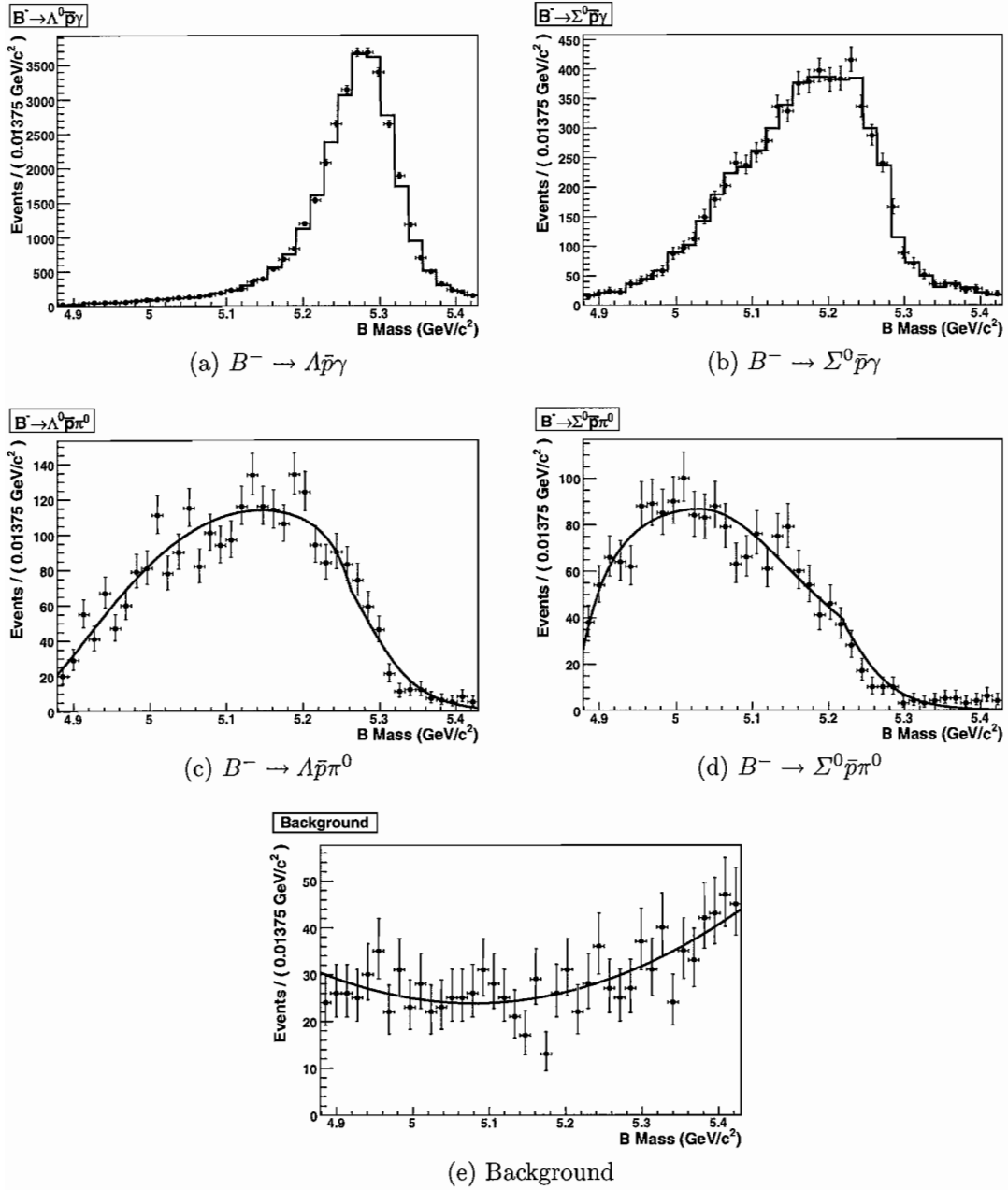


Fig. IV.16: Parametrization of the reconstructed mass for $B^- \rightarrow \Lambda \bar{p} \gamma$ candidates

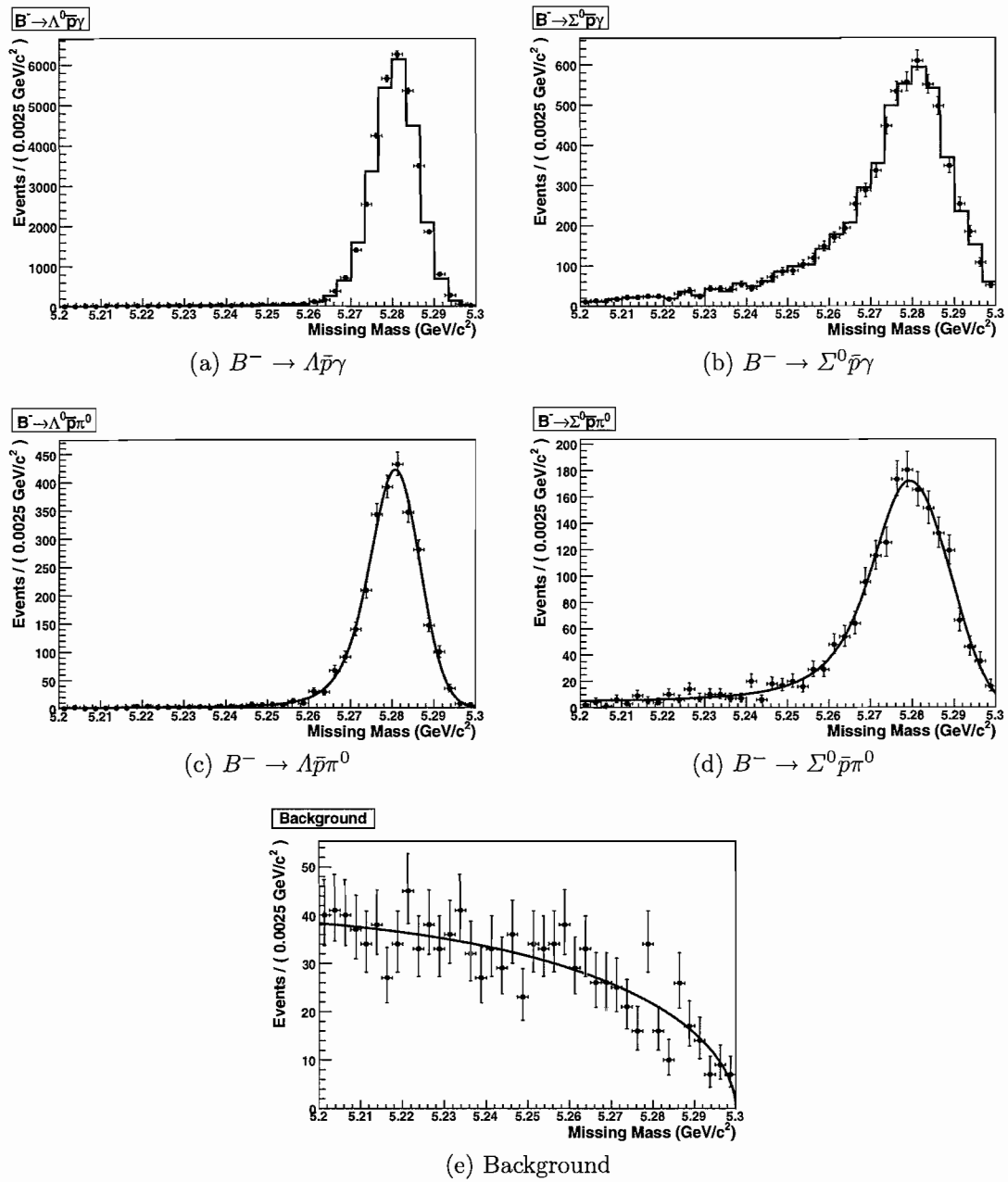


Fig. IV.17: Parametrization of the missing mass for $B^- \rightarrow \Lambda \bar{p} \gamma$ candidates

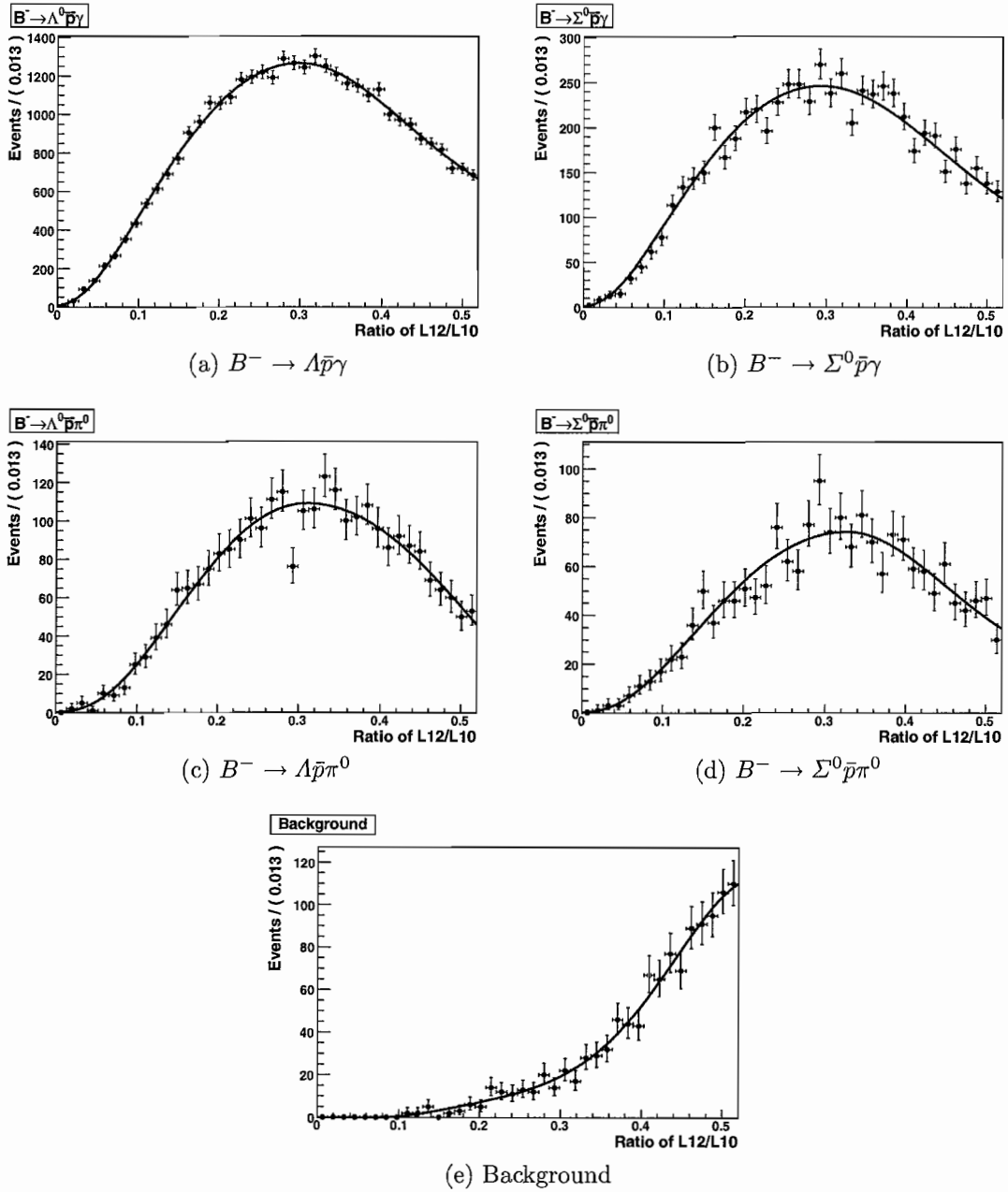


Fig. IV.18: Parametrization of the ratio of the Legendre moments for $B^- \rightarrow \Lambda \bar{p} \gamma$ candidates

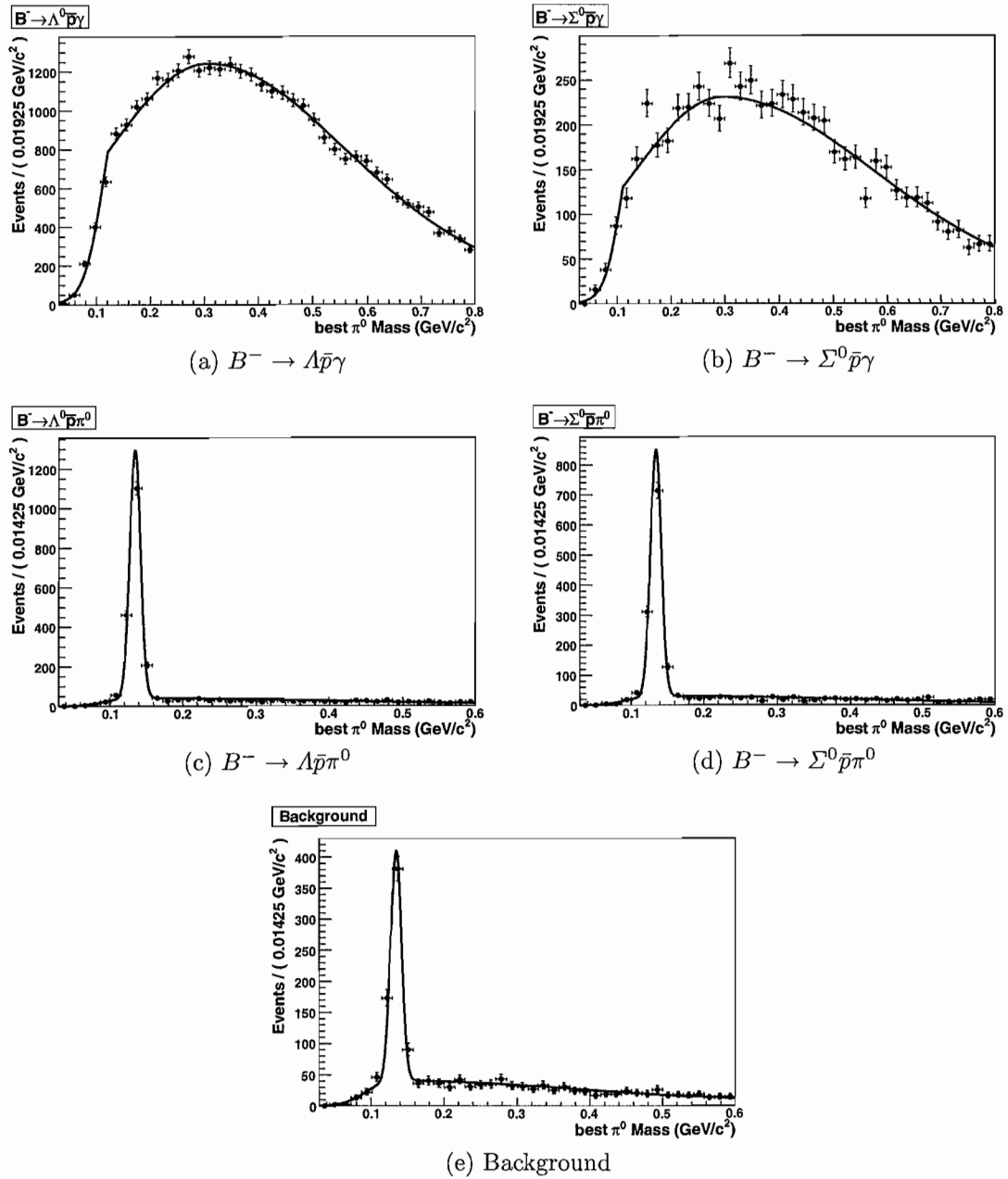


Fig. IV.19: Parametrization of the best π^0 mass for $B^- \rightarrow \Lambda \bar{p} \gamma$ candidates

parametrized differently, as summarized in Table IV.13. Figures IV.20, IV.21, IV.22 and IV.23 visualize the maximum-likelihood fit of these shapes to the simulated samples.

$B^- \rightarrow \Sigma^0 \bar{p} \gamma$ Candidates in Events That Also Contain a $B^- \rightarrow \Lambda \bar{p} \gamma$ Candidate

The choice of parametrizations for $B^- \rightarrow \Sigma^0 \bar{p} \gamma$ candidates is the same as for $B^- \rightarrow \Lambda \bar{p} \gamma$ candidates in the same events and summarized in Table IV.13. Figures IV.24, IV.25, IV.26, IV.27 visualize the projection of the four-dimensional shape to the respective variables.

IV.5.6 Combined Fit Strategy to Extract Yields

Events that contain both $B^- \rightarrow \Lambda \bar{p} \gamma$ and $B^- \rightarrow \Sigma^0 \bar{p} \gamma$ candidates are fit as follows: The data for each candidate is augmented with a category indicating the flavor. The pdf to fit to the data point is then chosen by the category. Thus each event is represented by two data points, x and y , corresponding to the $B^- \rightarrow \Lambda \bar{p} \gamma$ and $B^- \rightarrow \Sigma^0 \bar{p} \gamma$ candidates, respectively. The negative log-likelihood function is

$$-\mathcal{L}(\mathbf{N}; \theta^1, \theta^2) = -\ln L(\mathbf{N}; \theta^1, \theta^2) \quad (\text{IV.4})$$

$$= \sum_j n_j - \sum_{i=1}^N \ln \left[\sum_{j=1}^5 n_j (f_j(x_i; \theta_j^1) * g_j(y_i; \theta_j^2)) \right] \quad (\text{IV.5})$$

Sample	$m_{\text{rec.}}$	$m_{\text{miss.}}$	m_{π^0}	L_2/L_0
$B^- \rightarrow \Lambda \bar{p} \gamma$	40×40	40×40	Cruiff	Cruiff
$B^- \rightarrow \Sigma^0 \bar{p} \gamma$	2d hist	2d hist	w/ Fermi	
$B^- \rightarrow \Lambda \bar{p} \pi^0$	Cruiff		Gauss+Cruiff	4th order polynomial
$B^- \rightarrow \Sigma^0 \bar{p} \pi^0$	Cruiff		Gauss+Cruiff	
background	Chebychev w/ Fermi	Argus	Gauss+Cruiff	

Tab. IV.13: Pdf parametrization for events with two candidates

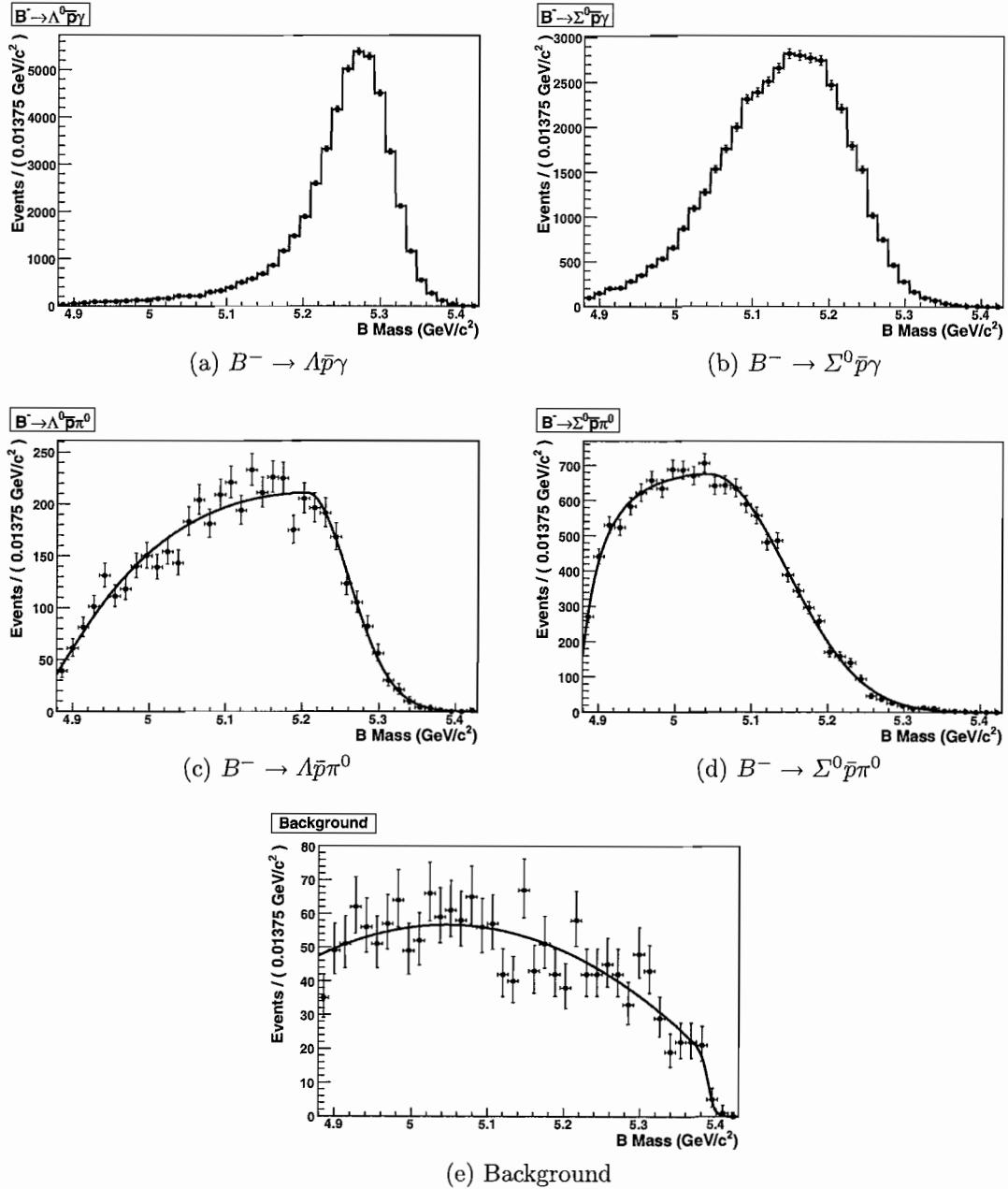


Fig. IV.20: Parametrization of the reconstructed mass of different samples reconstructed as $B^- \rightarrow \Lambda \bar{p} \gamma$ in events also containing a $B^- \rightarrow \Sigma^0 \bar{p} \gamma$ candidate.

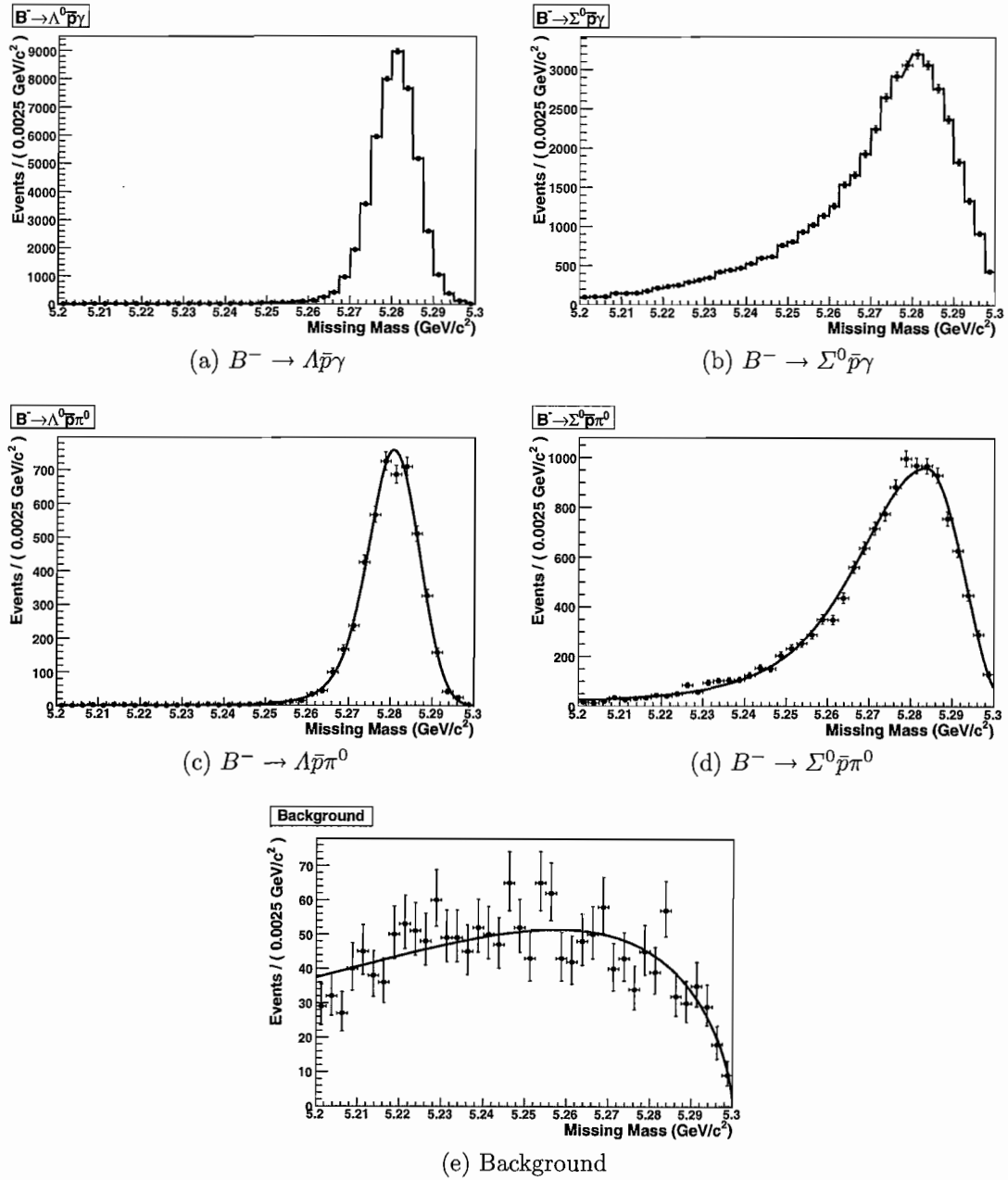


Fig. IV.21: Parametrization of the missing mass of different samples reconstructed as $B^- \rightarrow \Lambda \bar{p} \gamma$ in events also containing a $B^- \rightarrow \Sigma^0 \bar{p} \gamma$ candidate.

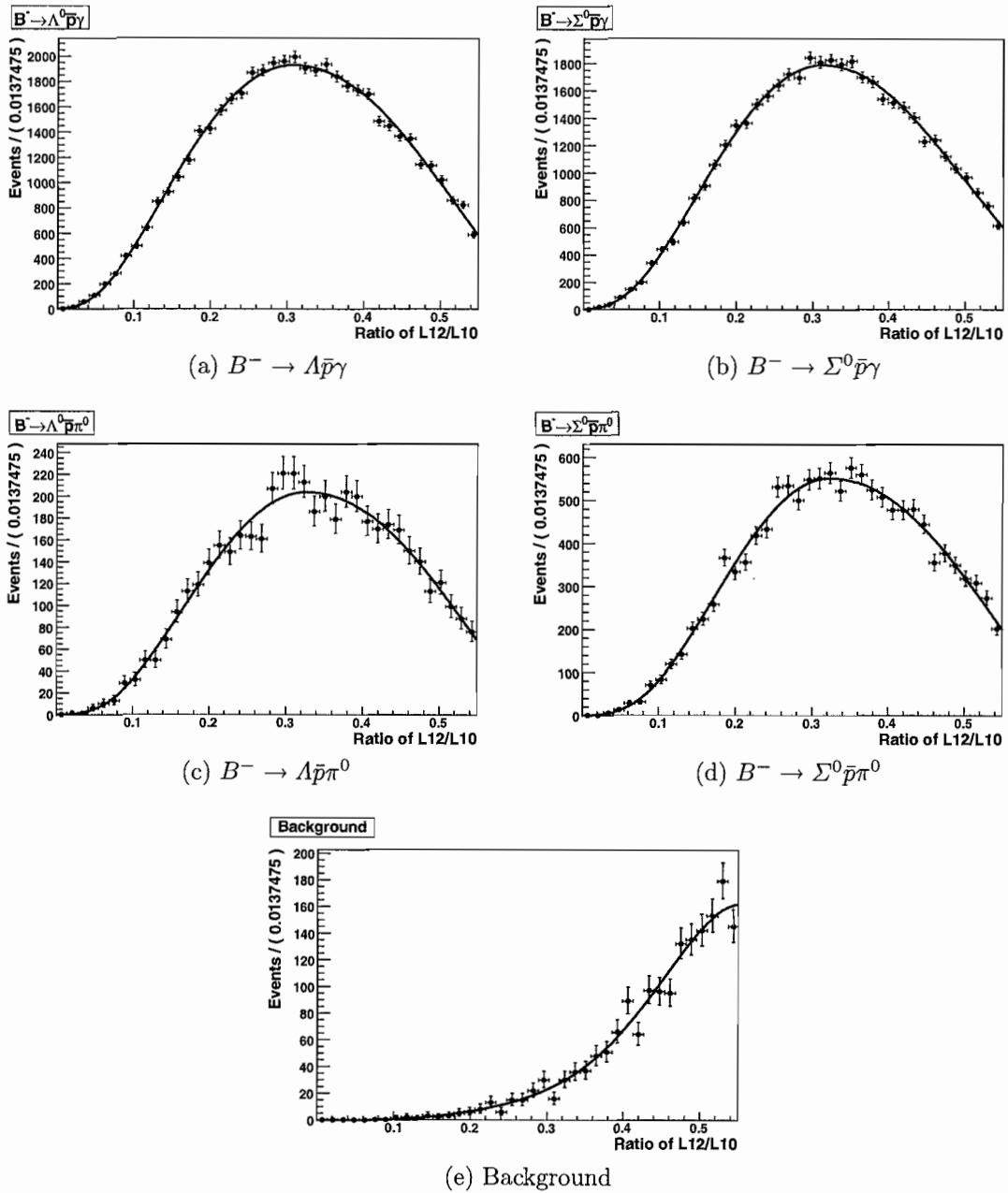


Fig. IV.22: Parametrization of the ratio of the Legendre moments L_2/L_0 of different samples reconstructed as $B^- \rightarrow \Lambda \bar{p} \gamma$ in events also containing a $B^- \rightarrow \Sigma^0 \bar{p} \gamma$ candidate.

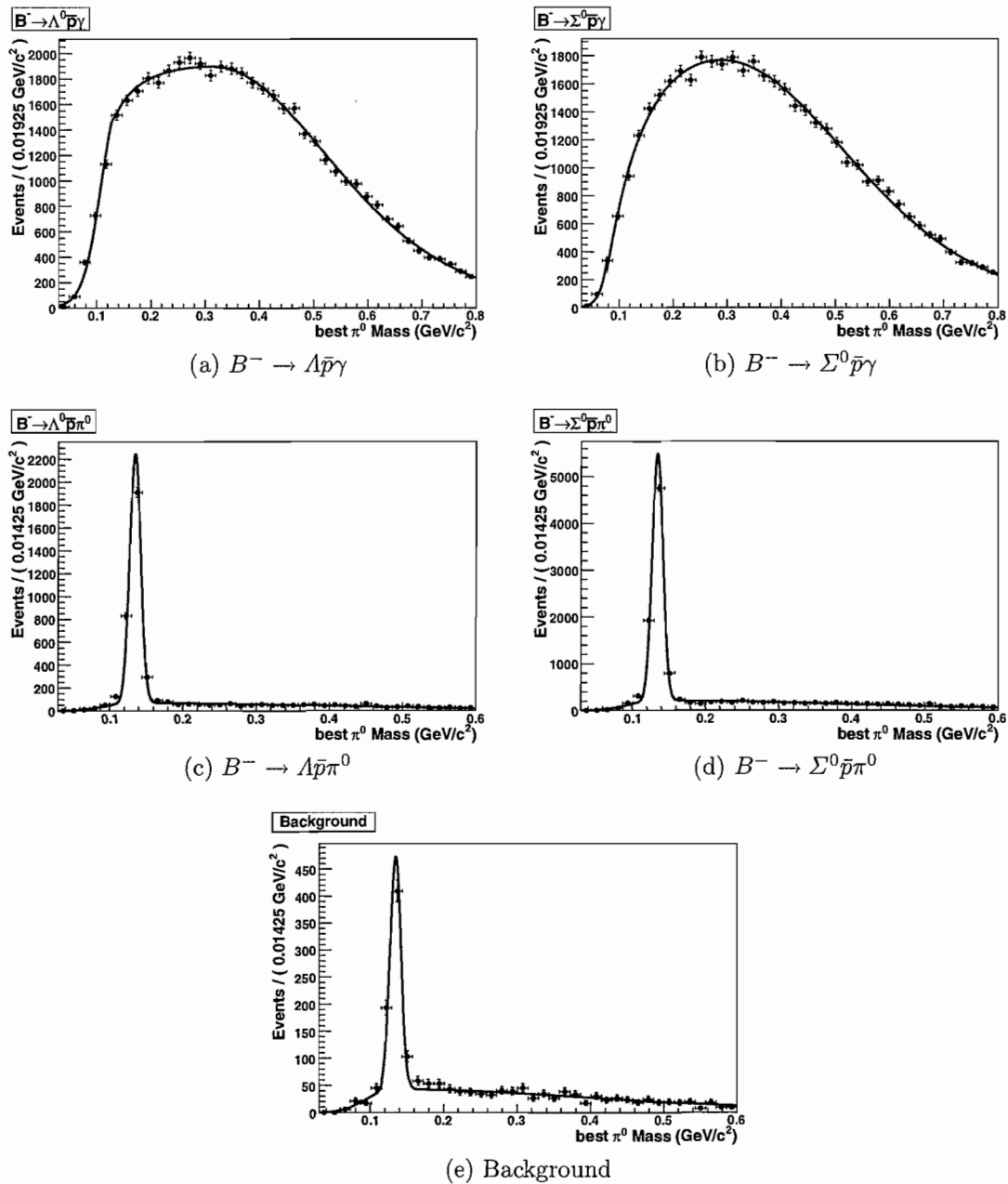


Fig. IV.23: Parametrization of the best π^0 mass of different samples reconstructed as $B^- \rightarrow \Lambda \bar{p} \gamma$ in events also containing a $B^- \rightarrow \Sigma^0 \bar{p} \gamma$ candidate.

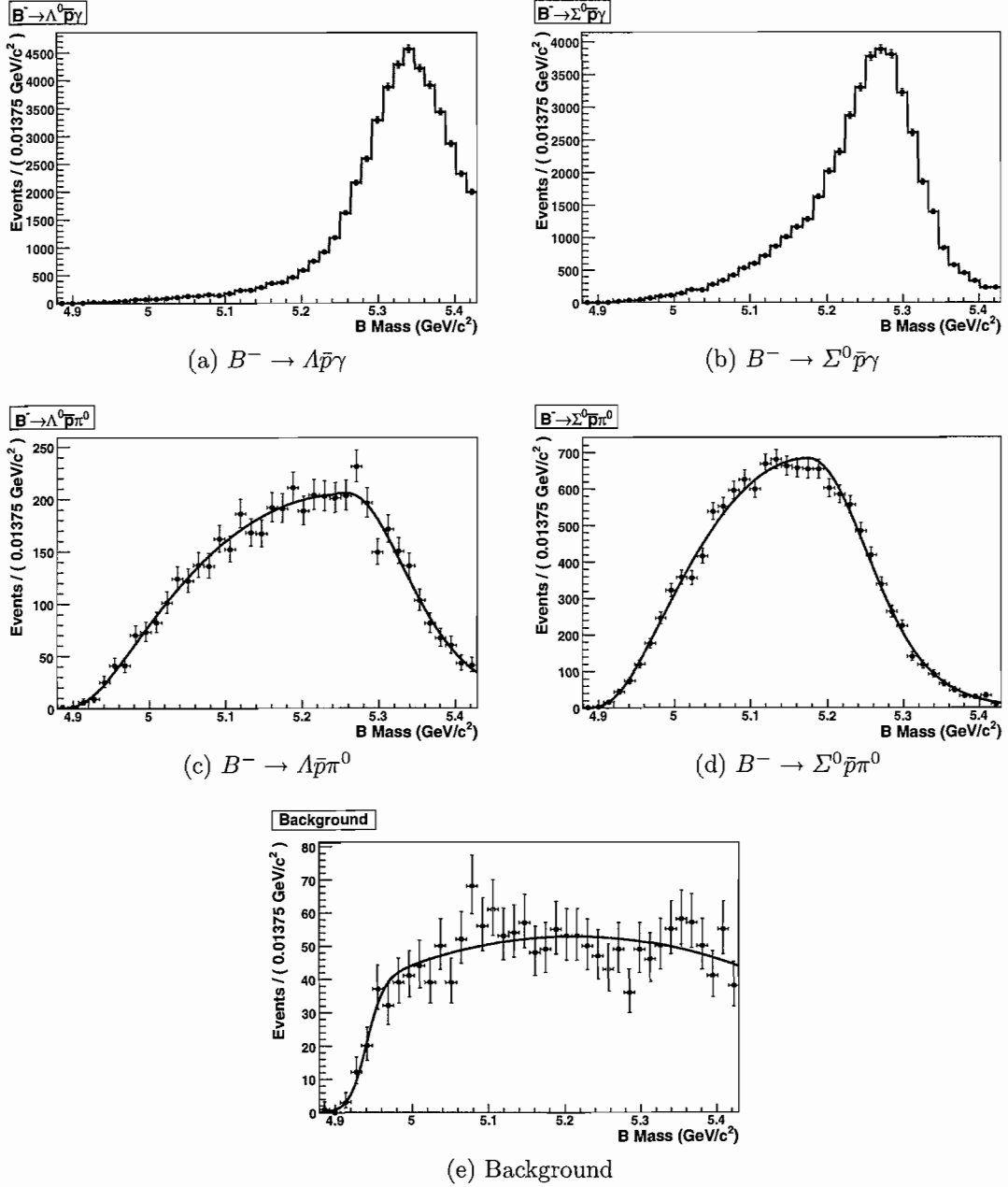


Fig. IV.24: Parametrization of the reconstructed mass of different samples reconstructed as $B^- \rightarrow \Sigma^0 \bar{p} \gamma$ in events also containing a $B^- \rightarrow \Lambda \bar{p} \gamma$ candidate.

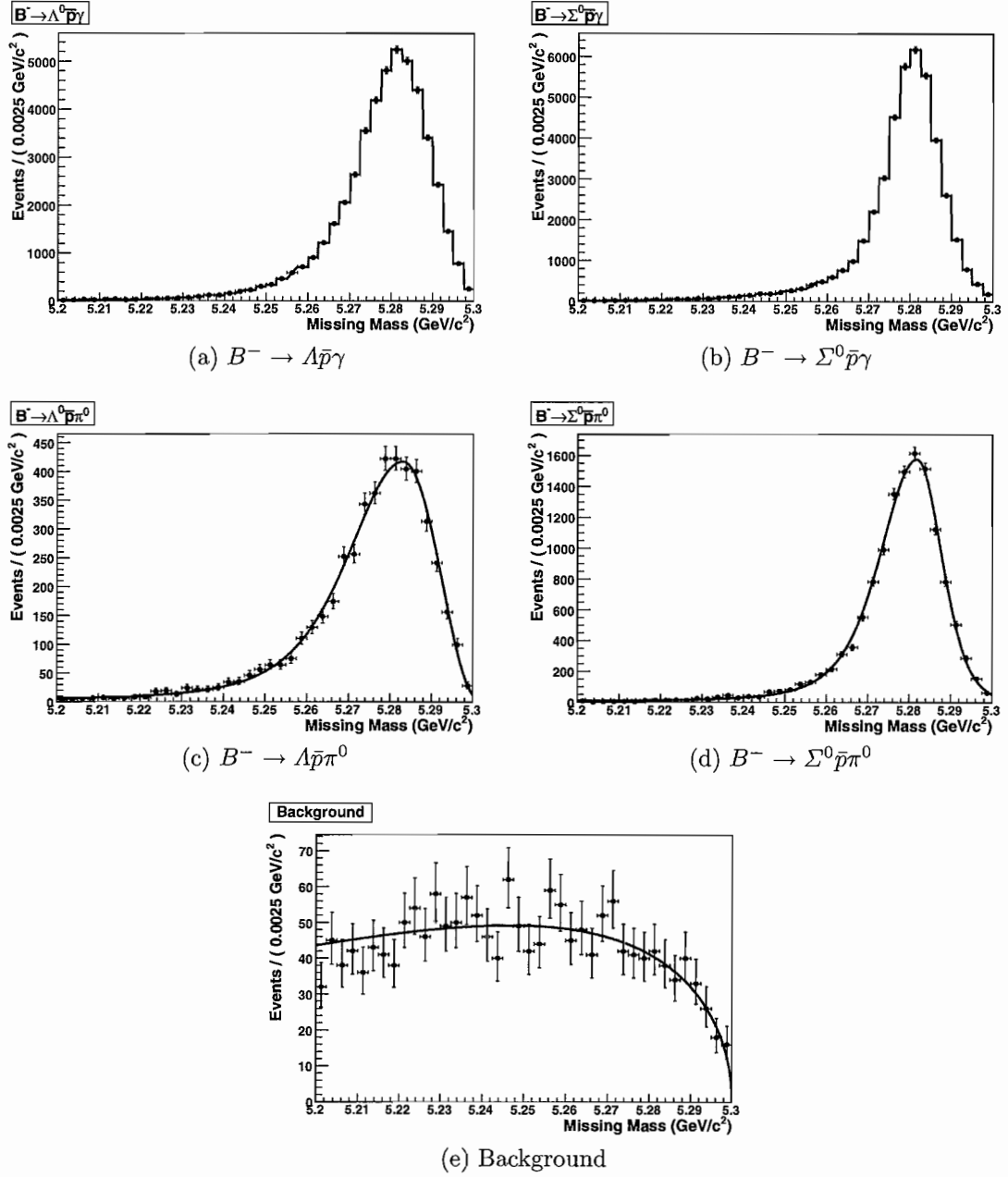


Fig. IV.25: Parametrization of the missing mass of different samples reconstructed as $B^- \rightarrow \Sigma^0 \bar{p} \gamma$ in events also containing a $B^- \rightarrow \Lambda \bar{p} \gamma$ candidate.

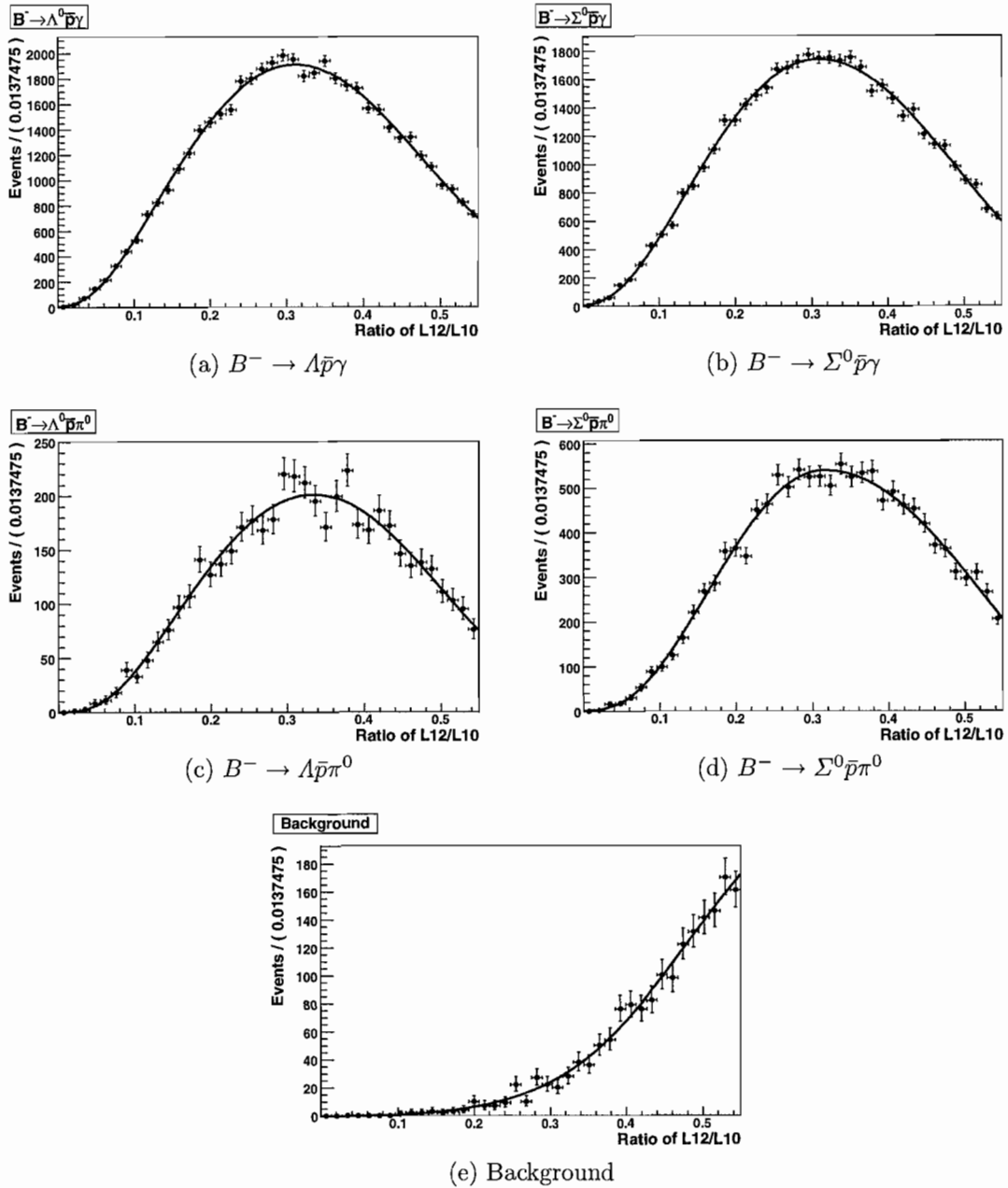


Fig. IV.26: Parametrization of the ratio of the Legendre moments L_2/L_0 of different samples reconstructed as $B^- \rightarrow \Sigma^0 \bar{p} \gamma$ in events also containing a $B^- \rightarrow \Lambda \bar{p} \gamma$ candidate.

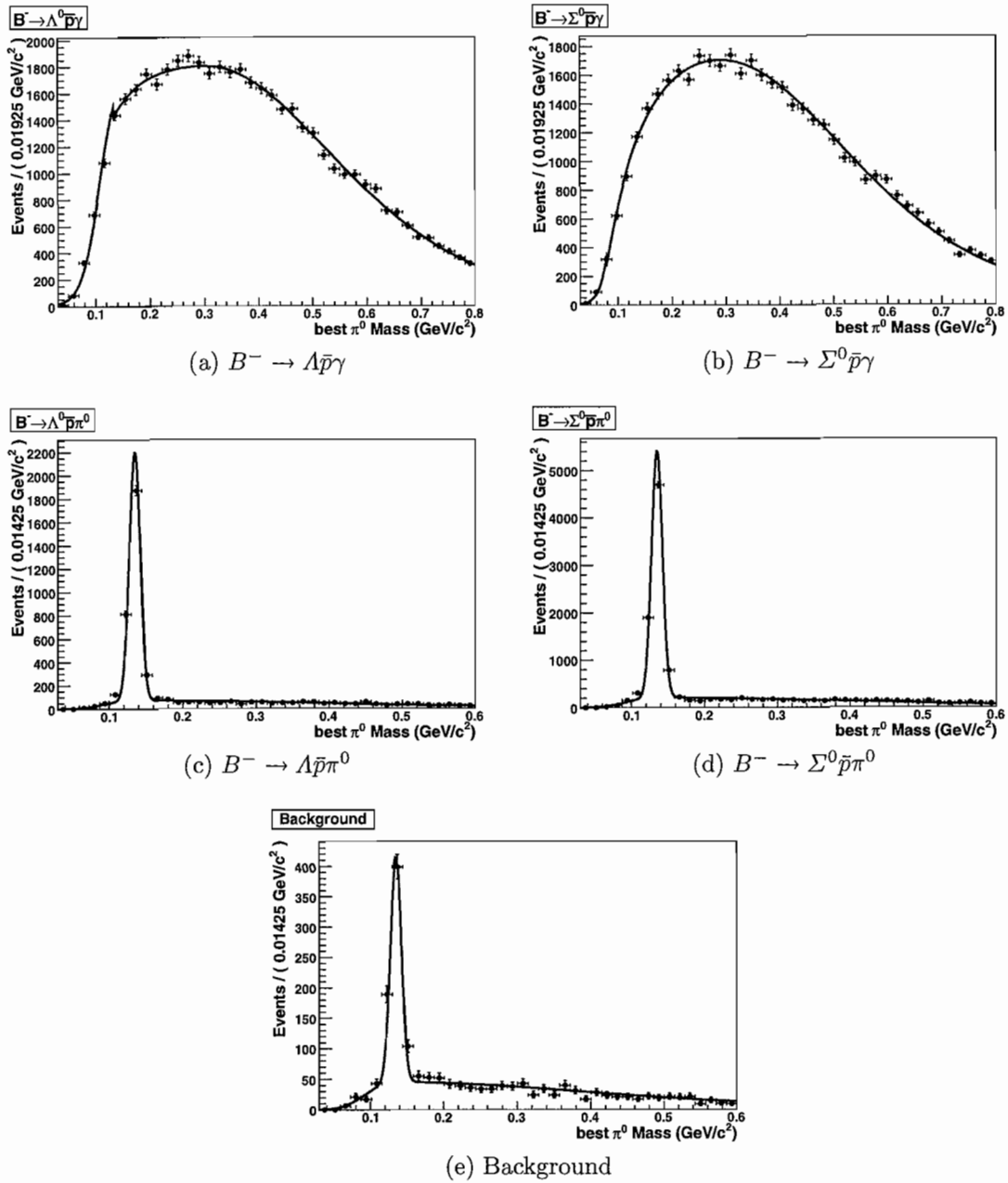


Fig. IV.27: Parametrization of the best π^0 mass of different samples reconstructed as $B^- \rightarrow \Sigma^0 \bar{p} \gamma$ in events also containing a $B^- \rightarrow \Lambda \bar{p} \gamma$ candidate.

with the additional constraint that $\sum_j n_j = N$, where j denotes the component, f and g are the pdf for the $B^- \rightarrow \Lambda \bar{p} \gamma$ and $B^- \rightarrow \Sigma^0 \bar{p} \gamma$ candidates, respectively, and θ^1 and θ^2 are the parameters for f and g and are fixed in the fit, while the yields n_j are floating. There is a subtlety in the definition of the likelihood in that the pdf is not properly normalized because of correlations between the fit variables. This is handled in Section IV.5.8. Events that only contain a $B^- \rightarrow \Lambda \bar{p} \gamma$ candidate are treated in a separate fit, which results in a separate set of yields m_j . The results from the two fits will then be combined as independent measurements to determine the branching fractions.

IV.5.7 Toy Studies

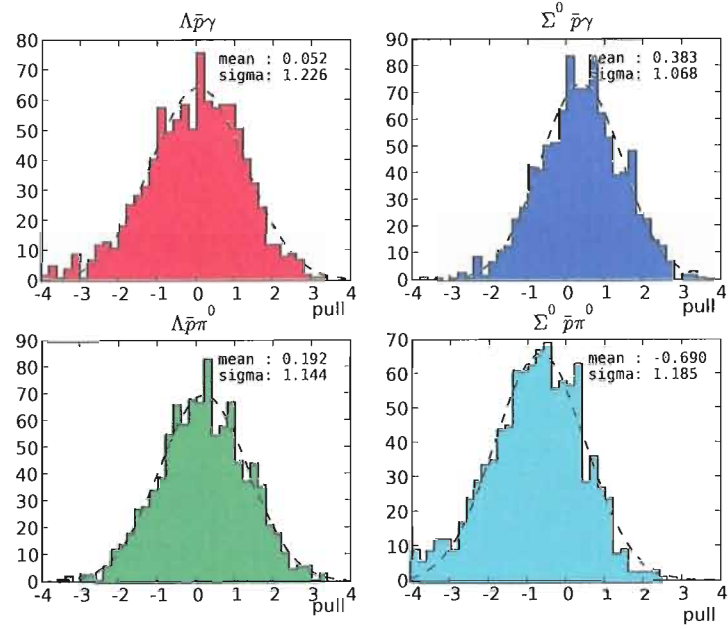
For the purpose of studying the stability of the fit, a number of so called toy Monte Carlo experiments is performed. In each experiment, the expected number of events are generated from the fitted pdf. An independent fit is then performed on the generated sample. The number of events generated in each experiment follows a Poisson distribution. The mean values for the $B^- \rightarrow \Lambda \bar{p} \gamma$ and $B^- \rightarrow \Sigma^0 \bar{p} \gamma$ events are on the order of the expected numbers in the data sample after all cuts, using Table IV.2 as reference. The number for the background component was taken to be the number of data events after cuts. The parameters of the pdfs used to generate the simulated events are obtained from a fit to Monte Carlo events for both $B^- \rightarrow \Lambda \bar{p} \gamma$ and $B^- \rightarrow \Sigma^0 \bar{p} \gamma$, as well as $B^- \rightarrow \Lambda \bar{p} \pi^0$ and $B^- \rightarrow \Sigma^0 \bar{p} \pi^0$, while the background components were obtained from a fit to a sample of light quark and generic B background. In each cycle of generating and fitting, the number of generated events was varied according to a Poisson distribution. The parameters for all five pdfs were fixed, while the yields are free parameters in the fit.

Embedded Toys

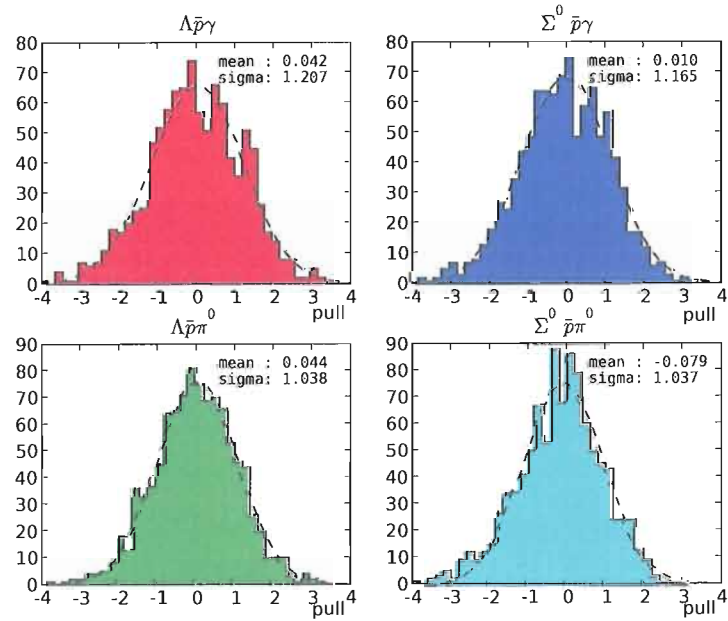
Instead of generating events from the fitted pdf, events can also be read in from the existing samples. This technique known as an “embedded toy study” is used to test how well the pdf models the simulated data. For a set of 1000 experiments each, the number of embedded events is varied around the number of expected events following a Poisson distribution. In these experiments, the background is sampled from the pdf shape described above. For each of the peaking mode, the expected number of events is taken from the simulated samples and embedded in this background. The pull is defined as $\hat{x} - \hat{x}_i / \sqrt{\sigma_i^2 - \sigma^2}$, where \hat{x} is the expected number of events, \hat{x} is the yield of experiment i , σ_i is the fit error of experiment i and σ is the statistical error on \hat{x} . Figure IV.28 shows pure and embedded toys for the simultaneous fit, while Figure IV.29 and Figure IV.30 show the validation for each of the components. Figure IV.31 shows the result of the toys for events that contain only a $B^- \rightarrow \Lambda \bar{p} \gamma$ candidate.

IV.5.8 Errors

In the simultaneous fit there are strong correlations between the variables used in the reconstruction of $B^- \rightarrow \Lambda \bar{p} \gamma$ and $B^- \rightarrow \Sigma^0 \bar{p} \gamma$. In order to evaluate the error from the likelihood, 1000 toy experiments are carried out. The distributions of the yield from these experiments are fit with a Gaussian distribution. The distribution of the errors on the fit are also fit with a Gaussian distribution. If the errors on a parameter from the likelihood fit are sensible, they should be comparable to the width of a Gaussian distribution of that parameter. Table IV.14 shows the mean and width for the yields and their errors from 1000 embedded toy fits. For comparison Table IV.15 shows the correlation coefficients for each of the peaking Monte Carlo data samples. If the error

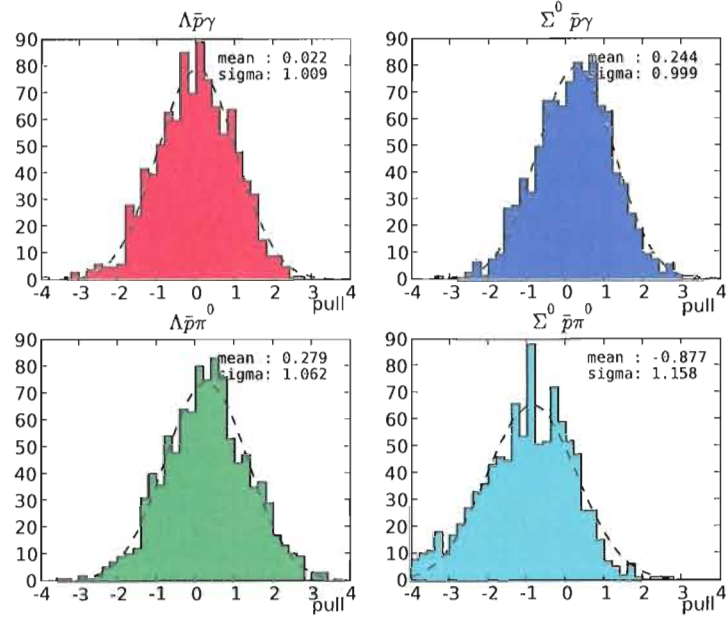


(a) embedded

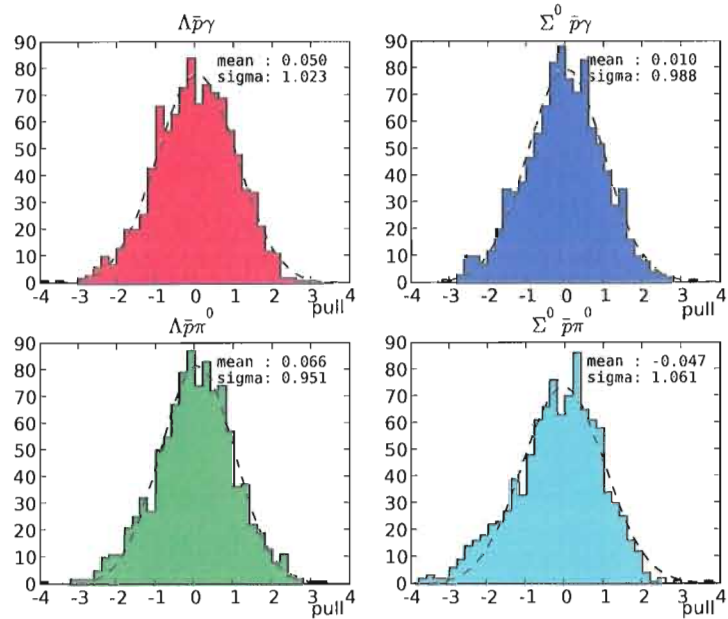


(b) pure

Fig. IV.28: Pure and Embedded Toy Studies – using a mixture of parameterization and 2d hist pdfs. Simultaneous Fit to events containing both candidates

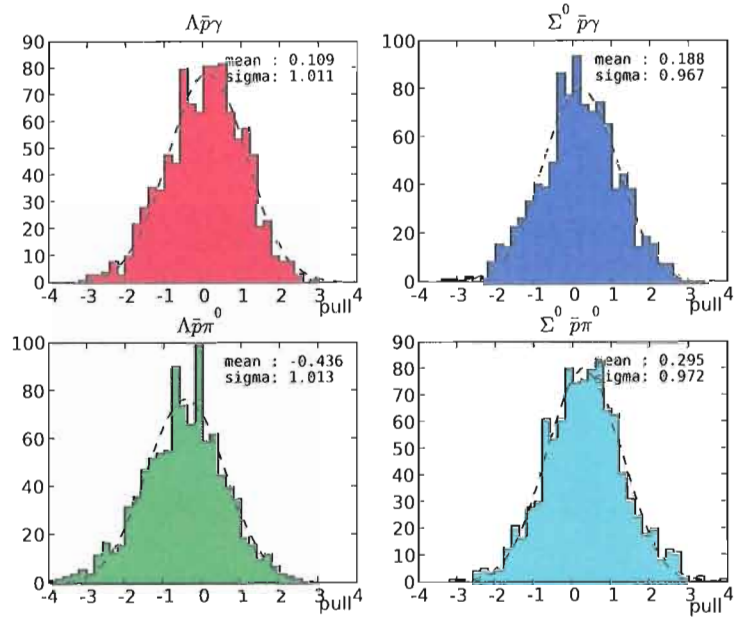


(a) embedded

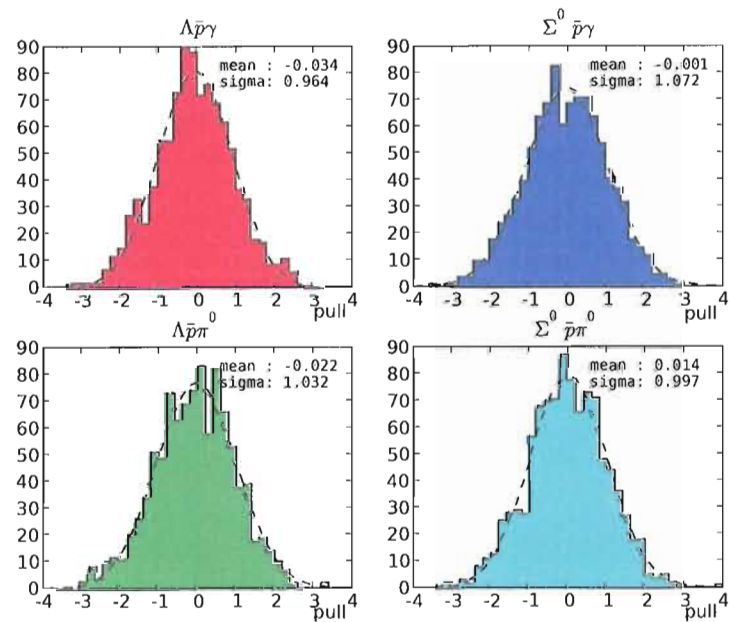


(b) pure

Fig. IV.29: Pure and Embedded Toy Studies – using a mixture of parameterization and 2d hist pdfs. Validation of the component to model $B^- \rightarrow \Lambda \bar{p}\gamma$

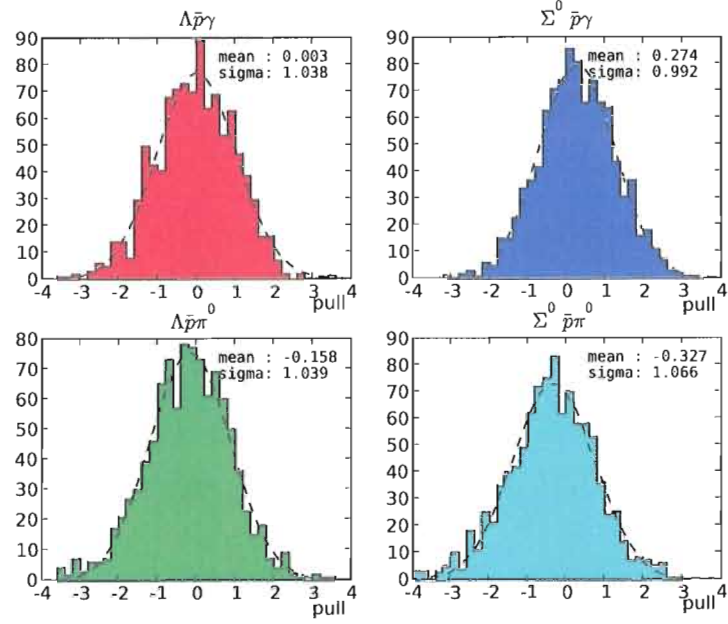


(a) embedded

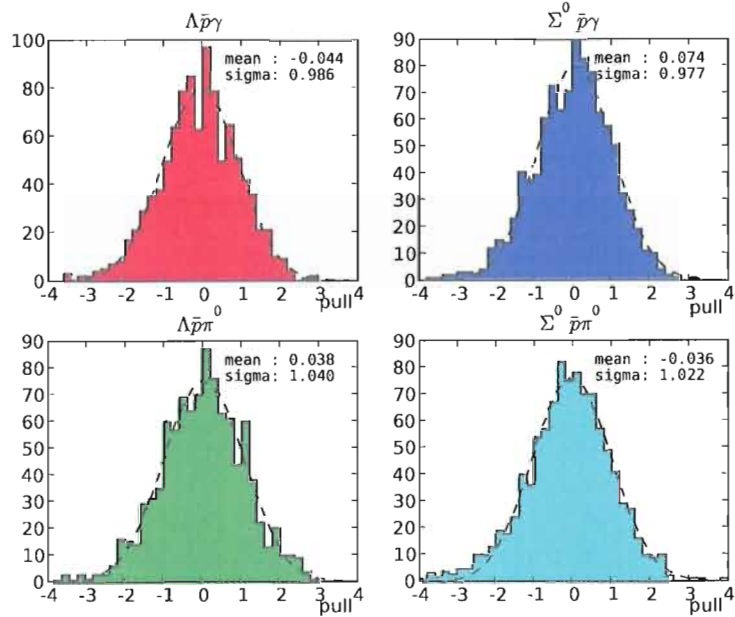


(b) pure

Fig. IV.30: Pure and Embedded Toy Studies – using a mixture of parameterization and 2d hist pdfs. Validation of the component to model $B^- \rightarrow \Sigma^0 \bar{p} \gamma$



(a) embedded



(b) pure

Fig. IV.31: Pure and Embedded Toy Studies – using a mixture of parameterization and 2d hist pdfs for events containing only a $B^- \rightarrow \Lambda \bar{p} \gamma$

from the fit is underestimated, the width of the Gaussian fit to the yields is wider than the mean of the errors. Table IV.16 shows the effect of fitting 1000 events with the $B^- \rightarrow \Lambda \bar{p} \gamma$ candidate embedded twice into the event. The events are then fit as if the two candidates were different. It is evident that the error is underestimated by a factor of $\sqrt{2}$.

sample		$B^- \rightarrow \Lambda \bar{p} \gamma$ only	$B^- \rightarrow \Sigma^0 \bar{p} \gamma$ only	simultaneous
$B^- \rightarrow \Lambda \bar{p} \gamma$	yield	118 ± 18	119 ± 28	119 ± 16
	error	19 ± 1	27 ± 1	15 ± 1
$B^- \rightarrow \Sigma^0 \bar{p} \gamma$	yield	124 ± 30	120 ± 27	124 ± 20
	error	29 ± 1	27 ± 1	19 ± 1
$B^- \rightarrow \Lambda \bar{p} \pi^0$	yield	23 ± 25	-13 ± 56	21 ± 24
	error	23 ± 2	56 ± 5	20 ± 2
$B^- \rightarrow \Sigma^0 \bar{p} \pi^0$	yield	0 ± 21	28 ± 44	6 ± 19
	error	20 ± 4	45 ± 4	29 ± 4

Tab. IV.14: Comparison of the spread of the yields from 1000 toy experiments with the error on the yield from the likelihood fit

variable	Correlation coefficient			
	$B^- \rightarrow \Lambda \bar{p} \gamma$	$B^- \rightarrow \Sigma^0 \bar{p} \gamma$	$B^- \rightarrow \Lambda \bar{p} \pi^0$	$B^- \rightarrow \Sigma^0 \bar{p} \pi^0$
B mass	0.857	0.735	0.904	0.830
missing mass	0.535	0.426	0.540	0.422
legendre moments	0.992	0.983	0.990	0.987
best π^0 mass	0.910	0.916	0.941	0.941

Tab. IV.15: Correlation coefficient between the $B^- \rightarrow \Lambda \bar{p} \gamma$ and the $B^- \rightarrow \Sigma^0 \bar{p} \gamma$ reconstruction for each of the fit variables

sample		simultaneous
$B^- \rightarrow \Lambda \bar{p} \gamma$	yield	84 ± 17
	error	12 ± 1
$B^- \rightarrow \Sigma^0 \bar{p} \gamma$	yield	242 ± 36
	error	24 ± 1
$B^- \rightarrow \Lambda \bar{p} \pi^0$	yield	31 ± 28
	error	19 ± 1
$B^- \rightarrow \Sigma^0 \bar{p} \pi^0$	yield	59 ± 30
	error	21 ± 2

Tab. IV.16: Comparison of the spread of the yields from 1000 toy experiments with the error on the yield from the likelihood fit. Candidates are fully correlated.

IV.6 Computation of the Branching Fraction

A common feature of B decays with a baryon pair among the final states is that the differential branching fraction in bins of the invariant mass of the baryon pair peaks at threshold. Additionally, this analysis, like many other $b \rightarrow s\gamma$ analyses, uses a cut on the high energy photon to reduce background. The signal reconstruction efficiency thus also depends on the di-baryon invariant mass, which causes a systematic error in taking the yields extracted from the likelihood fit in order to determine the branching fraction. Therefore, following the lead of the analysis of $B^0 \rightarrow \bar{\Lambda}p\pi^-$ (35), the sPlots(36) method will be used for the measurement of the branching fraction. See appendix K for a more detailed description of the method. In short, each event is assigned a weight for each subsample that depends on the covariance matrix of the fit. Thus, plots of variables of subsamples do not have to rely on background subtraction but rather use the full statistical information that is available. The weights for each event are

$$s\mathcal{P}_n(y_e) = \frac{\sum_{j=1}^N \mathbf{V}_{nj} \mathcal{P}_j}{\sum_{j=1}^N \mathbf{N}_j \mathcal{P}_j}$$

Filling a histogram in a variable that is not part of the fit with these weights should then correctly reproduce the distribution of that variable for the respective sample. The branching fraction of the decay is computed by extracting the yields in bins of the invariant mass of the baryon pair and dividing by the reconstruction efficiency for this bin. This should give the correct number of events in the BaBar data sample in each bin.

IV.6.1 Dependence on the Measurement Efficiency

The measurement efficiency is an unknown function in the variable *di-baryon invariant mass*. Because of the cut on the high-energy photon, it is highly correlated with the model that describes the branching fraction as a function of this mass. After validating the technique to extract the branching fraction for a flat measurement efficiency, the weights for each event are then divided by the reconstruction efficiency for each bin, obtaining the final set of sPlots that are then used to obtain the branching fraction. This means that every event is assigned a weight $s\mathcal{P}_n(y_e)/\varepsilon_e$, where ε_e is the efficiency for the event as a function of the invariant mass of the di-baryon system.

IV.6.2 sPlots Validation

If the properties of sPlots that are alluded to in the appendix are satisfied, binning the weighted events in any other variable will always be an unbiased estimator for the event yield in each bin separately. The sPlots formalism includes a description how to compute bin errors, but since we cannot be sure that the conditions under which those computed errors give a good description of the measurement uncertainty hold, we perform a set of toy Monte Carlo simulations to get an idea of the true value of the bin errors. One of the requirements of the sPlots method is that the variable of interest is uncorrelated with the fit variables. Tables IV.17, IV.18, and IV.19 shows the correlation of the di-baryon invariant mass with each of the fit variables for the four signal samples and for data. In 1000 samples with a mean of 5000 generated background events, events from the full simulation are embedded. The number of each sample is varied independently according to a Poisson distribution, with means of 120, 120, 20 and 20 for the samples $B^- \rightarrow \Lambda\bar{p}\gamma$, $B^- \rightarrow \Sigma^0\bar{p}\gamma$, $B^- \rightarrow \Lambda\bar{p}\pi^0$ and $B^- \rightarrow \Sigma^0\bar{p}\pi^0$, respectively.

Sample	$m_{\text{rec.}}$	$m_{\text{miss.}}$	L_2/L_0	best π^0 mass
$B^- \rightarrow \Lambda \bar{p} \gamma$	0.086	0.018	0.033	-0.161
$B^- \rightarrow \Sigma^0 \bar{p} \gamma$	0.085	0.036	0.012	-0.158
$B^- \rightarrow \Lambda \bar{p} \pi^0$	0.011	-0.014	-0.049	-0.098
$B^- \rightarrow \Sigma^0 \bar{p} \pi^0$	0.052	-0.034	-0.039	-0.100
data	0.160	-0.006	0.049	-0.212

Tab. IV.17: Correlation coefficient with each of the four fit variables for the four signal samples and for data for $B^- \rightarrow \Lambda \bar{p} \gamma$ candidates

Sample	$m_{\text{rec.}}$	$m_{\text{miss.}}$	L_2/L_0	best π^0 mass
$B^- \rightarrow \Lambda \bar{p} \gamma$	0.104	0.011	0.026	-0.178
$B^- \rightarrow \Sigma^0 \bar{p} \gamma$	0.035	0.020	0.017	-0.187
$B^- \rightarrow \Lambda \bar{p} \pi^0$	-0.027	-0.032	-0.022	-0.095
$B^- \rightarrow \Sigma^0 \bar{p} \pi^0$	0.019	0.006	-0.013	-0.109
data	0.114	-0.040	0.038	-0.193

Tab. IV.18: Correlation coefficient with each of the four fit variables for the four signal samples and for data for $B^- \rightarrow \Lambda \bar{p} \gamma$ candidates in events that also contain a $B^- \rightarrow \Sigma^0 \bar{p} \gamma$

Sample	$m_{\text{rec.}}$	$m_{\text{miss.}}$	L_2/L_0	best π^0 mass
$B^- \rightarrow \Lambda \bar{p} \gamma$	0.101	0.061	0.029	-0.156
$B^- \rightarrow \Sigma^0 \bar{p} \gamma$	0.090	0.021	0.015	-0.156
$B^- \rightarrow \Lambda \bar{p} \pi^0$	-0.006	0.023	-0.023	-0.080
$B^- \rightarrow \Sigma^0 \bar{p} \pi^0$	0.061	0.015	-0.019	-0.080
data	0.152	0.003	0.034	-0.170

Tab. IV.19: Correlation coefficient with each of the four fit variables for the four signal samples and for data for $B^- \rightarrow \Sigma^0 \bar{p} \gamma$ candidates

Because the non-negligible correlations between the di-baryon invariant mass and the fit variables and the relatively low expected yields of the signal samples, the sPlots method is validated as follows: For the background, a flat distribution in the di-baryon invariant mass is generated, and for each of the signal modes, a beta-like distribution is assumed in order to simulate the peaking behavior. The plots in Figure IV.32 show for each sample the histograms of the generated distribution and the sPlots. The height of each bin is the average of the 1000 values in that bin, while the error bar represents the standard deviation of the values in the bin. The events only contain a $B^- \rightarrow \Lambda \bar{p} \gamma$ candidate. Validations on $B^- \rightarrow \Sigma^0 \bar{p} \gamma$ and $B^- \rightarrow \Lambda \bar{p} \gamma$ candidates in events with both candidates are shown in Figures IV.33 and IV.34, respectively.

IV.7 Systematic Uncertainties

In addition to the statistical error that stems from the finite sample size, all physical measurements are affected by a systematical uncertainty. Inaccuracies in the physical devices, the inability to compute underlying models analytically, and the like propagate to an error in the determination of the yields of signal and background and ultimately to an uncertainty in the measurement of the branching fraction. The following sources of systematic errors are considered:

IV.7.1 Model Uncertainties

The model(32) that is used to generate the events for $B^- \rightarrow \Lambda \bar{p} \gamma$ and $B^- \rightarrow \Sigma^0 \bar{p} \gamma$ depends on several form factors that are not determined analytically. Estimating the systematic error due to the parameterization of the decay is quite challenging because of the limited experimental data that is available to validate the model against. One way would be to compare it to other models(3) that can be used to predict the

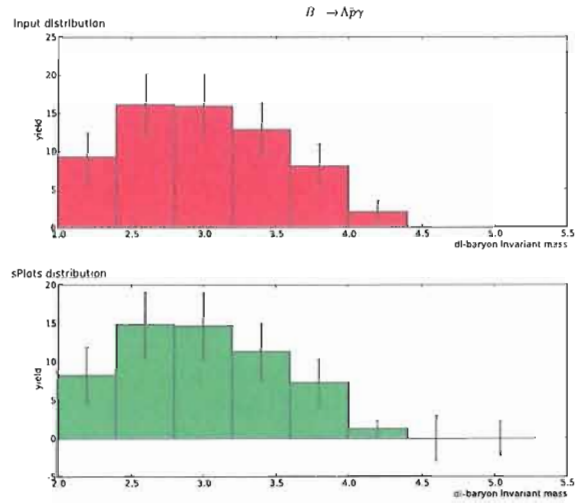
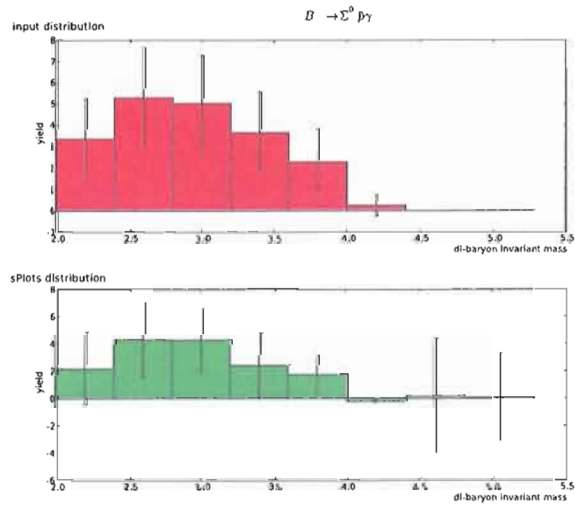
(a) $B^- \rightarrow \Lambda \bar{p} \gamma$ (b) $B^- \rightarrow \Sigma^0 \bar{p} \gamma$

Fig. IV.32: Validation plots of the sPlots method used to extract the branching fraction in bins of the di-baryon invariant mass. Events containing a single $B^- \rightarrow \Lambda \bar{p} \gamma$ candidate

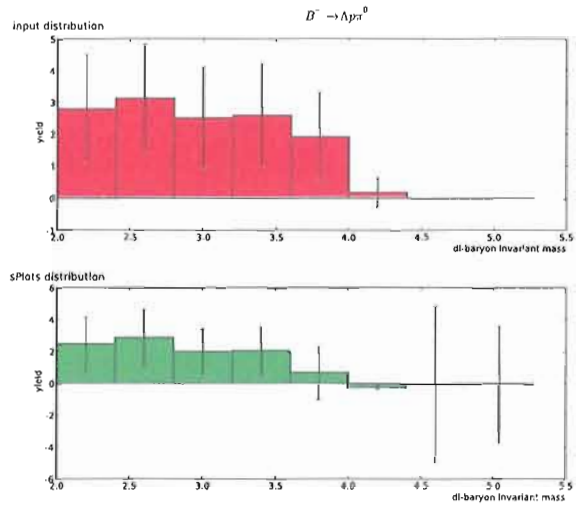
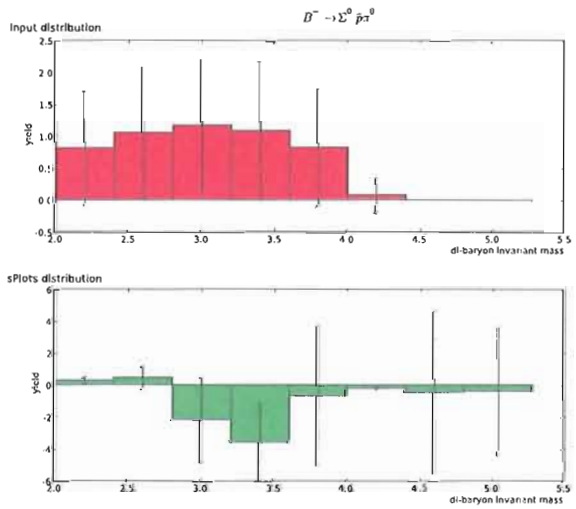
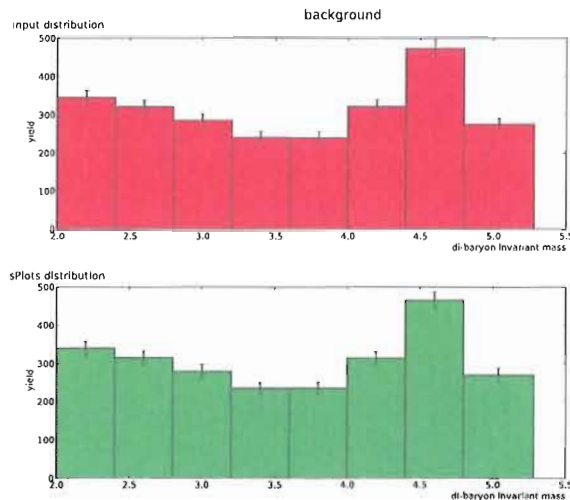
(c) $B^- \rightarrow \Lambda \bar{p} \pi^0$ (d) $B^- \rightarrow \Sigma^0 \bar{p} \pi^0$

Fig. IV.32: Validation plots of the sPlots method, continued



(e) Background

Fig. IV.32: continued

branching fraction of $B^- \rightarrow \Lambda \bar{p} \gamma$ and $B^- \rightarrow \Sigma^0 \bar{p} \gamma$. Figure IV.35 shows how the cut efficiency depends on the invariant mass of the di-baryon system. As the cut on the photon energy is correlated with the di-baryon invariant mass, figure IV.36 shows the cut efficiency on the two signal modes with this cut removed.

Based on error associated with the computed form factors - 10 % at zero recoil and 30 % on the q^2 dependence - events were generated with corresponding variations on these parameters. Out of 1000 generated events, between 366 and 361 are successfully reconstructed and between 146 and 141 pass all cuts. Based on the difference in the number of events that pass the cuts, a systematic error of 4% is assigned to the yield. Additionally, a systematic error of 0.5 % enters the reconstruction efficiency.

IV.7.2 B Counting

The number of B events as obtained from the BbkLumi script and shown in table IV.1 is 382.9 ± 4.219 events, from which we assign an uncertainty of 1.10 %.

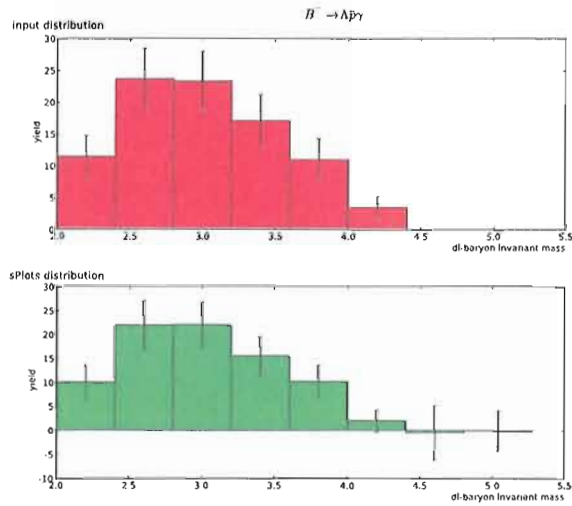
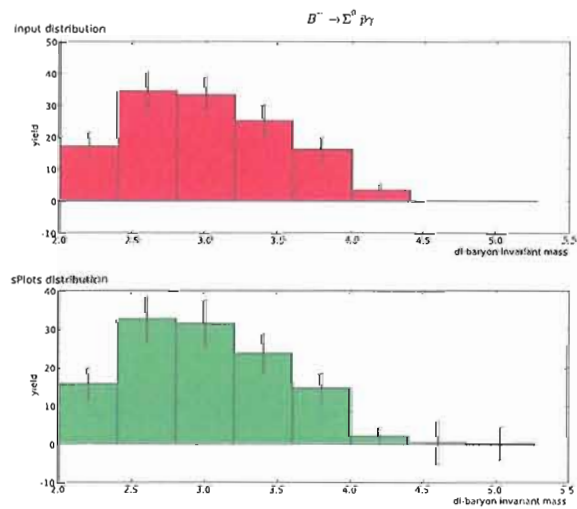
(a) $B^- \rightarrow \Lambda \bar{p} \gamma$ (b) $B^- \rightarrow \Sigma^0 \bar{p} \gamma$

Fig. IV.33: Validation plots of the sPlots method used to extract the branching fraction in bins of the $\Sigma^0 - p$ invariant mass for Events containing both a $B^- \rightarrow \Lambda \bar{p} \gamma$ candidate and a $B^- \rightarrow \Sigma^0 \bar{p} \gamma$ candidate

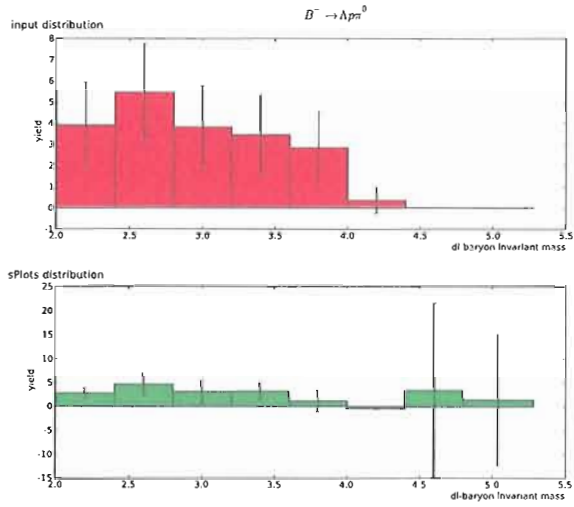
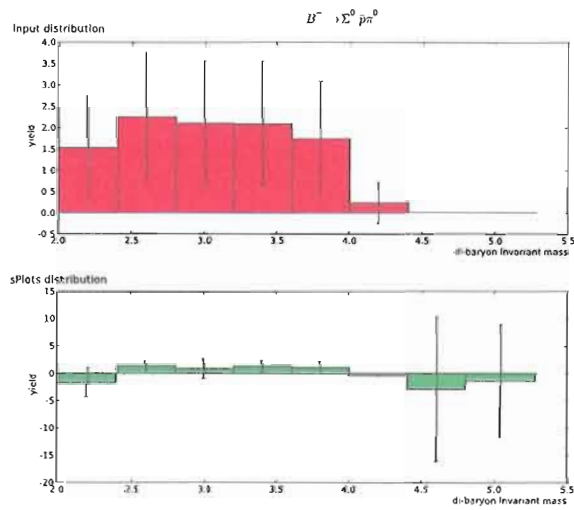
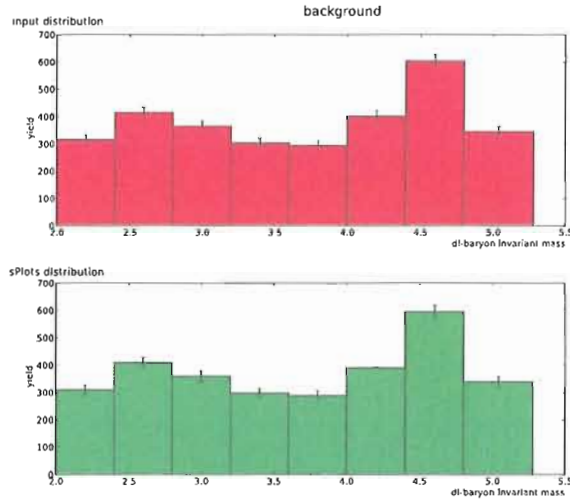
(c) $B^- \rightarrow \Lambda \bar{p} \pi^0$ (d) $B^- \rightarrow \Sigma^0 \bar{p} \pi^0$

Fig. IV.33: continued



(c) Background

Fig. IV.33: continued

$B^0\bar{B}^0 - B^+B^-$ – *asymmetry* For the purpose of calculating the number of B mesons from the luminosity, it is assumed that charged and neutral B mesons are produced in equal parts. Based on the PDG values, we assign an error of 1.4 % on the final yields due to this assumption.

IV.7.3 Cuts

The cuts have different efficiencies for data and MC. The error on the cut on the candidate type is akin to the $B^- \rightarrow \Sigma^0 \bar{p} \gamma$ candidate not passing at least one of the cuts, while the $B^- \rightarrow \Lambda \bar{p} \gamma$ candidate passes all cuts. For the cut on the separation between the EM cluster and the nearest track, a 2% error is assigned.

Plots in Figures F.5 and F.6 were made at an earlier stage of this analysis, before $B^- \rightarrow \Sigma^0 \bar{p} \gamma$ was added as a component of the sample. They show that the signal significance is fairly insensitive to changing the cuts. Based on Figures IV.37 and IV.38, a systematic error will be applied that is proportional to the fitted yield.

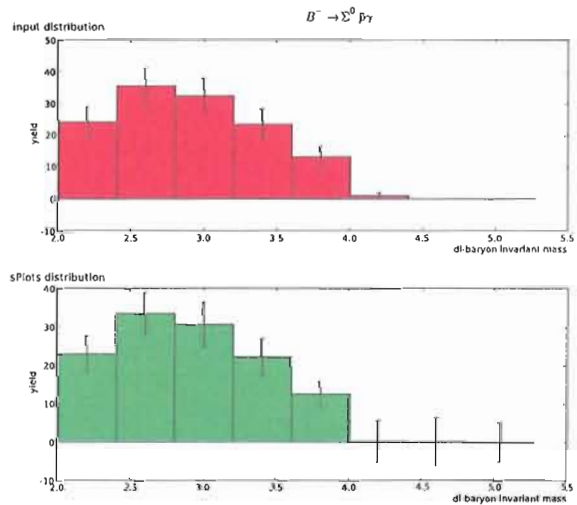
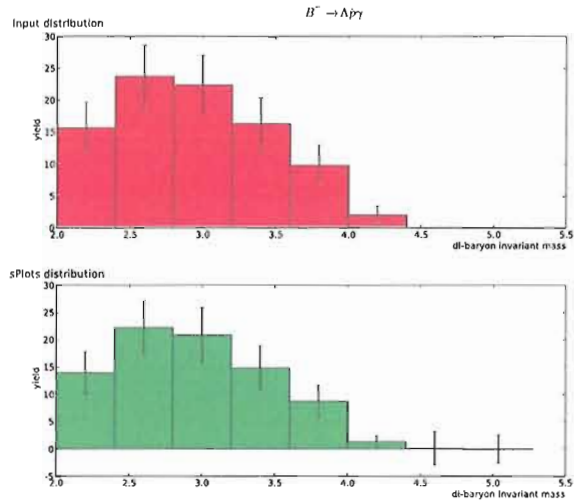


Fig. IV.34: Validation plots of the sPlots method used to extract the branching fraction in bins of the $\Lambda - p$ invariant mass for Events containing both a $B^- \rightarrow \Lambda \bar{p} \gamma$ candidate and a $B^- \rightarrow \Sigma^0 \bar{p} \gamma$ candidate

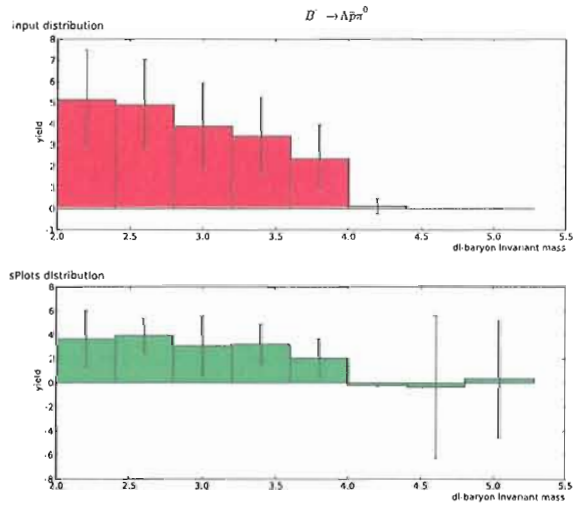
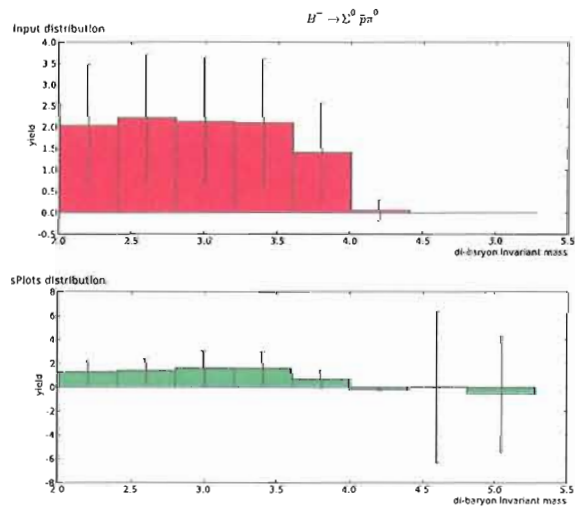
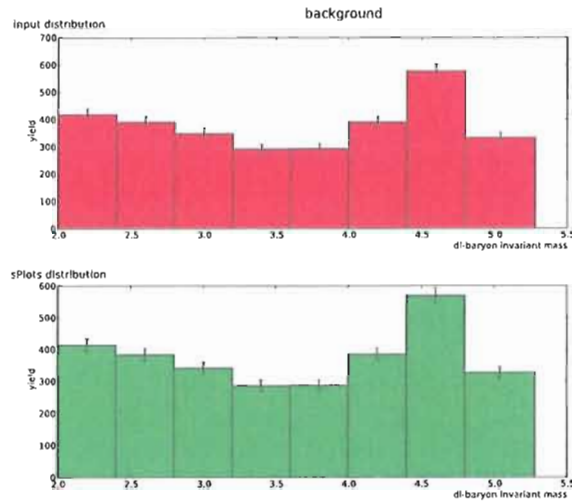
(c) $B^- \rightarrow \Lambda \bar{p} \pi^0$ (d) $B^- \rightarrow \Sigma^0 \bar{p} \pi^0$

Fig. IV.34: continued



(c) Background

Fig. IV.34: continued

Tables IV.20 and IV.38 summarize the slopes from these plots.

IV.7.4 Particle Identification

There is a systematic error associated with applying a particle identification (PID) selector, because it has different efficiencies for data and simulation. The PID working group spends their efforts on trying to understand exactly the amount and nature of these differences and supply correction factors, so called PID weights, $w_{\text{PID}} = \epsilon_{\text{data}}/\epsilon_{\text{simulation}}$. The PID weight is the ratio of the efficiencies for data and simulation and the recipe to correct for the difference is as follows:

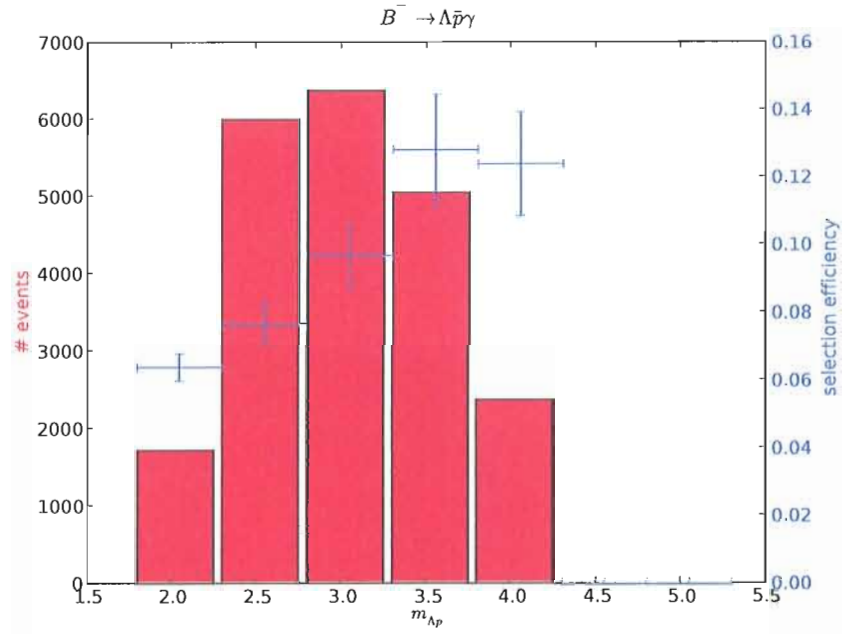
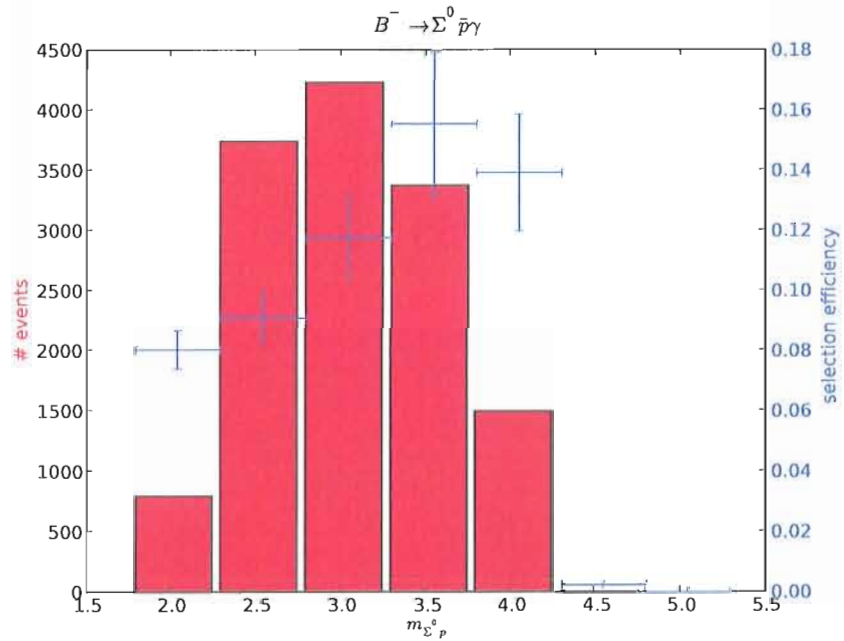
(a) $B^- \rightarrow \Lambda \bar{p} \gamma$ (b) $B^- \rightarrow \Sigma^0 \bar{p} \gamma$

Fig. IV.35: Cut efficiency for $B^- \rightarrow \Lambda \bar{p} \gamma$ and $B^- \rightarrow \Sigma^0 \bar{p} \gamma$ signal in bins of the di-baryon invariant mass

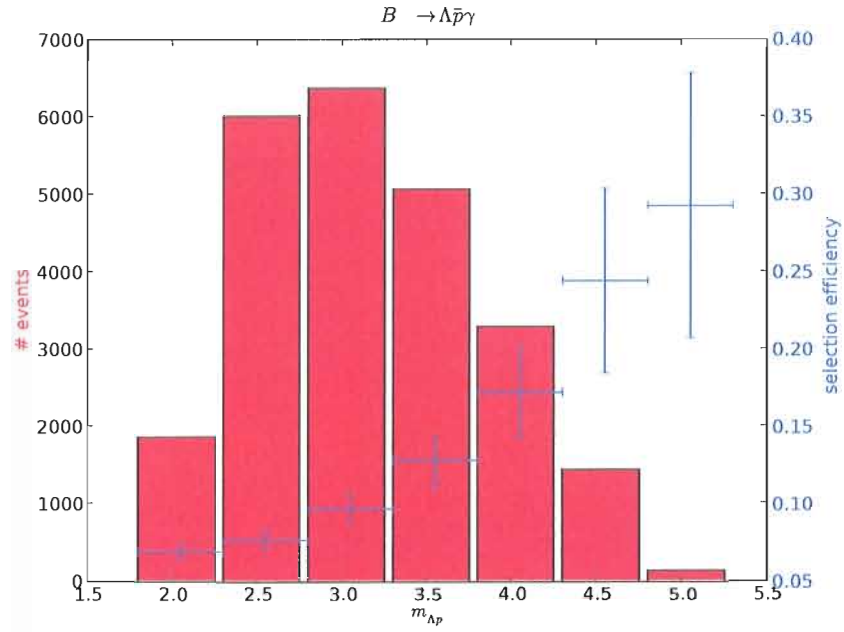
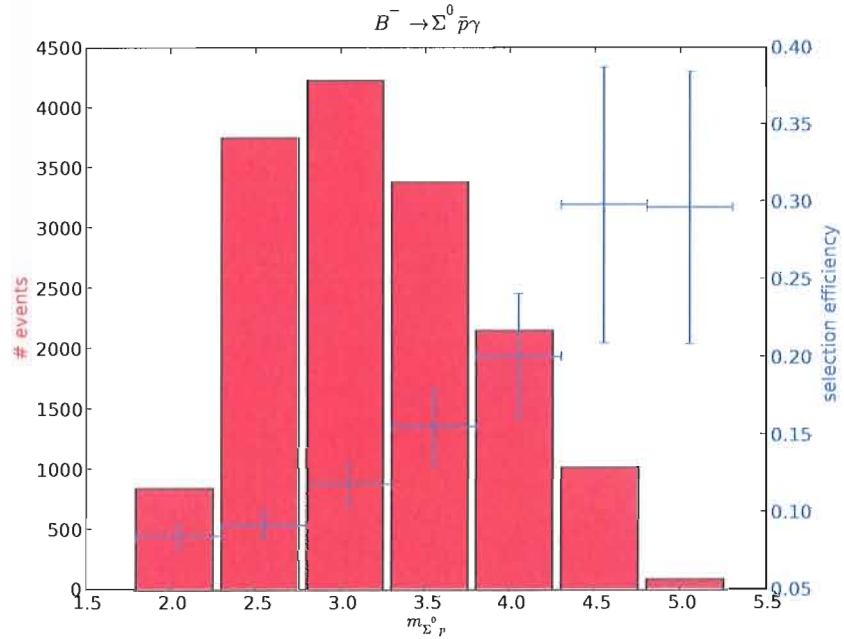
(a) $B^- \rightarrow \Lambda \bar{p} \gamma$ (b) $B^- \rightarrow \Sigma^0 \bar{p} \gamma$

Fig. IV.36: Cut efficiency for $B^- \rightarrow \Lambda \bar{p} \gamma$ and $B^- \rightarrow \Sigma^0 \bar{p} \gamma$ signal in bins of the di-baryon invariant mass. The cut on the photon energy has been removed

1. apply the selector to reject tracks that do not meet the criteria
2. if $w_{\text{PID}} < 1$, accept tracks that pass the selector with a probability $\frac{\epsilon_{\text{data}}}{\epsilon_{\text{simulation}}}$
3. if $w_{\text{PID}} > 1$, accept a rejected track with a probability $\frac{\epsilon_{\text{data}}}{\epsilon_{\text{simulation}}} - 1$

Applying the selector with and without the efficiency correction outlined above on the signal samples changes the number of candidates that pass the cuts by about 0.6%.

IV.7.5 Single Photon Efficiency

According to the neutrals group⁶, a correction to the single photon efficiency is unnecessary, with a systematic of 1.8%. This is valid up to 2.5 GeV, which is beyond the kinematically allowed photon energy for this decay. This uncertainty has to be applied to each photon not from a π^0 decay.

IV.7.6 Tracking

According to the recommendations of the tracking task force⁷, a correction is applied on a per-track basis. All tracks in this analysis are taken from the default list. Averaging over the different run periods yields a systematic uncertainty of 0.36% per track.

IV.7.7 Fitting

In order to estimate the uncertainty on the yield that is introduced by the fit, the parameters of the fit are randomly varied within their errors, and the fit is then redone with the new set of parameters fixed. The maximum difference in a set of 1000 yields

⁶<http://www.slac.stanford.edu/BFR00T/www/Physics/Analysis/AWG/Neutrals/validation/recipe18.html>

⁷<http://www.slac.stanford.edu/BFR00T/www/Physics/TrackEfficTaskForce/TrackingTaskForce-2006.html>

obtained this way is taken as the systematic uncertainty due to the fit. This is carried out in the following way:

- a) The same data set is fit 1000 times, all parameters are fixed, yields are floating, but initial values remain unchanged among the 1000 fits. This serves as a dummy check to ensure the stability of the fit.
- b) The same as before, but the initial values are varied within Poisson errors of the results of the previous experiment.
- c) The same data set is fit 1000 times with fixed parameters, varying all parameters within errors. The bins of the histogram pdf are varied within Poisson errors. Initial values are fixed.
- d) The same data set is fit with fixed parameters, but one of the yields is fixed, varying within 10σ . This is done for each of the yields in the fit.
- e) The number of events that are embedded in the data sample is varied in the following way: The embedded toy studies are carried out on 1000 data sets containing Poisson-distributed numbers of each of the components. For the study of the systematic error, the mean of one of the components is changed. For each of the components, a few values for the mean are considered, while the means of the other components are unchanged. For each of the different values for the mean, for each of the components, 100 events are generated.

IV.7.8 Summary

Table IV.22 summarizes the uncertainties associated with the different reconstruction modes.

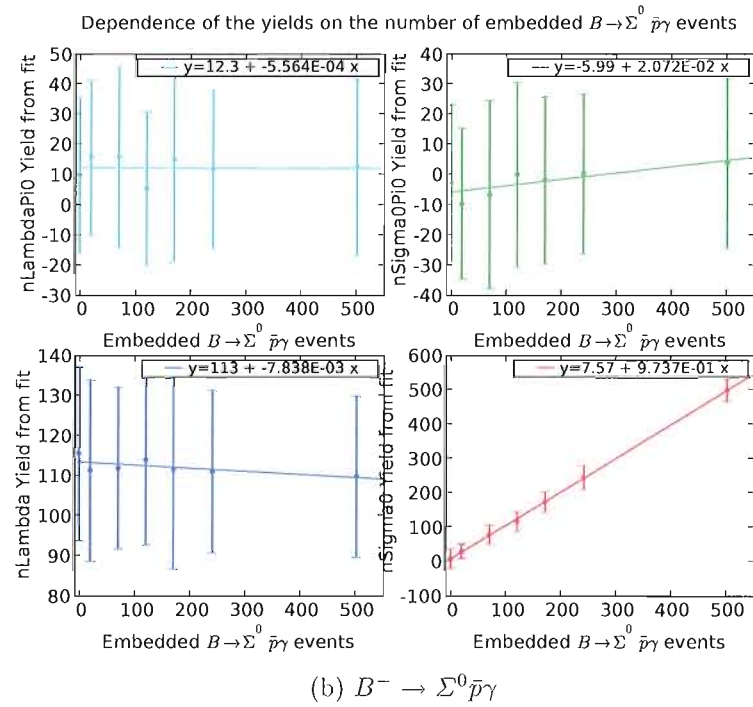
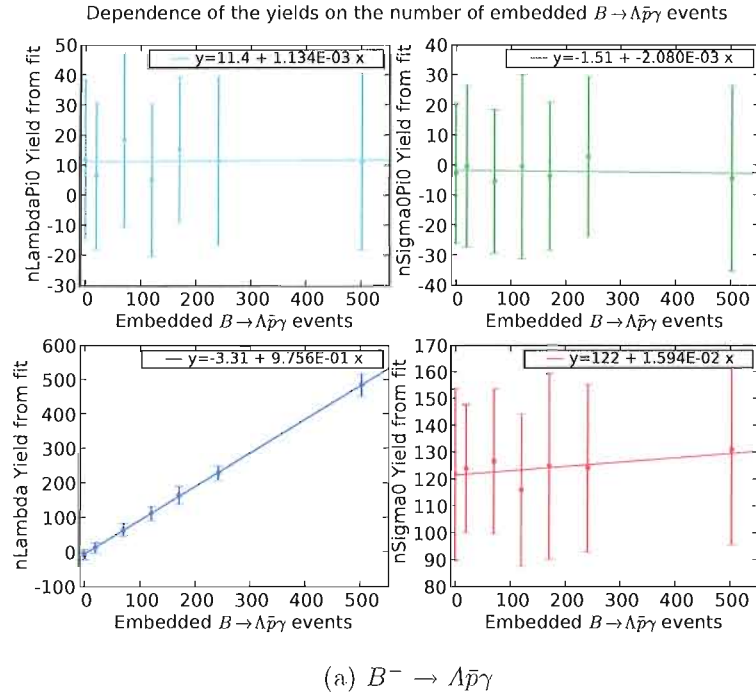


Fig. IV.37: Effect on the fit when changing the composition of the sample of one-candidate events.

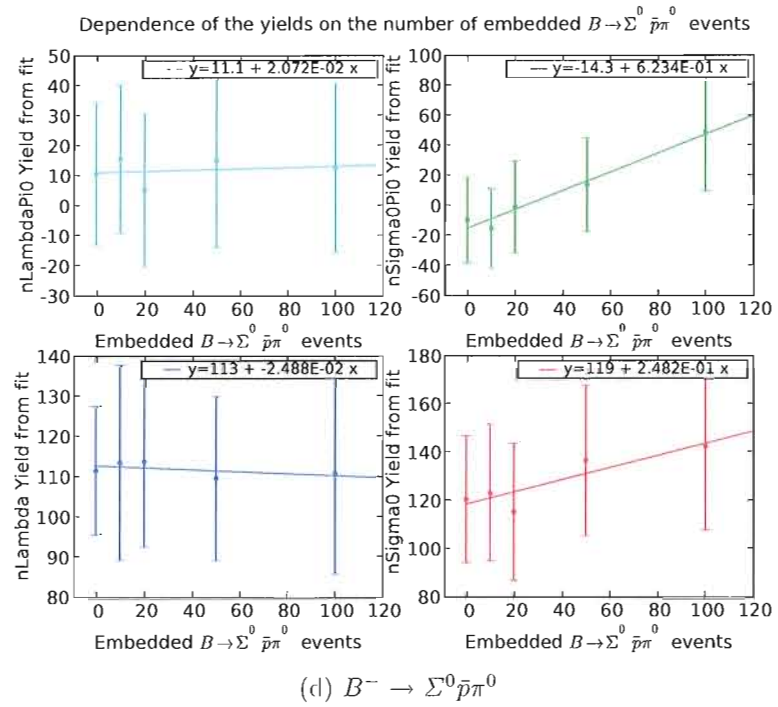
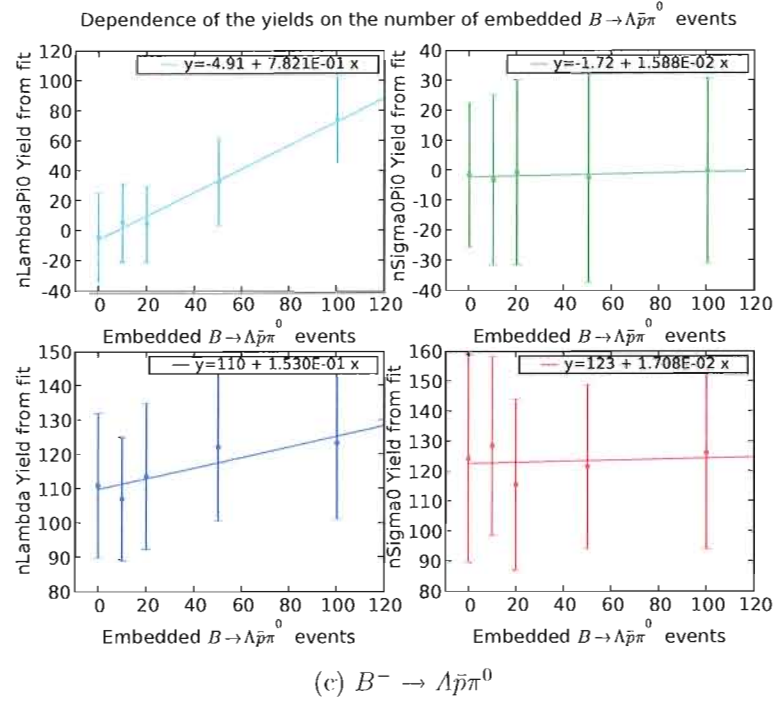


Fig. IV.37: continued

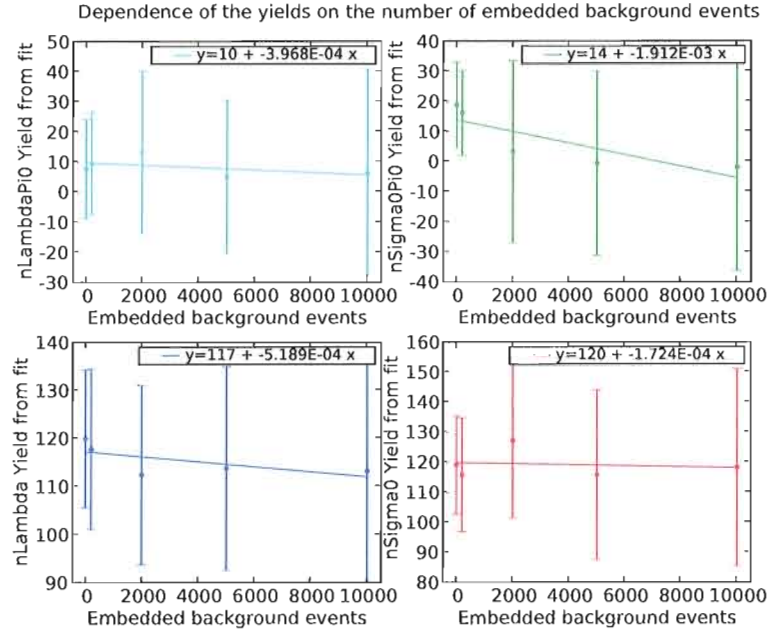


Fig. IV.37: continued

fitted yield $y = mx + b$	dependence m on embedded yield				
	$B^- \rightarrow \Lambda \bar{p} \gamma$	$B^- \rightarrow \Lambda \bar{p} \pi^0$	$B^- \rightarrow \Sigma^0 \bar{p} \gamma$	$B^- \rightarrow \Sigma^0 \bar{p} \pi^0$	background
$B^- \rightarrow \Lambda \bar{p} \gamma$	0.98	0.15	-0.0078	-0.025	-0.00052
$B^- \rightarrow \Lambda \bar{p} \pi^0$	0.0011	0.78	-0.00056	0.021	-0.00040
$B^- \rightarrow \Sigma^0 \bar{p} \gamma$	0.016	0.017	0.97	0.25	-0.00017
$B^- \rightarrow \Sigma^0 \bar{p} \pi^0$	-0.0021	0.016	0.021	0.62	-0.0019

Tab. IV.20: Summary of the systematic effect of changing the sample composition for one-candidate events (Figure IV.37)

fitted yield $y = mx + b$	dependence m on embedded yield				
	$B^- \rightarrow \Lambda \bar{p} \gamma$	$B^- \rightarrow \Lambda \bar{p} \pi^0$	$B^- \rightarrow \Sigma^0 \bar{p} \gamma$	$B^- \rightarrow \Sigma^0 \bar{p} \pi^0$	background
$B^- \rightarrow \Lambda \bar{p} \gamma$	0.97	0.063	-0.018	-0.10	-0.0034
$B^- \rightarrow \Lambda \bar{p} \pi^0$	0.0060	0.98	-0.00038	0.13	0.0047
$B^- \rightarrow \Sigma^0 \bar{p} \gamma$	0.064	0.016	1.11	0.19	0.010
$B^- \rightarrow \Sigma^0 \bar{p} \pi^0$	0.0027	0.12	0.0059	0.74	0.0058

Tab. IV.21: Summary of the systematic effect of changing the sample composition for simultaneous fits to two-candidate events (Figure IV.38)

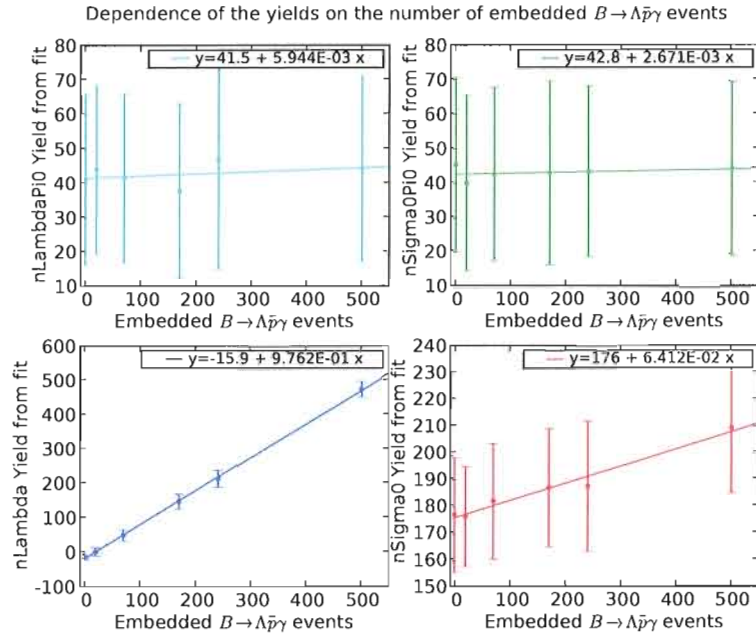
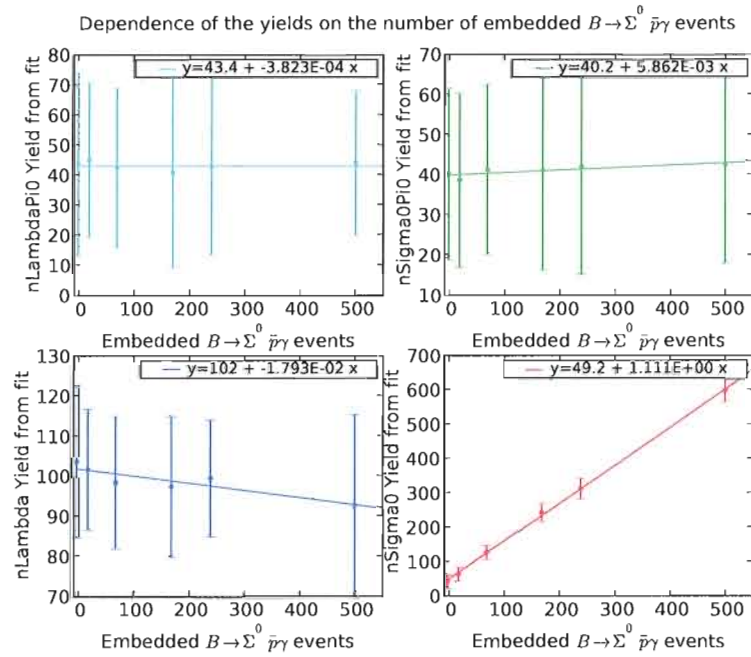
(a) $B^- \rightarrow \Lambda \bar{p} \gamma$ (b) $B^- \rightarrow \Sigma^0 \bar{p} \gamma$

Fig. IV.38: Effect on the fit when changing the composition of the sample of two-candidate events.

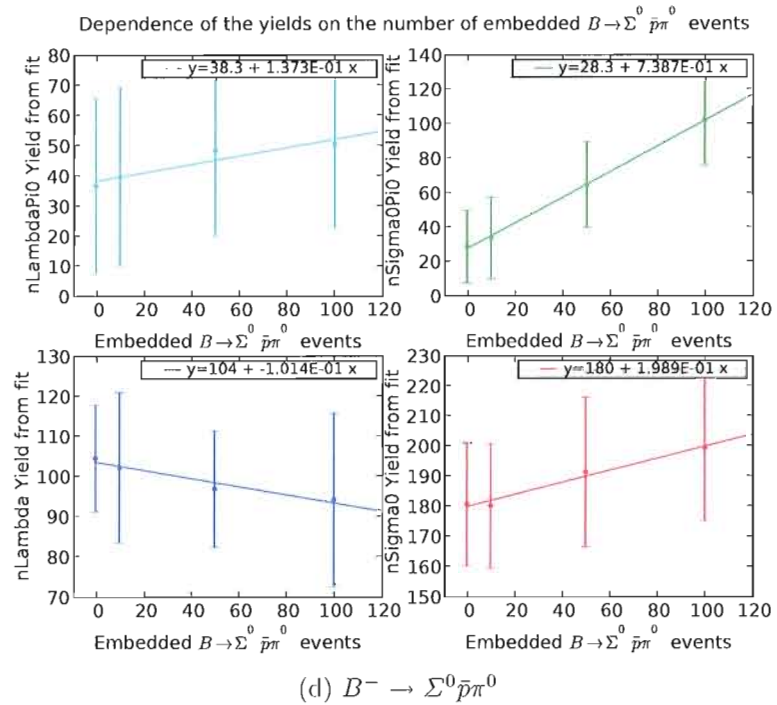
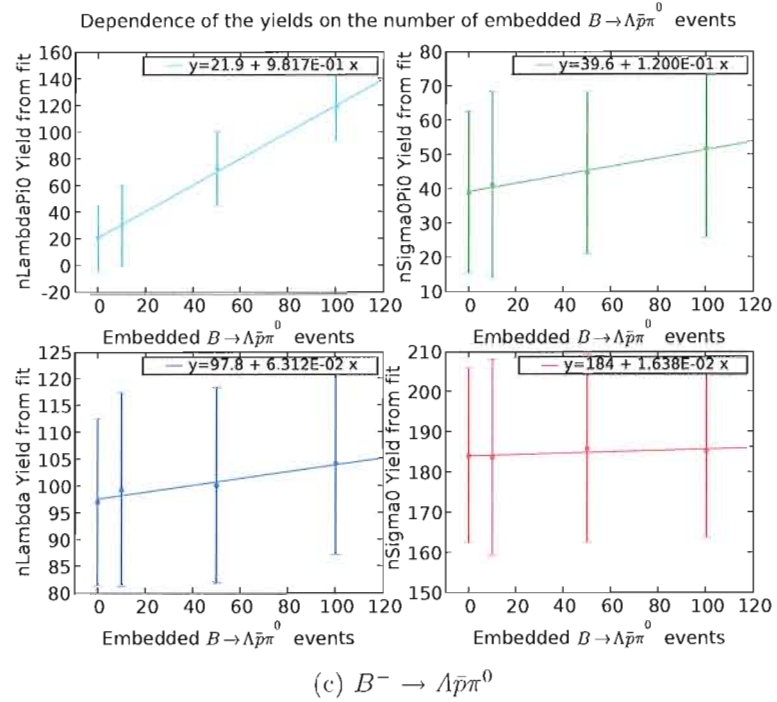
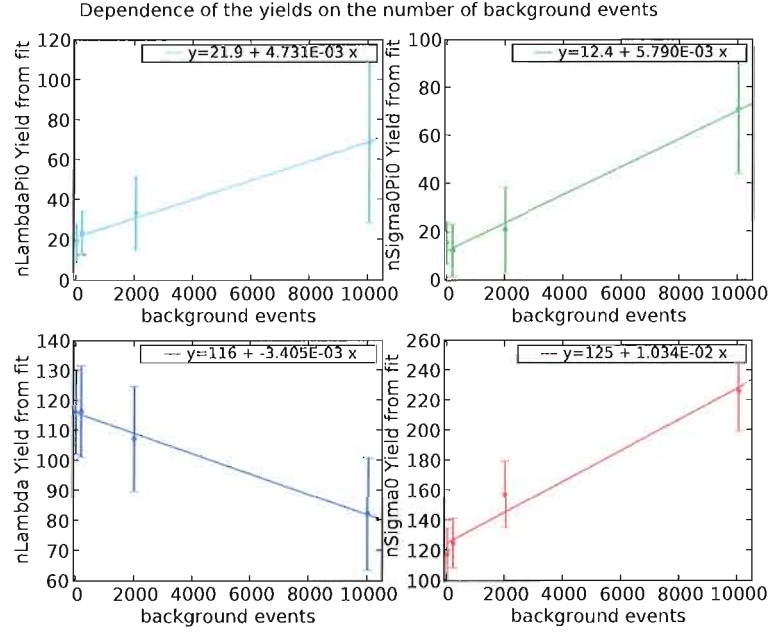


Fig. IV.38: continued



(c) Background

Fig. IV.38: continued

Source of error	$B^- \rightarrow \Lambda \bar{p} \gamma$ (%)	$B^- \rightarrow \Sigma^0 \bar{p} \gamma$ (%)
B counting	1.10	1.10
$B^0 \bar{B}^0 - B^+ B^-$ asymmetry	1.4	1.4
BF $\Lambda \rightarrow p \gamma$	0.8	0.8
single photon efficiency	1.8	3.6
tracking uncertainty	1.08	1.08
EM cluster - track separation	2	2
theoretical model (yield)	4	4
reconstruction efficiency	0.5	0.5
likelihood fit	dependent on sample	dependent on sample
PID	0.6	0.6
combined	5.37 + fit error	6.21 + fit error

Tab. IV.22: Systematic error on the yields for the different reconstruction modes

CHAPTER V

RESULTS

V.1 Visualization of the Four Fit Variables

The maximum likelihood fit finds values for the yields of the four samples and the background that maximize the value of the likelihood function (eq. IV.5) for each of the three possible parametrizations of B candidates. Figures V.1 and V.2 visualize the result of this fit for $B^- \rightarrow A\bar{p}\gamma$ candidates in one-candidate events, while Figures V.3 and V.4, and V.5 and V.6 do the same for $B^- \rightarrow A\bar{p}\gamma$ and $B^- \rightarrow \Sigma^0\bar{p}\gamma$ candidates, respectively, in two-candidate events. Each plot represents the projection of the four-dimensional probability density function to the given variable.

V.2 Yields in the Data Samples

Applying the analysis strategy that was developed and validated on simulated samples in the preceding chapters to the *BABAR* data sample is referred to as *unblinding* in *BABAR* jargon. The results of that process are shown and put into context in this chapter.

The yields of the different samples in both data sets are extracted from the likelihood fit as shown in Tables V.1 and V.2. The significance is computed as $\sqrt{-2(\mathcal{L}_{\min} - \mathcal{L}_0)}$, where \mathcal{L}_{\min} is the minimum of the negative log-likelihood function and \mathcal{L}_0 is the value of the negative log-likelihood function with the respective yield fixed to 0.

The negative value for the yield of the $B^- \rightarrow A\bar{p}\pi^0$ sample is of course unphysical. Because of the high correlation of the yields for $B^- \rightarrow A\bar{p}\pi^0$ and $B^- \rightarrow \Sigma^0\bar{p}\pi^0$ in both

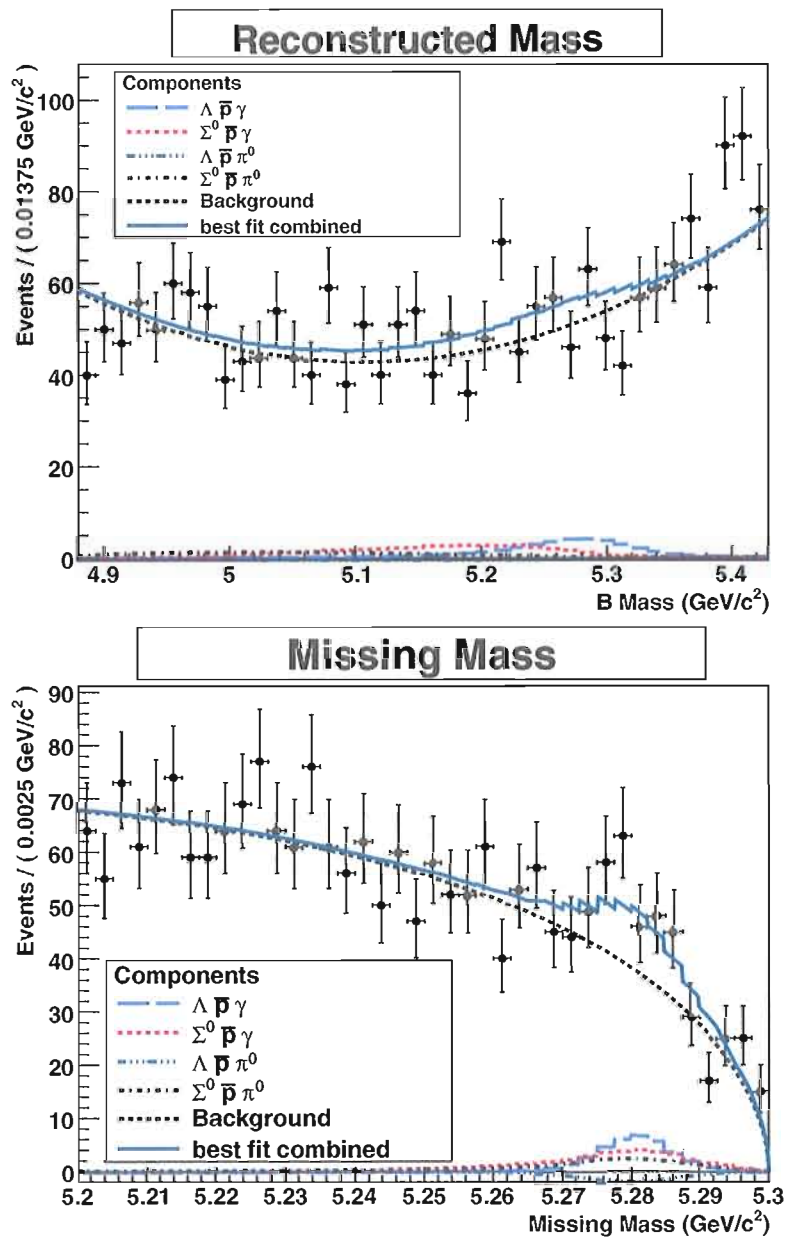


Fig. V.1: Likelihood fit to the kinematic fit variables *reconstructed candidate mass* and *missing mass* in events containing only one candidate

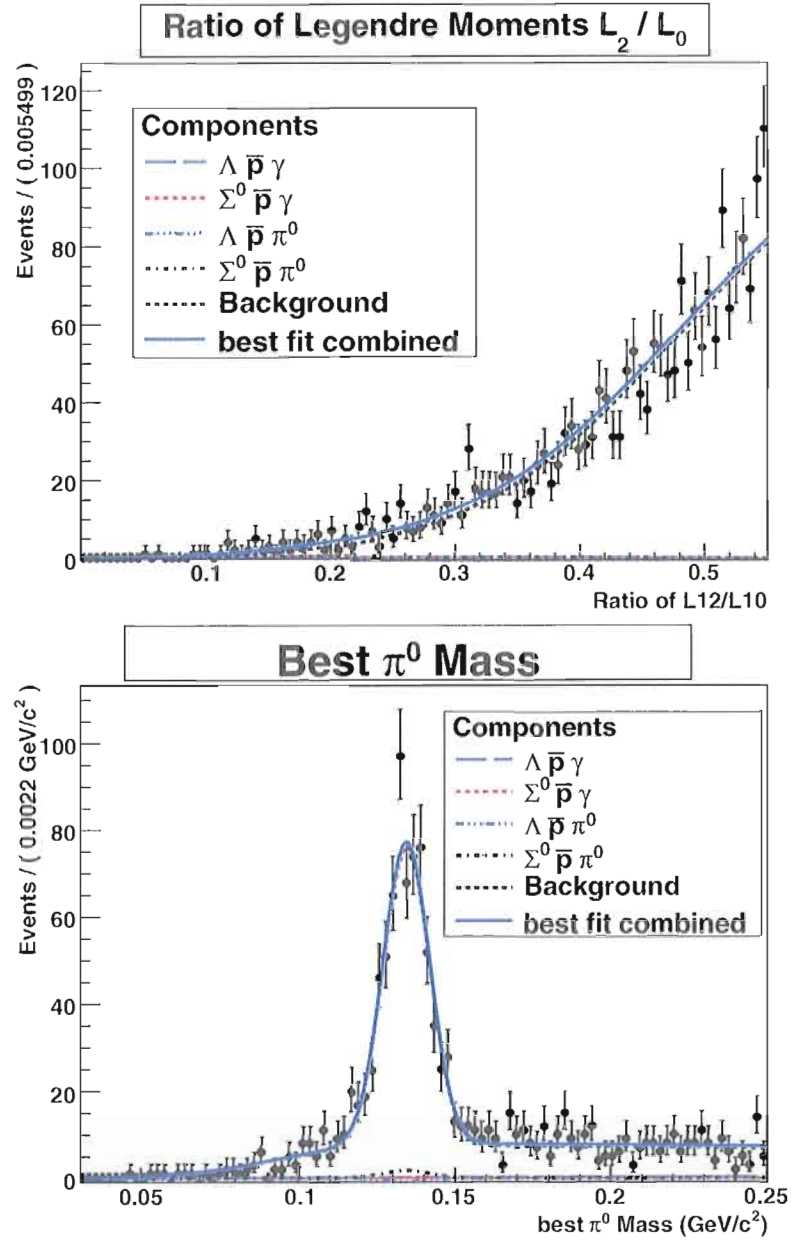


Fig. V.2: Likelihood fit to the kinematic fit variables *ratio of the Legendre Moments* L_2/L_0 and *best m_{π^0}* in events containing only one candidate

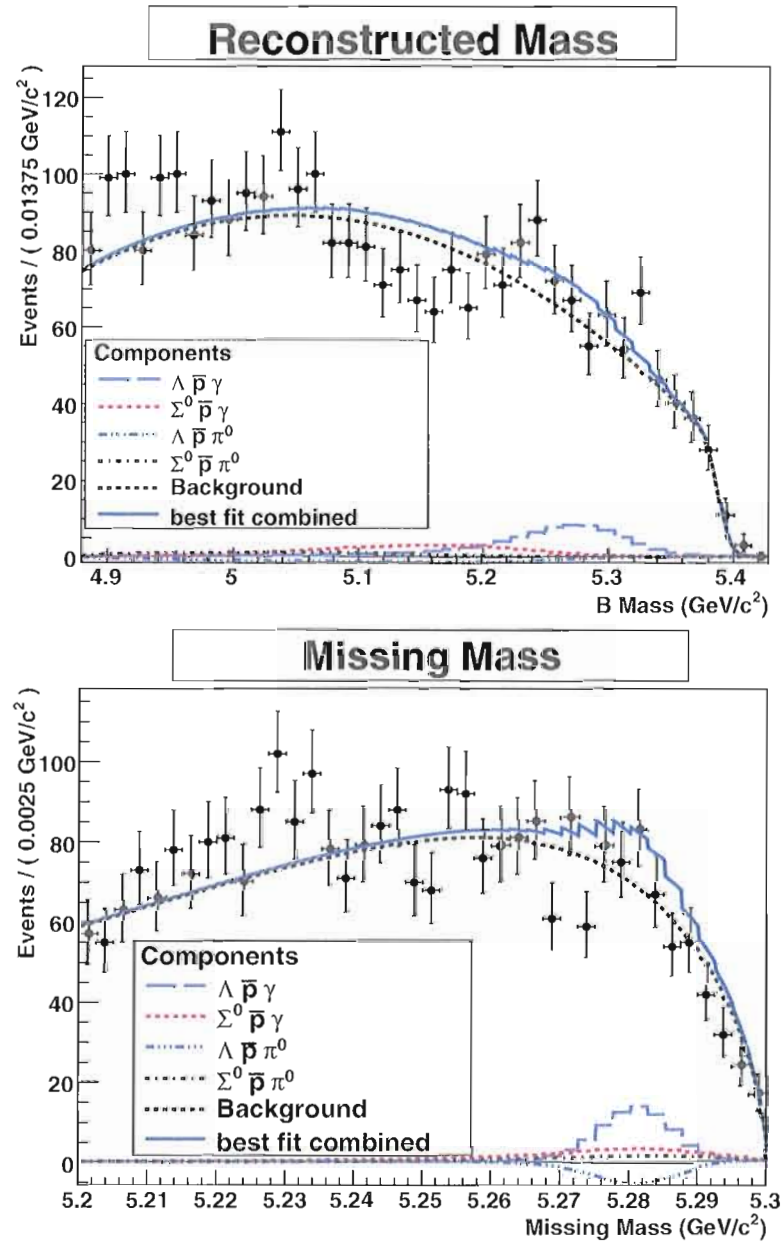


Fig. V.3: Likelihood fit to the kinematic fit variables *reconstructed candidate mass* and *missing mass* for $B^- \rightarrow \Lambda \bar{p} \gamma$ candidates in events containing two candidates

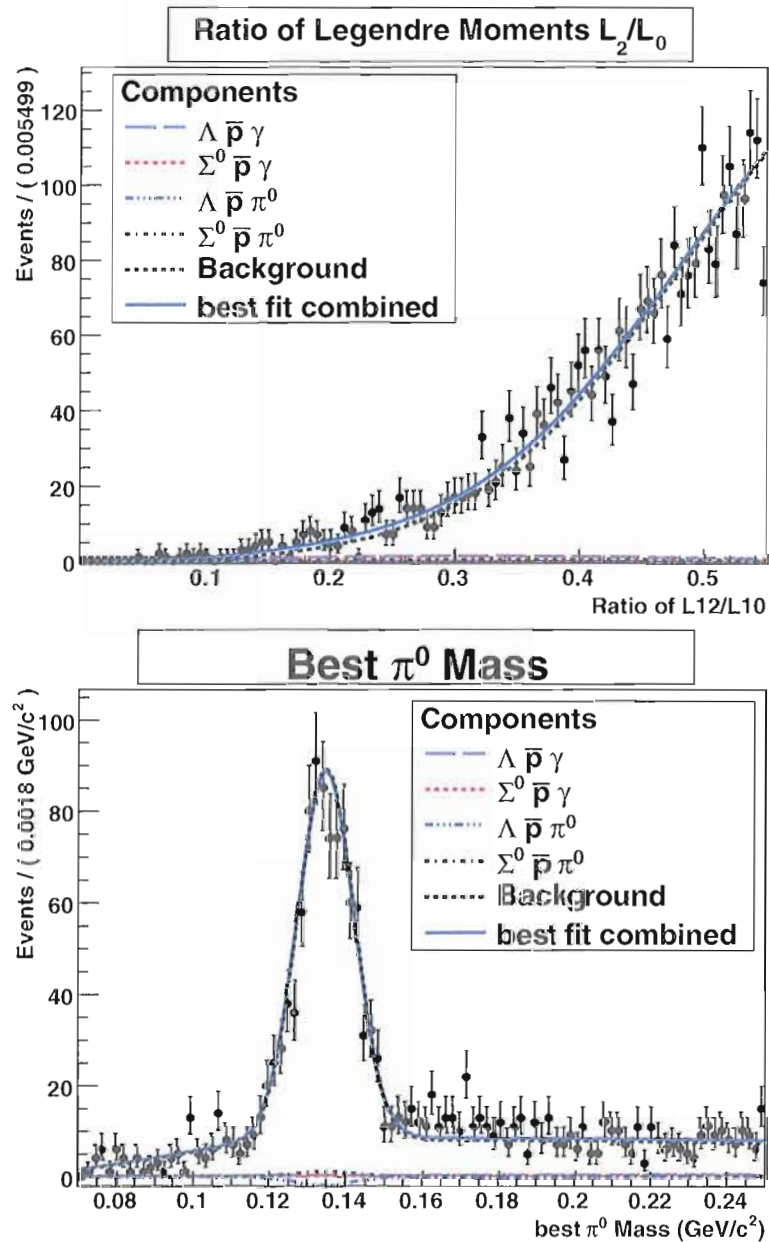


Fig. V.4: Likelihood fit to the kinematic fit variables *ratio of the Legendre Moments* L_2/L_0 and *best m_{π^0}* for $B^- \rightarrow \Lambda \bar{p} \gamma$ candidates in events containing two candidates

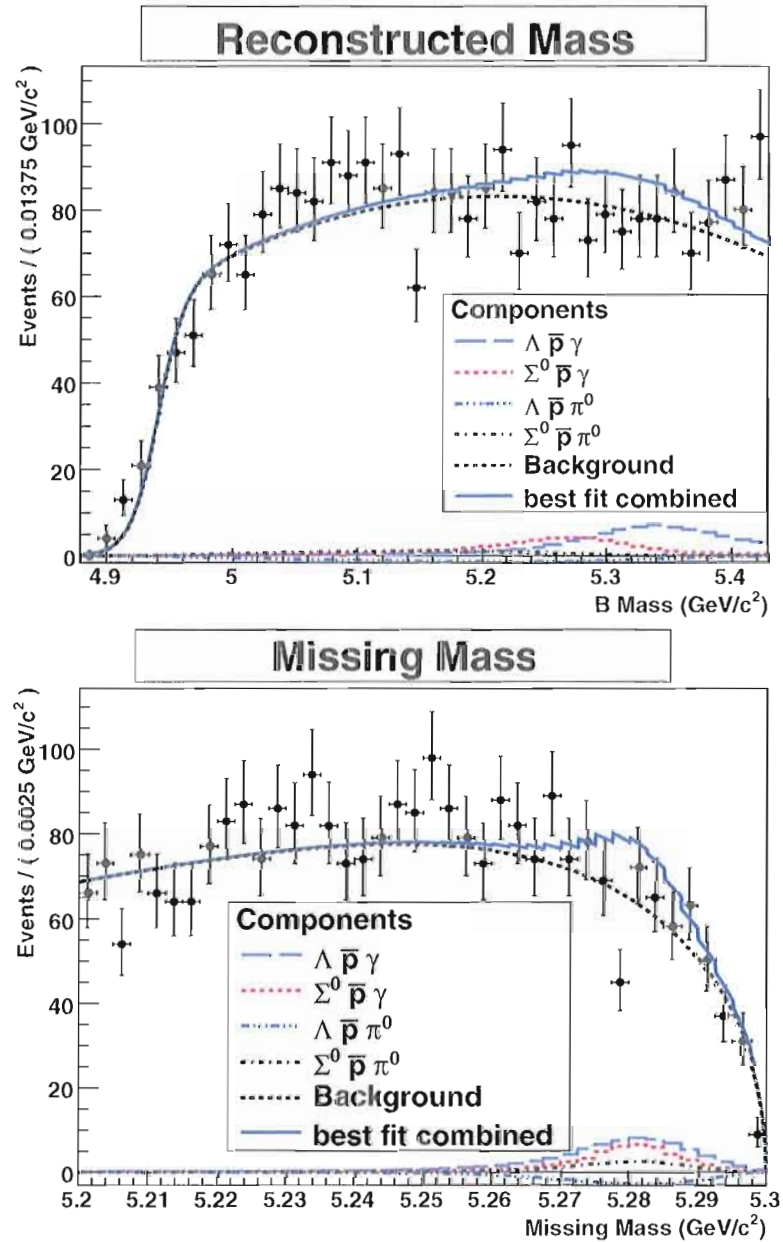


Fig. V.5: Likelihood fit to the kinematic fit variables *reconstructed candidate mass* and *missing mass* for $B^- \rightarrow \Sigma^0 \bar{p} \gamma$ candidates in two-candidate events

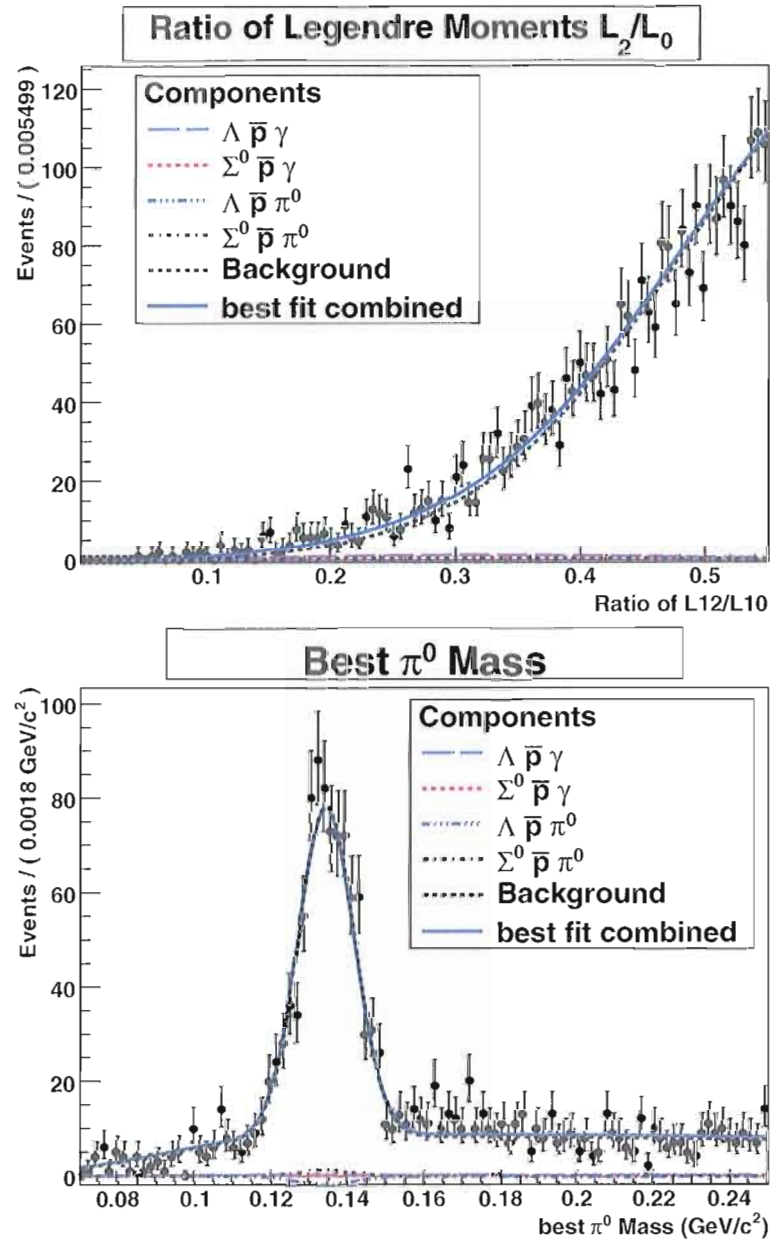


Fig. V.6: Likelihood fit to the kinematic fit variables *ratio of the Legendre Moments* L_2/L_0 and *best m_{π^0}* for $B^- \rightarrow \Sigma^0 \bar{p} \gamma$ candidates in two-candidate events

Sample	yield	error hi	error lo	significance
$B^- \rightarrow \Lambda \bar{p} \gamma$	71	12	-11	8.5
$B^- \rightarrow \Sigma^0 \bar{p} \gamma$	45	14	-13	3.2*
$B^- \rightarrow \Lambda \bar{p} \pi^0$	-34	12	-9	2.5
$B^- \rightarrow \Sigma^0 \bar{p} \pi^0$	22	16	-14	1.4*

Tab. V.1: Yields, errors and significance in the sample of two-candidate events. Significances marked with * are computed by dividing the yield by the larger of the asymmetric errors.

Sample	yield	error hi	error lo	significance
$B^- \rightarrow \Lambda \bar{p} \gamma$	37	14	-12	3.5
$B^- \rightarrow \Sigma^0 \bar{p} \gamma$	46	17	-16	3.0
$B^- \rightarrow \Lambda \bar{p} \pi^0$	-12	12	-10	1.0
$B^- \rightarrow \Sigma^0 \bar{p} \pi^0$	28	21	-18	1.3*

Tab. V.2: Yields, errors and significance in the sample of one-candidate events. Significances marked with * are computed by dividing the yield by the larger of the asymmetric errors.

samples (see C.4 and C.5), we compute the significance of the combined yield, i.e. the difference in likelihood between fixing the yield for both channels to 0 and floating them in the fit. The values for the significance of the two final states containing a pion is 2.6 for the simultaneous fit and 1.5 for the fit to the one-candidate sample only. The yields for the two final states containing a photon are relatively unchanged by fixing the yield of the two decays containing a pion, as Tables V.3 and V.4 show.

The yields can be reconstructed in bins of the invariant mass of the baryon pair by means of statistical unfolding. The results of this procedure are presented in

Sample	yield	error hi	error lo
$B^- \rightarrow \Lambda \bar{p} \gamma$	35	13	12
$B^- \rightarrow \Sigma^0 \bar{p} \gamma$	48	17	16

Tab. V.3: Yields of the likelihood fit to one-candidate events, where the yields of $B^- \rightarrow \Lambda \bar{p} \pi^0$ and $B^- \rightarrow \Sigma^0 \bar{p} \pi^0$ are fixed at 0

Sample	yield	error hi	error lo
$B^- \rightarrow \Lambda \bar{p} \gamma$	69	11	10
$B^- \rightarrow \Sigma^0 \bar{p} \gamma$	42	14	13

Tab. V.4: Yields of the likelihood fit to two-candidate events, where the yields of $B^- \rightarrow \Lambda \bar{p} \pi^0$ and $B^- \rightarrow \Sigma^0 \bar{p} \pi^0$ are fixed at 0

Figures V.7 and V.8. The sum of the bins is by design the yield in the sample.

Figure V.9 shows the sum of the yields of $B^- \rightarrow \Lambda \bar{p} \pi^0$ and $B^- \rightarrow \Sigma^0 \bar{p} \pi^0$ in the one- and two-candidate samples.

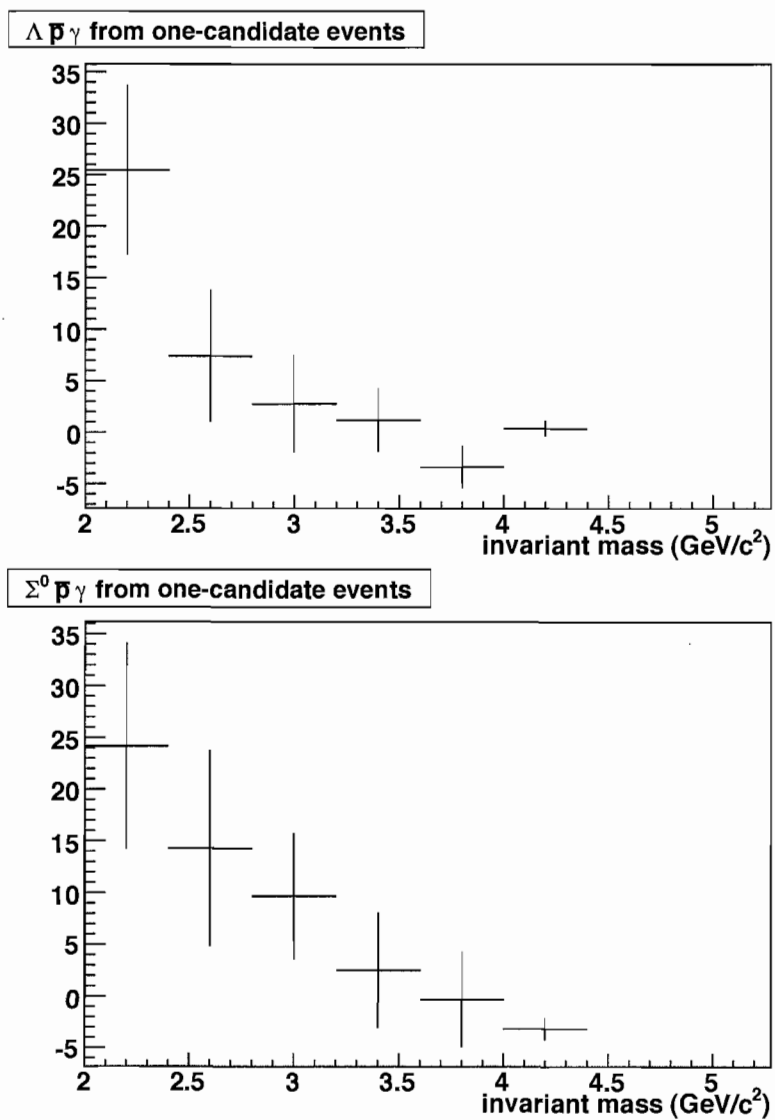


Fig. V.7: Yield bins of the invariant mass of the baryon pair in the one-candidate sample

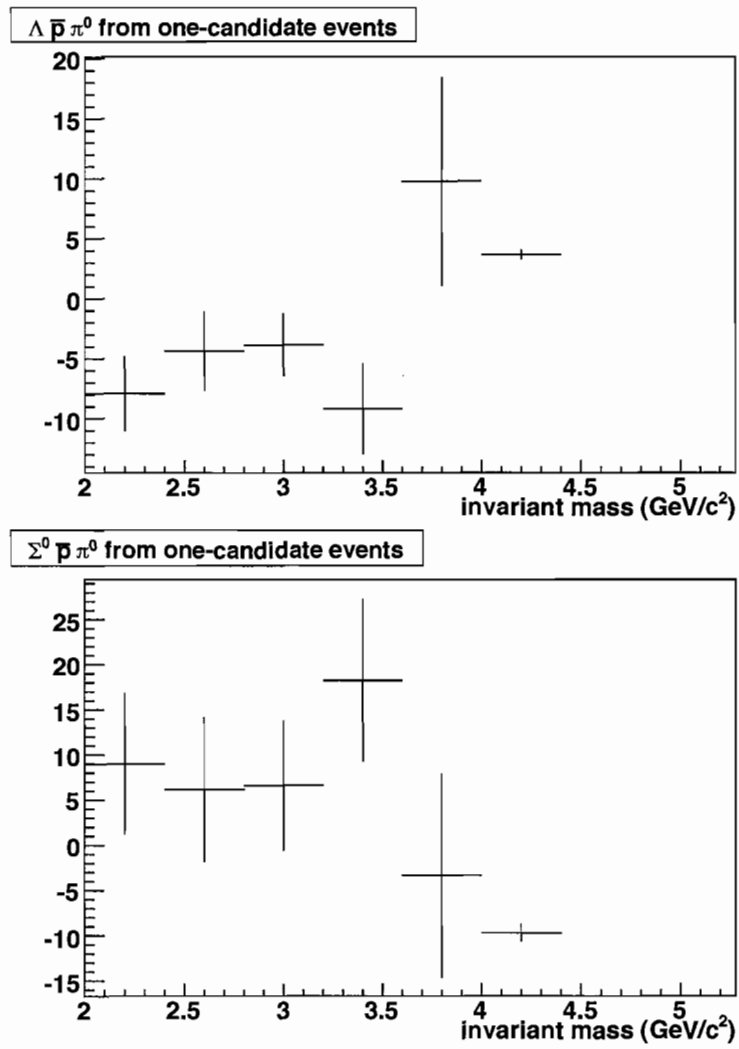


Fig. V.7: continued

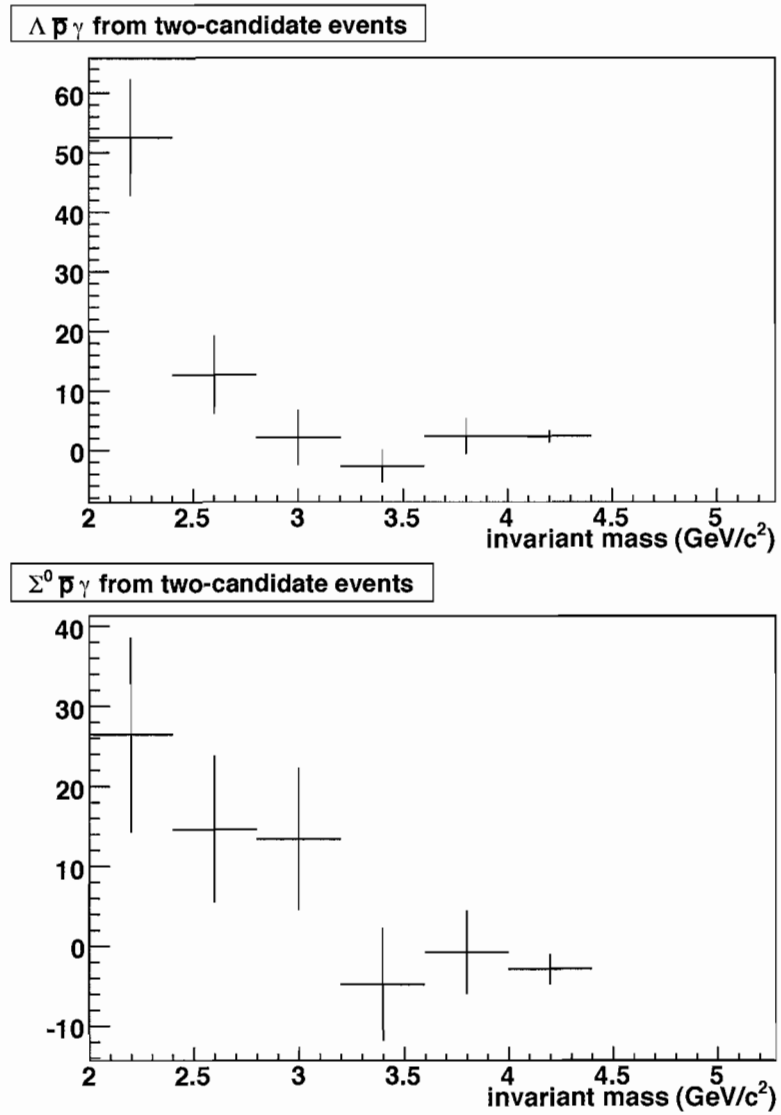


Fig. V.8: Yield bins of the invariant mass of the baryon pair in the two-candidate sample

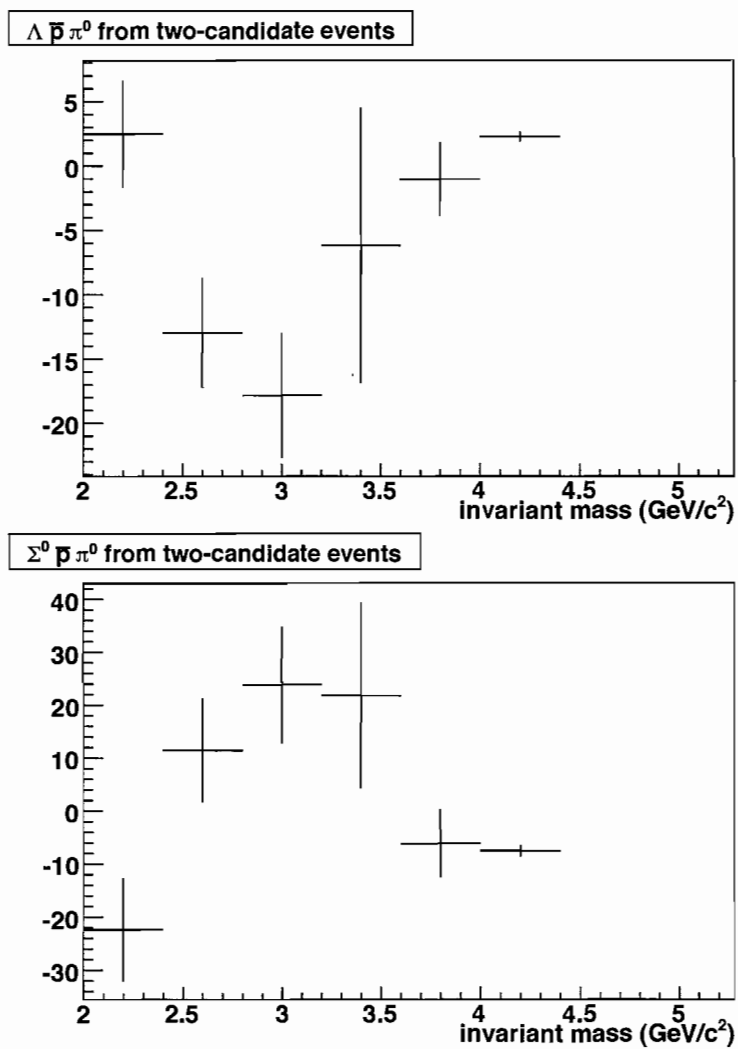


Fig. V.8: continued

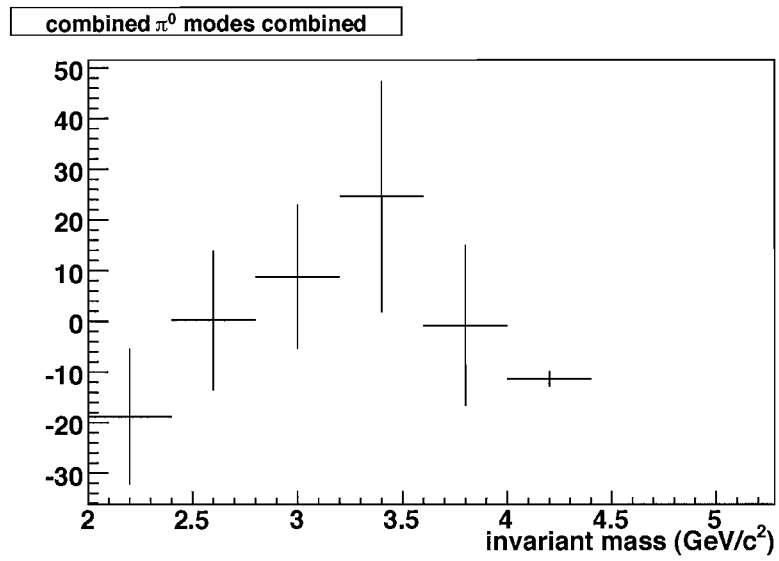


Fig. V.9: Sum of the yields of the channels $B^- \rightarrow \Lambda \bar{p} \pi^0$ and $B^- \rightarrow \Sigma^0 \bar{p} \pi^0$ in the one- and two-candidate samples combined

V.3 Reconstruction Efficiencies

In order to obtain a branching fraction for each of the modes, the yields are corrected for the reconstruction efficiency, which is obtained from the simulated samples. The efficiencies in bins of the invariant mass of the baryon pair are shown in Figure V.10 for the combination of the one-candidate and two-candidate samples. Each bin represents the number of simulated events in the final sample after all cuts and for which the invariant mass of the baryons falls between the edges of the bin, divided by the total number of simulated events for the respective channel in that bin of the invariant mass of the baryon pair.

V.4 Branching Fractions and Upper Limits

The fraction of particles of a certain species that decay into a given final state is referred to as the *branching fraction* for this final state. We compute the branching fraction of a certain channel as the yield of that channel in the data sample divided by the reconstruction efficiency, corrected for the fact that we only reconstruct Λ decays to the $p\pi^-$ final state (and the conjugate decay) and divided by the number of B^- and B^+ mesons in the *BABAR* data sample. For example:

$$\mathcal{B}(B^- \rightarrow \Lambda \bar{p} \gamma) = \frac{N_{\text{obs}}(B^- \rightarrow \Lambda \bar{p} \gamma)}{\epsilon_{\text{reco}} \mathcal{B}(\Lambda^0 \rightarrow p \pi^-) \frac{1}{2} N(B)}$$

$$\mathcal{B}(B^+ \rightarrow \bar{\Lambda}^0 p \gamma) = \frac{N_{\text{obs}}(B^+ \rightarrow \bar{\Lambda}^0 p \gamma)}{\epsilon_{\text{reco}} \mathcal{B}(\bar{\Lambda}^0 \rightarrow \bar{p} \pi^+) \frac{1}{2} N(B)}$$

For decays for which the significance of an observation is too low to quote a measurement, we compute the upper limit, i.e. the one-sided confidence interval, such that the actual yield is less than the computed upper limit with a probability of

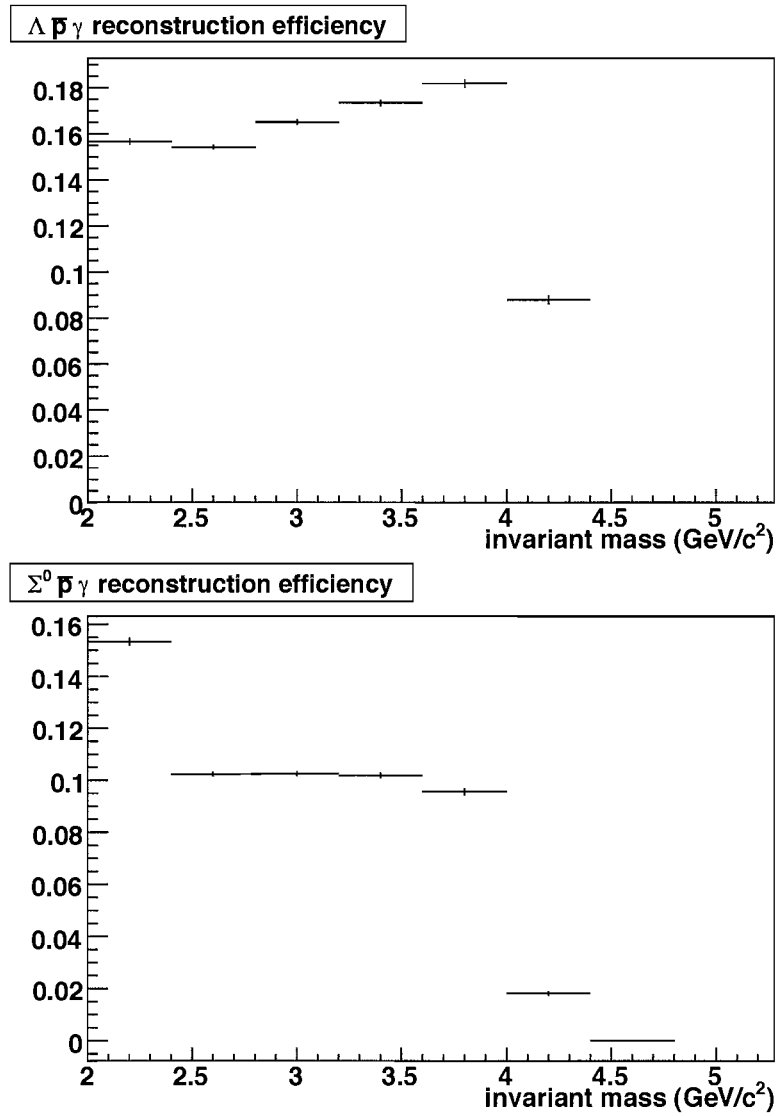


Fig. V.10: Reconstruction efficiencies of the four signal channels. The efficiency is computed on simulated events as the ratio of events in the fit region to the total number of available events for each sample

95 %. The value of the upper limit can be computed(37) as the product of the error and the inverse of the integral of the normal distribution. In order to account for negative yields, which would otherwise lead to low upper limits with high confidence, we shift the yields upward to 0, if necessary. The upper limit is then

$$N_{\text{up}} = \max(N, 0) + 1.645 * \sigma_N,$$

where N_{up} is the upper limit for the branching fraction, N is the computed value and σ_N is the error on the computed value. The efficiency correction then results in the relative abundance of events in the *BABAR* data sample and corresponds to the branching fractions reported in Table V.5. As can be gathered from Table IV.11, the ratio of the number of two-candidate events to one-candidate events is 1.17 for simulated events, but 1.33 for data. In order to minimize the effect of discrepancies between the simulation and data on the measurement of the branching fraction, only the combined result will be quoted here, i.e. the one-candidate and two-candidate samples are combined in the computation of the branching fraction.

The reconstruction efficiency-corrected sPlots for the decay channels $B^- \rightarrow \Lambda \bar{p} \gamma$ and $B^- \rightarrow \Sigma^0 \bar{p} \gamma$ are shown in Figure V.11. The predictions of the phasespace and pole models are overlaid in Figure V.11a.

$B^- \rightarrow \Lambda \bar{p} \gamma$	$(2.76 \pm 0.47 \pm 0.33) \times 10^{-6}$
$B^- \rightarrow \Sigma^0 \bar{p} \gamma$	$(1.93 \pm 1.04 \pm 1.3) \times 10^{-6}$
$B^- \rightarrow \Lambda \bar{p} \gamma$	$< 2.3 \times 10^{-6}$
$B^- \rightarrow \Sigma^0 \bar{p} \gamma$	$< 22 \times 10^{-6}$

Tab. V.5: Branching fractions and upper limits of the signal modes in data samples accumulated in *BABAR* runs 1-5

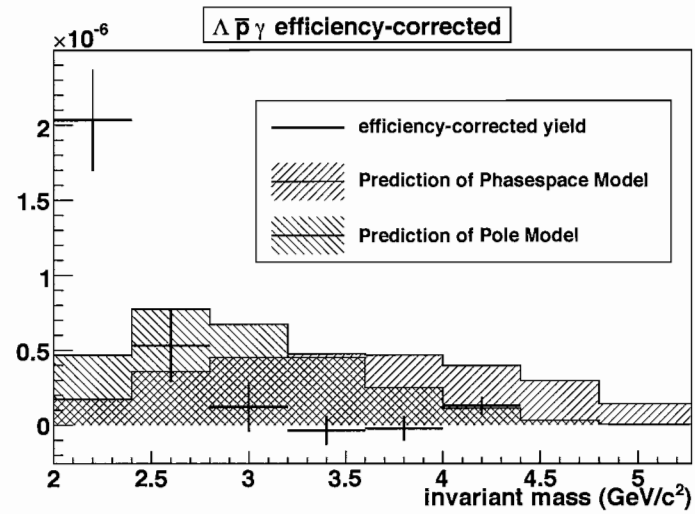
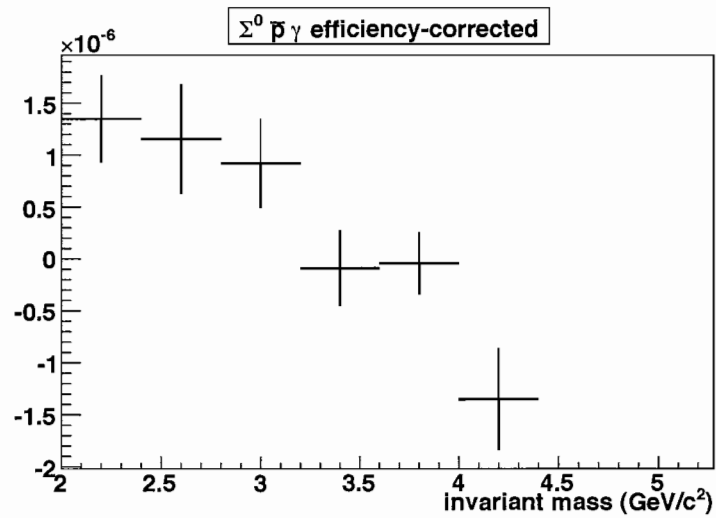
(a) $B^- \rightarrow \Lambda \bar{p} \gamma$ (b) $B^- \rightarrow \Sigma^0 \bar{p} \gamma$

Fig. V.11: Efficiency-corrected sPlots of the invariant mass of the baryon pair. The result of the fits to both data sets are combined

V.5 Discussion

V.5.1 Comparison with Expectation

Based on validation on the simulated samples, it was expected that the two data samples – the one-candidate sample and the two-candidate sample – have $B^- \rightarrow \Lambda \bar{p} \gamma$ candidates in roughly equal amounts, while the sample containing events with two candidates was expected to be more abundant in $B^- \rightarrow \Sigma^0 \bar{p} \gamma$ candidates (see Table IV.11). The fact that the data samples show the relative abundances in Tables V.1 and V.2 is a deviation from this expectation and may be related to discrepancies between simulation and experiment that do not affect the overall validity of the result.

V.5.2 Comparison with Other Experimental Results

The results presented here influence the published results of the inclusive branching fraction of the decay $b \rightarrow s \gamma$ at 1.3 per cent, which is larger than the achievable precision of the analyses, and establish that decays of this transition to baryonic final states occur at rates that can not only be measured at the B factories, but will have to be taken into account by other analyses as possible backgrounds. While the analysis on the presented data set does not allow for a precision measurement of the decay rates, it establishes the $B^- \rightarrow \Sigma^0 \bar{p} \gamma$ decay at a branching ratio that surpasses that of the decay $B^- \rightarrow \Lambda \bar{p} \gamma$. Because of the similar shape of the two kinematic variables that are most commonly used in measurements of branching fractions, the missing mass and the reconstructed candidate mass, future analyses will have to be careful to seriously consider one decay as background to the other and vice versa.

Because of the low significance and the fact that the yields as reported by the likelihood fit for $B^- \rightarrow \Lambda \bar{p} \pi^0$ is negative and of the same magnitude as the yield for $B^- \rightarrow \Sigma^0 \bar{p} \pi^0$, only a combined result is reported here. The currently best measure-

ment of the Belle collaboration(33) of $B^- \rightarrow \Lambda \bar{p} \pi^0$ is $(3.00^{+0.61}_{-0.53} \pm 0.33) \times 10^{-6}$ while an upper limit on $B^- \rightarrow \Sigma^0 \bar{p} \pi^0$ can be estimated from the analysis of the decay $\bar{B}^0 \rightarrow \Sigma^0 \bar{p} \pi^-$; in the factorization model, the branching fraction of $B^- \rightarrow \Sigma^0 \bar{p} \pi^0$ is 1/2 that of $\bar{B}^0 \rightarrow \Sigma^0 \bar{p} \pi^-$ due to isospin symmetry. From the Belle result(17) $\mathcal{B}(\bar{B}^0 \rightarrow \Sigma^0 \bar{p} \pi^-) < 3.8 \times 10^{-6}$, we obtain $\mathcal{B}(B^- \rightarrow \Sigma^0 \bar{p} \pi^0) < 1.9 \times 10^{-6}$. Both of these results are compatible with the results of this analysis. The measurement of $\mathcal{B}(B^- \rightarrow \Lambda \bar{p} \gamma) = (2.45^{+0.44}_{-0.38} \pm 0.22) \times 10^{-6}$ by the Belle collaboration(33) agrees with result of this analysis within errors, and the observation of $B^- \rightarrow \Sigma^0 \bar{p} \gamma$ does not contradict the upper limit with 90 % confidence level established by the Belle collaboration $\mathcal{B}(B^- \rightarrow \Sigma^0 \bar{p} \gamma) < 4.6 \times 10^{-6}$. While the statistical significance of the yield of about 3σ gives a strong indication of a signal, we cannot quote a statistically significant measurement of a branching fraction. Therefore we also give an upper limit. The yields of both decays $B^- \rightarrow \Lambda \bar{p} \pi^0$ and $B^- \rightarrow \Sigma^0 \bar{p} \pi^0$ are not statistically significant and we give an upper limit on these decays. The relevant branching fractions and upper limits by established by other analyses are summarized in Table V.6. It should be noted that the CLEO collaboration has also established limits on the decays $B^- \rightarrow \Lambda \bar{p} \gamma$ and $B^- \rightarrow \Sigma^0 \bar{p} \gamma$ (38) of $\mathcal{B}(B^- \rightarrow \Lambda \bar{p} \gamma) + 0.3\mathcal{B}(B^- \rightarrow \Sigma^0 \bar{p} \gamma) < 3.3 \times 10^{-6}$ and $\mathcal{B}(B^- \rightarrow \Sigma^0 \bar{p} \gamma) + 0.4\mathcal{B}(B^- \rightarrow \Lambda \bar{p} \gamma) < 7.9 \times 10^{-6}$ and they agree with both the results by the Belle collaboration and this analysis within errors.

decay	BF / upper limit (10^{-6})	
	current result	this analysis
$B^- \rightarrow \Lambda \bar{p} \gamma$	$2.45^{+0.44}_{-0.38} \pm 0.22$	$2.76 \pm 0.47 \pm 0.33$
$B^- \rightarrow \Sigma^0 \bar{p} \gamma$	< 4.6	$1.93 \pm 1.04 \pm 1.3 (< 5.8)$
$B^- \rightarrow \Lambda \bar{p} \pi^0$	$3.00^{+0.61}_{-0.53} \pm 0.33$	< 2.3
$B^- \rightarrow \Sigma^0 \bar{p} \pi^0$	< 1.9 (isospin)	< 22

Tab. V.6: Comparison of this analysis with current results

The distribution of the invariant mass of the baryon system displays the peaking behavior that has been reported by other analyses of B decays to baryonic final states at both the Belle and the *BABAR* collaborations (16; 33; 17; 39; 35). The distribution of the invariant mass of the baryon pair in the decay $B^- \rightarrow \Sigma^0 \bar{p} \gamma$ displays a peaking behavior but shows otherwise little resemblance to the sharp peak in $B^- \rightarrow \Lambda \bar{p} \gamma$.

Because of the peaking nature of the distribution and the low yield, only very little information about the Fermi motion of the b quark inside the meson can be gained from the photon energy spectrum in the range between 1 and 1.7 GeV that is not accessible experimentally to other analyses of $b \rightarrow s \gamma$ (40; 41; 42).

V.5.3 Comparison with Theory

The measured branching fraction of $B^- \rightarrow \Lambda \bar{p} \gamma$ is in excellent agreement with the existing measurement by the Belle collaboration. The values for both measurements is slightly higher than a computation in perturbative QCD(3), but agree with a pole model treatment(23). It is evident in Figure V.11a that the shape of the distribution of the invariant mass of the baryon pair is inconsistent with the prediction of the pole model in the case of $B^- \rightarrow \Lambda \bar{p} \gamma$. For $B^- \rightarrow \Sigma^0 \bar{p} \gamma$, the shape seems to be more consistent, but more data is needed to perform a significant comparison. While no value for the branching fraction of $B^- \rightarrow \Sigma^0 \bar{p} \gamma$ can be quoted with confidence, the statistical significance of the observation of this decay indicates an incompatibility with the prediction of 10^{-9} of the pole model, because the predicted value is well below the sensitivity of this analysis. The prediction of $(1.2 \pm 1.2) \times 10^{-7}$ from QCD counting rules, albeit lower than the observed central value, is consistent with the observation within errors. The predicted shape of the invariant mass of the $\Lambda - p$ system agrees better with the observation than for the pole model.

V.6 Conclusions

An analysis of the branching fraction and decay dynamics of the exclusive decays $B^- \rightarrow \Lambda \bar{p} \gamma$, $B^- \rightarrow \Sigma^0 \bar{p} \gamma$, $B^- \rightarrow \Lambda \bar{p} \pi^0$ and $B^- \rightarrow \Sigma^0 \bar{p} \pi^0$ has been presented. The analyzed data sample comprises data of collisions at the $\Upsilon(4S)$ resonance at the PEP-II facility at SLAC, collected by the *BABAR* collaboration during the years 2001-2007. This is the first indication of the decay $B^- \rightarrow \Sigma^0 \bar{p} \gamma$, and the first time the distribution of the invariant mass of this decay has been analyzed.

The analysis of the invariant mass of the baryon-baryon system was validated on detailed studies on Monte Carlo simulations based on theoretical treatments of the respective decays, which has not been done in this form at the *BABAR* experiment, and the method to extract the information about the distribution of this variable takes into account the full information of the likelihood fit.

The analysis was carried out on a subset of the data sample that is available today. Including the additional data in the future is going to reduce the statistical error on the branching fraction measurements, which is the dominant source of uncertainty in the present analysis. Additionally, future iterations of this analysis may benefit from improvements to the selection of tracks from displaced vertices, such as those from a Λ decay, that became available too late to be included in this work. The statistical impact of the additional data on this analysis is about 5 %.

We are looking forward to an analysis of these and similar baryonic final states of the $b \rightarrow s \gamma$ transition at B factories with higher luminosities, that will further help develop the theoretical treatment of these decays, establish the validity of the pole model approach versus the computation in perturbative QCD and deepen the understanding of the decay dynamics involving baryons.

APPENDIX A

LIKELIHOOD FIT IN THE SIGNAL REGION OF $B^- \rightarrow \Lambda \bar{p} \gamma$

In order to better evaluate the validity of the fit, Figures A.1 and A.2, A.3 and A.4, and A.5 and A.6 show the best likelihood shape and data events, where $5.27 < m_{\text{miss.}} < 5.3$. The yields for the $B^- \rightarrow \Lambda \bar{p} \gamma$ sample in these events are $36 + 13 - 12$ for the one-candidate events and $56 + 10 - 9$ for the two-candidate events, respectively.

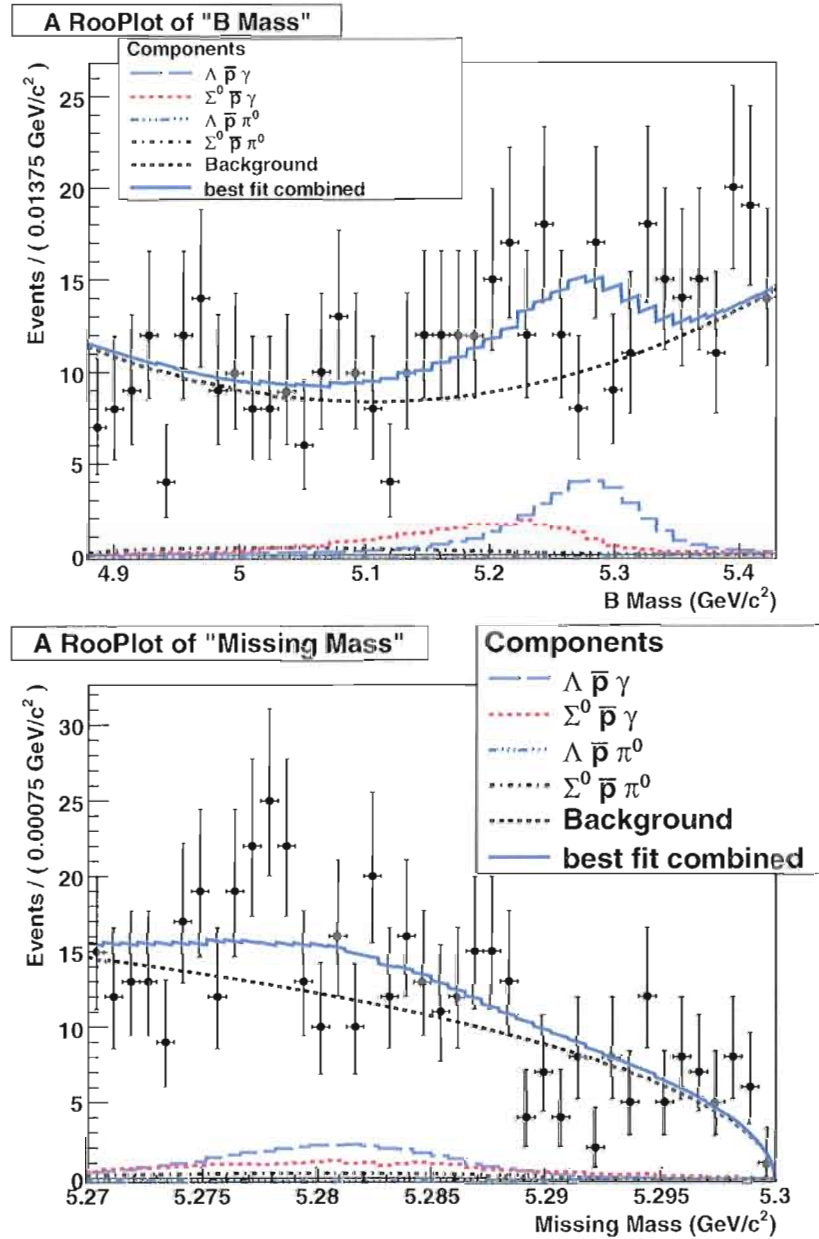


Fig. A.1: Likelihood fit to the kinematic fit variables *reconstructed candidate mass* and *missing mass* in events containing only one candidate

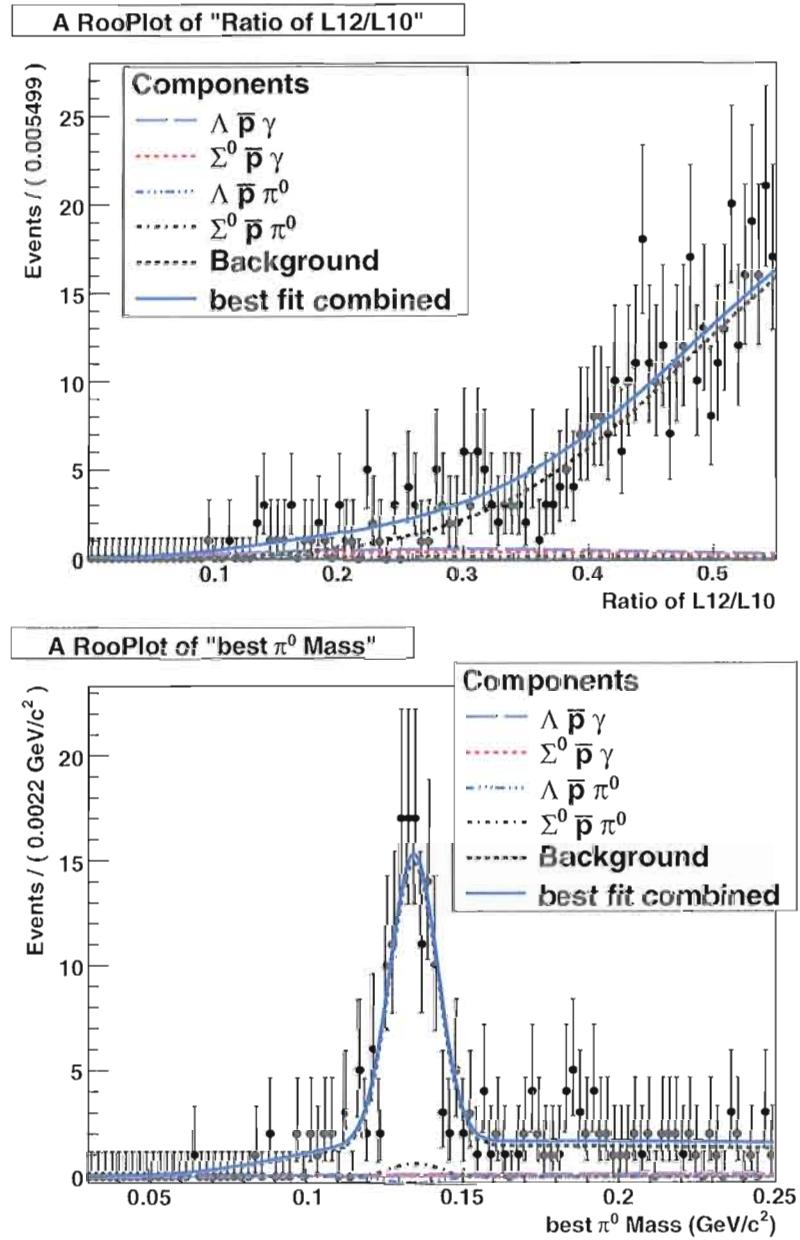


Fig. A.2: Likelihood fit to the kinematic fit variables *ratio of the Legendre Moments* L_2/L_0 and *best m_{π^0}* in events containing only one candidate

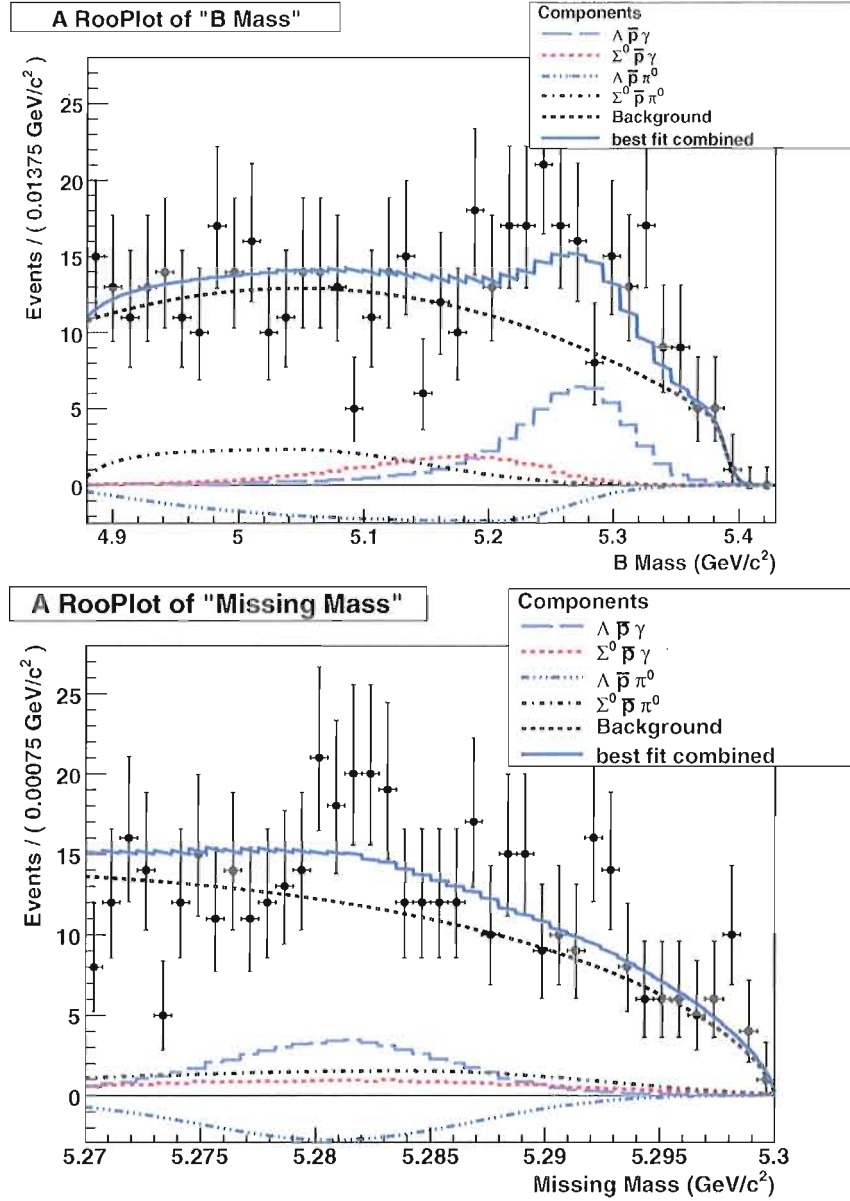


Fig. A.3: Likelihood fit to the kinematic fit variables *reconstructed candidate mass* and *missing mass* for $B^- \rightarrow \Lambda \bar{p} \gamma$ candidates in events containing two candidates

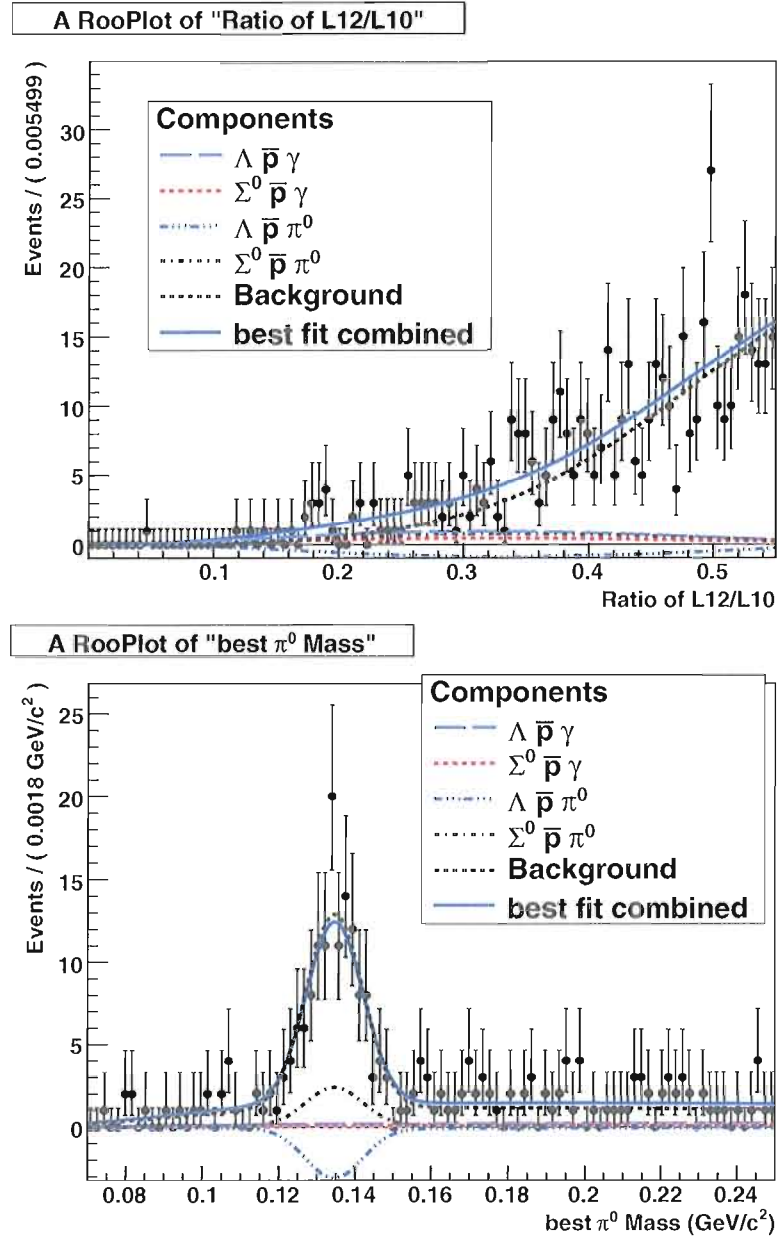


Fig. A.4: Likelihood fit to the kinematic fit variables *ratio of the Legendre Moments* L_2/L_0 and *best m_{π^0}* for $B^- \rightarrow \Lambda \bar{p} \gamma$ candidates in events containing two candidates

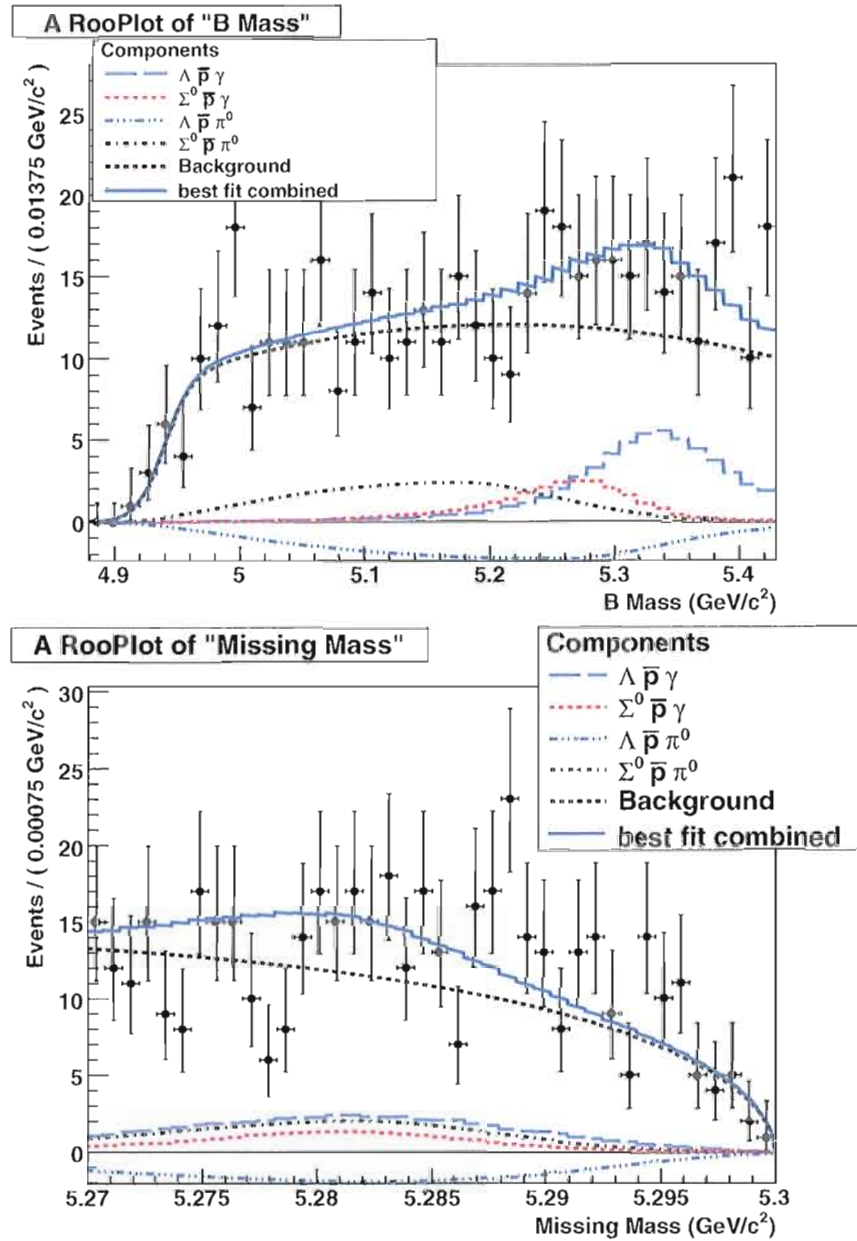


Fig. A.5: Likelihood fit to the kinematic fit variables *reconstructed candidate mass* and *missing mass* for $B^- \rightarrow \Sigma^0 \bar{p} \gamma$ candidates in two-candidate events

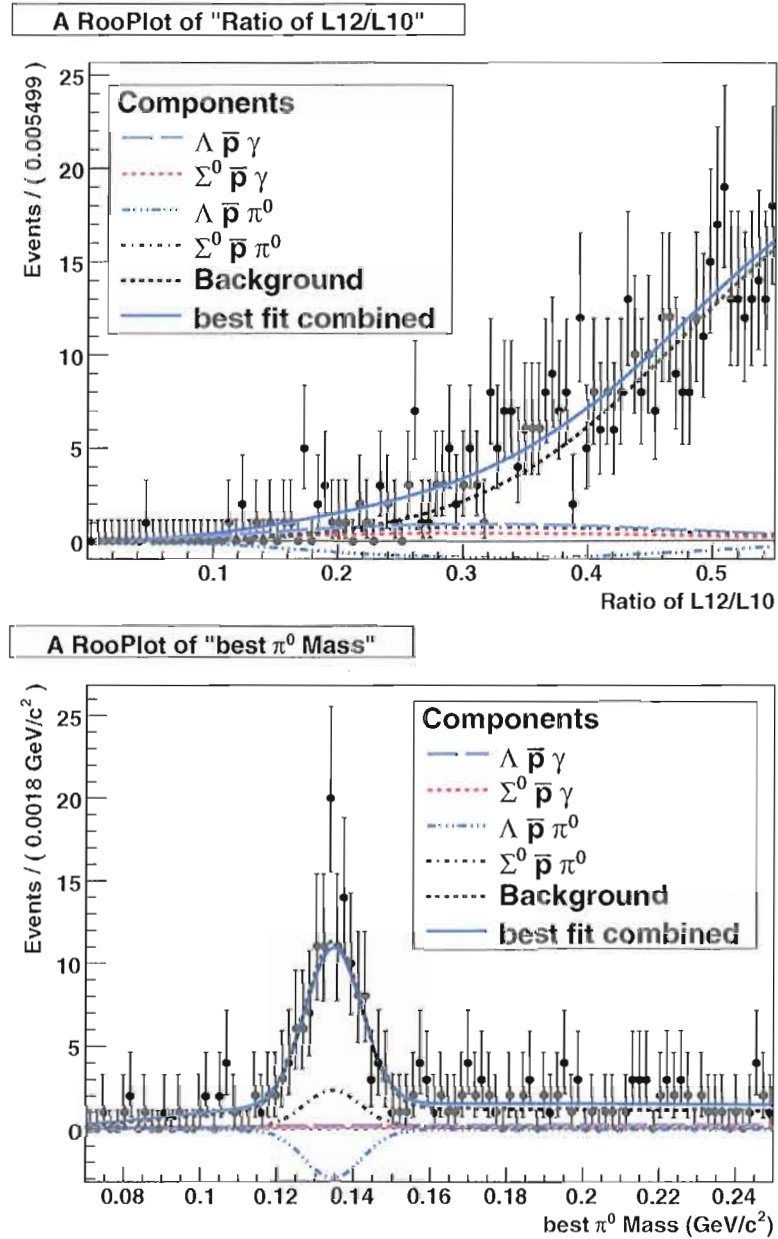
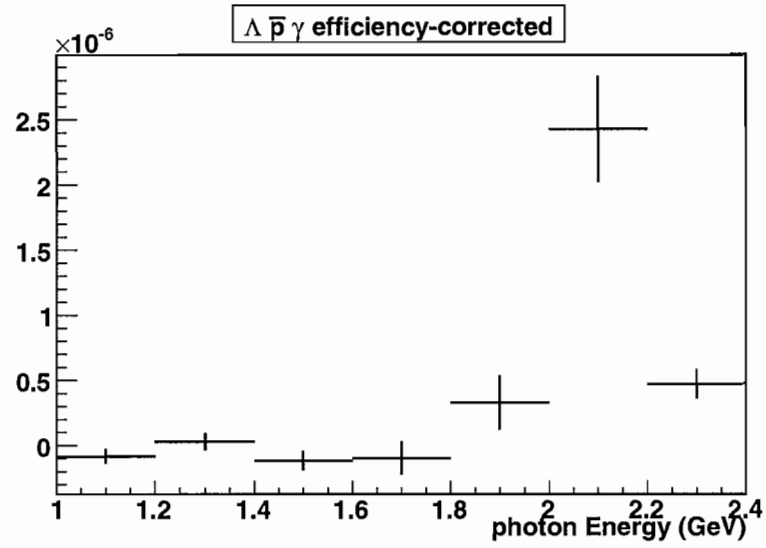
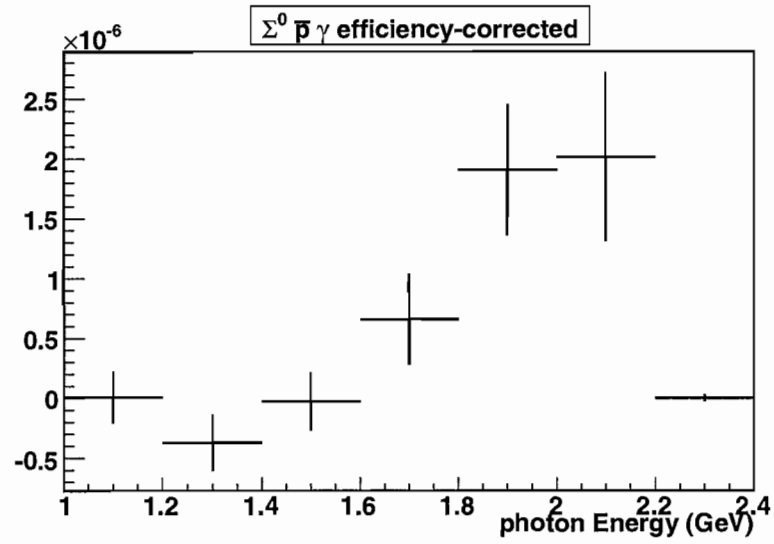


Fig. A.6: Likelihood fit to the kinematic fit variables *ratio of the Legendre Moments* L_2/L_0 and *best m_{π^0}* for $B^- \rightarrow \Sigma^0 \bar{p} \gamma$ candidates in two-candidate events

APPENDIX B

SLOTS OF THE PHOTON ENERGY

For decays of the kind $b \rightarrow s\gamma$ to baryons, the energy of the photon is of course highly correlated with the invariant mass of the baryon pair. However, because of the finite width of the reconstructed B mass the distribution of the photon energy cannot be computed from the distribution of the invariant mass of the baryon pair in a straightforward way. Figure B.1 shows sPlots of the distribution of the energy of the photon from $b \rightarrow s\gamma$.

(a) $B^- \rightarrow \Lambda \bar{p} \gamma$ (b) $B^- \rightarrow \Sigma^0 \bar{p} \gamma$ Fig. B.1: sPlots of the photon energy in $B^- \rightarrow \Lambda \bar{p} \gamma$ and $B^- \rightarrow \Sigma^0 \bar{p} \gamma$ events

APPENDIX C

CORRELATION OF THE FIT VARIABLES

The correlation of the fit variables is shown in Tables C.1, C.2 and C.3. As explained in section IV.5.5, correlations between $m_{\text{rec.}}$ and $m_{\text{miss.}}$ are taken into account for the four signal modes, as they are modeled with a 2d histogram of simulated events. Correlations between other pairs of variables in signal events and between all variables in background events are not modeled in the fit, however.

Tables C.4 and C.5 show the correlation coefficients between the yields as obtained from the extended likelihood fit to the two-candidate and one-candidate samples, respectively. The sPlots method takes these correlations into account in the covariance matrix. Large correlations between fit parameters have a negative effect on the stability of the minimization technique used to determine the extremal value, but do not affect the value of the extremum itself.

	$m_{\text{rec.}}$	$m_{\text{miss.}}$	L_2/L_0	m_{π^0}
$m_{\text{rec.}}$	1	0.027	0.043	0.027
$m_{\text{miss.}}$	0.027	1	-0.023	0.006
L_2/L_0	0.043	-0.023	1	-0.123
m_{π^0}	0.027	0.006	-0.123	1

Tab. C.1: Correlation of fit variables in one-candidate events

	$m_{\text{rec.}}$	$m_{\text{miss.}}$	L_2/L_0	m_{π^0}
$m_{\text{rec.}}$	1	0.053	-0.034	0.075
$m_{\text{miss.}}$	0.053	1	-0.026	0.000
L_2/L_0	-0.034	-0.026	1	-0.163
m_{π^0}	0.075	0.000	-0.163	1

Tab. C.2: Correlation of fit variables in $B^- \rightarrow \Lambda \bar{p} \gamma$ candidates in two-candidate events

	$m_{\text{rec.}}$	$m_{\text{miss.}}$	L_2/L_0	m_{π^0}
$m_{\text{rec.}}$	1	0.081	-0.016	0.075
$m_{\text{miss.}}$	0.081	1	-0.057	0.018
L_2/L_0	-0.016	-0.057	1	-0.173
m_{π^0}	0.075	0.018	-0.173	1

Tab. C.3: Correlation of fit variables in $B^- \rightarrow \Sigma^0 \bar{p} \gamma$ candidates in two-candidate events

decay	$B^- \rightarrow \Lambda \bar{p} \gamma$	$B^- \rightarrow \Sigma^0 \bar{p} \gamma$	$B^- \rightarrow \Lambda \bar{p} \pi^0$	$B^- \rightarrow \Sigma^0 \bar{p} \pi^0$	background
$B^- \rightarrow \Lambda \bar{p} \gamma$	1	-0.48	-0.10	0.12	-0.05
$B^- \rightarrow \Sigma^0 \bar{p} \gamma$	-0.48	1	0.06	-0.19	-0.12
$B^- \rightarrow \Lambda \bar{p} \pi^0$	-0.10	0.06	1	-0.78	-0.00
$B^- \rightarrow \Sigma^0 \bar{p} \pi^0$	0.083	-0.133	-0.78	1	-0.11
background	-0.05	-0.12	-0.00	-0.11	1

Tab. C.4: Correlation of the yields in the simultaneous fit

decay	$B^- \rightarrow \Lambda \bar{p} \gamma$	$B^- \rightarrow \Sigma^0 \bar{p} \gamma$	$B^- \rightarrow \Lambda \bar{p} \pi^0$	$B^- \rightarrow \Sigma^0 \bar{p} \pi^0$	background
$B^- \rightarrow \Lambda \bar{p} \gamma$	1	-0.56	-0.14	0.11	-0.03
$B^- \rightarrow \Sigma^0 \bar{p} \gamma$	-0.56	1	-0.00	-0.11	-0.10
$B^- \rightarrow \Lambda \bar{p} \pi^0$	-0.14	-0.00	1	-0.83	0.13
$B^- \rightarrow \Sigma^0 \bar{p} \pi^0$	0.11	-0.11	-0.83	1	-0.10
background	-0.03	-0.10	0.13	-0.10	1

Tab. C.5: Correlation of the fit variables in the fit to the one-candidate sample

APPENDIX D

ADDITIONAL PLOTS OF THE FIT VARIABLES

In order to emphasize the region of the function that has more structure and is harder to fit, the plotted range of the best π^0 mass was reduced. As a cross-check, Figures D.1, D.2 and D.3 show additional plots over the whole range of the π^0 mass for one-candidate events, $B^- \rightarrow \Lambda \bar{p} \gamma$ candidates and $B^- \rightarrow \Sigma^0 \bar{p} \gamma$ candidates in two-candidate events, respectively.

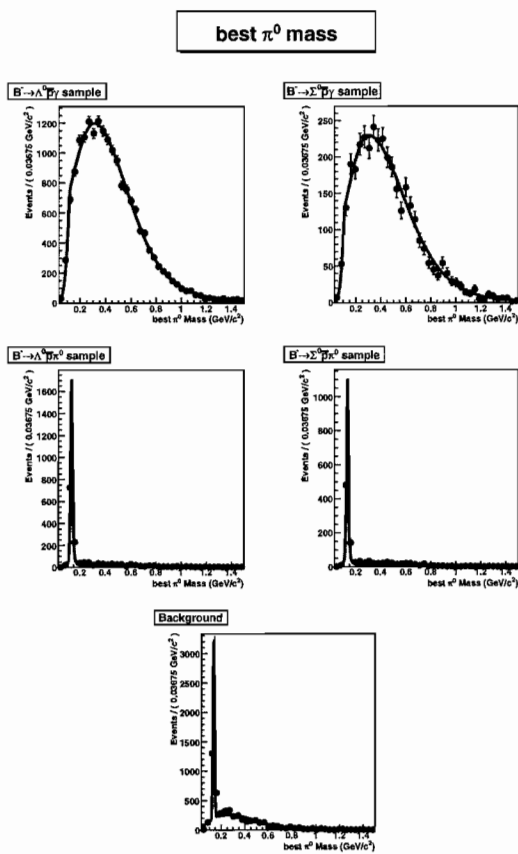


Fig. D.1: Fit shape for the best π^0 mass of one-candidate $B^- \rightarrow \bar{\Lambda} \pi^0 \gamma$ events

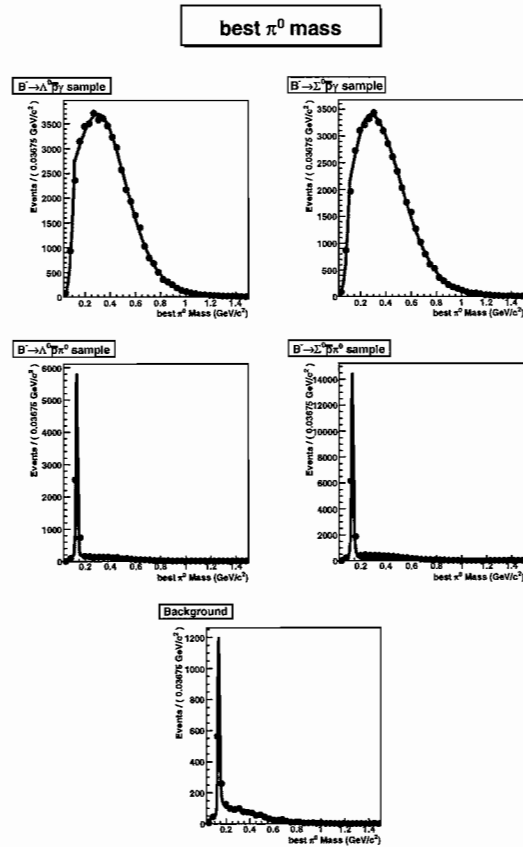


Fig. D.2: Fit shape for the best π^0 mass of $B^- \rightarrow \Lambda \bar{p} \gamma$ candidates in events that also contain a $B^- \rightarrow \Sigma^0 \bar{p} \gamma$ candidates

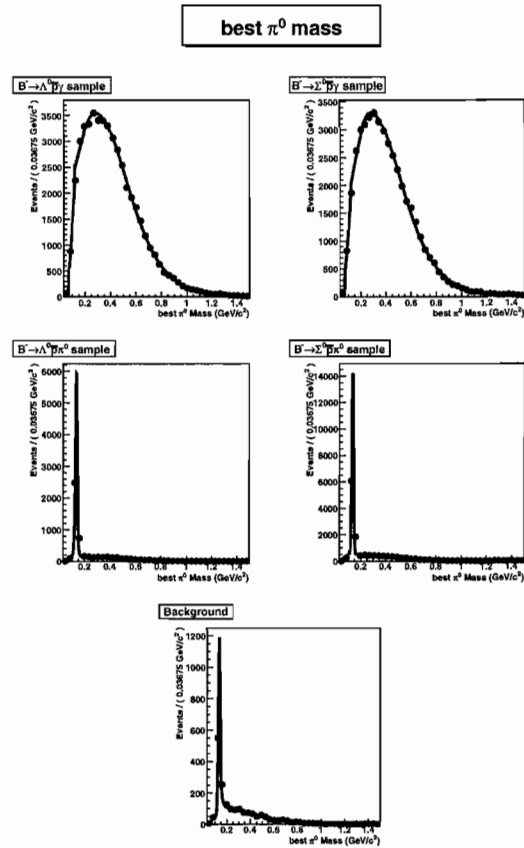


Fig. D.3: Fit shape for the best π^0 mass of $B^- \rightarrow \Sigma^0 \bar{p} \gamma$ candidates in events that also contain a $B^- \rightarrow \Lambda \bar{p} \gamma$ candidates

APPENDIX E

ALTERNATIVE FIT SHAPES

For the $B^- \rightarrow \Lambda \bar{p} \pi^0$ and $B^- \rightarrow \Sigma^0 \bar{p} \pi^0$, the variables m_{miss} and m_{rec} are parametrized with the “Cruiff” function (eq. IV.3). This function does a much better job of approximating the data distributions for both variables than a more commonly used “Crystal Ball” parametrization, which is shown in Figure E.1. For $B^- \rightarrow \Sigma^0 \bar{p} \gamma$ events reconstructed as $B^- \rightarrow \Lambda \bar{p} \gamma$, even the Cruiff function does not approximate the data points appropriately, as shown in figure E.2. This fact, together with apparent correlation in the fit variables that are not modeled by this parametrization (Table H.2), causes poor performance of the fit and embedded toy fits clearly show that an accurate yield cannot be extracted from the data this way (E.4). Table E.1 and Figure E.3 summarize the choices of parameterization for events reconstructed as $B^- \rightarrow \Lambda \bar{p} \gamma$.

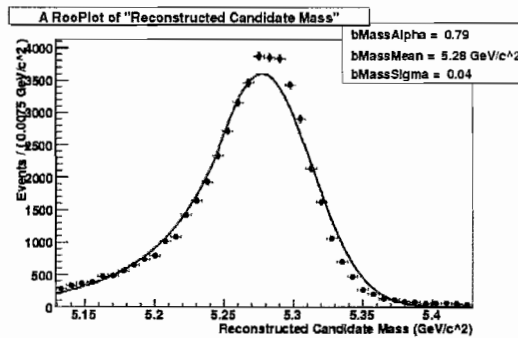


Fig. E.1: Parametrization of m_{rec} in $B^- \rightarrow \Lambda \bar{p} \gamma$ events with a “Crystal Ball” shape

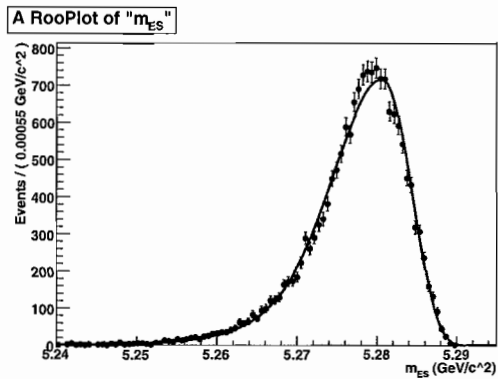


Fig. E.2: Parametrization of misreconstructed $B^- \rightarrow \Sigma^0 \bar{p} \gamma$ events with a Cruijff function

Sample Variable	$m_{\text{rec.}}$	$m_{\text{miss.}}$	“best π^0 mass”	L_2/L_0
$B^- \rightarrow \Lambda \bar{p} \gamma$	Cruijff	Cruijff	Steps	Steps
$B^- \rightarrow \Sigma^0 \bar{p} \gamma$	KEYS	Cruijff	Steps	Steps
$B^- \rightarrow \Lambda \bar{p} \pi^0$	Cruijff	Cruijff	Cruijff	Steps
$B^- \rightarrow \Sigma^0 \bar{p} \pi^0$	Cruijff	Cruijff	Cruijff	Steps
background	Argus	Chebychev	Cruijff + Chebychev	Steps

Tab. E.1: Parameterization of the four samples – $m_{\text{rec.}}$, $m_{\text{miss.}}$. Toy studies based on this parameterization show that it doesn’t model the data sufficiently.

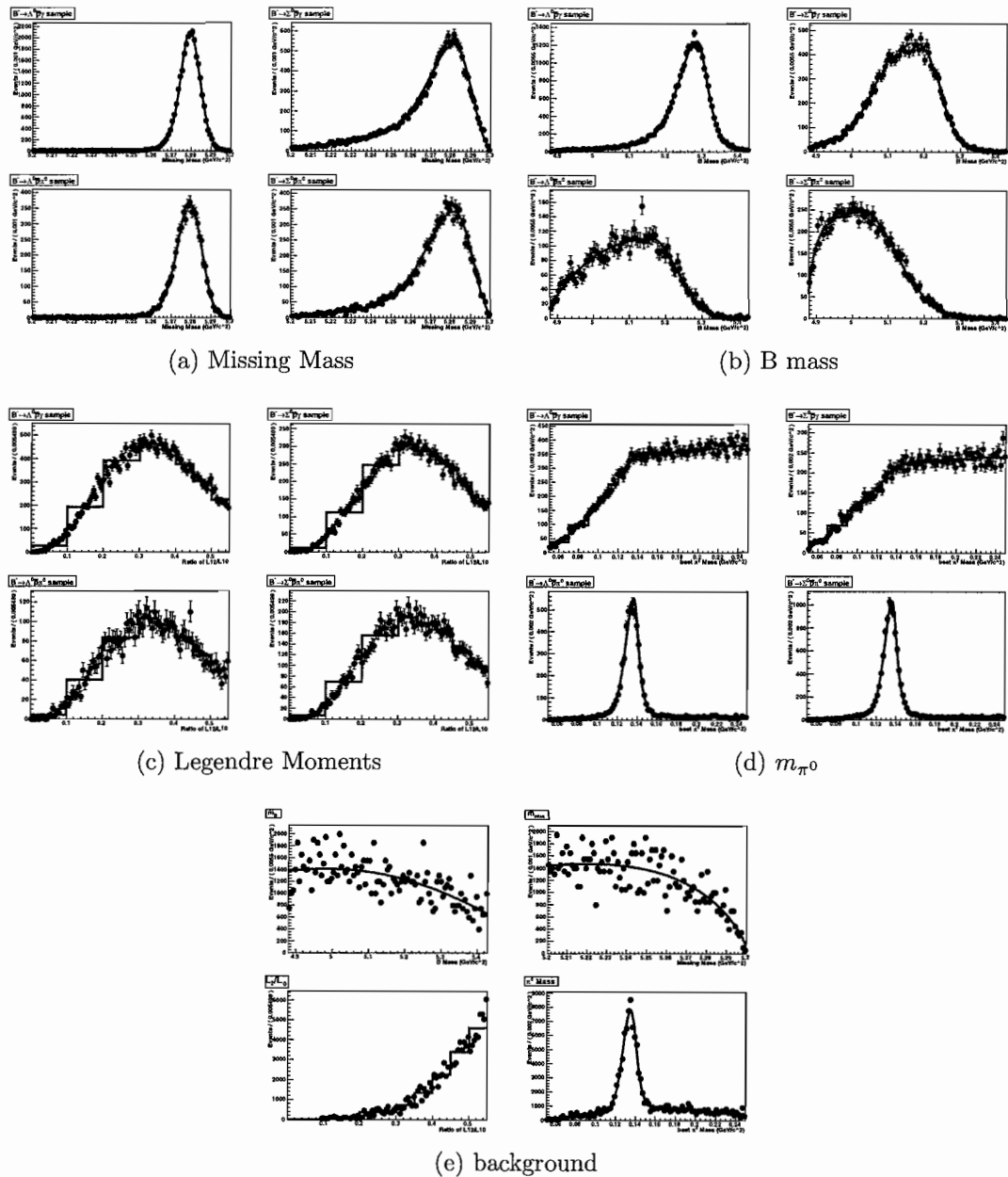


Fig. E.3: Datasets and fit shapes of different samples reconstructed as $B^- \rightarrow \Lambda \bar{p} \gamma$. With this choice of fit shapes, the embedded toys show a poor performance of the fit.

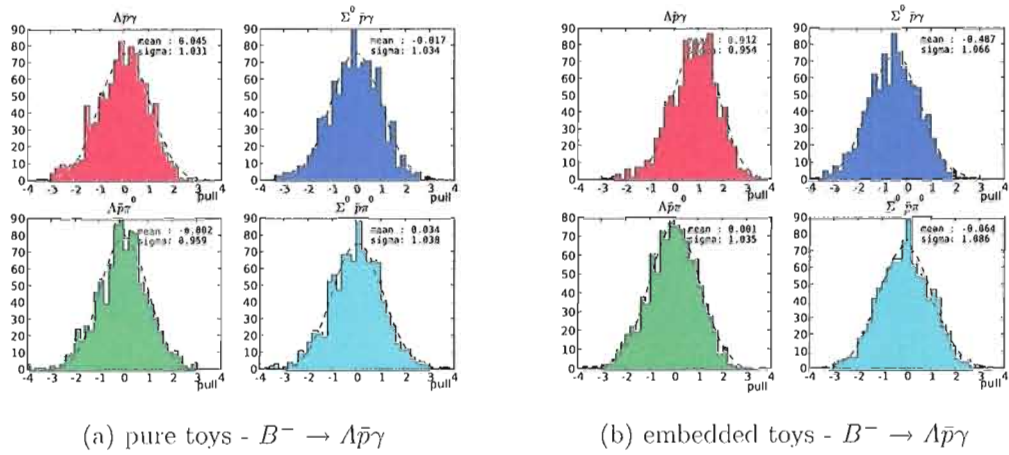


Fig. E.4: Pull distributions of toy studies - pure and embedded for the pure parameterization

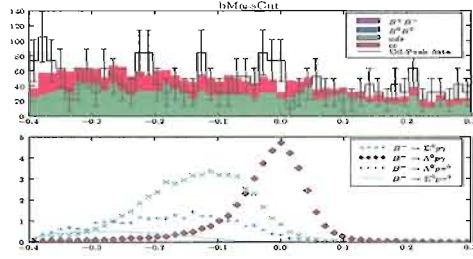
APPENDIX F

CUT VARIABLES

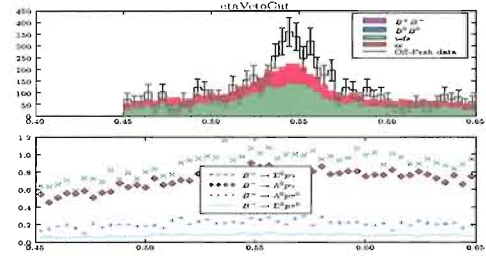
Section IV.4.2 explains the variables that are presented in Figures F.1 and F.2. A plot on a logarithmic scale can emphasize small differences between the different samples. This is shown in Figure F.3 and F.4.

F.1 Cut Optimization

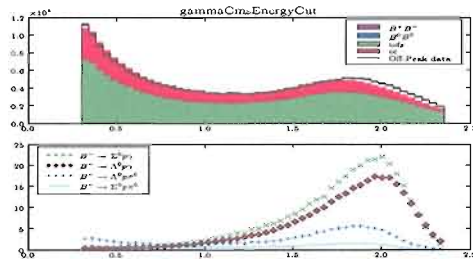
The values for the cuts are chosen based on experience. A less subjective measure is the signal significance in the final sample. This is computed by varying the different cuts in small steps and obtaining the efficiencies for the different samples at each step. For each value of the cut, 200 samples are generated in the right composition, and the likelihood fit is performed on each sample. Figures F.5 and F.6 show the values of the signal significance for some cuts obtained from these 200 samples. The data points correspond to the mean of the 200 experiments, and the error bars represent the standard deviation. For a two-dimensional cut, a two-dimensional plot is shown. This experiment was carried out only for the significance of the $B^- \rightarrow \Lambda \bar{p} \gamma$ yield. Because there was no significant dependence of the significance on the cuts, the results of this study did not influence the choice of cuts.



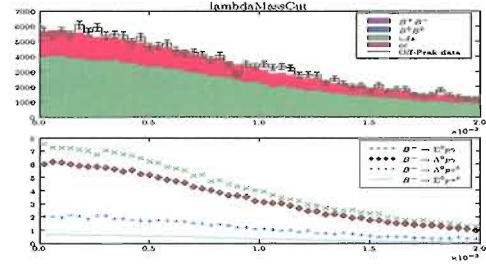
(a) bMassCut



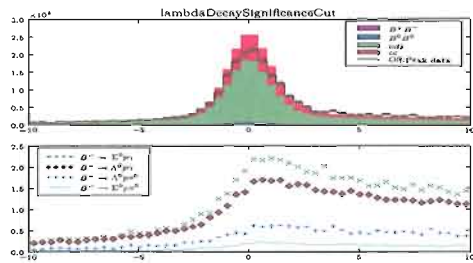
(b) etaVetoCut



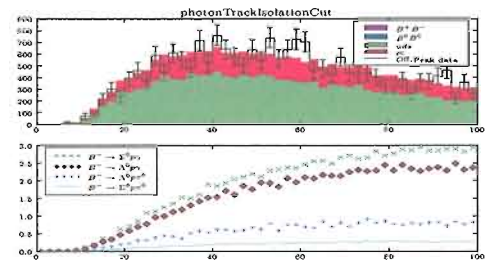
(c) gammaCmsEnergyCut



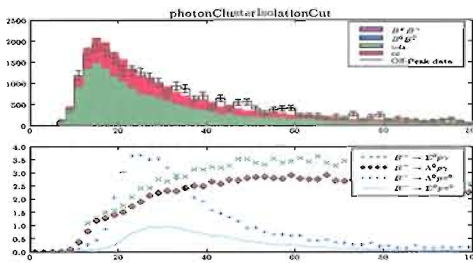
(d) lambdaMassCut



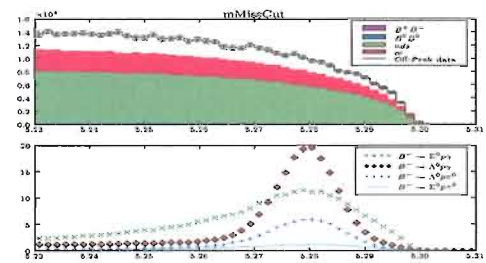
(e) lambdaDecaySignificance



(f) photonTrackIsolationCut

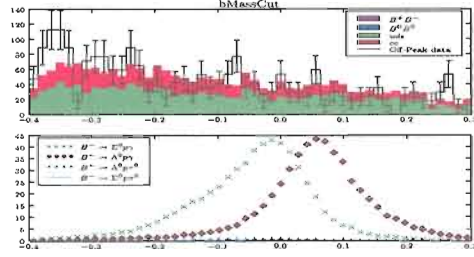


(g) photonClusterIsolationCut

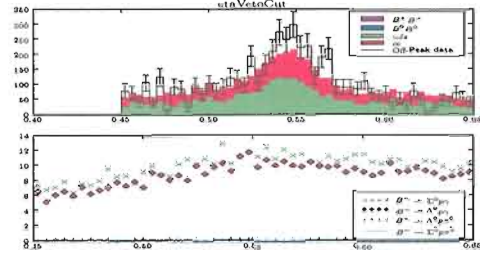


(h) mMissCut

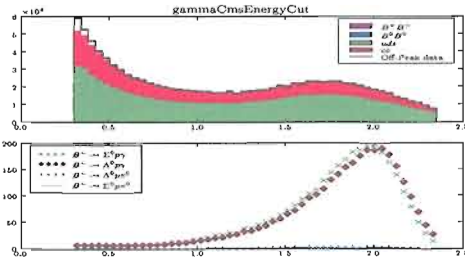
Fig. F.1: Distribution of the cut variables before the cuts – reconstruction as $B^- \rightarrow \Lambda \bar{p} \gamma$



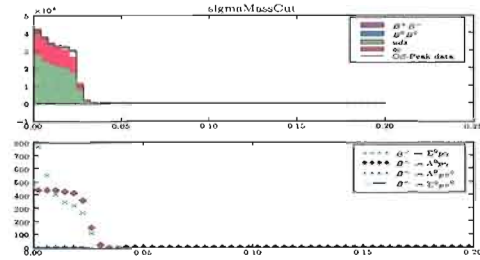
(a) bMassCut



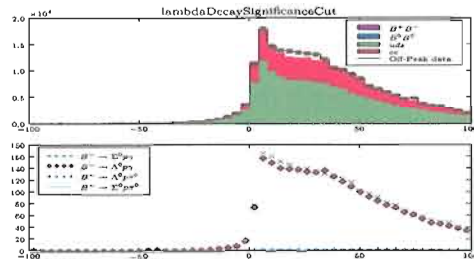
(b) etaVetoCut



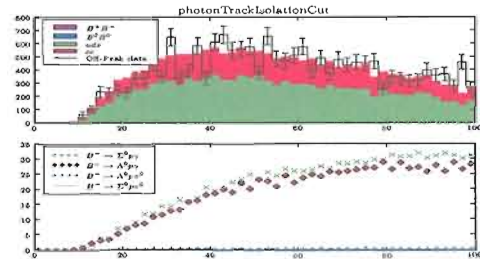
(c) gammaCmsEnergyCut



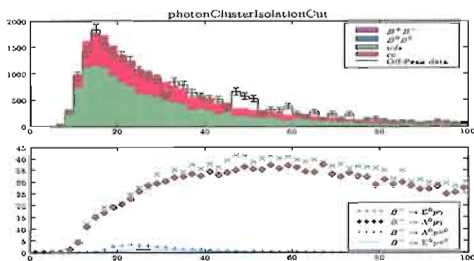
(d) sigmaMassCut



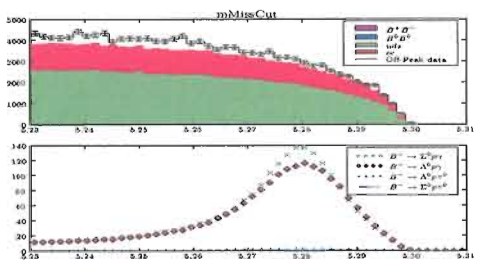
(e) lambdaDecaySignificance



(f) photonTrackIsolationCut

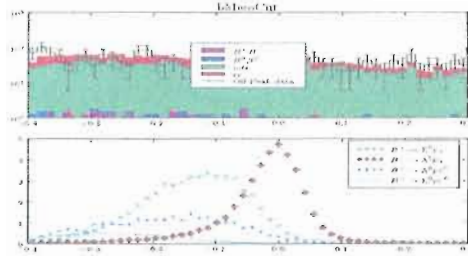


(g) photonClusterIsolationCut

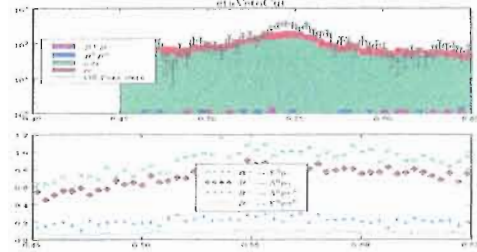


(h) mMissCut

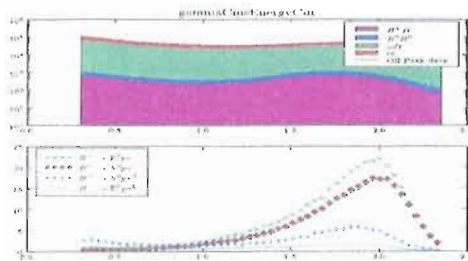
Fig. F.2: Distribution of the cut variables before the cuts – reconstruction as $B^- \rightarrow \Sigma^0 \bar{p} \gamma$



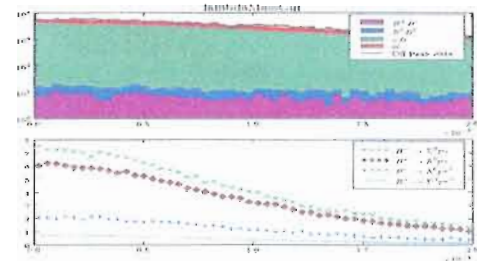
(a) bMassCut



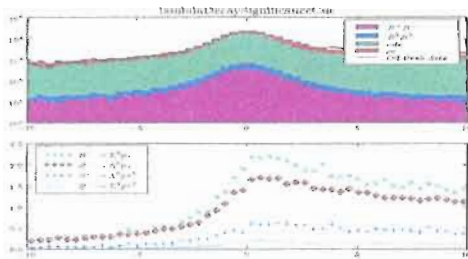
(b) etaVetoCut



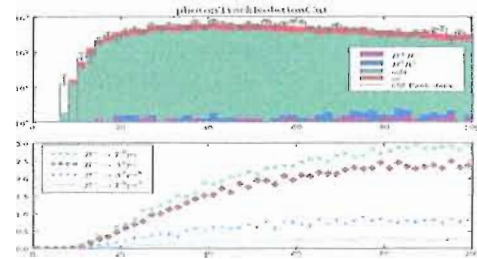
(c) gammaCmsEnergyCut



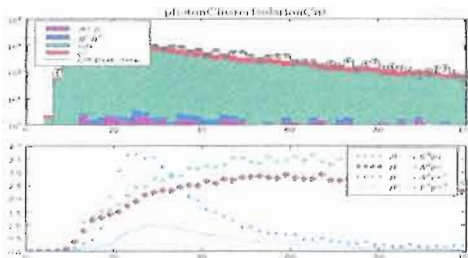
(d) lambdaMassCut



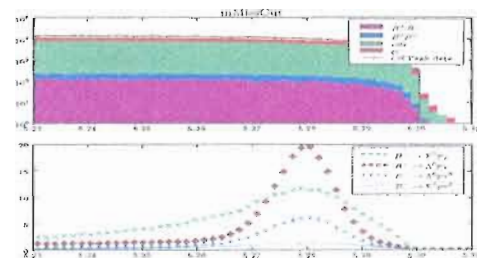
(e) lambdaDecaySignificance



(f) photonTrackIsolationCut

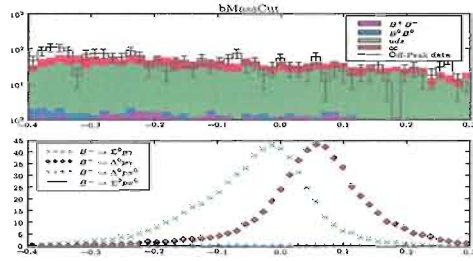


(g) photonClusterIsolationCut

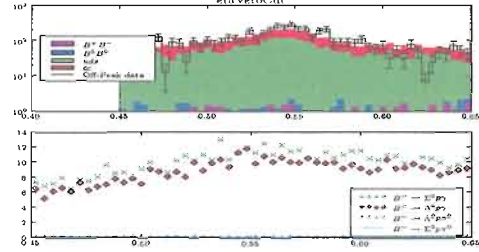


(h) mMissCut

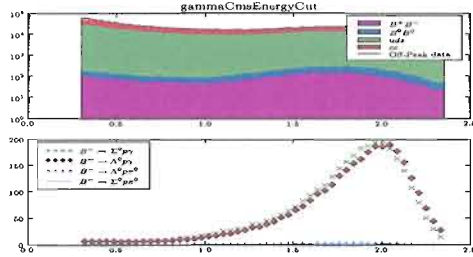
Fig. F.3: Distribution of the cut variables before the cuts - log scale - reconstruction as $B^- \rightarrow \Lambda \bar{p} \gamma$



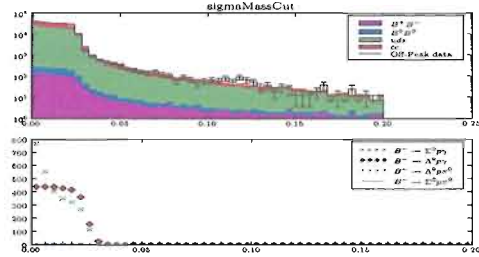
(a) bMassCut



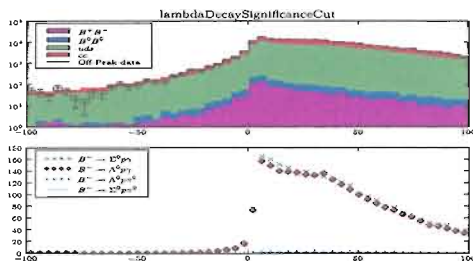
(b) etaVetoCut



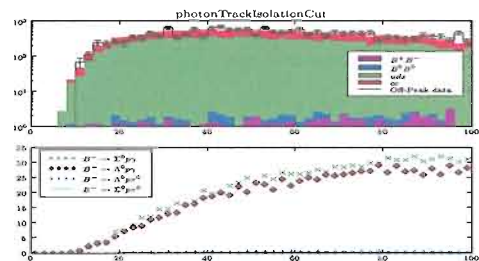
(c) gammaCmsEnergyCut



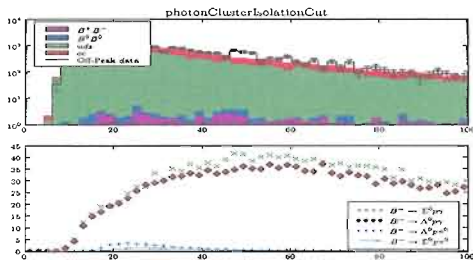
(d) sigmaMassCut



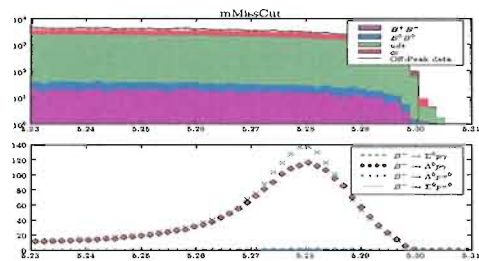
(e) lambdaDecaySignificance



(f) photonTrackIsolationCut

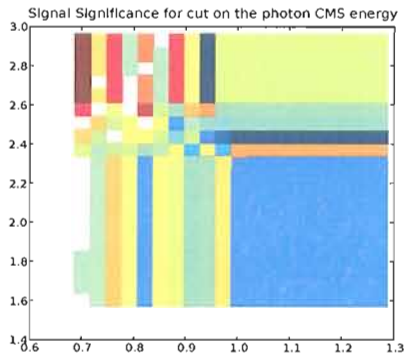


(g) photonClusterIsolationCut

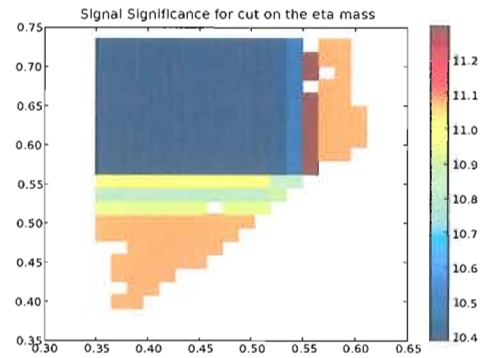


(h) mMissCut

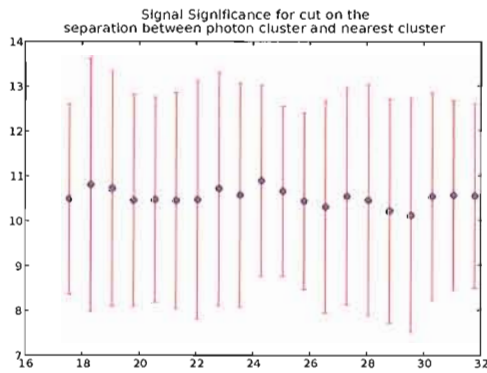
Fig. F.4: Distribution of the cut variables before the cuts - log scale - reconstruction as $B^- \rightarrow \Sigma^0 \bar{p} \gamma$



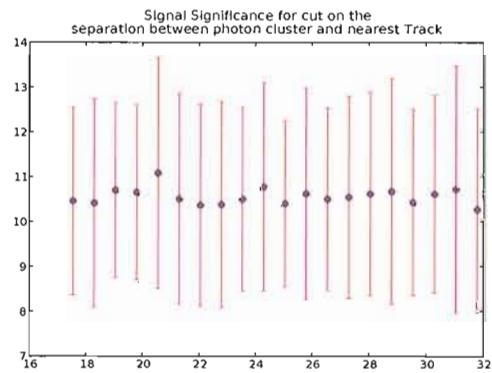
(a) photon cms energy



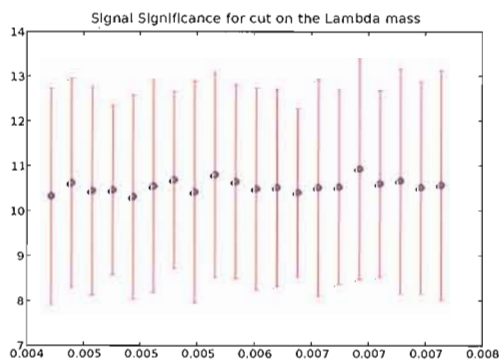
(b) eta veto



(c) separation of photon and neutral in the calorimeter

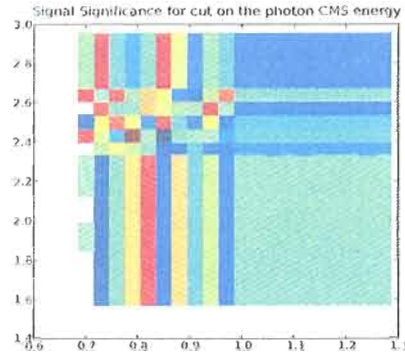


(d) separation of photon and track in the calorimeter

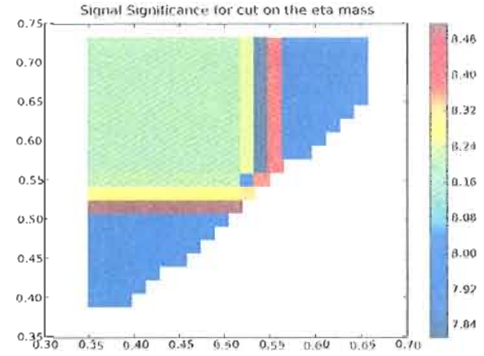


(e) Lambda mass

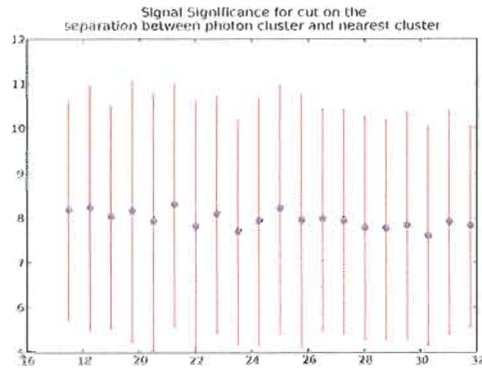
Fig. F.5: Optimization of signal significance for the different cuts – reconstruction as $B^- \rightarrow \Lambda \bar{p} \gamma$



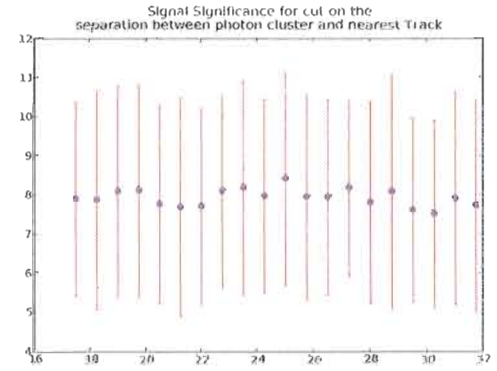
(a) photon cms energy



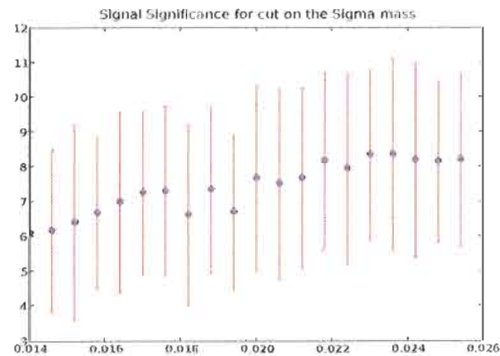
(b) eta veto



(c) separation of photon and neutral in the calorimeter



(d) separation of photon and track in the calorimeter



(e) Sigma mass

Fig. F.6: Optimization of signal significance for the different cuts reconstruction as $B^- \rightarrow \Sigma^0 \bar{p} \gamma$

APPENDIX G

CUT EFFICIENCIES

The efficiencies for the cuts outlined in section IV.4.2 are summarized in Tables G.1 and G.2 for the candidates reconstructed as $B^- \rightarrow \Lambda \bar{p} \gamma$ and in Tables G.3 and G.4 for candidates that are reconstructed as a $B^- \rightarrow \Sigma^0 \bar{p} \gamma$ decay.

Cut	$B^- \rightarrow \Lambda \bar{p} \gamma$	$B^- \rightarrow \Sigma^0 \bar{p} \gamma$	$B^- \rightarrow \Lambda \bar{p} \pi^0$	$B^- \rightarrow \Sigma^0 \bar{p} \pi^0$	background	data
Candidates	296.44	366.66	130.30	47.27	2,331,648.93	2,865,144
$1.0 < E_{cms}(\gamma) < 2.3$	277.75	344.68	98.65	33.09	1,245,410.37	1,544,226
$5.2 < \text{missing mass}$	269.85	330.02	94.18	31.26	661,535.17	811,405
$0.001 < \chi^2(\Lambda \text{ vtx})$	239.92	291.61	83.58	27.51	489,652.87	597,533
$5 < \sigma(\Lambda \text{ decay length})$	214.82	258.52	74.09	24.30	252,713.60	333,903
$m_{\Sigma^0} < 0.02$	208.04	250.48	71.72	23.49	220,500.91	293,237
$16 < \text{Proton PID}$	158.94	191.16	54.47	17.65	29,855.72	46,446
$25 < \text{photon - track distance}$	155.95	187.34	53.22	17.21	27,719.42	43,337
$25 < \text{photon - cluster distance}$	146.73	176.39	40.88	14.84	15,013.92	24,711
$0.51 < m_\eta \text{ veto} < 0.57$	134.75	161.66	37.23	13.47	12,482.39	19,949
Legendre moments < 0.55	120.69	145.11	32.78	9.23	3,837.86	6,850
$-0.4 < m_B < 0.15$	119.73	144.78	32.66	9.2	3,215.19	5,535

Tab. G.1: Cut efficiencies for reconstruction as $B^- \rightarrow \Lambda \bar{p} \gamma$

Cut	$B^- \rightarrow \Lambda \bar{p} \gamma$	$B^- \rightarrow \Sigma^0 \bar{p} \gamma$	$B^- \rightarrow \Lambda \bar{p} \pi^0$	$B^- \rightarrow \Sigma^0 \bar{p} \pi^0$	background	data
$1.0 < E_{cms}(\gamma) < 2.3$	0.94	0.94	0.76	0.70	0.53	0.54
$5.2 < \text{missing mass}$	0.97	0.96	0.95	0.94	0.53	0.53
$0.001 < \chi^2(\Lambda \text{ vtx})$	0.89	0.88	0.89	0.88	0.74	0.74
$5 < \sigma(\Lambda \text{ decay length})$	0.9	0.89	0.89	0.88	0.52	0.56
$m_{\Sigma^0} < 0.02$	0.97	0.97	0.97	0.97	0.87	0.88
$16 < \text{Proton PID}$	0.76	0.76	0.76	0.75	0.14	0.16
$25 < \text{photon - track distance}$	0.98	0.98	0.98	0.98	0.93	0.93
$25 < \text{photon - cluster distance}$	0.94	0.94	0.77	0.86	0.54	0.57
$0.51 < m_\eta \text{ veto} < 0.57$	0.92	0.92	0.91	0.91	0.83	0.81
Legendre moments < 0.55	0.9	0.9	0.88	0.69	0.31	0.34
$-0.4 < m_B < 0.15$	0.99	1	1	1	0.84	0.81

Tab. G.2: Relative cut efficiencies for reconstruction as $B^- \rightarrow \Lambda \bar{p} \gamma$

Cut	$B^- \rightarrow \Lambda \bar{p} \gamma$	$B^- \rightarrow \Sigma^0 \bar{p} \gamma$	$B^- \rightarrow \Lambda \bar{p} \pi^0$	$B^- \rightarrow \Sigma^0 \bar{p} \pi^0$	background	data
Candidates	176.69	279.25	96.23	52.11	1,153,230.39	1,593,858
$1.0 < E_{cms}(\gamma) < 2.3$	165.38	261.18	73.50	35.41	589,661.82	812,445
$5.2 < \text{missing mass}$	158.68	251.52	68.91	33.22	250,372.78	340,755
$0.001 < \chi^2 \Lambda \text{vtx}$	158.68	251.52	68.91	33.22	250,372.78	340,755
$5 < \sigma(\Lambda \text{decay length})$	153.05	242.32	66.12	31.96	226,858.36	308,086
$ m_{\Sigma^0}^{\text{PDG}} - m_{\Sigma^0} < 0.02$	136.72	233.66	59.10	30.63	196,670.32	269,120
$16 < \text{Proton PID}$	103.62	177.37	44.32	23.01	26,790.23	43,889
$25 < \text{photon - track distance}$	101.64	173.80	43.26	22.44	24,867.75	40,920
$25 < \text{photon - cluster distance}$	95.14	163.28	29.53	17.33	13,645.37	23,431
$0.51 < m_\eta \text{ veto} < 0.57$	87.12	149.59	26.69	15.56	11,285.42	18,964
Legendre moments < 0.55	78.70	135.07	23.70	11.22	3,548.92	6,576
$-0.4 < m_B < 0.15$	71.52	133.66	23.14	11.07	2,896.44	5,207

Tab. G.3: Cut efficiencies for reconstruction as $B^- \rightarrow \Sigma^0 \bar{p} \gamma$

Cut	$B^- \rightarrow \Lambda \bar{p} \gamma$	$B^- \rightarrow \Sigma^0 \bar{p} \gamma$	$B^- \rightarrow \Lambda \bar{p} \pi^0$	$B^- \rightarrow \Sigma^0 \bar{p} \pi^0$	background	data
$1.0 < E_{cms}(\gamma) < 2.3$	0.94	0.94	0.76	0.68	0.51	0.51
$5.2 < \text{missing mass}$	0.96	0.96	0.94	0.94	0.42	0.42
$0.001 < \chi^2 \Delta \text{vtx}$	1	1	1	1	1	1
$5 < \sigma(\Lambda \text{decay length})$	0.96	0.96	0.96	0.96	0.91	0.9
$ m_{\Sigma^0}^{\text{PDG}} - m_{\Sigma^0} < 0.02$	0.89	0.96	0.89	0.96	0.87	0.87
$16 < \text{Proton PID}$	0.76	0.76	0.75	0.75	0.14	0.16
$25 < \text{photon - track distance}$	0.98	0.98	0.98	0.98	0.93	0.93
$25 < \text{photon - cluster distance}$	0.94	0.94	0.68	0.77	0.55	0.57
$0.51 < m_\eta \text{ veto} < 0.57$	0.92	0.92	0.9	0.9	0.83	0.81
Legendre moments < 0.55	0.9	0.9	0.89	0.72	0.31	0.35
$-0.4 < m_B < 0.15$	0.91	0.99	0.98	0.99	0.82	0.79

Tab. G.4: Relative cut efficiencies for reconstruction as $B^- \rightarrow \Sigma^0 \bar{p} \gamma$

APPENDIX H

CORRELATION OF FIT VARIABLES

In order to determine how to best model the fit to the *BABAR* data sample, it is important to understand correlations between variables in the fit, because they affect the overall normalization of the parametrized shapes to the samples. Figures H.1, H.2, H.3 and H.4 visualize the correlations between the four variables $m_{\text{rec.}}$, $m_{\text{miss.}}$, L_2/L_0 and m_{π^0} of $B^- \rightarrow \Lambda \bar{p} \gamma$ candidates in simulated samples of the decay channels $B^- \rightarrow \Lambda \bar{p} \gamma$, $B^- \rightarrow \Sigma^0 \bar{p} \gamma$, $B^- \rightarrow \Lambda \bar{p} \pi^0$ and $B^- \rightarrow \Sigma^0 \bar{p} \pi^0$, respectively. Correlations between the four variables of $B^- \rightarrow \Sigma^0 \bar{p} \gamma$ candidates in the four simulated samples are shown in Figures H.5, H.6, H.7 and H.8. The correlation coefficients extracted from the samples are summarized in Tables H.1, H.2, H.3 and H.4 for reconstruction of $B^- \rightarrow \Lambda \bar{p} \gamma$ candidates in the samples $B^- \rightarrow \Lambda \bar{p} \gamma$, $B^- \rightarrow \Sigma^0 \bar{p} \gamma$, $B^- \rightarrow \Lambda \bar{p} \pi^0$ and $B^- \rightarrow \Sigma^0 \bar{p} \pi^0$. The correlation coefficients for variables of $B^- \rightarrow \Sigma^0 \bar{p} \gamma$ candidates in these samples are listed in Tables H.5, H.6, H.7 and H.8

H.1 Reconstruction as $B^- \rightarrow \Lambda \bar{p} \gamma$

	mMiss	mrec	legendre	pi0Mass
mMiss	1	0.103	-0.007	-0.006
mrec	0.103	1	0.007	-0.004
legendre	-0.007	0.007	1	0.091
pi0Mass	-0.006	-0.004	0.091	1

Tab. H.1: Correlations of the fit variables in correctly reconstructed $B^- \rightarrow \Lambda \bar{p} \gamma$ events. Parametrization of $m_{\text{rec.}}$, $m_{\text{miss.}}$

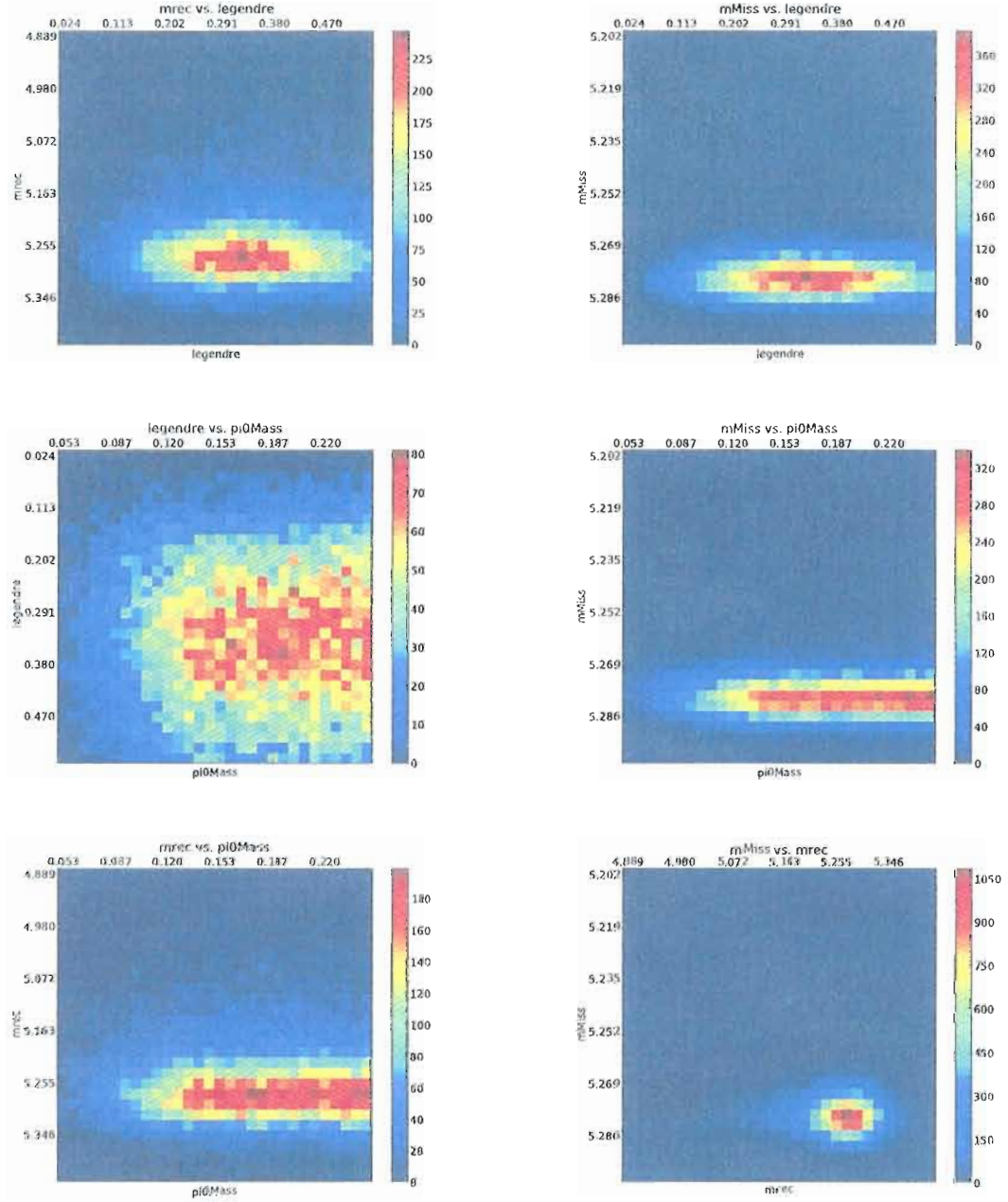


Fig. H.1: Scatter plots of the four fit variables in $A\bar{p}\gamma$ MC

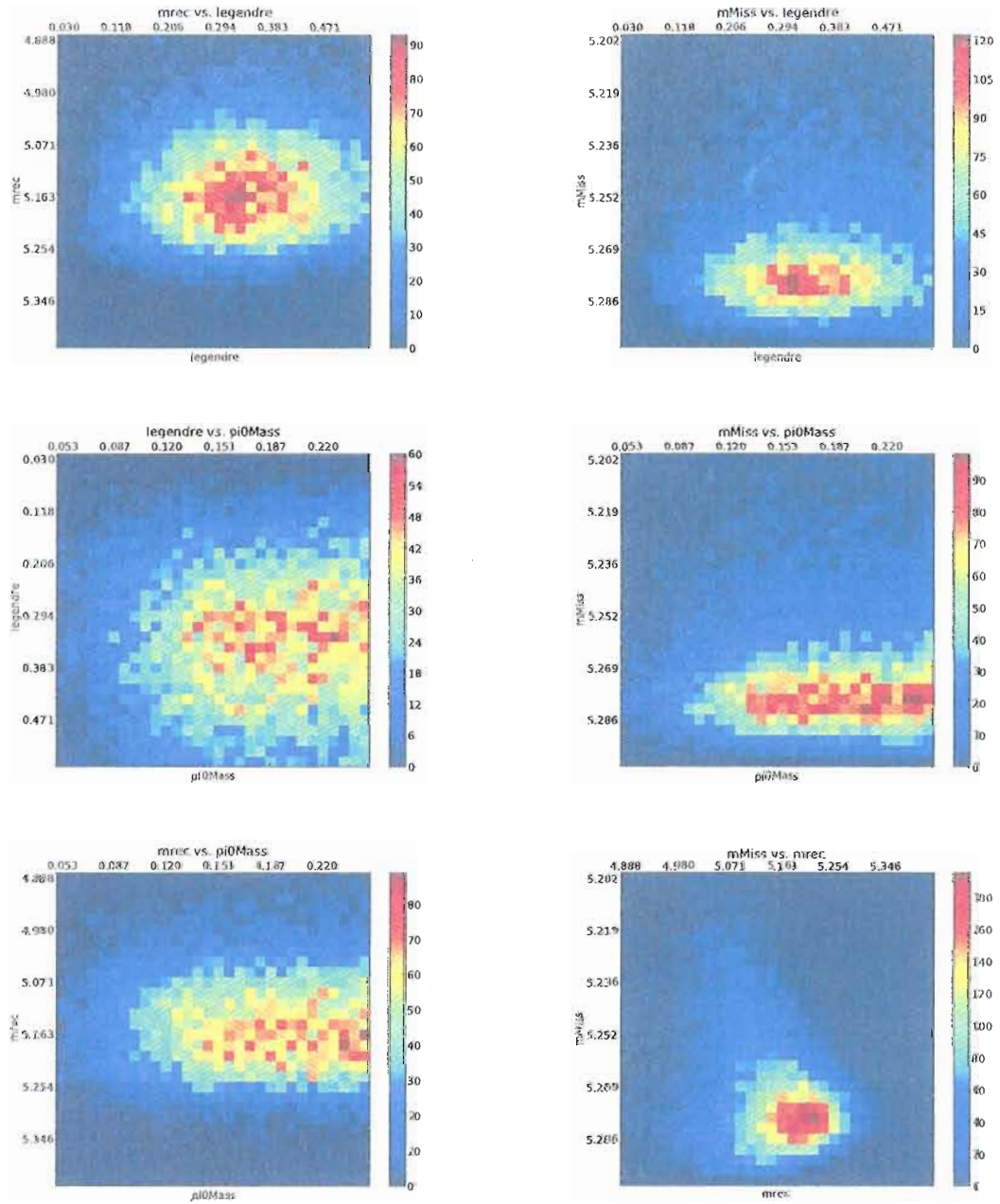


Fig. H.2: Scatter plots of the four fit variables in $\Sigma^0 \bar{p} \gamma$ MC

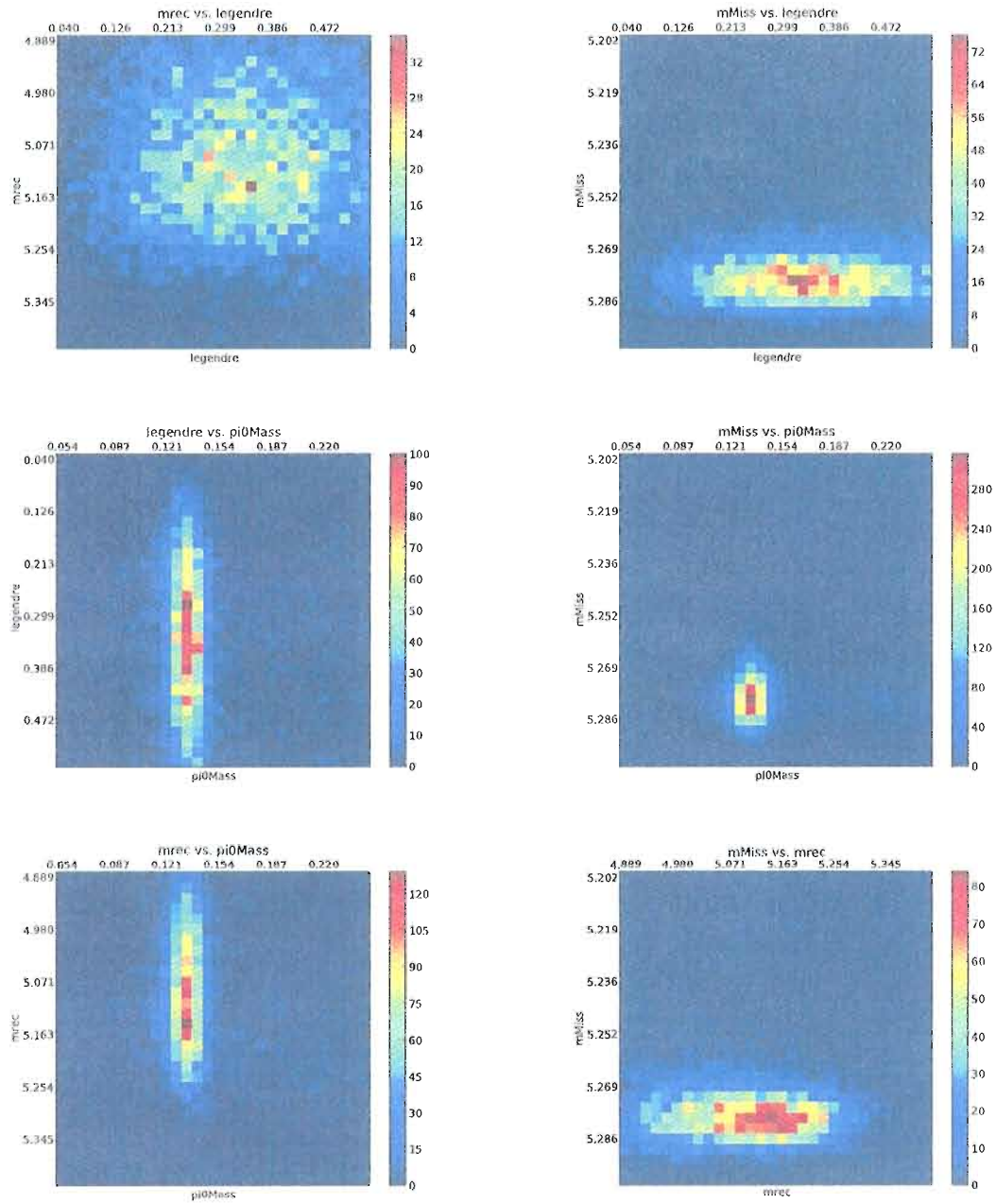


Fig. H.3: Scatter plots of the four fit variables in $A\bar{p}\pi^0$ MC

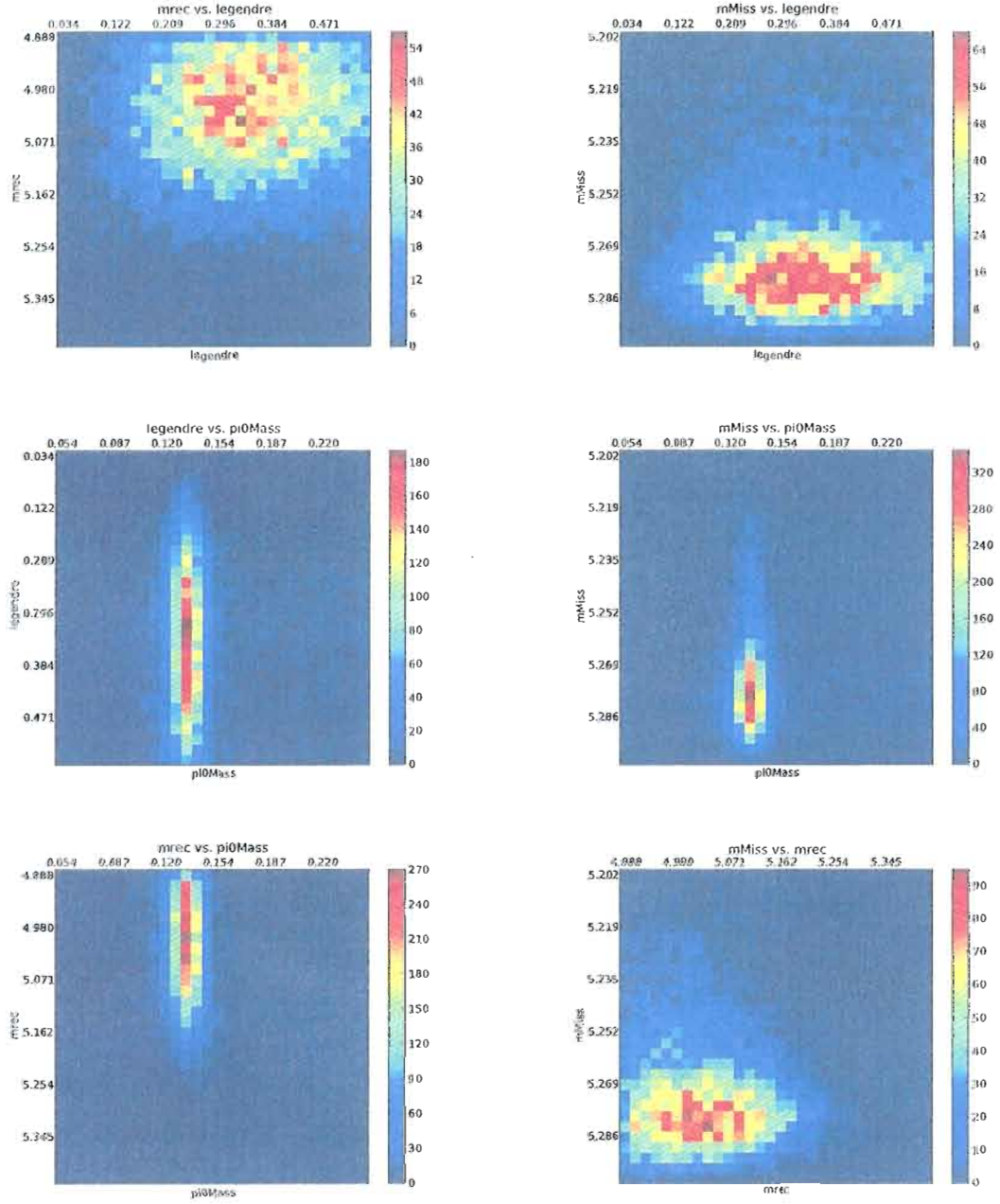


Fig. H.4: Scatter plots of the four fit variables in $\Sigma^0 \bar{p} \pi^0$ MC

	mMiss	mrec	legendre	pi0Mass
mMiss	1	0.304	-0.025	0.027
mrec	0.304	1	-0.034	0.002
legendre	-0.025	-0.034	1	0.091
pi0Mass	0.027	0.002	0.091	1

Tab. H.2: Correlations of the fit variables in $B^- \rightarrow \Sigma^0 \bar{p} \gamma$ events that are incorrectly reconstructed as $B^- \rightarrow \Lambda \bar{p} \gamma$. Parametrization of $m_{\text{rec.}}$, $m_{\text{miss.}}$.

	mMiss	mrec	legendre	pi0Mass
mMiss	1	0.067	-0.018	-0.006
mrec	0.067	1	-0.031	-0.166
legendre	-0.018	-0.031	1	0.078
pi0Mass	-0.006	-0.166	0.078	1

Tab. H.3: Correlations of the fit variables in $B^- \rightarrow \Lambda \bar{p} \pi^0$ events that are incorrectly reconstructed as $B^- \rightarrow \Lambda \bar{p} \gamma$. Parametrization of $m_{\text{rec.}}$, $m_{\text{miss.}}$.

	mMiss	mrec	legendre	pi0Mass
mMiss	1	0.113	-0.019	0.028
mrec	0.113	1	-0.054	-0.133
legendre	-0.019	-0.054	1	0.073
pi0Mass	0.028	-0.133	0.073	1

Tab. H.4: Correlations of the fit variables in $B^- \rightarrow \Sigma^0 \bar{p} \pi^0$ events that are incorrectly reconstructed as $B^- \rightarrow \Lambda \bar{p} \gamma$. Parametrization of $m_{\text{rec.}}$, $m_{\text{miss.}}$.

H.2 Reconstruction as $B^- \rightarrow \Sigma^0 \bar{p} \gamma$

	mMiss	mrec	legendre	pi0Mass
mMiss	1	0.048	-0.011	0.002
mrec	0.048	1	0.013	-0.025
legendre	-0.011	0.013	1	0.085
pi0Mass	0.002	-0.025	0.085	1

Tab. H.5: Correlations of the fit variables in $B^- \rightarrow \Lambda \bar{p} \gamma$ events that are incorrectly reconstructed as $B^- \rightarrow \Sigma^0 \bar{p} \gamma$. Parametrization of $m_{\text{rec.}}$, $m_{\text{miss.}}$.

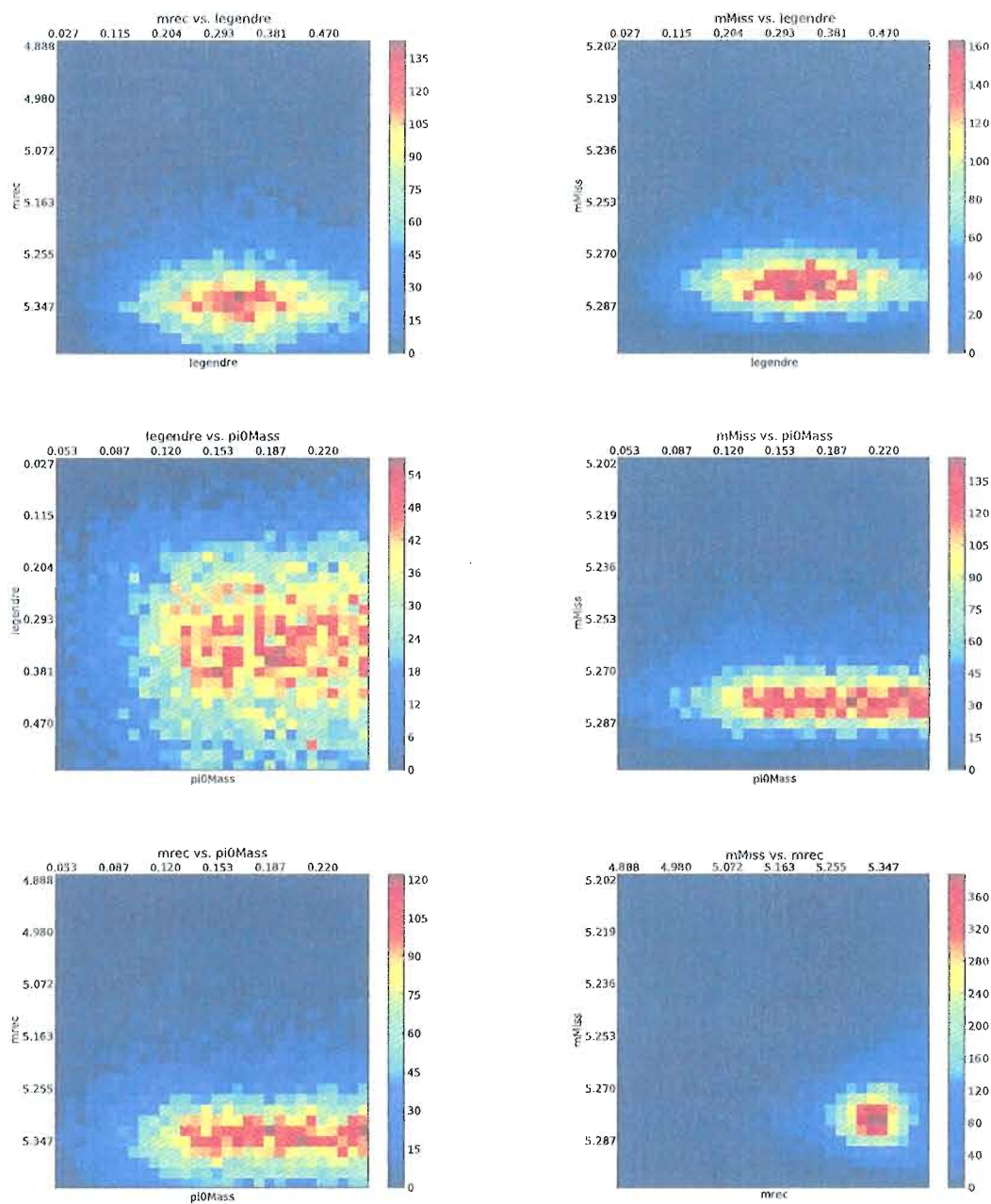


Fig. H.5: Scatter plots of the four fit variables in $A\bar{p}\gamma$ MC

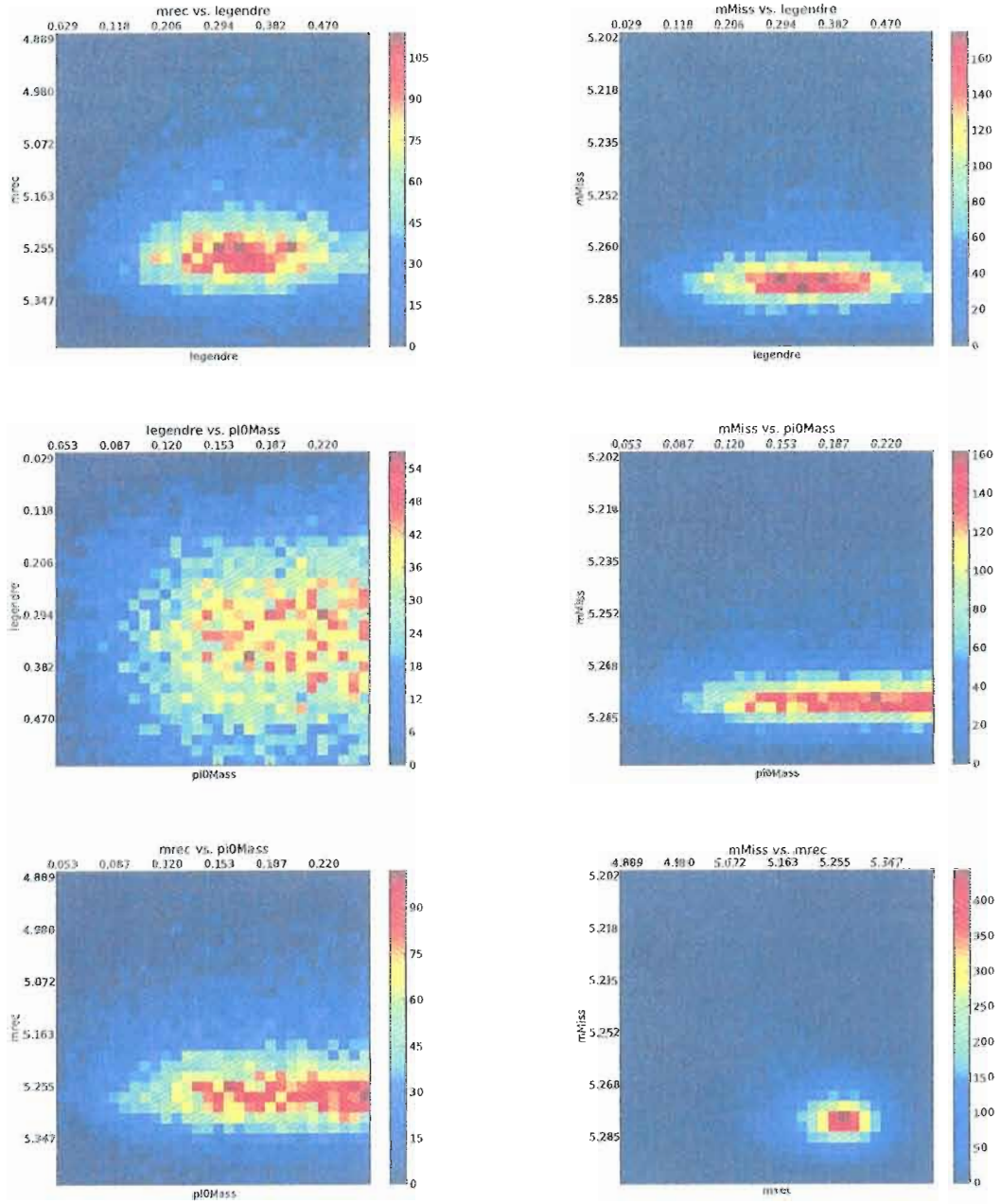


Fig. H.6: Scatter plots of the four fit variables in $\Sigma^0 p \gamma$ MC

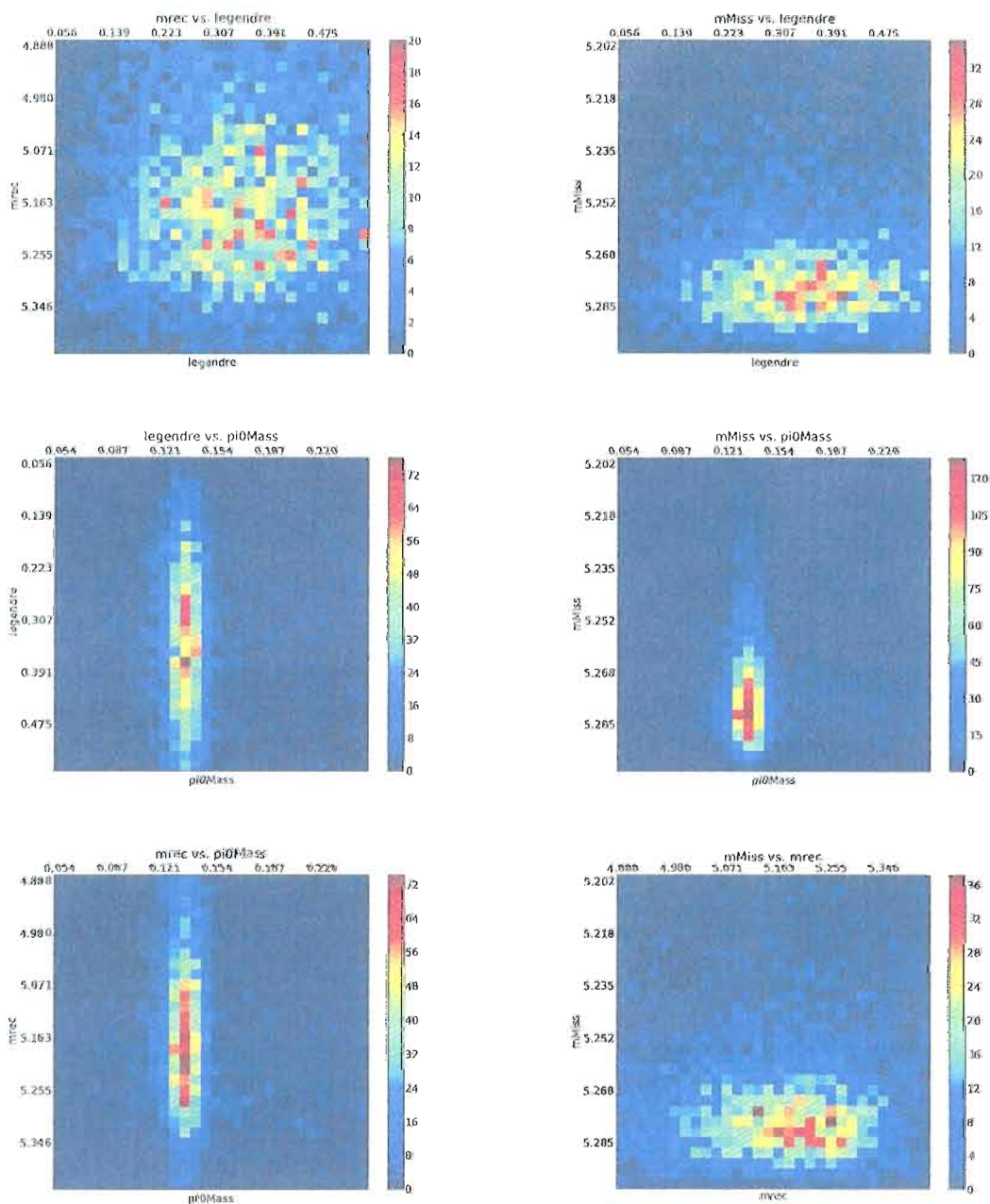


Fig. H.7: Scatter plots of the four fit variables in $\Lambda\bar{p}\pi^0$ MC

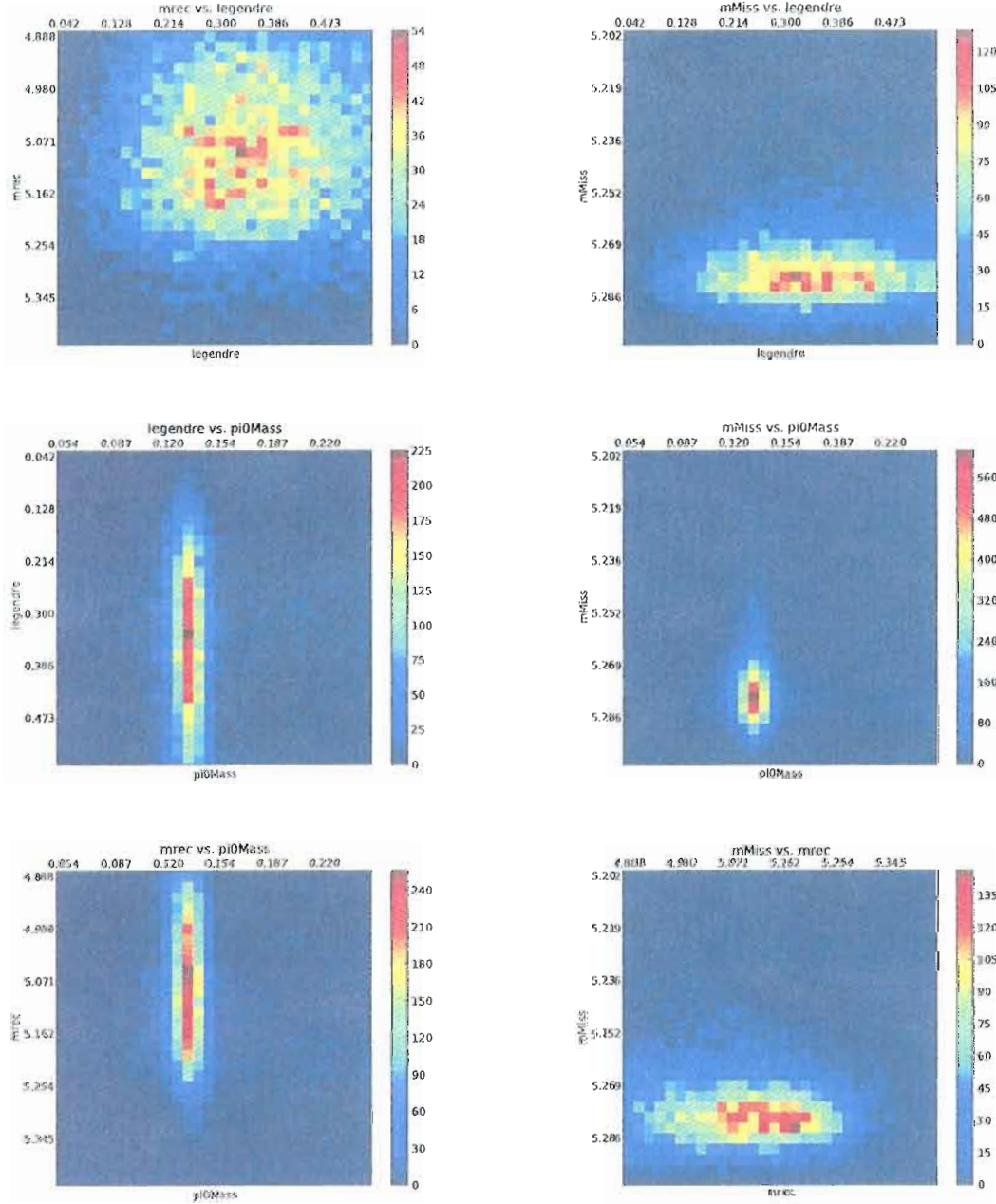


Fig. H.8: Scatter plots of the four fit variables in $\Sigma^0 \eta \pi^0$ MC

	mMiss	mrec	legendre	pi0Mass
mMiss	1	0.201	-0.020	-0.017
mrec	0.201	1	-0.009	-0.019
legendre	-0.017	-0.019	1	0.088
pi0Mass	-0.017	-0.019	0.088	1

Tab. H.6: Correlations of the fit variables in correctly reconstructed $B^- \rightarrow \Sigma^0 \bar{p} \gamma$ events. Parametrization of $m_{\text{rec.}}$, m_{miss} .

	mMiss	mrec	legendre	pi0Mass
mMiss	1	0.026	-0.022	-0.013
mrec	0.026	1	-0.041	0.114
legendre	-0.022	-0.041	1	0.068

Tab. H.7: Correlations of the fit variables in $B^- \rightarrow \Lambda \bar{p} \pi^0$ events incorrectly reconstructed as $B^- \rightarrow \Sigma^0 \bar{p} \gamma$. Parametrization of $m_{\text{rec.}}$, m_{miss} .

	mMiss	mrec	legendre	pi0Mass
mMiss	1	0.064	-0.026	-0.009
mrec	0.064	1	-0.050	-0.147
legendre	-0.026	-0.050	1	0.071
pi0Mass	-0.009	-0.147	0.071	1

Tab. H.8: Correlations of the fit variables in $B^- \rightarrow \Sigma^0 \bar{p} \pi^0$ events incorrectly reconstructed as $B^- \rightarrow \Sigma^0 \bar{p} \gamma$. Parametrization of $m_{\text{rec.}}$, m_{miss} .

APPENDIX I

ALTERNATIVE FIT VARIABLES

The variables $m_{\text{rec.}}$ and $m_{\text{miss.}}$ are by construction statistically uncorrelated. However, it is known that for incorrectly reconstructed candidates, these variables can show a certain degree of correlation. This chapter gives an overview over a few analysis steps using the more common combination of m_{ES} and ΔE as fit variables.

I.1 Correlation Coefficients

Similar to section H this section gives an overview over correlations between the alternative set of fit variables m_{ES} , ΔE , L_2/L_0 and m_{π^0} . Tables I.1, I.2, I.3 and I.4 show the correlation coefficients of the fit variables of $B^- \rightarrow \Lambda \bar{p} \gamma$ candidates in simulated samples of $B^- \rightarrow \Lambda \bar{p} \gamma$, $B^- \rightarrow \Sigma^0 \bar{p} \gamma$, $B^- \rightarrow \Lambda \bar{p} \pi^0$ and $B^- \rightarrow \Sigma^0 \bar{p} \pi^0$ events, respectively, while Tables I.5, I.6, I.7, I.8 are for $B^- \rightarrow \Sigma^0 \bar{p} \gamma$ candidates in those samples.

	mES	deltaE	legendre	pi0Mass
mES	1	0.253	-0.001	-0.020
deltaE	0.253	1	0.006	0.036
legendre	-0.001	0.006	1	0.001
pi0Mass	-0.020	0.036	0.001	1

Tab. I.1: Correlations of the fit variables in correctly reconstructed $B^- \rightarrow \Lambda \bar{p} \gamma$ events. Parametrization of $m_{\text{ES}}, \Delta E$

	mES	deltaE	legendre	pi0Mass
mES	1	0.092	-0.015	0.009
deltaE	0.092	1	-0.035	0.018
legendre	-0.015	-0.035	1	-0.009
pi0Mass	0.009	0.018	-0.009	1

Tab. I.2: Correlations of the fit variables in $B^- \rightarrow \Sigma^0 \bar{p} \gamma$ events incorrectly reconstructed as $B^- \rightarrow \Lambda \bar{p} \gamma$. Parametrization of m_{ES} , ΔE

	mES	deltaE	legendre	pi0Mass
mES	1	0.388	-0.029	0.050
deltaE	0.388	1	-0.015	0.152
legendre	-0.029	-0.015	1	0.049
pi0Mass	0.050	0.152	0.049	1

Tab. I.3: Correlations of the fit variables in $B^- \rightarrow \Lambda \bar{p} \pi^0$ events incorrectly reconstructed as $B^- \rightarrow \Lambda \bar{p} \gamma$. Parametrization of m_{ES} , ΔE

	mES	deltaE	legendre	pi0Mass
mES	1	0.145	-0.013	0.028
deltaE	0.145	1	-0.041	0.188
legendre	-0.013	-0.041	1	-0.002
pi0Mass	0.028	0.188	-0.002	1

Tab. I.4: Correlations of the fit variables in $B^- \rightarrow \Sigma^0 \bar{p} \pi^0$ events incorrectly reconstructed as $B^- \rightarrow \Lambda \bar{p} \gamma$. Parametrization of m_{ES} , ΔE

	mES	deltaE	legendre	pi0Mass
mES	1	0.215	-0.011	0.018
deltaE	0.215	1	0.009	0.039
legendre	-0.011	0.009	1	-0.003
pi0Mass	0.018	0.039	-0.003	1

Tab. I.5: Correlations of the fit variables in $B^- \rightarrow \Lambda \bar{p} \gamma$ events incorrectly reconstructed as $B^- \rightarrow \Sigma^0 \bar{p} \gamma$. Parametrization of m_{ES} , ΔE

	mES	deltaE	legendre	pi0Mass
mES	1	0.155	-0.019	0.020
deltaE	0.155	1	-0.003	0.035
legendre	-0.019	-0.005	1	-0.010
pi0Mass	0.020	0.035	-0.010	1

Tab. I.6: Correlations of the fit variables in correctly reconstructed $B^- \rightarrow \Sigma^0 \bar{p} \gamma$ events. Parametrization of m_{ES} , ΔE

	mES	deltaE	legendre	pi0Mass
mES	1	0.335	-0.021	0.016
deltaE	0.335	1	-0.017	0.085
legendre	-0.021	-0.017	1	0.024
pi0Mass	0.016	0.085	0.024	1

Tab. I.7: Correlations of the fit variables in $B^- \rightarrow \Lambda \bar{p} \pi^0$ events incorrectly reconstructed as $B^- \rightarrow \Sigma^0 \bar{p} \gamma$. Parametrization of m_{ES} , ΔE

	mES	deltaE	legendre	pi0Mass
mES	1	0.297	-0.030	0.030
deltaE	0.297	1	-0.038	0.150
legendre	-0.030	-0.038	1	-0.008
pi0Mass	0.030	0.150	-0.008	1

Tab. I.8: Correlations of the fit variables in $B^- \rightarrow \Sigma^0 \bar{p} \pi^0$ events incorrectly reconstructed as $B^- \rightarrow \Sigma^0 \bar{p} \gamma$. Parametrization of m_{ES} , ΔE

I.1.1 Reconstruction as $B^- \rightarrow \Lambda \bar{p} \gamma$

I.1.2 Reconstruction as $B^- \rightarrow \Sigma^0 \bar{p} \gamma$

I.2 Parametrization of the Samples

Figure I.1 shows the parametrization of $B^- \rightarrow \Lambda \bar{p} \gamma$ candidates with the alternative set of fit variables. Table I.9 names the choice of fit shapes in Figure I.1.

I.2.1 Pure Toys

The result of 1000 “pure toy” experiments, i.e. the fit on 1000 samples generated from the parametrized shapes, is shown in Figure I.2.

I.2.2 Embedded Toys

Embedding simulated events into data sampled from the parametrization of the background shapes gives a more realistic study of the performance of the fit. The result of 1000 of these experiments is shown in Figure I.3.

Sample Variable	m_{ES}	ΔE	“best π^0 mass”	L_2/L_0
$B^- \rightarrow \Lambda \bar{p} \gamma$	Cruijff	Cruijff	Steps	Steps
$B^- \rightarrow \Sigma^0 \bar{p} \gamma$	KEYS	Cruijff	Steps	Steps
$B^- \rightarrow \Lambda \bar{p} \pi^0$	Cruijff	Cruijff	Voigtian	Steps
$B^- \rightarrow \Sigma^0 \bar{p} \pi^0$	Cruijff	Cruijff	Voigtian + Chebychev	Steps
background	Argus	Chebychev	Voigtian + Chebychev	Steps

Tab. I.9: Parameterization of the four samples using m_{ES} , ΔE

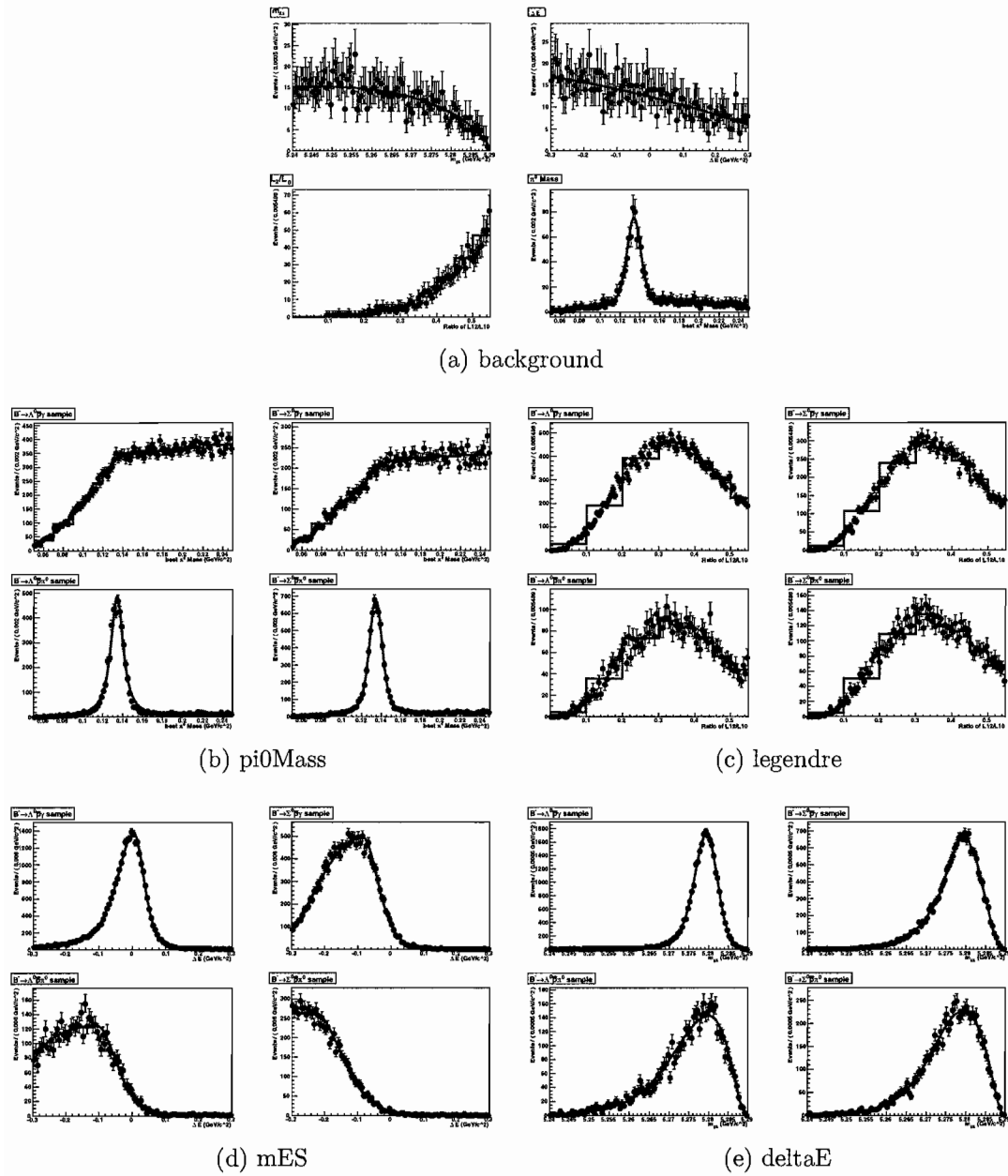


Fig. I.1: Parameterization with m_{ES} and ΔE

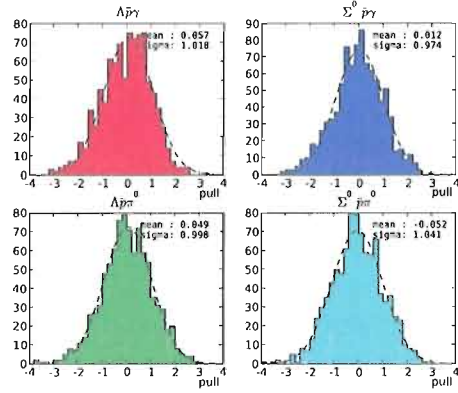


Fig. I.2: Pure Toys of events reconstructed as $B^- \rightarrow \Lambda \bar{p} \gamma$

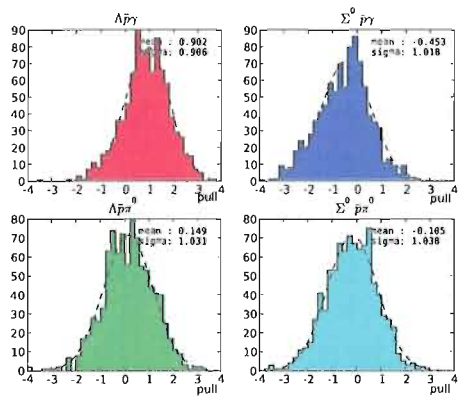


Fig. I.3: Embedded Toys of events reconstructed as $B^- \rightarrow \Sigma^0 \bar{p} \gamma$

APPENDIX J

VALIDATION OF SPLOTS

As an additional cross-check of the method to obtain the branching fraction in bins of the invariant mass of the two baryons, the two samples of events were each fit in bins of the invariant mass. Figures J.1 and J.2 show the result for one-candidate and two-candidate events, respectively.

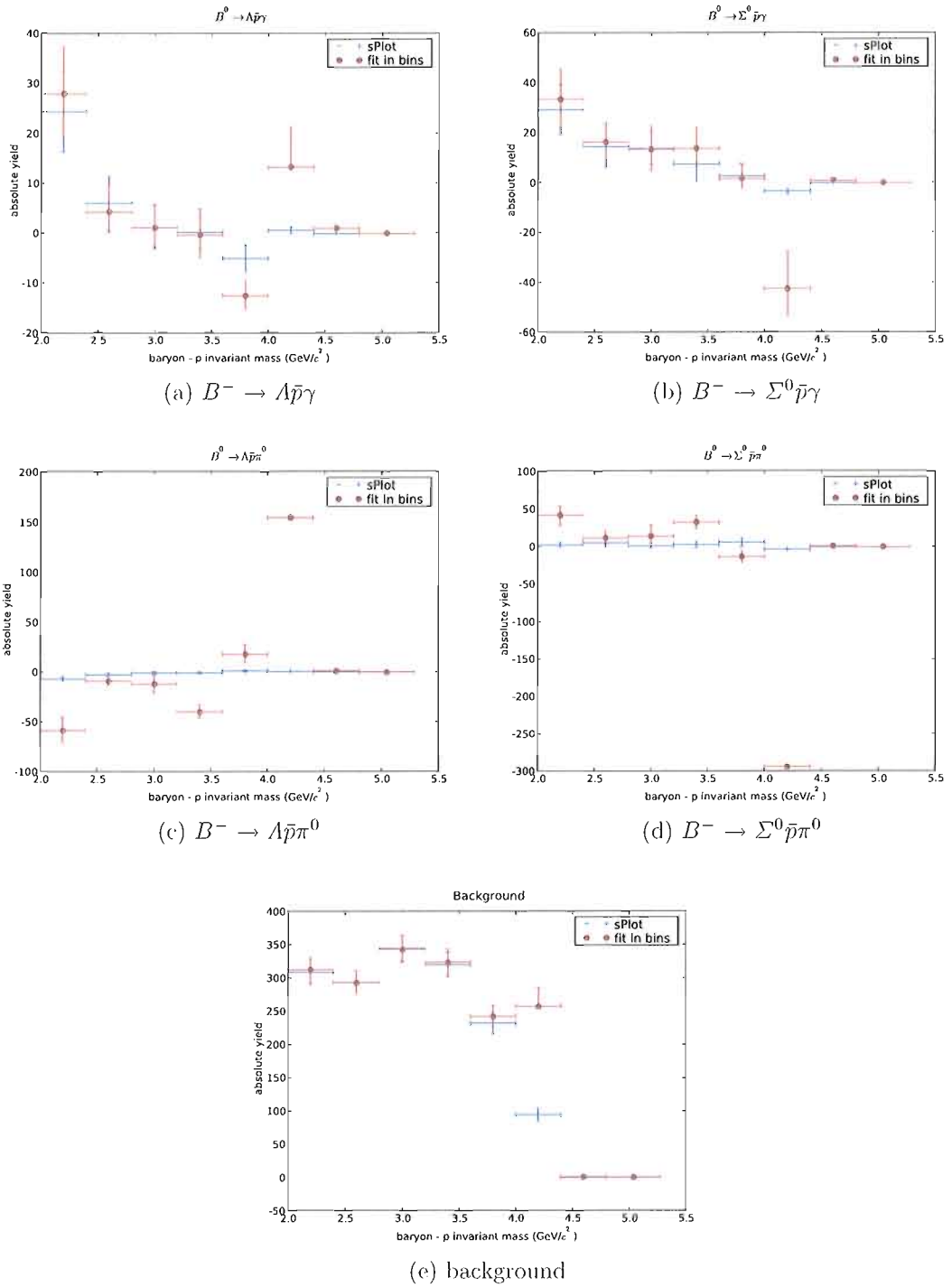


Fig. J.1: Validation of the sPlots method for events with one candidate. The sample is fit in bins of the invariant mass

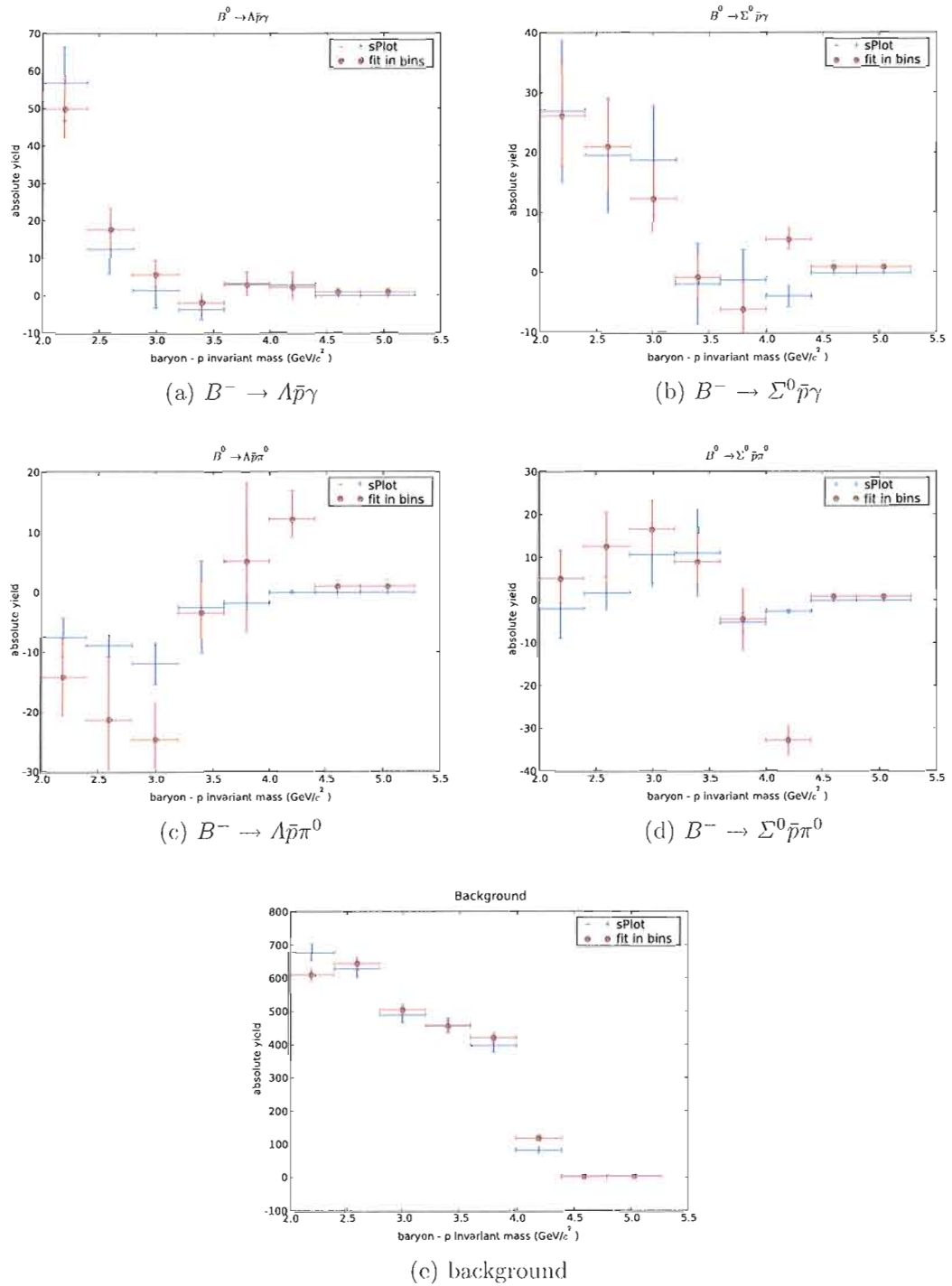


Fig. J.2: Validation of the sPlots method for events with two candidates. The sample is fit in bins of the invariant mass

APPENDIX K

SLOTS

A method for unfolding of distributions, sPlots are a method to obtain unbiased estimators for unknown distributions. They were developed by BaBar collaborators(36) and we shall give a brief overview of the method.

K.1 inPlots

As a first step towards understanding sPlots, we treat the case when the variable under consideration is part of the set of fit variables. We assign to each event the naive weight

$$\mathcal{P}_n(y_e) = \frac{N_n f_n(y_e)}{\sum_{k=1}^{N_s} N_k f_k(y_e)} \quad (\text{K.1})$$

With this weight, the histogram of the variable under consideration is an estimator of the true distribution. Constructing the histogram $N_n \tilde{M}_n(x) \delta x := \sum_{e \in \delta x}^N \mathcal{P}_n(y_e)$, and going from the discrete to the continuous case by replacing $\sum_{e \in \delta x}^N$ with the integral $\int dy$, we obtain the true distribution of the variable x , $\mathbf{M}_n(x)$

$$N_n \tilde{M}_n(x) = \int dy \sum_{i=1}^{N_s} N_i f_i(y) \delta(x(y) - x) \frac{N_n f_n(y)}{\sum_{k=1}^{N_s} N_k f_k(y)} \quad (\text{K.2})$$

$$= N_n \int dy \delta(x(y) - x) f_n(y) \quad (\text{K.3})$$

$$=: N_n \mathbf{M}_n(x) \quad (\text{K.4})$$

This prescription, however, assumes that we already know the distribution of x , because we have made use of the fact that x was used in the likelihood fit. In general

we want to be able to apply the procedure to variables that are uncorrelated with the set of fit variables y and for which we don't necessarily know the pdf.

K.2 sPlots

This is where the sPlots technique comes into play. The naive weight we have used in the previous section is no longer applicable, because the integral over y is not canceled by a Dirac δ any longer. However, we can still separate the dependencies on x and y and it turns out that the remaining integral over y can be expressed using the covariance matrix of the fit.

$$\mathbf{V}_{ni}^{-1} = \frac{\delta^2(-\mathcal{L})}{\delta N_n \delta N_i} = \sum_{e=1}^N \frac{f_n(y_e) f_i(y_e)}{(\sum_{k=1}^{N_s} N_k f_k(y_e))^2} \quad (\text{K.5})$$

$$= \int dy \frac{f_n(y) f_i(y)}{\sum_{k=1}^{N_s} N_k f_k(y)} \quad (\text{K.6})$$

Plugging this in and inverting the equation then yields

$$N_n M_n(x) = \sum_{i=1}^{N_s} \mathbf{V}_{ni} \tilde{M}_i(x) \quad (\text{K.7})$$

K.3 Properties

Because of the fact that the likelihood fit has converged, i.e., the likelihood is at a minimum, the sWeights \mathcal{P} have the following useful properties.

1. Maximum likelihood sum rule

$$\sum_{e=1}^N \frac{f_j(y_e)}{\sum_{k=1}^{N_s} N_k f_k(y_e)} = 1, \quad \forall j$$

2. Variance matrix sum rule

$$\sum_{i=1}^{N_s} N_i \mathbf{V}_{ij}^{-1} = 1$$

3. Covariance matrix sum rule

$$\sum_{j=1}^{N_s} \mathbf{V}_{jl} = N_l$$

The third sum rule is of vital importance in the context of this analysis. Summing over the elements in a row or a column in the covariance matrix, gives the yield for the corresponding sample. Provided this property is satisfied, we can then just rebin the events in the variable “dibaryon invariant mass” to account for reconstruction efficiency and the dependence of the branching fraction on this variable.

APPENDIX L

VERTEX FITTING

Combining reconstructed objects to create decay trees is done by adding the momentum information from the reconstructed objects. The resolution can be greatly improved by taking into account the fact that two or more objects originate from the same point. A vertex fitting algorithm can be used to find this point in space where one particle decays into two or more reconstructed objects. Using the information on the vertex can then in principle be used to improve the measurements of the decay products by treating the vertex as an additional point of measurement. In this analysis, the two algorithms `Cascade` and `Treefitter` are used. `Cascade` is a generic algorithm capable of fitting any number of tracks and applying constraints.

`Treefitter` is a Kalman algorithm specifically designed to deal with decay chains and capable of handling a number of constraints. The advantage of a Kalman vertex fitter over conventional algorithms is that the latter require inversion of the full covariance matrix, whereas the former requires only the inversion of a matrix of the size of one measurement, resulting in a large increase in computational speed.

L.1 A Brief Introduction to the Kalman Algorithm for Vertex Fitting

The reconstruction of B decays can involve simple addition of two Lorentz vectors, as in the search for the decay $B \rightarrow \gamma\gamma$, but most analyses attempt to build complicated decay chains that involve charged tracks and neutral particles and extend over many generations. In this case the mass resolution of the reconstructed B candidate can be greatly improved by making use of the information that two or more tracks are coming

from one and the same point in space. Additionally, measurements of time-dependent CP violation depend crucially on the precise determination of the B decay vertex. In *BABAR* a vertex fitting algorithm to handle these decay chains was developed based on a Kalman algorithm.

In general, the vertex fit is carried out by minimizing a χ^2 value, which can be defined as the sum of contributions from all individual measurements with errors.

$$\chi^2 = \sum \chi_i^2 = \sum r_i^T(x) V_i^{-1} r_i(x)$$

where $r_i = m_i - h(x)$ is the residual of the measurement, i.e. the difference between measurement and hypothesis. This value can then be minimized using standard minimization routines. The variance in the parameter set x can be found via error propagation to

$$C(x) = 2 \left(\frac{\partial^2 \chi^2}{\partial x^2} \right)^{-1}$$

This procedure, however, requires the inversion of a matrix whose dimension is proportional to the number of tracks in the fit. Applying constraints adds to the size of the matrix. The computing complexity for the inversion of a matrix scales as $O(n^3)$, so that for large matrices a more efficient algorithm can result in a great increase in speed, which is essential to apply this algorithm to the large sample of events in the *BABAR* data store.

A *progressive fit* only computes a local χ^2 , which is then improved in an iterative process. For each measurement constraint the contribution to the current value of the χ^2 is defined in terms of the current measurement and the values for the previously best estimate

$$\chi_k^2 = (x - x_{k-1})^T C_{k-1}^{-1} (x - x_{k-1}) + (h_k(x) - m_k)^T V_k^{-1} (h_k(x) - m_k)$$

Using the least-squares approach, this equation can be solved for x , i.e. we are looking for an updated result taking into account the current measurement. This leads to the equation

$$C_{k-1}^{-1} (x - x_{k-1}) + H_k^T V_k^{-1} (h_k(x) - m_k) = 0$$

where $H_k = \partial h / \partial x|_{x_{k-1}}$ is the derivative of the measurement and we assume linearity of the measurements, i.e. $h_k(x_k) = h_k(x_{k-1}) + H_k(x_k - x_{k-1})$. The solution of this equation then becomes the new best estimate if more measurements are available. After the first iteration of finding the solution taking into account all measurements, the value for x could still depend on the initial value x_0 . Therefore this procedure is repeated with the result x of the previous iteration as a new initial value x_0 until the value for the χ^2 converges.

REFERENCES

- [1] M. Misiak *et al.* , *Phys. Rev. Lett.* **98** (2007) 022002.
- [2] C.-K. Chua and W.-S. Hou *Eur. Phys. J.* **C29** (2003) 27–35.
- [3] C. Q. Geng and Y. K. Hsiao , *Phys. Lett.* **B610** (2005) 67–73.
- [4] S. L. Glashow, J. Iliopoulos, and L. Maiani , *Phys. Rev.* **D2** (1970) 1285–1292.
- [5] S. Weinberg , *Phys. Rev. Lett.* **19** (Nov, 1967) 1264–1266.
- [6] A. Salam. Originally printed in *Svartholm: Elementary Particle Theory, Proceedings Of The Nobel Symposium Held 1968 At Lerum, Sweden*, Stockholm 1968, 367-377.
- [7] M. Peskin, *Introduction to Quantum Field Theory*. Addison-Wesley Pub. Co, Reading, 1995.
- [8] N. Cabibbo , *Phys. Rev. Lett.* **10** (Jun, 1963) 531–533.
- [9] M. Kobayashi and T. Maskawa , *Prog. Theor. Phys.* **49** (1973) 652–657.
- [10] W. Schmidt-Parzefall *Nuclear Physics B - Proceedings Supplements* **3** (1988) 257–287.
- [11] C. Bebek, K. Berkelman, E. Blucher, J. Byrd, D. G. Cassel, E. Cheu, D. M. Coffman, T. Copie, G. Crawford, R. DeSalvo, J. W. DeWire, P. Drell, R. Ehrlich, R. S. Galik, B. Gittelman, S. W. Gray, A. M. Halling, D. L. Hartill, B. K. Heltsley, J. Kandaswamy, R. Kowalewski, D. L. Kreinick, Y. Kubota, J. D. Lewis, N. B. Mistry, J. Mueller, and R. Namjoshi , *Phys. Rev. Lett.* **62** (Jan, 1989) 8, .
- [12] V. Chernyak and I. Zhitnitsky *Nuclear Physics B* **345** (Nov, 1990) 137–172.
- [13] e. . Tran Thanh Van, J. Gif-sur-Yvette, France: Ed. Frontieres (1989) 612 p. (Moriond particle physics meetings - Leptonic session).C.
- [14] Belle Collaboration, K. Abe *et al.* , *Phys. Rev. Lett.* **88** (2002) 181803.
- [15] BELLE Collaboration, K. Abe *et al.* , *Phys. Rev.* **D71** (2005) 072007.
- [16] Y. J. Lee *et al.* , *Phys. Rev. Lett.* **95** (2005) 061802.
- [17] Belle Collaboration, M. Z. Wang *et al.* , *Phys. Rev. Lett.* **90** (2003) 201802.
- [18] J. L. Rosner , *Phys. Rev.* **D68** (2003) 014004.

- [19] W.-S. Hou and A. Soni , *Phys. Rev. Lett.* **86** (2001) 4247–4250.
- [20] N. G. Deshpande, J. Trampetic, and A. Soni *Mod. Phys. Lett.* **3A** (1988) 749.
- [21] M. Jarfi, O. Lazrak, A. L. Yaouanc, L. Oliver, O. Pène, and J.-C. Raynal *Phys. Rev. D* **43** (Mar, 1991) 1599–1632.
- [22] H.-Y. Cheng and K.-C. Yang , *Phys. Rev.* **D66** (2002) 014020.
- [23] H.-Y. Cheng and K.-C. Yang , *Phys. Lett.* **B633** (2006) 533–539.
- [24] C.-K. Chua, W.-S. Hou, and S.-Y. Tsai , *Phys. Rev. D* **66** (Sep, 2002) 054004.
- [25] **BABAR** Collaboration, B. Aubert *et al.* , *Nucl. Instrum. Meth.* **A479** (2002) 1–116.
- [26] SLAC-418.
- [27] **BABAR** Collaboration, e. Harrison, P. F. and e. Quinn, Helen R. Papers from Workshop on Physics at an Asymmetric B Factory (BaBar Collaboration Meeting), Rome, Italy, 11-14 Nov 1996, Princeton, NJ, 17-20 Mar 1997, Orsay, France, 16-19 Jun 1997 and Pasadena, CA, 22-24 Sep 1997.
- [28] **GEANT4** Collaboration, S. Agostinelli *et al.* , *Nucl. Instrum. Meth.* **A506** (2003) 250–303.
- [29] J. R. Klein and A. Roodman , *Ann. Rev. Nucl. Part. Sci.* **55** (2005) 141–163.
- [30] D. J. Lange , *Nucl. Instrum. Meth.* **A462** (2001) 152–155.
- [31] T. Sjostrand , *Comput. Phys. Commun.* **82** (1994) 74–90.
- [32] H.-Y. Cheng and K.-C. Yang , *Phys. Lett.* **B533** (2002) 271–276.
- [33] **Belle** Collaboration, M. Z. Wang *et al.* , *Phys. Rev.* **D76** (2007) 052004.
- [34] **ARGUS** Collaboration, H. Albrecht *et al.* , *Z. Phys.* **C48** (1990) 543–552.
- [35] **BABAR** Collaboration, B. Aubert *et al.* , arXiv:hep-ex/0608020.
- [36] M. Pivk and F. R. Le Diberder , *Nucl. Instrum. Meth.* **A555** (2005) 356–369.
- [37] G. Cowan, *Statistical Data Analysis*. Clarendon Press, Oxford, 1998.
- [38] K. W. Edwards and Others *Phys. Rev.* **D68** (2003) 011102.
- [39] **BABAR** Collaboration, B. Aubert *et al.* , *Phys. Rev.* **D72** (2005) 051101.

- [40] **BABAR** Collaboration, B. Aubert *et al.* , arXiv:0804.1580v1 [hep-ex].
- [41] **BABAR** Collaboration, B. Aubert *et al.* , *Phys. Rev.* **D77** (2008) 051103.
- [42] **Belle** Collaboration, K. Abe *et al.* , *Phys. Lett.* **B511** (2001) 151–158.